

Ph.D. Thesis

**Interplay between electronic, magnetic and structural
instabilities in $\text{Ca}_{2-x}\text{Sr}_x\text{RuO}_4$:
A neutron scattering study**

submitted to the
Université Paris XI
for the degree of Doctor of Natural Science

Oliver Friedt

March 2003

External Examiner:

Prof. Dr. Manfred Sigrist
Dr. Louis-Pierre Regault

Date of Final Oral Examination:

June 20, 2003

Contents

| | | |
|----------|--|-----------|
| 1 | Introduction | 1 |
| 2 | Basic physical properties of $\text{Ca}_{2-x}\text{Sr}_x\text{RuO}_4$ | 3 |
| 2.1 | Superconductivity in Sr_2RuO_4 | 3 |
| 2.2 | The system $\text{Ca}_{2-x}\text{Sr}_x\text{RuO}_4$ | 6 |
| 3 | Experimental | 9 |
| 3.1 | Synthesis and Single-Crystal Growth of $\text{Ca}_{2-x}\text{Sr}_x\text{RuO}_4$ | 9 |
| 3.2 | Neutron Scattering | 12 |
| 3.2.1 | Powder Diffractometer | 14 |
| 3.2.2 | Single Crystal Diffractometer | 17 |
| 3.2.3 | Three-axis Spectrometer | 19 |
| 4 | The Phase Diagram of $\text{Ca}_{2-x}\text{Sr}_x\text{RuO}_4$ | 21 |
| 4.1 | Introduction | 21 |
| 4.2 | The Mott transition in Ca_2RuO_4 | 25 |
| 4.2.1 | The first order structural phase transition as a function of temperature | 26 |
| 4.2.2 | The crystal structure of the metallic phase | 30 |
| 4.2.3 | The pressure dependence of the crystal structure | 34 |
| 4.3 | The Mott transition in $\text{Ca}_{2-x}\text{Sr}_x\text{RuO}_4$ | 38 |
| 4.3.1 | Structural aspects of the metal insulator transition | 38 |
| 4.3.2 | Magnetic structure of $\text{Ca}_{2-x}\text{Sr}_x\text{RuO}_4$ | 41 |
| 4.3.3 | The metal-insulator transition in $\text{Ca}_{2-x}\text{Sr}_x\text{RuO}_4$ | 45 |
| 4.3.4 | Summary | 47 |
| 4.4 | The magnetically correlated metallic state | 48 |
| 4.4.1 | Structural analysis of $\text{Ca}_{1.8}\text{Sr}_{0.2}\text{RuO}_4$ by single crystal neutron diffraction | 49 |
| 4.4.2 | Neutron powder diffraction study on structural properties of $\text{Ca}_{1.8}\text{Sr}_{0.2}\text{RuO}_4$ | 61 |
| 4.4.3 | The second order structural phase transition as function of Strontium content x | 66 |
| 4.5 | The ferromagnetic instability and the rotational distortion | 68 |
| 4.5.1 | The crystal structure of $\text{Ca}_{1.5}\text{Sr}_{0.5}\text{RuO}_4$ | 68 |

| | | |
|--------------|---|------------|
| 4.5.2 | The evolution of the rotational distortion | 70 |
| 4.6 | Conclusion | 73 |
| Appendix 4.A | Results of the high resolution powder diffraction analyses on $\text{Ca}_{2-x}\text{Sr}_x\text{RuO}_4$ | 78 |
| 5 | Lattice Dynamics of $\text{Ca}_{2-x}\text{Sr}_x\text{RuO}_4$ | 83 |
| 5.1 | Introduction | 83 |
| 5.2 | Soft Mode character of the tilt transition in $\text{Ca}_{2-x}\text{Sr}_x\text{RuO}_4$ | 86 |
| 5.3 | The rotational mode | 93 |
| 5.4 | Summary | 95 |
| 6 | Quasi-Ferromagnetic Fluctuations in $\text{Ca}_{2-x}\text{Sr}_x\text{RuO}_4$ | 97 |
| 6.1 | Introduction | 97 |
| 6.2 | Magnetic Excitations related to the magnetic instability at $x_c=0.5$. . | 100 |
| 6.2.1 | Experimentally details | 100 |
| 6.2.2 | Evidence for strong magnetic fluctuations close to the zone center | 101 |
| 6.2.3 | The temperature dependence of the incommensurate signal . . | 110 |
| 6.3 | Variation of the Fermi surface topography | 114 |
| 7 | Summary | 119 |
| | References | 121 |

Chapter 1

Introduction

At the center of present-day interest in solid-state physics is the comprehension of the electronic states of materials in the intermediate region between a simple metal and a Mott-insulator where electronic correlations cannot be neglected. Well known examples for the variety of unconventional phenomena appearing just next to the Mott transition are the interplay between charge, orbital and spin degrees of freedom in transition metal oxides and the high T_c superconductivity in the layered perovskite cuprates [1]. Another example illustrating the intriguing and complex physics correlated with a Mott transition is the recently discovered layered perovskite system $\text{Ca}_{2-x}\text{Sr}_x\text{RuO}_4$ [2, 3].

This isoelectronic alloy series is quite unique, because of its extraordinary rich and fascinating phase diagram, in which the Mott insulator Ca_2RuO_4 evolves into the spin triplet superconductor Sr_2RuO_4 . Especially Sr_2RuO_4 has attracted significant attention interest during the last years, which aroused initially from its structural similarity to the high T_c cuprate superconductor $\text{La}_{2-x}\text{Ba}_x\text{CuO}_4$, with the characteristic quasi-two-dimensional network of CuO_2 planes replaced by RuO_2 [4, 5]. The present interest in this compound goes far beyond the simple comparison with the superconducting cuprates. It has been pointed out that Sr_2RuO_4 must be close to a ferromagnetic instability, because the 3-dimensional analog of this material, SrRuO_3 , is a ferromagnetic metal. Since ferromagnetic fluctuations eliminate the even-parity pairing channels for superconductivity, such as s-wave and d-wave pairing, it has been suggested that superconductivity in Sr_2RuO_4 should be accompanied by the triplet (p-wave) odd-parity pairing. Recent experiments support this scenario [5].

In addition to the triplet superconductivity in Sr_2RuO_4 , the system $\text{Ca}_{2-x}\text{Sr}_x\text{RuO}_4$ exhibits complex structural, electronic and magnetic properties [2, 3]. With the Ca substitution for Sr, superconductivity is rapidly destroyed and the system is successively driven to a nearly ferromagnetic metal for $x=0.5$. Upon further substitution the system finally transforms via a magnetically correlated state into an antiferromagnetic insulator for Sr concentrations $x < 0.2$. This phase diagram provides us, hence, with a good opportunity to study a number of remarkable phenomena, including itinerant magnetism, superconductivity, and the Mott transition. Since Sr and Ca are both divalent cations, these profound differences in the physical properties cannot be due to carrier doping. In fact, it turned out that the rich variety

of magnetic and electronic states in ruthenates are intimately related to structural distortions [6]. In order to get new insights into the relation between the structural modifications and the changes in the magnetic and electronic properties, caused by the Ca substitution, we have studied the phase diagram of $\text{Ca}_{2-x}\text{Sr}_x\text{RuO}_4$ over the whole region of x by neutron diffraction on powder and single-crystalline samples. In addition, the relation between the superconductivity and the magnetism in Sr_2RuO_4 , motivated our investigations of spin fluctuations in $\text{Ca}_{2-x}\text{Sr}_x\text{RuO}_4$ close to the magnetic unstable point $x=0.5$, by inelastic neutron scattering

The present Ph.D. thesis is organized as follows: in chapter 2 the basic physical properties of $\text{Ca}_{2-x}\text{Sr}_x\text{RuO}_4$ are presented. Here, the focus is put on the superconducting state of Sr_2RuO_4 . Furthermore, we will take a first look at the phase diagram of $\text{Ca}_{2-x}\text{Sr}_x\text{RuO}_4$. In the following chapter 3, we briefly comment on the preparation conditions for the studied polycrystalline and single crystalline samples, which we received from the Forschungszentrum Karlsruhe and the University of Kyoto. In addition, we present the successful results of our own attempts to grow single crystals of $\text{Ca}_{2-x}\text{Sr}_x\text{RuO}_4$ worked out with the collaboration of the Laboratoire de Physico-Chimie de l'Etat Solide of the University Paris-Sud. Furthermore, the basic ideas of neutron scattering techniques and the experimental setup of the utilized neutron diffractometers are presented.

In chapter 4 our experimental results on the evolution of the structural and magnetic properties with Sr substitution in $\text{Ca}_{2-x}\text{Sr}_x\text{RuO}_4$ as observed by elastic neutron scattering, are presented and discussed in detail. For low Sr concentrations ($x < 0.2$) the experiments reveal antiferromagnetic order and structural distortions of the ideal K_2NiF_4 structure type characterised by tilts and rotations of the RuO_6 octahedra. As a key result a clear correlation between characteristic changes of the Ru-O bonds and tilt angles and the metal-insulator transition and antiferromagnetic order is presented. Further indications of a strong coupling between the lattice and the magnetic and electronic properties in this system come from the observation that the suppression of the tilt distortion, observed for $x \simeq 0.5$, is accompanied by a critical increase of low temperature susceptibility.

In Chapter 5 a lattice dynamical study of the structural phase transition from the tetragonal to orthorhombic structure in $\text{Ca}_{2-x}\text{Sr}_x\text{RuO}_4$ with $0.2 \leq x \leq 0.5$ by inelastic neutron scattering is presented. Our study reveals that this phase transition, which can be characterized by the onset of a tilt of the RuO_6 octahedra, shows typical soft-phonon behavior.

Chapter 6 deals with the magnetic excitations in $\text{Ca}_{2-x}\text{Sr}_x\text{RuO}_4$ close to the concentration where the static low temperature susceptibility indicates nearness to ferromagnetism. Instead of usual paramagnons we find incommensurate scattering at wave vectors close to the zone center. These wave vectors are different from those observed in Sr_2RuO_4 and appear to be associated with topological changes of the Fermi surface. Finally, the present work is summarized and an outlook to future research issues is given in chapter 7.

Chapter 2

Basic physical properties of $\text{Ca}_{2-x}\text{Sr}_x\text{RuO}_4$

2.1 Superconductivity in Sr_2RuO_4

The discovery by Maeno *et al.* of superconductivity in high-quality crystals of Sr_2RuO_4 at about 1.5 K [4, 7] has attracted great scientific interest during the last years. This remarkable attention aroused on the one hand from the early theoretical suggestion that its superconducting state might be analogous to superfluid ^3He a spin-triplet state [8, 9] and on the other hand from its structural similarity to the high T_c cuprate superconductors. As shown in Fig. 2.1, Sr_2RuO_4 has the same K_2NiF_4 -type structure as the original high T_c cuprate superconductor, $\text{La}_{2-x}\text{Ba}_x\text{CuO}_4$, but without containing copper in the two-dimensional MeO_2 layers (Me=transition metal ion).

The K_2NiF_4 structure (also referred to as 214-structure) with tetragonal space group $I4/mmm$ is adopted by Sr_2RuO_4 down to lowest temperatures [10–13]. The cell parameters are $a = 3.87\text{\AA}$ and $c = 12.47\text{\AA}$ at room temperature. In this high-symmetry structure each ruthenium is coordinated to four O(1) oxygens in a perfect corner-linked array of square planes, with Ru-O(1) distances of approximately 1.94\AA (equals $a/2$). Two additional O(2) oxygens lie above and below each ruthenium (Ru-O(2) $\simeq 2.06\text{\AA}$), forming together with the four basal oxygens the RuO_6 octahedron. Layers of these corner-linked octahedra are topologically identical to those of the other known members of the Ruddlesden-Popper series $\text{Sr}_{n+1}\text{Ru}_n\text{O}_{3n+1}$, such as the perovskite SrRuO_3 ($n = \infty$, referred to as 113-structure) or the double perovskite $\text{Sr}_3\text{Ru}_2\text{O}_7$ ($n = 2$, referred to as 327-structure). While in the perovskite structure the RuO_6 octahedra are linked to adjacent layers via the apical oxygens, leading to a three-dimensional octahedral array, the RuO_2 layers in the 214-structure are separated in the c direction by rock-salt-like Sr-O blocks, reducing the dimensionality of the system from three to two. Furthermore, the adjacent RuO_6 octahedra layers are shifted by $[a/2, a/2, 0]$ with respect to each other.

In spite of the structural similarity between Sr_2RuO_4 and the high T_c cuprates the physical properties of the two superconductors are otherwise quite different. The stoichiometric compound La_2CuO_4 is an antiferromagnetic Mott insulator and metallic conductivity as well as superconductivity can be induced only upon doping carriers. On the other hand Sr_2RuO_4 is in the normal state a metallic Pauli paramagnetic material with thermodynamic properties which can be well described by a quasi-

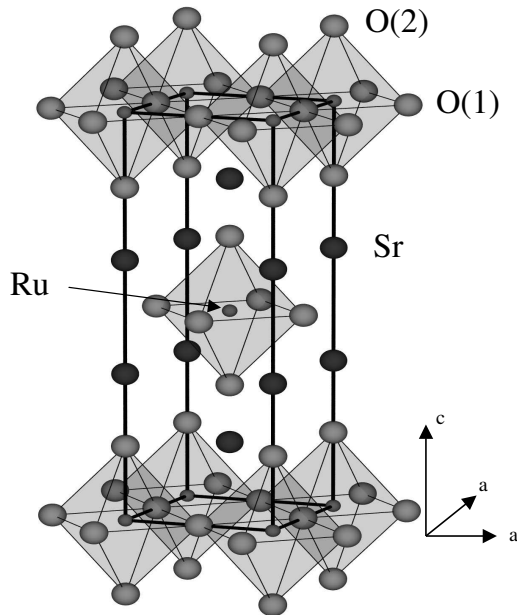


Figure 2.1: Layered perovskite (K_2NiF_4 -type) structure of Sr_2RuO_4 . Also shown are the directions of the tetragonal principal axes.

two-dimensional Fermi liquid: The electrical resistivity exhibits a T^2 dependence below 25 K and the T linear specific heat coefficient $\gamma = 39 \text{ mJ/molK}^2$ and the temperature-independent susceptibility, $\chi = 9.7 \times 10^{-4} \text{ emu/mol}$ are considerably enhanced over the free Fermi gas values [14, 15]. Consistent with the Fermi liquid description quantum oscillations revealed three cylindrical Fermi surfaces sheets, with enhanced effective electron masses (factors of 3-5) [16]. These sheets may be regarded as arising from the three conduction bands, called α , β , and γ , which originate from the hybridised Ru t_{2g} orbitals, $4d_{xz}$, $4d_{yz}$, and $4d_{xy}$, respectively (see Fig. 2.2) [17, 18]. This triply degenerate t_{2g} manifold is occupied by the four electrons of the tetravalent Ru^{4+} (low-spin $S=1$ state), while the e_g orbitals stay empty, since in contrast to the manganites the crystal field splitting between e_g and t_{2g} orbitals is larger than Hund's coupling energy.

The large mass enhancement in Sr_2RuO_4 which indicates the existence of strong carrier correlations and the fact that the related material, SrRuO_3 , shows ferromagnetism, led to the early theoretical suggestion by Rice and Sigrist that the superconducting state of Sr_2RuO_4 is formed by spin-triplet pairing, presumably with a p-wave symmetry of the superconducting order parameter [8, 19]. In their scenario the Cooper pairing is mediated by ferromagnetic spin fluctuations in analogy to the triplet superfluid phases of ^3He . In the meanwhile various experiments provided strong evidence for the unconventional superconductivity and in particular for the spin triplet pairing in Sr_2RuO_4 (for recent reviews, see Ref. [5, 20–23]). For instance,

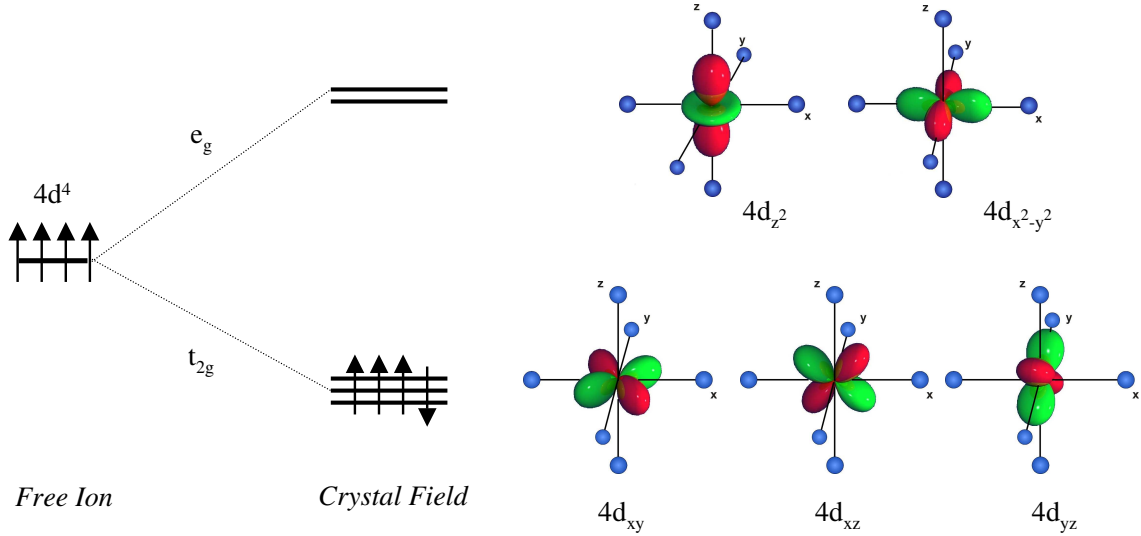


Figure 2.2: The schematic electronic configurations of Ru^{4+} , with the relevant valence state $4d^4$ in the low spin configuration with spin $S = 1$. The crystal field of the O^{2-} ions splits the five 4d states into threefold (t_{2g}) and twofold (e_g) subshells. The spatial density of the corresponding d-orbitals and the oxygen octahedron surrounding them are shown.

the superconducting transition temperature T_c is strongly suppressed by even small amounts of impurities and nuclear quadrupole resonance (NQR) experiments do not show any coherence peak in the nuclear spin-lattice relaxation rate $1/T_1$ below T_c [24]. While these experiments indicate that the pairing symmetry is unconventional, the most direct evidence for spin-triplet pairing is the absence of detectable change in the spin susceptibility with the onset of superconductivity as measured by ^{17}O Knight shift [25] and polarized neutron scattering [26]. In addition, muon spin resonance experiments in zero field have revealed a spontaneous internal magnetic field for $T < T_c$, implying a time reversal symmetry breaking superconducting state [27]. Such states can arise in a simple manner only with a p -wave spin triplet pairing.

While the above mentioned experiments indicate the realisation of an isotropic p -wave state, which would lead to a full gap (without nodes) on the Fermi surface, recent experiments have revealed that the situation is not so simple. Inelastic neutron scattering measurements detected sizeable incommensurate antiferromagnetic fluctuations, but did not observe any enhancement of ferromagnetic components [28–30], which cast some doubt on the unique role of ferromagnetism for the understanding of superconductivity in Sr_2RuO_4 . Furthermore, the power law temperature dependence of the specific heat [31, 32], penetration depth [33], ultrasonic attenuation [34], NQR relaxation rate $1/T_1$ [35], and thermal conductivity [36, 37] in the superconducting state require a superconducting gap which vanishes along lines on

the Fermi surface. Such a gap function would be incompatible to the early proposed superconducting state with a complete energy gap [5, 38]. In order to resolve this controversy several new theoretical models have been suggested in literature, which are currently under intensive debate. Most of these propose a f -wave state with line nodes in the order parameter [39–42], which give a consistent description of the reported thermodynamic properties of Sr_2RuO_4 . An alternative scenario has been proposed by Zhitomirsky and Rice based on a multi-gap model [43]. According to this model the superconductivity arises mainly in the single γ band (“active” band) with a nodeless p-wave order parameter, while a secondary gap with line nodes develop simultaneously in the α and β bands (“passive” bands) due to an interband proximity effect. Within this approach the authors could reproduce perfectly the temperature dependence of the specific heat and the recent observation of a double superconducting transition in the specific heat under a magnetic field agrees, furthermore, with this model [44]. In regard of the incommensurate antiferromagnetic fluctuations the multi-gap scenario is also coherent since these fluctuations are related with the passive α and β bands, while in the active γ band ferromagnetic spin fluctuations are slightly enhanced, because of a Van Hove singularity near the Fermi level [17, 18, 45]. However, an unambiguous determination of the symmetry of unconventional superconductivity in Sr_2RuO_4 has to await further experimental and theoretical studies.

2.2 The system $\text{Ca}_{2-x}\text{Sr}_x\text{RuO}_4$

When replacing Sr through the smaller but *isovalent* Ca one finds an extraordinarily rich phase diagram, with a variety of magnetic and metallic phases [2, 3, 46]. With the Ca substitution superconductivity is rapidly destroyed and the system evolves successively from a two-dimensional Fermi liquid to a nearly ferromagnetic metal for $x=0.5$. Upon further substitution the system finally transforms via a magnetically correlated state into an antiferromagnetic insulator for Sr concentrations $x < 0.2$. The isoelectronic system $\text{Ca}_{2-x}\text{Sr}_x\text{RuO}_4$ connects, hence, two quite distinct ground states – the spin triplet superconductor Sr_2RuO_4 on one side and the antiferromagnetic Mott insulator Ca_2RuO_4 on the other side – through intermediate regions with quite unconventional phenomena. Since Sr and Ca are both divalent cations these differences cannot be due to carrier doping as in cuprates, so that changes to the band filling and the band width are necessary to explain the insulating ground state of Ca_2RuO_4 . As will be discussed in detail in chapter 4 we have revealed by neutron scattering that all these different magnetic and electronic phenomena observed for $\text{Ca}_{2-x}\text{Sr}_x\text{RuO}_4$ are intimately coupled to structural distortions caused by the Ca substitution.

From these experiments three types of structural distortions have been identified. First, the smaller ionic radius of Ca implies a rotation of the RuO_6 octahedra around

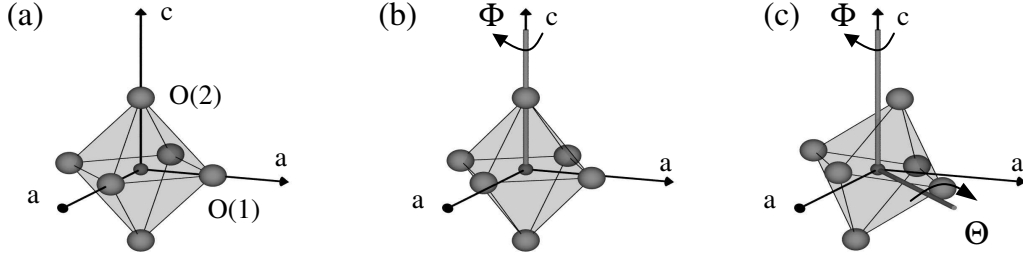


Figure 2.3: The RuO_6 octahedron in different tilt and rotational distorted forms: (a) the undistorted tetragonal $I4/mmm$ structure ($\Phi = \Theta = 0^\circ$), (b) rotation of the octahedron around the c axis ($\Phi \neq 0^\circ$, $\Theta = 0^\circ$) (c) combined tilt and rotational distortion of the octahedron ($\Phi \neq 0^\circ$, $\Theta \neq 0^\circ$).

the c -axis with a rotation angle Φ (see Fig. 2.3 (b)) which increases with decreasing Sr concentration x . The observed rotation angles are typically several degrees, with values up to 13.6° . Already, Sr_2RuO_4 itself which is stable in the tetragonal $I4/mmm$ structure seems to be close to a rotational instability, as can be deduced from the rather low frequency of the corresponding phonon mode [47]. For a Sr content $x = 0.5$ a second structural deformation occurs at low temperatures which can be characterized by an additional rotation about an axis lying in the (a, b) plane with an angle Θ (see Fig. 2.3 (c)). Throughout this work we will distinguish between these two rotational distortions in designating all deformations where the octahedra are turned around the long axis as *rotational* distortions and all deformations where the octahedra are tilted around an axis lying in the RuO_2 planes as *tilt* distortions, in analogy to the characteristic deformations in isostructural $\text{La}_{2-x}\text{Sr}_x\text{CuO}_4$ [48–51]. While the rotation of the RuO_6 octahedra about the crystallographic c axis leads only to a displacement of the oxygen atoms in the RuO_2 layers [O(1)], the tilting of the octahedra involves motions of both in-plane and apical oxygen atoms. Particularly, the different combinations of the tilt and rotational deformations give rise to a series of structural phases in $\text{Ca}_{2-x}\text{Sr}_x\text{RuO}_4$. A third type of structural distortions is characterized by a flattening of the RuO_6 octahedra with an increase of the in-plane bond lengths and a reduction of the Ru-O(2) distance. This compression of the RuO_6 octahedra occurs simultaneously with the metal-insulator transition as a function of temperature for Sr concentrations below $x=0.2$.

Already the variations of the room temperature lattice parameters with Sr content x reported by Nakatsuji *et al.* [3, 52], which are shown in Fig. 2.4, give strong indications for the described structural distortions. While the unit cell volume increases linearly over the entire concentration range as might be expected qualitatively by the substitution of the smaller Ca ion, there is a sudden change in the rate of decrease of the lattice parameter a and c at $x=0.2$ and a simultaneous orthorhombic splitting of the in-plane parameters. This kind of distinct changes reflect the onset of the addi-

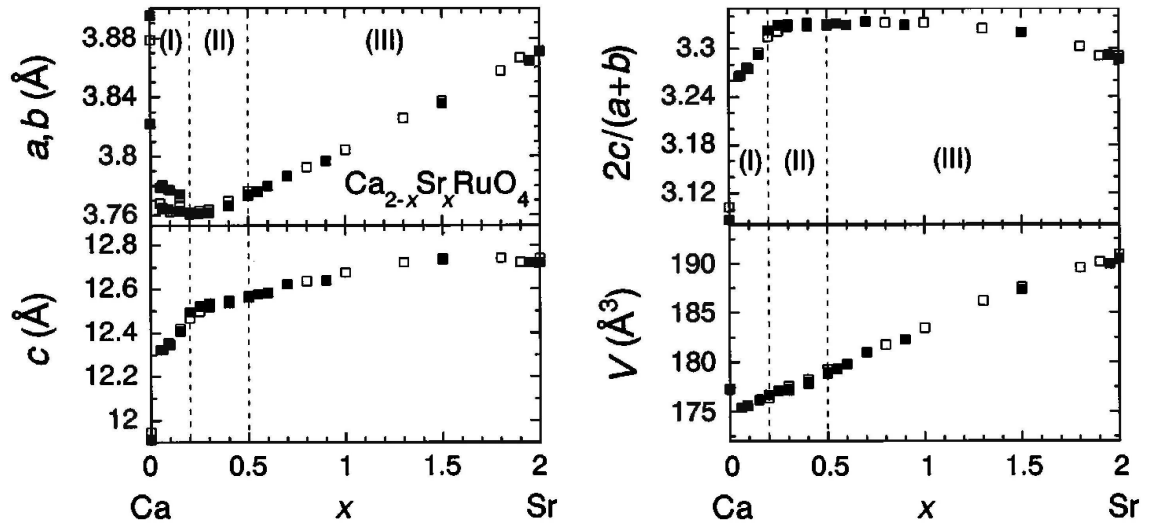


Figure 2.4: Variation of the room temperature lattice parameters with Sr content x in the $\text{Ca}_{2-x}\text{Sr}_x\text{RuO}_4$ system, according to Nakatsuji *et al.* [3, 52]. The open and solid squares represent parameters which were obtained from polycrystalline and single-crystalline samples, respectively.

tional tilt distortion of the RuO_6 octahedra at room temperature, as will be shown in section 4.4. Finally, the discontinuous jump of the cell parameters close to $x=0$, can be related to the change from a slightly elongated to a compressed RuO_6 octahedra with an increased tilt angle, which coincides with the metal-insulator transition.

Chapter 3

Experimental

3.1 Synthesis and Single-Crystal Growth of $\text{Ca}_{2-x}\text{Sr}_x\text{RuO}_4$

Apart of all advantages of neutron scattering the intensity of the neutron beam, obtained from a nuclear reactor, is effectively very weak in comparison to other scattering techniques. However, to benefit from its interesting properties as a probe for the study of condensed matter a rather large quantity of the material under investigation is needed. In the following we will briefly comment on the synthesis conditions for the polycrystalline samples as well as for the single-crystals of $\text{Ca}_{2-x}\text{Sr}_x\text{RuO}_4$, used in this study.

Synthesis of polycrystalline samples

The studied powder samples of $\text{Ca}_{2-x}\text{Sr}_x\text{RuO}_4$ (cf. Table 4.3) were synthesized by Dr. P. Adelman from the Forschungszentrum Karlsruhe in Germany and by Dr. S. Nakatsuji from the University of Kyoto in Japan. The sample preparation is based on a standard ceramic processing method, which consists in mixing stoichiometric amounts of the appropriate carbonates and oxides. The mixture is then pressed into pellets and sintered several times at high temperature. In the case of $\text{Ca}_{2-x}\text{Sr}_x\text{RuO}_4$ the synthesis is rather difficult, since the appropriate heating temperature and atmosphere restricts the sample preparation to specific conditions, that are heavily dependent on x .

Nevertheless Nakatsuji *et al.* [52, 53] have succeeded in synthesizing single-phase powder samples of $\text{Ca}_{2-x}\text{Sr}_x\text{RuO}_4$ in the entire solution range, by tuning carefully the heating temperature and atmosphere for each value of x . They reported that the formation of the 214 phase may be favored by reducing conditions, which can be achieved in the sintering process by using rather high temperatures and/or reducing atmospheres. Since under high heating temperatures the evaporation of RuO_2 increases and the use of reducing atmospheres encourages the reduction of RuO_2 into Ru metal [54], the synthesizing conditions are considerably limited. The single-phase powder samples used in this study could be obtained by adjusting the heating

| Composition | a (Å) | c (Å) | V (Å ³) | Size (mm ³) | Crystal Growth |
|---------------------|-----------|------------|---------------------|-------------------------|----------------------|
| x=0.15 | 5.338(1) | 12.435(3) | 354.3(1) | 12 | S. Nakatsuji |
| x=0.20 | 5.310(1) | 12.487(2) | 352.1(1) | 14 | " |
| x=0.50 | 5.335(1) | 12.569(3) | 357.8(1) | 3 × 20 | " |
| x=0.50 ^c | 5.3407(3) | 12.5760(6) | 358.70(4) | 68 | P. Reutler/O. Friedt |
| x=0.52 ^a | 5.337 | 12.577 | 358.2 | 2 × 70 | S. Nakatsuji |
| x=0.55 | 5.333(2) | 12.556(3) | 357.1(1) | 14 | " |
| x=0.62 | 5.345(2) | 12.594(2) | 359.8(1) | 350 | " |
| x=1.00 ^b | 5.3829(1) | 12.6761(3) | 367.30(1) | 55 | " |
| x=2.00 ^c | 5.4730(5) | 12.7376(7) | 381.53(5) | 600 | P. Reutler/O. Friedt |

^a Taken from [52].

^b 3T.2 result from the nominally equivalent powder sample (cf. Tab. 4.3).

^c Determined by powder X-ray diffraction.

Table 3.1: List of studied Ca_{2-x}Sr_xRuO₄ single-crystals, their size and their room temperature cell parameters, which were determined on 3T.1. Additionally we give these parameters for two single crystals, which were synthesized in collaboration with the Laboratoire de Physico-Chimie de l'Etat Solide of the University Paris-Sud.

temperature between 1100 and 1570°C and an O₂ partial pressure between 0 and 0.01 bar in Ar+O₂ atmosphere with the total pressure of 1 bar.

All samples were characterized by X-ray diffraction and magnetic measurements. The systematic changes of the lattice parameter indicate well the homogeneous mixing of Ca and Sr in the samples [3, 52] (see also Fig.2.4). Furthermore, thermogravimetric studies of some representative samples, signify a stoichiometric oxygen content in this compounds [55].

Single Crystal Growth

The studied single crystals of Ca_{2-x}Sr_xRuO₄ were grown by Dr. S. Nakatsuji using a floating zone method. This method consists of melting a rod, composed of the presintered starting material and mounted without any physical contact with a crucible in the focus of double-elliptical mirrors. The heat is delivered by the infrared radiation of two halogen lamps (for details see [56, 57]). The growth conditions of the Ca substituted series were adapted from the well elaborated single crystal growth of Sr₂RuO₄ [52, 53, 58–61].

Due to the high temperatures ($\simeq 2200^\circ\text{C}$) necessary to melt Sr₂RuO₄ the volatility of RuO₂ is a serious problem for the single crystal growth of 214 ruthenates by the floating zone method. In order to compensate for this loss, the ratio of Ca/Sr to Ru in the ceramic feed rod has to be as high as 2 to 1.15 and the crystal growth has to be performed at an extremely fast rate of $\simeq 35\text{ mm/h}$ (note that the higher Ru content serves also as a self-flux). With this method one obtains high-quality

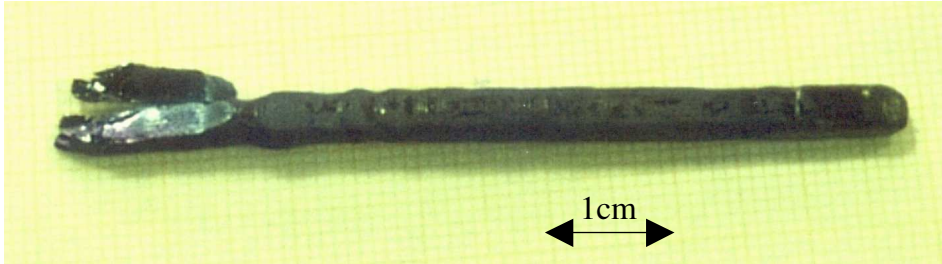
Sr_2RuO_4 

Figure 3.1: Photo of a large Sr_2RuO_4 single crystal grown by the floating-zone method at the Laboratoire de Physico-Chimie de l'Etat Solide. The left part of the crystal corresponds to the beginning of the crystal growth and is composed of several single crystals (note the breaking of the crystal). The remaining 50 mm of the crystal is single domain, with no important mosaic spread. Note the two facets running parallel to the growth direction on opposite sides of the rod. These facets were found to be parallel to the ab -planes.

single crystals of Sr_2RuO_4 as large as $\simeq 80 \times 4 \times 3 \text{ mm}^3$, while for the Ca substituted system the size of single crystals is still substantially smaller, cf. Table 3.1.

The studied single crystals have been characterized, with regard to their single crystallinity and the possible intergrowth of 113- or 327-contaminations, on the thermal neutron two-axis diffractometer 3T.1. All crystals were found to be single crystalline over their entire crystal volume with a typical mosaic spread¹ of $\simeq 0.01^\circ$. Only negligible signals ($< 10^{-2} \dots 10^{-3}$ of fundamental reflections) from 113- or 327-contaminations were detected in some crystals. Additionally the room temperature cell parameters were determined on 3T.1. For this purpose the incident wavelength of the diffractometer has been calibrated with a Cu powder sample and a maximal set of Bragg reflections was acquired. The results are given in Table 3.1.

In addition to the single crystals which we received from Dr. S. Nakatsuji, we performed the crystal growth of $\text{Ca}_{2-x}\text{Sr}_x\text{RuO}_4$ by the floating zone method in collaboration with the Laboratoire de Physico-Chimie de l'Etat Solide of the University of Paris XI. The crystal preparation for two compositions $x=2.0$ and 0.5 were carried out using a commercial image furnace equipped with double-elliptical mirrors (NEC Machinery, Model SC-N15HD). The detailed preparation method was adapted from Ref. [52, 61] and will not be repeated here. In the case of Sr_2RuO_4 we succeeded in growing a rather large crystal with dimensions of $\sim 3 \times 4 \times 65 \text{ mm}^3$, which shows a shiny, bluish black surface. The crystal rod has a slightly oval cross section, with two large facets on opposite sides, as may be seen in Fig. 3.1. The phase purity of

¹The rocking scans determining the mosaic spread were performed on the three axis spectrometer 4F.2, due to the better resolution.

this sample was determined by powder X-ray diffraction on crushed parts and the bulk crystalline quality was checked by neutron scattering at the beam line 3T.1. Apart from the beginning of the crystal growth, the entire rod was found to be single crystalline with a high crystalline quality, as demonstrated by small width of the rocking curves ($< 0.5^\circ$ FWHM). Moreover, the acquired X-ray diffraction patterns did not show any contribution of an impurity phase and the obtained cell parameters, given in Table 3.1, are in good agreement with those reported in literature [4, 12, 58]. In spite of its good crystalline quality, a.c. susceptibility measurements at the University of Karlsruhe on two crystals cut from the rod gave no indication of superconductivity down to 0.3 K [62]. From early studies of the impurity effects in Sr_2RuO_4 it is well known that already extremely low levels of impurities or slight structural inhomogeneities lead to a rapid suppression of T_C [7, 63]. Therefore, it can not be excluded that contaminations by the Al_2O_3 crucible, utilized during the rod preparation, destroys superconductivity in our sample. In order to avoid any contamination via the crucible it might be helpful in future to perform already the sintering of the feed rod in a crucible-free process, i.e. in a rotating lifter furnace.

For the performed crystal growth of the composition $\text{Ca}_{1.5}\text{Sr}_{0.5}\text{RuO}_4$ the volatility of RuO_2 was an even more serious problem than in the case of Sr_2RuO_4 , due to the higher melting temperature. Especially, the deposit of the heavily evaporated RuO_2 on the interior of the silica tube resulted in a reduction of the infrared radiation on the rod. In order to retain a constant liquid zone volume, it was necessary to increase frequently the heating power, limiting finally the growth process to just ~ 20 mm of the feed rod before the maximal heating power was reached. The obtained $\text{Ca}_{1.5}\text{Sr}_{0.5}\text{RuO}_4$ cylinder decomposed after one night exposed to air in several tiny crystals with shiny black surfaces and one bigger part with dimensions $3 \times 3 \times 8 \text{ mm}^3$. Powder X-ray measurements on crushed parts of the small crystals showed that these specimen consists basically of a single 214 phase with only slight contaminations of $(\text{Ca}, \text{Sr})\text{RuO}_3$ ($< 5 \text{ vol}\%$). Investigations of the bigger crystal by neutron diffraction demonstrated that the entire specimen is single crystalline, with only a small amount of the expected perovskite compound. These first own attempts to prepare single crystals of $\text{Ca}_{2-x}\text{Sr}_x\text{RuO}_4$ by the floating zone technique, have shown that adequate samples can likely be grown. In future it should be easy to overcome the remaining difficulties and optimize the existing growth parameters of the rather complicated preparation process.

3.2 Neutron Scattering

Neutron scattering is a very powerful tool for the study of condensed matter from many points of view. The thermal neutron is a particle that allows the study of both structural and dynamical aspects of matter, due to its absence of an electrical charge, due to a wavelength (1-3 Å) comparable to that of interatomic distances,

due to an energy (1-100 meV) of the order of the energy of excitations (phonons, magnons, etc.) and due to a magnetic moment ($\mu_n = 1.91 \mu_N$, in units of the nuclear magneton μ_N).

In respect to other *elastic* scattering techniques, like X-ray or electron diffraction, neutrons provide, due to their physical properties, significant additional information, where the other techniques fail. One of the crucial differences between neutrons and X-rays for a nuclear structure determination is that neutrons interact with the nuclei of the atoms rather than with the electron cloud. As a result of this, the intensity of the diffraction peaks for neutrons is not dependent on the number of electrons, like for X-rays, but follows a much more irregular pattern. This is particularly useful when dealing with light atoms in the presence of heavier atoms, like in the present study. For example, the ratio of the square of the atomic form factor and accordingly the ratio of the scattering length for neutrons – quantities which are approximatively equivalent to the diffracted intensity – of Ca-Sr-Ru-O is 0.21/0.75/1.0/0.03 and 0.67/1.0/1.0/0.82, respectively [64]. While neutron scattering is thus very sensitive to subtle changes in the oxygen positions and permits their determination with reliable accuracy, with X-ray diffraction little or no information on the oxygen position is accessible.

The neutron scattering length shows not only an irregular, element specific distribution, but it is also independent of the scattering angle Θ . This can be attributed again to the fact that the neutron interacts strongly with the atomic nuclei, whose dimension is small in comparison with the wavelength. In contrast, the atomic form factor of X-rays decreases rapidly with $\sin(\Theta)/\lambda$, which makes an exact determination of temperature factors with X-rays extremely difficult. This follows directly from the weighted contribution of the temperature factors to the intensity via the Debye-Waller factor. Since the Debye-Waller factor varies with $(\sin\Theta)/\lambda)^2$ it affects in particular the diffracted intensity at large scattering angles. Consequently, neutron diffraction is more adapted for the precise determination of atomic displacement parameters, which can be even anisotropic as for oxygen in $\text{Ca}_{2-x}\text{Sr}_x\text{RuO}_4$.

Another important feature of neutrons is their interaction with unpaired electron spins, making them a powerful probe for magnetic scattering. The magnetic moments of the neutrons and those of the atoms or ions with unpaired electron spins interact, giving rise to additional peaks in the diffraction pattern. While ferromagnets produce magnetic peaks, which are superimposed onto nuclear peaks, antiferromagnets lead to extra reflections in the pattern, as the magnetic cell is a supercell of the nuclear cell. Not only does magnetic neutron diffraction reveal the periodicity of the magnetic unit cell, but it also provides information about the magnitude and the direction of the ordered magnetic moment [66].

In addition to the so far presented significant advantages of neutron diffraction over other *elastic* scattering techniques, neutrons yield also the possibility of investigating dynamical processes in solids. The importance of neutrons for the study of such processes is due to the fact that the energy-momentum relation of neutrons

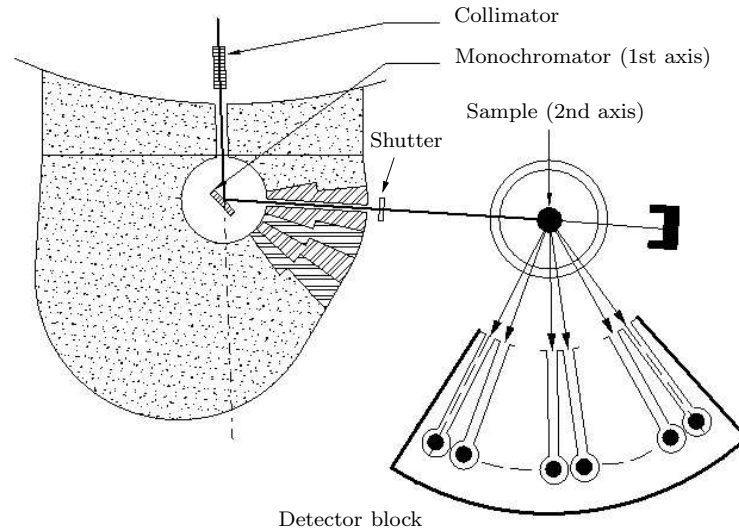


Figure 3.2: Schematic diagram of the high-resolution powder diffractometer 3T.2 [65].

corresponds to the energy ranges of excitations in solids. Inelastic neutron experiments probe the dispersion relation $\hbar\omega(\mathbf{k})$ of phonons or magnons throughout the whole Brillouin zone or other type of excitation appropriate to the system under study, like for example the magnetic excitations related to Fermi surface effects as observed in Sr_2RuO_4 [28, 30, 67].

In the following we give a brief description of the neutron spectrometers used for our studies. For a more detailed description of neutron diffraction techniques and for neutron scattering theory we refer to Ref. [68–71]. The structural studies exploring the (x-T) phase diagram of $\text{Ca}_{2-x}\text{Sr}_x\text{RuO}_4$ were carried out on the two powder diffractometers 3T.2 and G4.1, and supplementary single-crystal structure analyses were performed on the four-circle diffractometer 5C.2. For the inelastic neutron experiments, dealing (i) with the soft-mode behavior of the structural distortions in $\text{Ca}_{2-x}\text{Sr}_x\text{RuO}_4$ and (ii) with the magnetic excitations observed near $x_c \simeq 0.5$, the thermal three axis spectrometer 1T.1 was used.

3.2.1 Powder Diffractometer

High-resolution two-axis diffractometer 3T.2

Figure 3.2 shows the high-resolution powder diffractometer 3T.2 [65]. This two-axis spectrometer is used to acquire diffraction patterns over a wide range of scattering angles, permitting the refinement of magnetic and nuclear structures by the Rietveld method [72–74].

The thermal neutrons needed for this instrument are produced in the reactor

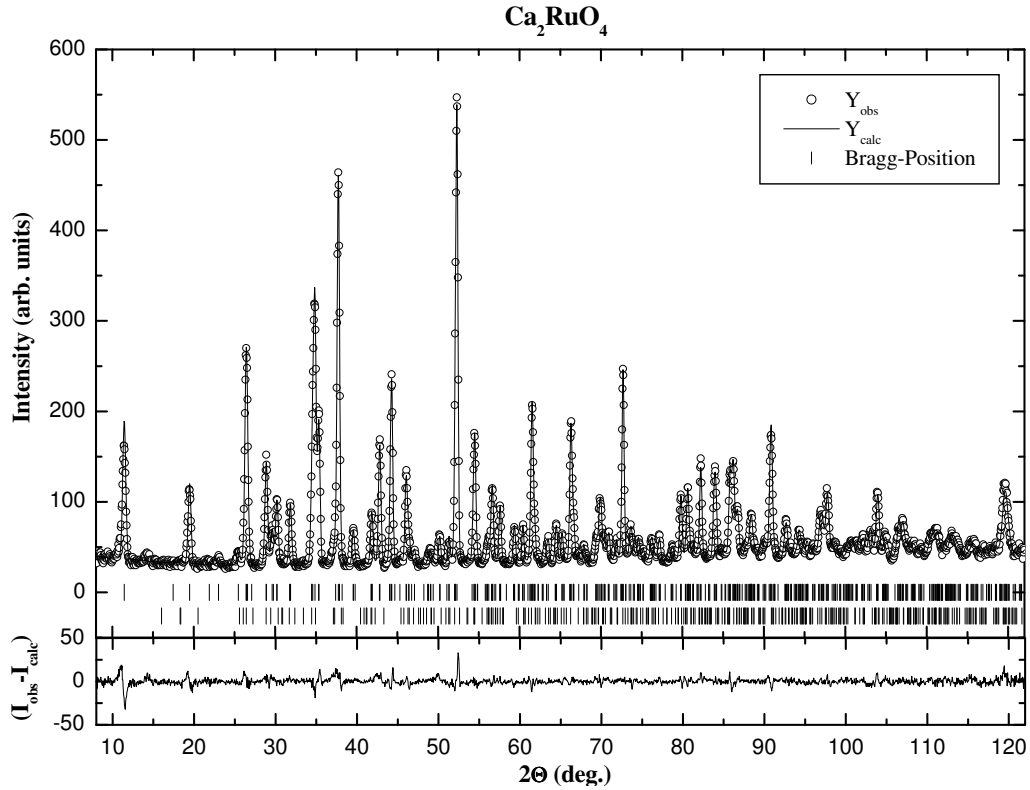
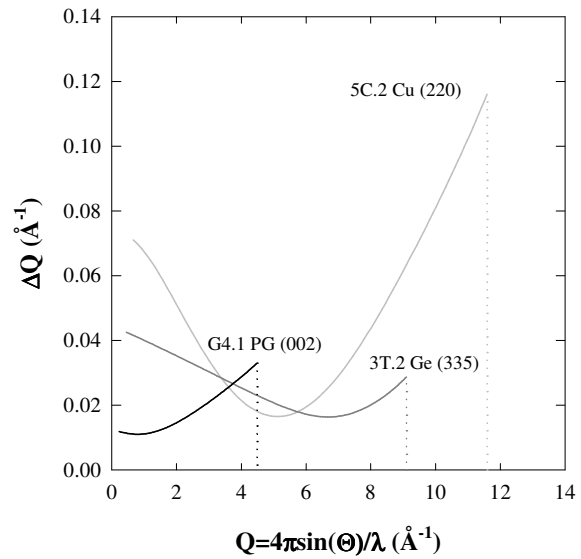


Figure 3.3: An example of Rietveld neutron powder diffraction pattern for Ca_2RuO_4 . The present data were collected at 400 K on the high-resolution diffractometer 3T.2. The vertical bars indicate the Bragg positions belonging to the main Ca_2RuO_4 phase (upper row) and those of the impurity CaRuO_3 phase (lower row).

and moderated by D_2O . An arrangement of several Germanium crystals is used for monochromating the white beam. The fixed wavelength for this diffractometer ($\lambda = 1.23 \text{ \AA}$) is selected from the (335) Bragg reflection of the monochromator crystals. The monochromatic beam of neutrons then falls on a polycrystalline sample which is contained in a cylindrical vanadium can. The neutrons diffracted by the sample are collected by a bank of 20 ^3He counting tubes arranged in a circle segment at 3° intervals, in order to reduce the counting time. In front of each detector a separate collimator with a fixed divergence of $10'$ is installed, ensuring together with the high monochromator take-off angle of 90° a high resolution up to large scattering angles. The whole detector block can be moved, usually in steps of 0.05° , so that an angular range of $5^\circ < 2\Theta < 125^\circ$ can be covered. With the used wavelength one gets thus a diffraction pattern with $0.5 < Q = 4\pi \sin(\Theta)/\lambda < 9.1 \text{ \AA}^{-1}$ and an instrument dependent momentum resolution which is shown in Fig. 3.4. A standard orange ILL-cryostat and a cryofurnace were used for regulating the temperature in-between 1.5 and 600 K. Due to the resolution optimized layout of this instrument complete scans

Figure 3.4: Comparison of the maximal accessible Q values and the experimental resolution, calculated by using the Caglioti's relation [75], of the two-axis diffractometer 3T.2 ($\lambda = 1.23 \text{ \AA}$), G4.1 ($\lambda = 2.43 \text{ \AA}$), and 5C.2 ($\lambda = 0.83 \text{ \AA}$).



take normally 24 hours, so that only a limited number of spectra can be collected as a function of temperature. In Fig. 3.3 a diffraction pattern for Ca_2RuO_4 at 400 K with the described set-up is shown.

The Rietveld method was used to extract the detailed structural information from the collected neutron data. The refinements were carried out using the FULLPROF program [76], developed by J. Rodríguez-Carvajal. Due to the large Q range available at 3T.2, reliable and precise refinements of the structural parameters and of the temperature factors can be performed.

High Flux two-axis diffractometer G4.1

Complementary to 3T.2, G4.1 is a two-axis diffractometer optimized for powder diffraction experiments requesting a high neutron flux [65], for example the determination of magnetic structures or the detection and characterization of structural phase transitions by scanning temperature. It is installed on the cold neutron guide G4 and exploits a variable range of wavelengths from 2.43 to 5.5 Å.

G4.1 is equipped with a vertically curved (002) pyrolytic graphite monochromator, giving an incident wavelength of $\lambda = 2.43 \text{ \AA}$. In order to suppress $\lambda/2$ contributions a pyrolytic graphite resonance filter is positioned between the monochromator and the sample. In contrast to 3T.2 the detector system of G4.1 consists of 800 linear multi-detector BF_3 cells, which span a 2Θ range of 80° . Furthermore the detector cells have no separate secondary collimation, avoiding an extra loss of neutron intensity. Nevertheless at small scattering angles ($2\Theta < 60^\circ$) where, for example in the studied system $\text{Ca}_{2-x}\text{Sr}_x\text{RuO}_4$ magnetic peaks are expected, a high Q -resolution can be achieved; the FWHM reaches a value of less than 0.3° (cf. Fig. 3.4). As for 3T.2 the whole detector system of G4.1 can be moved in steps of 0.02° in an accessible

angular range of $3 < 2\Theta < 120^\circ$. For the studied problems the detector block was left stationary, covering an angular range of $20 < 2\Theta < 100^\circ$. The acquisition of a typical data pattern took only 30-40 minutes, so a complete thermal variation of the diffraction patterns (1.5 - 300 K) could be achieved in one day. A standard orange ILL-cryostat ($1.5 < T < 300$ K) as well as a furnace ($RT < T < 1400$ K) were used to maintain the required temperatures.

In contrast to 3T.2 only Q -values up to 4.5 \AA^{-1} can be reached as a result of the longer incident wavelength of G4.1. This limited Q range prevents a full structure determination, with the refinement of all free structural parameters, by the Rietveld method (note that the number of observable reflections varies with Q_{max}^3). However reliable results could be obtained, together with the data from 3T.2, by fixing parameters not depending on temperature and constraining thermal parameters to the high-resolution data. Furthermore, the high flux at $\lambda = 2.43 \text{ \AA}$ and the large multi-detector of G4.1 facilitated the detection of weak magnetic peaks in the studied system, with the lower detection limit of $0.15 \mu_B$ for a long range ordered antiferromagnetic moment.

3.2.2 Single Crystal Diffractometer

Four-Circle Diffractometer 5C.2

Figure 3.5 (a) shows the setup of the four-circle diffractometer installed on the hot beam 5C.2 of the Orphée reactor. This diffractometer was used for precise measurements of Bragg intensities up to very high momentum transfer of several single crystals in this thesis, permitting a detailed structural analysis.

The geometry of this instrument consists of a monochromator, a centric Eulerian cradle that orients the crystal relative to the neutron beam and a ^3He detector. The monochromator is a vertical focusing Cu-(220) crystal, giving an incident wavelength of $\lambda = 0.83 \text{ \AA}$. The detector can be moved independently to the Eulerian cradle horizontally, defining the scattering angle 2Θ and the diffraction plane. A ω -rotation turns the entire Eulerian cradle, which is schematically shown in Fig. 3.5 (b), around an axis normal to the diffraction plane. To orient the crystal in any direction in space the cradle consists of two further motions. These are the χ motion, around the vertical circle and the Φ motion, about the axis of the crystal support itself. These four angles are in general sufficient to bring a desired reciprocal lattice node to the diffraction plane, where the scattered intensity can be measured.

In order to obtain the integrated intensity of a Bragg reflection, the entire volume of the reciprocal lattice node has to be scanned. In practice this is realized by a ω or a $\omega - 2\Theta$ -scan. In a ω scan the detector is fixed at the appropriate 2Θ angle while the crystal is moved by a rotation of ω , corresponding to a transversal sampling of the chosen reciprocal lattice node. This scan mode ensures the complete integration of a Bragg reflection, since firstly an adequate detector-aperture is chosen and secondly

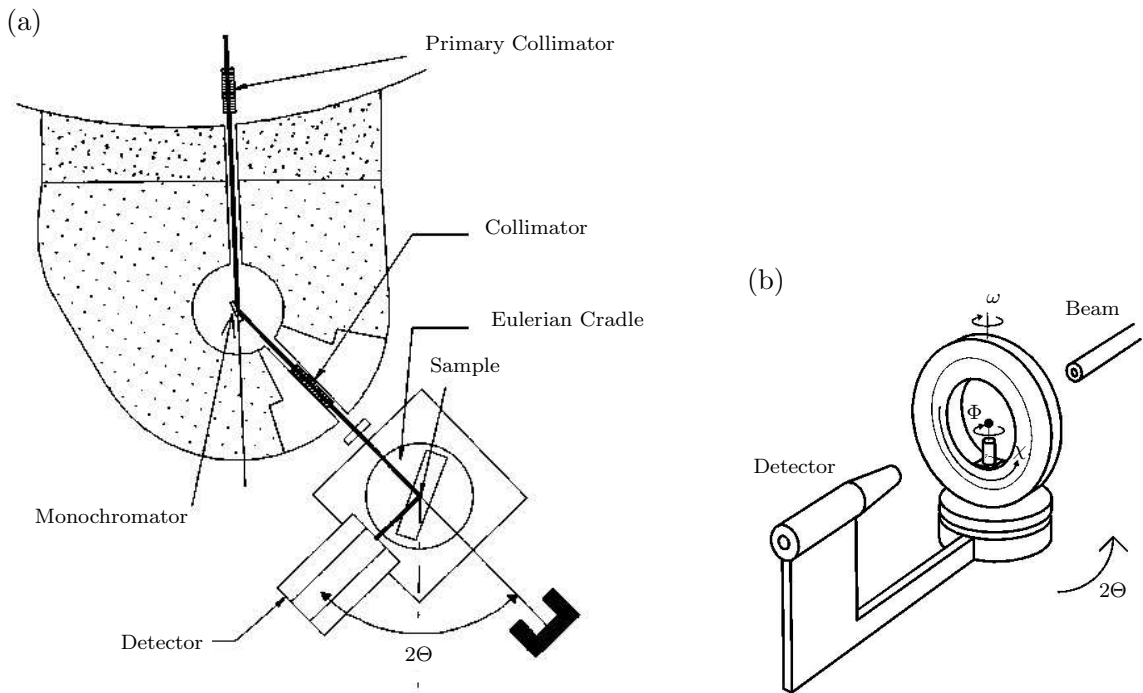


Figure 3.5: (a) Setup of the four-circle Diffractometer on the hot beam 5C.2; (b) A general sketch of the Eulerian cradle, which performs the χ and Φ motions and carries the crystal in the diffractometer [65].

the resolution of the four-circle diffractometer in χ direction is largely reduced, due to the vertical-focusing of the monochromator and the absence of a vertical collimation in-between reactor and monochromator. Above $2\theta \simeq 75^\circ$ the $\omega - 2\theta$ -scan mode was used, because of the finite wavelength distribution in the incoming beam and the enhanced angular splitting at high diffraction angles. In this scan mode the crystal is moved in the same way as for a ω -scan but the detector follows longitudinally the ω rotation at twice the angular speed of the crystal position.

The data treatment of the observed reflections and the structural refinement were carried out using the PROMETHEUS program package [77]. At first the integrated intensities were calculated by subtracting for each reflection the background and correcting the intensities by the Lorentz factor. In a next step the data was corrected for absorption effects, taking into account the individual crystal shape, and then the intensities of symmetrically equivalent reflections were averaged. This set of structure factors was then finally used to refine, by a least-square refinement, a given structure model. The neutron scattering lengths ($\times 10^{-12}$ cm) for the elements in the $\text{Ca}_{2-x}\text{Sr}_x\text{RuO}_4$ system used in the refinements were 0.470 for Ca, 0.702 for Sr, 0.703 for Ru, and 0.5803 for O [64].

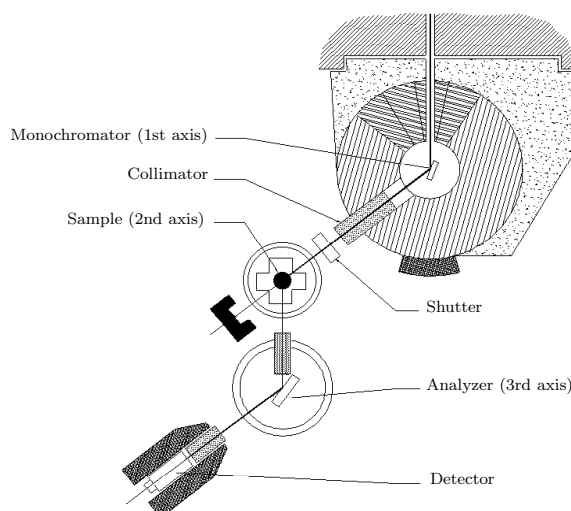


Figure 3.6: Schematic diagram of the three-axis spectrometer installed on the thermal beam 1T [65].

Two-axis diffractometer 3T.1

Another instrument, frequently used in this study, is the two axis diffractometer at the thermal beam 3T.1 [65]. This diffractometer exploits a wavelength range from $0.8 < \lambda < 2.4 \text{ \AA}$, operating yet in standard configuration with a vertically curved (002) pyrolytic graphite monochromator. The single ^3He detector covers an angular range of $0 < 2\Theta < 120^\circ$, corresponding to a maximum momentum transfer of 4.6 \AA^{-1} . In addition 3T.1 is equipped with a double goniometer, which may achieve tilts of $\pm 20^\circ$ of the sample out of the diffraction plane. This setup restricts however, in contrast to 5C.2, a single crystal diffraction study to reflections of a single layer in reciprocal space. Nevertheless 3T.1 permits due to its high flux at $\lambda = 2.37 \text{ \AA}$ the rapid measurement of characteristic superstructure reflections or of satellites as a function of temperature up to a lower detection limit of about 10^{-4} of the intensity of a strong fundamental reflection.

3.2.3 Three-axis Spectrometer

In addition to the so far described two-axis spectrometer, a three-axis spectrometer incorporates also an energy analyzer, which permits to measure the energy change of the neutrons during the scattering process. The energy analysis is performed by using the Bragg reflection from an analyzing single-crystal. The neutrons passing through the analyzer, with the appropriate energy, are then counted in the detector. The general layout of a three-axis spectrometer is shown in Fig. 3.6, on the basis of 1T.1.

1T.1 is installed on the thermal beam 1T and equipped with three different monochromators – a (002) pyrolytic graphite (PG), a Cu (220), and a Cu (111). Due to the study of only low lying excitations (< 40 meV) in this thesis, for all measurements the double focusing PG monochromator was used. Together with the also double focusing (002)-PG analyzer this experimental setup provides an essential gain of neutron flux that proved to be crucial for the realized experiments. Almost all scans were performed with a fixed final energy of 14.7 meV, where the used PG resonance filter may suppress higher order contaminations. Typical values of the instrumental resolution in this configuration are for example, referring to $\mathbf{Q} = (100)$ (in reciprocal lattice units) with $|\mathbf{Q}| = 1.66 \text{ \AA}^{-1}$: $\Delta Q = 0.09 \text{ \AA}^{-1}$ (in longitudinal and transversal direction) and $\Delta E = 0.94 \text{ meV}$ for an energy transfer of 4.1 meV [78]. However, for the study of the magnetic excitations in $\text{Ca}_{2-x}\text{Sr}_x\text{RuO}_4$ all diaphragms determining the beam paths were opened more widely than usually, yielding a reduction of the Q -resolution. Since the observed magnetic signals are quite broad in \mathbf{Q} -space, this modification leads to no loss of essential information, but increases significantly the intensity.

Chapter 4

The Phase Diagram of $\text{Ca}_{2-x}\text{Sr}_x\text{RuO}_4$

4.1 Introduction

The phase diagram of $\text{Ca}_{2-x}\text{Sr}_x\text{RuO}_4$ presents a rich variety of different physical phenomena although the substitution is isovalent. On one end one finds the spin-triplet superconductor Sr_2RuO_4 , which has become one of the most appropriate materials to study unconventional superconductivity [4, 5, 20, 22]. On the other side, Ca_2RuO_4 is an insulator at low temperature which orders antiferromagnetically below $T_N \simeq 150$ K [6, 79, 80] and which exhibits a metal-insulator transition at $T_{MI} = 357$ K [80, 81]. In between several metallic phases are observed with rather different magnetic properties. Therefore, $\text{Ca}_{2-x}\text{Sr}_x\text{RuO}_4$ can be considered as a prototype material to investigate the evolution of electronic structures, connecting the insulating ground state in Ca_2RuO_4 with the spin-triplet superconductivity in Sr_2RuO_4 , controlled mainly by substitution of Sr for smaller Ca ions ($r_{Ca} = 1.18 \text{ \AA} < r_{Sr} = 1.31 \text{ \AA}$ [82]).

Nakatsuji *et al.* [2, 3, 53] have recently determined the magnetic and electronic phase diagram of $\text{Ca}_{2-x}\text{Sr}_x\text{RuO}_4$ in the whole region of x , which is shown in Fig. 4.1. Starting with the end member, Sr_2RuO_4 , they observed at first a suppression of superconductivity by already slight Ca substitution ($x < 1.95$). With further decrease of the Sr content the system is then continuously driven from a paramagnetic metallic ground state to a nearly ferromagnetic one, which is indicated by a simultaneous enhancement of the low-temperature susceptibility $\chi(T \simeq 0)$ (cf. right part of Fig. 4.1). Near the critical concentration $x_c \simeq 0.5$, $\chi(T \simeq 0)$ becomes maximal being almost 150 times larger than that of pure Sr_2RuO_4 , with a high Wilson ratio and a strongly enhanced electronic specific heat coefficient. Very recently the authors observed short range ferromagnetic order below 1 K for compounds with x close to 0.5 [83]. Decrease of the Sr content below $x = 0.5$, leads to an intermediate antiferromagnetically correlated state ($0.2 < x < 0.5$), which is characterized by an anomalous broad peak in the magnetic susceptibility with a strong anisotropy in the (a, b) -plane. Moreover, for magnetic fields applied in the (a, b) -plane Nakatsuji and co-workers observed itinerant metamagnetism below the peak temperature T_P [84]. Finally, for $x < 0.2$ one finds, as for Ca_2RuO_4 , the insulating antiferromagnetic ground state. The metal-insulator transition temperature shifts rapidly to higher temperature as

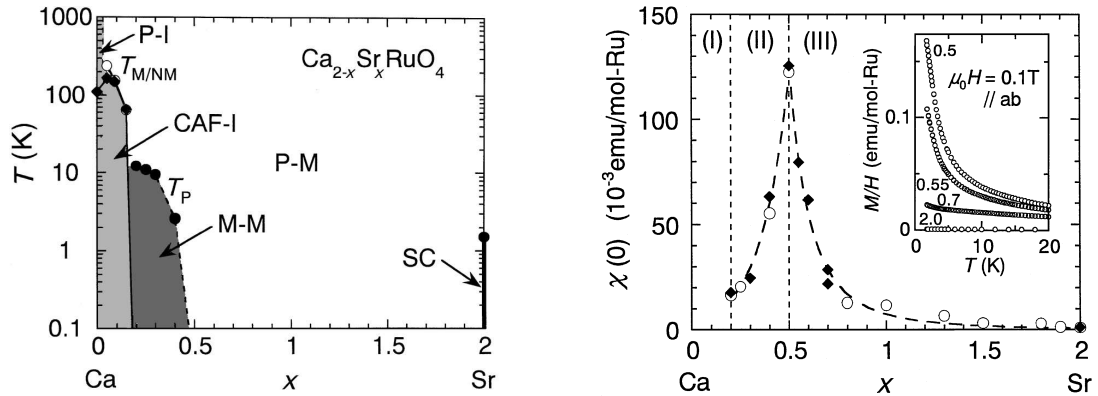


Figure 4.1: *Left:* The electronic and magnetic phase diagram of $\text{Ca}_{2-x}\text{Sr}_x\text{RuO}_4$, determined by Nakatsuji *et al.* [2, 3]. The abbreviations have the following meaning: P stands for the paramagnetic, CAF for canted antiferromagnetic, M for magnetic, SC for superconducting phase, while -M and -I distinguish between the metallic and the insulating phase. The symbols denote the metal-nonmetal temperature $T_{M/NM}$, the CAF transition temperature T_{CAF} and the peak temperature of the susceptibility T_P . *Right:* The low temperature magnetic susceptibility $\chi(0)$ as a function of Sr concentration x in the metallic region. The inset shows $\chi(T)$ for Sr concentrations $x \geq 0.5$.

a function of substitution. We have found strong evidence by neutron diffraction that all these reported features are strongly correlated to characteristic structural distortions which will be discussed in detail in this chapter. Before this discussion we give a brief overview of the possible symmetry reductions from the ideal K_2NiF_4 structure, which lead to crystal structures with characteristic deformations of the rigid RuO_6 octahedra. Fig. 4.2 shows the resulting tilt and rotation schemes of the RuO_6 octahedron together with the corresponding group-subgroup relations.

Sr_2RuO_4 has the body-centered tetragonal K_2NiF_4 structure with space group $I4/mmm$ [12, 13], in which the characteristic structural units are staggered planes of RuO_6 octahedra. From space group $I4/mmm$ two structural variants can be derived. In one variant the corner shared RuO_6 octahedra rotate about an axis lying in the RuO_2 plane (*tilt* distortion), while the other possible variant consists of a rotation of the octahedra around the c -axis (*rotational* distortion). The tilt distortion is related to a condensation of the soft mode, belonging to the Σ_4 irreducible representation, with wavevector corresponding to the X point of the Brillouin zone [85]. Due to the degeneracy of the X point mode one may obtain three different modifications of tilt distortions, with the following space groups: orthorhombic $Abma^1$ or $Pccn$ or tetragonal $P4_2/ncm$. The three space groups differ only in the orientation of their

¹The standard setting is $Cmca$, where $b > a > c$; in this work nonstandard settings are used when necessary in order to keep the long axis always as c . Furthermore we use for simplicity, and in order to get a better comparison between structural parameters of the different phases, always the nonstandard space-group $F4/mmm$ instead of $I4/mmm$.

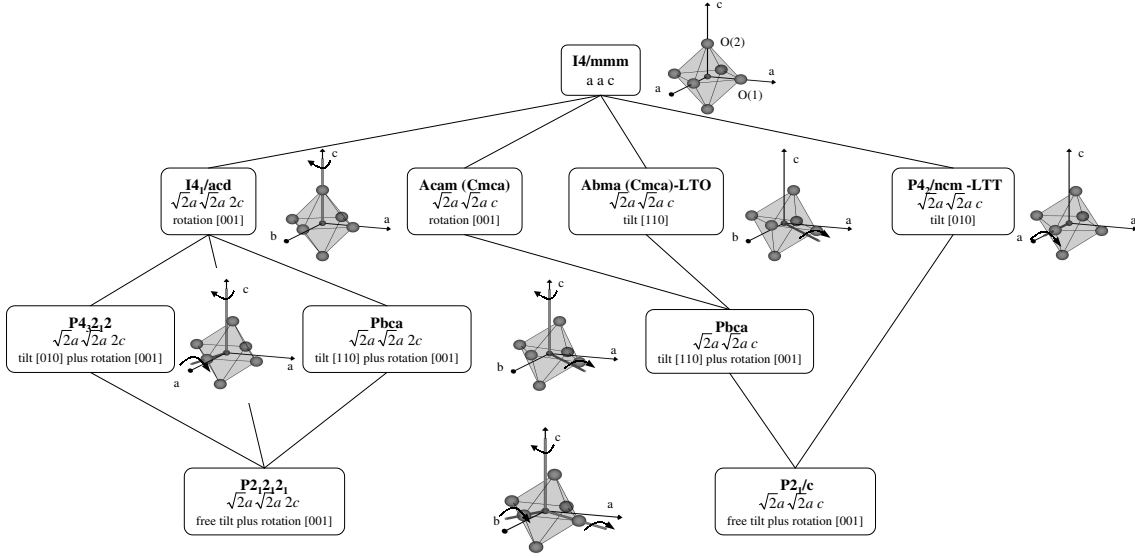


Figure 4.2: Schematic diagram of the group-subgroup relations of the $I4/mmm$ structure for the observed structural modifications (a line indicates a transition into a subgroup). Additionally the associated distortion types and lattice changes are indicated, together with the rotation and tilt schemes of an ideal rigid octahedra. The given cell parameters correspond to the undistorted tetragonal $I4/mmm$ structure.

tilt axis: in $Abma$ the corner shared octahedra are rotated about the $I4/mmm$ (1 1 0) axis, in $P4_2/ncm$ the octahedra rotate about (1 0 0), which is parallel to the basal Ru-O bonds and in $Pccn$ they may be rotated about any axis lying in the plane. The first two tilt modifications are well known for the isostructural compounds La_2CuO_4 and La_2NiO_4 [48–51, 86–88] and are commonly called in literature low temperature orthorhombic (LTO) and low temperature tetragonal (LTT), respectively.

Referring to the group theoretically possibilities listed by Stokes and Hatch [85] the rotational distorted structures can be derived from the parent $I4/mmm$ space group involving either a Brillouin zone boundary phonon with wavevector corresponding to the X point, $(\frac{1}{2}, \frac{1}{2}, 0)$, or to the P point $(\frac{1}{2}, \frac{1}{2}, \frac{1}{2})$. While the X point mode, which belongs to the irreducible Σ_3 representation, does not induce a larger unit cell than that of the LTO or LTT structure the condensation of the P point phonon mode generates an enlarged unit cell with dimensions $a_{LTO} \times a_{LTO} \times 2c$, with $a_{LTO} = \sqrt{2}a$. The space group of the so distorted phase is $I4_1/acd$, in which the rotated octahedra separated by c are distorted with an opposite phase, which explains the doubling of the c parameter in respect to the $I4/mmm$ symmetry. A similar structural distortion has been observed in the related compounds Sr_2IrO_4 , Sr_2RhO_4 and Ca_2MnO_4 [89–93]. The second rotational variant, which belongs to orthorhombic $Acam$ (standard setting $Cmca$, where a corresponds to the long axis), differs only in that the stacking of the octahedra rotated about (0 0 1) exhibits a period of just one c parameter.

Such a rotational distortion, with just one c period, has been observed in the related compound Gd_2CuO_4 [94, 95]. Though Sr_2RuO_4 remains undistorted down to lowest temperatures, the described rotational distortions are of special interest, since the analysis of the phonon dispersion has revealed that the system is very close to the structural instability with respect to the RuO_6 rotation [47].

A combination of the described rotational and tilt distortions may be obtained for the symmetries with no doubling of the c axis either in orthorhombic space group $Pbca$ or in monoclinic space group $P2_1/c$. One important difference between $Pbca$ and $P2_1/c$ symmetry is that, in the latter one, the basal oxygens (O(1)) of the octahedron are no longer equivalent since two different crystallographic O(1)-positions exist. Therefore the monoclinic symmetry is related to structural distortions due to a free tilt plus a rotation. Since in $Pbca$ symmetry only one O(1) position exists, all in-plane oxygens have the same distance to the planes formed by the Ru atoms. Consequently, the corresponding structural distortions may be described by a rotation of the rigid octahedra plus a tilt about an axis which is almost parallel to [110] direction, similar to the distortion scheme of the GdFeO_3 structure type in related perovskites [96–99]. This combination of tilt and rotational distortions has been observed for the other end member of the studied series, Ca_2RuO_4 [6]. While insulating Ca_2RuO_4 possesses the orthorhombic $Pbca$ symmetry, for a sample containing excess-oxygen, $\text{Ca}_2\text{RuO}_{4.07}$, one finds a structural distortion due to a rotation of the octahedra together with a LTT-like tilt deformation, belonging to $P2_1/c$ symmetry.

The $I4_1/acd$ symmetry with doubled c parameter may be further reduced by tilting the rotated octahedra around an axis lying in the basal plane. This is related to a condensation of the soft mode with wavevector corresponding to the M point (in $I4_1/acd$ settings; in $I4/mmm$ the equivalent point is the X point) of the Brillouin Zone [85]. As for the LTO, LTT transition this leads to three different space groups: orthorhombic $Pbca$ or $P2_12_12_1$ or tetragonal $P4_32_12$. Completely equivalent to the LTO, $Pccn$ and LTT-phases these three space-groups differ only in the orientation of their tilt axis: While $Pbca$ combines the $I4_1/acd$ rotation with the LTO octahedron tilt, $P2_12_12_1$ and $P4_32_12$ represent the rotation scheme of $I4_1/acd$ together with a $Pccn$ and LTT tilt, respectively. Interestingly these symmetry transformations involve a different stacking period of the tilt and rotational distortion. The tilt distortion exhibits a period of just one c parameter, whereas the period of the rotation is $2c$. These symmetries will be further discussed in the context of the observed second order structural transition in section 4.4.

This chapter is primarily devoted to the structural and magnetic phase diagram of $\text{Ca}_{2-x}\text{Sr}_x\text{RuO}_4$, as observed by neutron diffraction. In the above discussion we already introduced the space-group symmetries necessary to understand the structural modifications which occurs as a function of temperature, pressure, and Sr concentration in $\text{Ca}_{2-x}\text{Sr}_x\text{RuO}_4$. Since the observed structural distortions correlate with the changes in the magnetic and the electronic properties we have organized this chapter

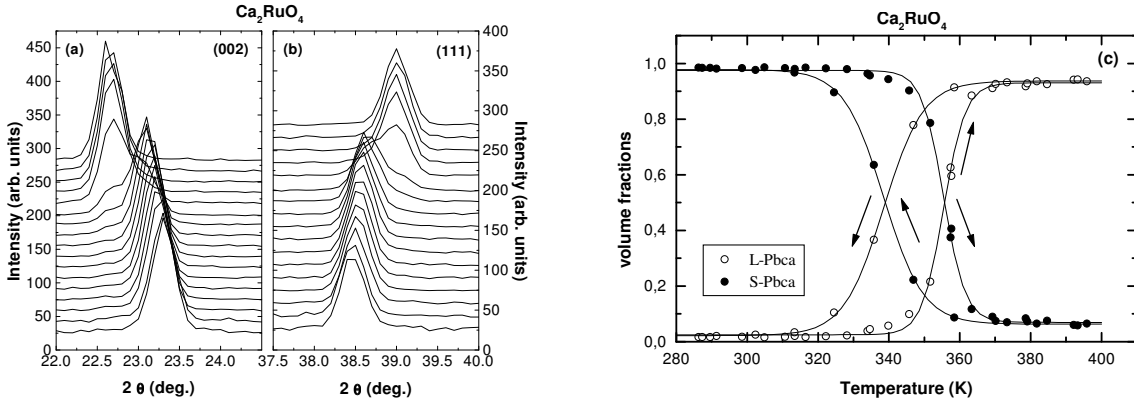


Figure 4.3: Comparison of the high flux powder diffraction patterns, showing the (002) (a) and (111) (b) reflections, obtained in Ca_2RuO_4 between 286 and 400 K. The bottom curves correspond to $T = 286$ K. The upper ones were taken approximately every 5 K up to 398 K. Temperature dependence of the volume fractions of the *L-Pbca* and *S-Pbca* phases for Ca_2RuO_4 measured on the high flux neutron diffractometer. The temperature variation is indicated by arrows.

according to the three characteristic regions represented in Fig. 4.1. We start with the discussion of the metal-insulator transition in Ca_2RuO_4 which coincides with a first-order structural phase transition. Then the influence of the Sr substitution on this cooperative feature and the corresponding magnetic structure are presented. In section 4.4 we report on the detailed structural analysis of the intermediate magnetically correlated metallic state ($0.2 < x < 0.5$). Finally, we discuss the effect of the structural distortions on the enhancement of the low temperature susceptibility near $x=0.5$. The main part of these results was published in Ref. [46, 100].

4.2 The Mott transition in Ca_2RuO_4

While Sr_2RuO_4 is a good metal, with an extremely low residual resistivity of $\rho_{res} = 0.15 \mu\Omega\text{cm}$ [7], Ca_2RuO_4 is an insulator at room temperature with a resistivity which was found to increase by eight orders of magnitude, upon cooling [79, 101]. Furthermore, the insertion of the smaller Ca^{2+} -ion leads for Ca_2RuO_4 to strong structural distortions of the ideal K_2NiF_4 -structure, which is retained by Sr_2RuO_4 down to lowest temperatures. Braden *et al.* [6] have demonstrated that these structural distortions are characterized by a rotation of the RuO_6 octahedra around the long *c*-axis combined with a tilt around [110] (Space group *Pbca*; see discussion above). They obtained rather large angles for the rotation and the tilt of the octahedra, with $\Phi = 11.8^\circ$, $\Theta\text{-O}(1) = 13.1^\circ$ and $\Theta\text{-O}(2) = 11.5^\circ$ at 11 K [Throughout this work we use the same notations as in Ref. [6, 46]: The rotation angle is unique and designed by Φ , whereas the tilt angle may be determined at the two oxygen sites $\Theta\text{-O}(1)$ and

Θ -O(2); in the notation used here the tilt is always around an axis close to the b axis in $Pbca$]. The strong temperature dependence of these parameters, observed in Ref. [6], indicates already a structural phase transition right above room temperature. However, for a sample containing excess oxygen $\text{Ca}_2\text{RuO}_{4.07}$ a related structural transition from a metallic high-temperature phase into a nonmetallic distorted phase has been observed [6]. Since $\text{Ca}_2\text{RuO}_{4.07}$ shows antiferromagnetic order in the non-metallic phase one may interpret this transition as a Mott transition. Concerning stoichiometric Ca_2RuO_4 Alexander *et al.* [81] have recently reported a discontinuous decrease in the resistivity at 357 K which coincides with a structural transition. Based on these studies one may suggest that the metal insulator transition seen in $\text{Ca}_2\text{RuO}_{4.07}$ occurs just at higher temperature in the stoichiometric compound. But the detailed structural analysis of the metal insulator transition presents significant differences.

4.2.1 The first order structural phase transition as a function of temperature

Using a cryofurnace the structure of Ca_2RuO_4 was studied above room temperature on G4.1 by recording a complete hysteresis cycle. At temperatures near 340 K, one already observes two phases, the low-temperature phase is characterized by a small c -lattice parameter compared to the high-temperature phase with long c ; the averaged in-plane parameter exhibits the opposite behavior as can be seen in Fig. 4.3 (b). The transition in stoichiometric Ca_2RuO_4 is sharper than that in $\text{Ca}_2\text{RuO}_{4.07}$: at 365 K it is almost complete and at 395 K there is no sign of the low-temperature phase in the high flux pattern, parts of the high flux patterns are shown in Fig. 4.3 (a),(b). In Fig.4.3 (c) the temperature dependence of the low- and high-temperature phase is shown. The transition temperature² obtained in up-strike, $T_S = 356$ K is in excellent agreement with that observed by Alexander *et al.*. Therefore, one can conclude that the combined electronic and structural transition first observed in $\text{Ca}_2\text{RuO}_{4.07}$ also occurs in the stoichiometric compound.

In addition to the high flux data, high resolution patterns have been recorded at 400 and 180 K on 3T.2. The Rietveld refinement of the low temperature pattern in space group $Pbca$ fits well with the results obtained by Braden *et al.* on the same sample (cf. Table 4.3). Due to the quasitragonality of the lattice, the structure of the equivalent high-temperature metallic phase of $\text{Ca}_2\text{RuO}_{4.07}$ could not be established unambiguously by the authors. The best description was obtained in space group $P2_1/c$, by fixing the displacement along c (z -O(1)) of one of the two distinct O(1) positions to zero, leading to a LTT equivalent tilt scheme. In case of the stoichiometric compound at 400 K the data is again difficult to analyze, but it

²We have considered as transition temperature the point with the strongest slope of the relative volume fractions.

gives quite different results. In space group $Pbca$ one obtains a R value of 5.39% which increases to 5.62% for the $P2_1/c$ model with one $z\text{-O}(1)$ fixed to zero. Refining the $P2_1/c$ phase independently still gives a slightly lower R value than $Pbca$, but this difference is not significant any more. Therefore, one can conclude that the high-temperature structure in Ca_2RuO_4 has the same space group $Pbca$ as the low temperature structure, although the corresponding structural changes are rather drastic. This result has been perfectly confirmed by a detailed structural analysis of a single crystal of an equivalent composition, which will be described in detail in the next section. We differentiate these two phases as $L\text{-}Pbca$ and $S\text{-}Pbca$, respectively, due to their different c parameters. The large amount of excess oxygen seems to be responsible for the distinct diffraction pattern in $\text{Ca}_2\text{RuO}_{4.07}$.

Combining these results and those obtained by Braden *et al.* one gets the entire picture of the phase transition in Ca_2RuO_4 . First, Fig. 4.4 presents the temperature dependence of the lattice constants a, b and c , the cell volume V and the orthorhombicity ϵ , defined as $\epsilon = (b - a)/(b + a)$. The transition to the metallic high temperature phase is characterized by discontinuous changes of all these parameters: a and b increase, whereas c decreases, resulting in an expansion of the cell volume, upon cooling. As for the temperature dependence of these parameters in the $S\text{-}Pbca$ -phase [6] the observed behavior reflects the pronounced changes of the shape of the RuO_6 octahedra at the $L\text{-}Pbca\text{-}S\text{-}Pbca$ transition. Figure 4.4 presents the Ru-O bond-lengths, which show a discontinuous change at the phase transition: the in-plane bonds become elongated and the out-of-plane one is shrinking upon cooling. Close to the transition – but in the $S\text{-}Pbca$ phase –, the octahedron is still elongated along c in the temperature range 300–330 K. Upon further cooling one observes a continuous and even larger change in the same sense: the octahedron at low temperature is finally flattened along c . The edge lengths of the octahedron basal plane also show a discontinuous effect at the transition followed by a pronounced change in the $S\text{-}Pbca$ phase. In accordance to the elongation of the Ru-O(1)-bonds these lengths increase upon cooling into the $S\text{-}Pbca$ -phase where they are still split, the octahedron basal plane is shorter along the tilt axis immediately below the transition. Upon further cooling, the ratio, however, becomes inversed, and the basal plane is strongly stretched along the tilt axis.

In La_2CuO_4 [51] and also in all $L\text{-}Pbca$ phase ruthenates studied here, the orthorhombic splitting is opposite to the expectation of a rigid tilt, i.e. the lattice is longer perpendicular to the tilt-axis. This effect originates from the forces in the La-O- or Sr-O-layer where one distance strongly decreases due to the opposite displacements of an apical oxygen and a neighboring La/Sr-site. The stretching of the lattice perpendicular to the tilt axis reduces the pronounced shrinking of this bond and may be seen in the orthorhombic splitting. One should hence consider this behavior as the normal one arising from the structural arrangement. Nevertheless the elongation of the octahedron basal plane might influence the electronic and magnetic properties, see the discussion below.

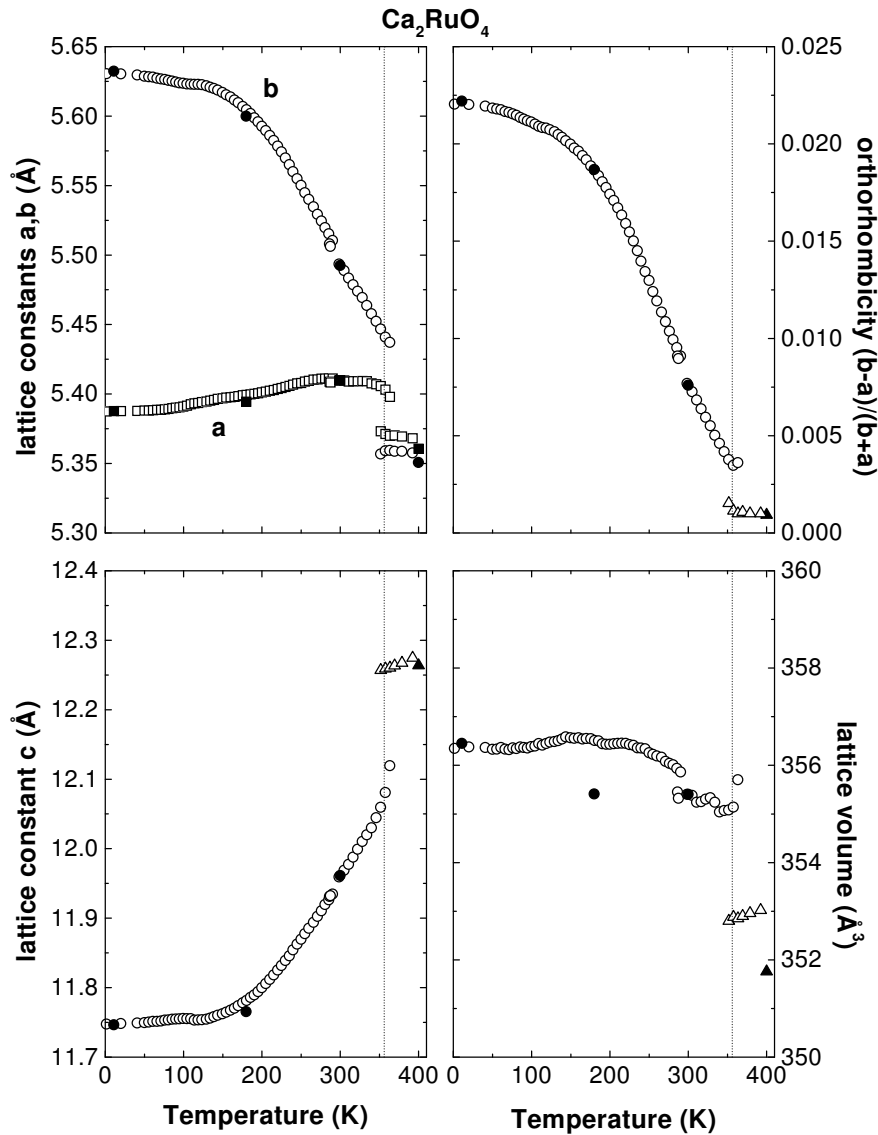


Figure 4.4: Temperature dependence of the lattice parameters in Ca_2RuO_4 . Open symbols designate the results obtained from the high-flux patterns and closed symbols those from the high resolution studies. The dashed lines indicate T_S , determined upon heating.

The transition from $L\text{-}Pbca$ to $S\text{-}Pbca$ is further characterized by an increase in the tilt angles, $\Theta\text{-O}(1)$ ($\Theta\text{-O}(2)$) increase from 7.5° (5.9°) at 400 K to 11.2° (9.2°) at 295 K. Upon cooling in the $S\text{-}Pbca$ phase these angles first continue to increase till about 180 K and are almost constant below, see Fig. 6 in Ref. [6]. The rotation angle decreases by about one degree during the transition into the $S\text{-}Pbca$ phase and is constant over the whole $S\text{-}Pbca$ temperature range.

Therefore, one can conclude that the distinction between the metallic and in-

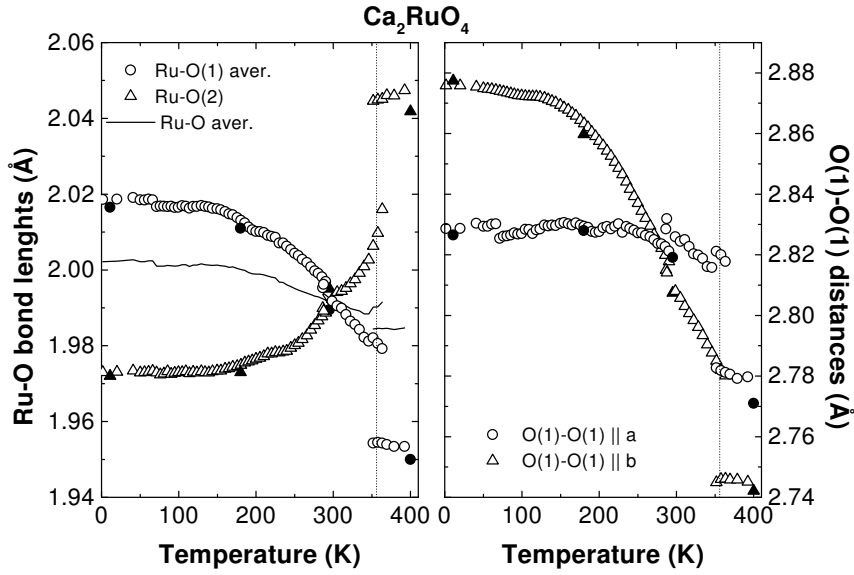


Figure 4.5: The Ru-O(1) bond distances and the edge lengths of the octahedron basal plane in Ca_2RuO_4 as a function of temperature. T_S is indicated by the dashed line.

ulating phases in Ca_2RuO_4 appears to arise from an enhanced in-plane Ru-O(1) bond and a larger tilt. Based on this properties, one might suggest that Ca_2RuO_4 forms a simple band insulator, due to the structural changes at T_S . Such a model is, however, not compatible to the long-range antiferromagnetic order at $T_N \simeq 150$ K, since the equally filled bands of spin-up and spin-down electrons in a band insulator would not show magnetic ordering. In many aspects the metal insulator transition in Ca_2RuO_4 resembles rather that in V_2O_3 [102, 103] and should be interpreted to be of Mott type. For a classical Mott insulator the localization of the electrons in the insulating phase is caused by the electron-electron interaction U , which gives rise to *local* moments and a Mott-Hubbard gap. These moments can but need not be ordered. The magnitude of the gap in the insulating phase depends only on U and the bandwidth W . Within such a Mott scenario one may phenomenologically explain the nonmetallic behavior in Ca_2RuO_4 , since both the tilting of the octahedra and the increase of the in-plane distances should strongly reduce the band-width of all bands related to the t_{2g} orbitals. In particular the band corresponding to the $4d_{xy}$ orbital should become lower in energy and should be filled. Consequently, the metal-insulator transition in Ca_2RuO_4 should be interpreted as a structurally driven Mott like transition from a paramagnetic, correlated metallic state to a paramagnetic, insulating state above T_N , which will be stabilized once the gain in elastic energy due to the structural changes overcomes the cost of kinetic energy of localizing the electrons. As first discussed by Nakatsuji *et al.* and Anisimov *et al.* [2, 3, 104] the half-filled configuration of the d_{yz} and d_{zx} bands (resulting electronic

configuration: $d_{xy}^2 d_{yz}^1 d_{zx}^1$) favors antiferromagnetic superexchange coupling between neighboring spins and may finally explain the antiferromagnetic long range order below T_N .

However, the characteristic temperature dependence of the Ru-O bond distances below room temperature clearly indicates that some further coupling mechanism has to be taken into account. The transition in Ca_2RuO_4 is not complete immediately below T_S ; instead the octahedron becomes flattened mainly due to the elongation of the basal plane along the b axis which is the direction of the spins in the antiferromagnetic ordered structure. Even if the flattening of the octahedra below room temperature could be simply understood by Jahn-Teller effect, the pronounced octahedra deformation parallel to the spin direction, approaching T_N , suggests a strong spin-orbit interaction. The important role of spin orbit coupling in Ca_2RuO_4 has been recently proved by Mizokawa *et al.* [105]. They have detected, by spin-resolved circularly polarized photoemission, a substantial orbital angular momentum along the [001] axis at 300 K, which on cooling to 90 K alters its direction to within the ab plane. In addition, they showed, based on Hartree Fock calculations (see also [106]), that the flattening of the RuO_6 octahedra is accountable for the direction change of the orbital momentum: while an elongated or regular octahedron favors an orbital momentum along (001), it is perpendicular to the [001] axis for flattened RuO_6 octahedra. This would perfectly explain the observed stretching of the basal plane along the b axis due to the orientation change of the orbital momentum. Strong spin-orbit coupling may furthermore be responsible for the preferred orientation of the magnetic moment parallel to the tilt axis [6, 104].

4.2.2 The crystal structure of the metallic phase

While the low temperature phase symmetry of Ca_2RuO_4 can be determined with a sufficient reliability by neutron powder diffraction, the method is limited in its ability to distinguish between the two possible space-groups $Pbca$ and $P2_1/c$ of the high temperature phase, due to the observed pseudo-tetragonality of the unit cell (see discussion above). In order to determine unambiguously the crystal symmetry of the metallic phase a detailed structural analysis by single-crystal neutron diffraction has been performed. Since single crystals of Ca_2RuO_4 shatter at the first order structural phase transition, preventing a detailed analysis by neutron diffraction due to inappropriate size of the crystals, we have used an equivalent $\text{Ca}_{1.85}\text{Sr}_{0.15}\text{RuO}_4$ single crystal for the analysis. Nakatsuji *et al.* [3, 52, 53] have demonstrated, by resistivity and magnetic susceptibility measurements, that the metal-insulator transition in $\text{Ca}_{2-x}\text{Sr}_x\text{RuO}_4$ is just shifted to lower temperature for increasing Sr content. For the single crystal with $x=0.15$, studied here, they observe the metal-insulator transition at $T_{MI} = 75$ K. Since our own diffraction studies of several $\text{Ca}_{2-x}\text{Sr}_x\text{RuO}_4$ compositions, showing the metal-insulator transition, have revealed no substantial structural differences in the metallic phase (cf. discussion in section 4.2.2), the crystal

symmetry of the metallic phase should be independent of the Sr content.

| Composition | x=0.15 | x=0.2 | x=0.2 | x=2.0 |
|---|---------------|---------------------------|---------------------------|---------------|
| Temperature | 295 K | 295 K | 20 K | 295 K |
| Space group | <i>L-Pbca</i> | <i>I4₁/acd</i> | <i>D-Pbca</i> | <i>F4/mmm</i> |
| Refl. | 613 | 466 | 944 | |
| R_w (%) | 3.73 | 2.88 | 7.10 | Ref. [13] |
| R_{uw} (%) | 3.08 | 1.77 | 5.63 | |
| α (%) | 79.1 | / | 55.2 | / |
| Ca/Sr x | 0.0081(2) | 0 | 0.0081(11)/-0.0101(11) | 0 |
| y | 0.0176(2) | 1/4 | 0.2407(5)/0.2265(5) | 0 |
| z | 0.34824(4) | 0.54902(1) | 0.54908(3)/(3/4 - z_1) | 0.35316(2) |
| U_{11} (\AA^2) | 0.0093(3) | 0.0118(1) | 0.0020(7) | 0.00678(8) |
| U_{22} (\AA^2) | 0.0104(3) | = U_{11} | 0.0065(8) | = U_{11} |
| U_{33} (\AA^2) | 0.0037(1) | 0.0049(1) | 0.0016(3) | 0.00488(9) |
| U_{13} (\AA^2) | -0.0017(3) | 0.0014(2) | 0 | / |
| Ru x | 0 | 0 | 0 | 0 |
| y | 0 | 1/4 | 0.2434(3) | 0 |
| z | 0 | 3/8 | 3/8 | 0 |
| $U_{11} = U_{22}$ (\AA^2) | 0.00134(5) | 0.00300(9) | 0.0018(2) | 0.00227(9) |
| U_{33} (\AA^2) | 0.0031(1) | 0.0040(1) | 0.0015(2) | 0.00357(12) |
| O(1) x | 0.1918(1) | 0.18973(5) | 0.1916(6)/0.6912(6) | 1/4 |
| y | 0.3083(1) | $x+1/4$ | 0.4341(5)/0.5528(5) | 1/4 |
| z | 0.01058(5) | 1/8 | 0.1300(1)/0.1196(1) | 0 |
| $U_{\perp\text{-plane}}$ (\AA^2) | 0.0072(1) | 0.0087(1) | 0.0053(3) | 0.0110(1) |
| $U_{\parallel\text{-plane}}$ (\AA^2) | 0.0024(1) | 0.0035(1) | 0.0023(3) | 0.0031(1) |
| $U_{\text{long-axis}}$ (\AA^2) | 0.0134(3) | 0.0172(2) | 0.0065(4) | 0.0107(1) |
| O(2) x | -0.0275(1) | 0 | -0.0340(9)/0.0233(8) | 0 |
| y | -0.0060(1) | 1/4 | 0.2380(4)/0.2506(4) | 0 |
| z | 0.16491(3) | 0.45727(1) | 0.45737(2)/(3/4 - z_1) | 0.16169(2) |
| U_{\perp} (\AA^2) | 0.0123(2) | 0.0153(1) | 0.0061(7) | 0.00969(10) |
| U_{\parallel} (\AA^2) | 0.0040(1) | 0.0049(1) | 0.0025(2) | 0.00458(12) |
| Ru-O(1) (\AA) | 1.9426(6) | 1.9311(12) | 1.936(3)/1.936(3) | 1.9355 |
| | 1.9418(6) | / | 1.935(3)/1.937(3) | / |
| Ru-O(2) (\AA) | 2.0561(5) | 2.0545(4) | 2.052(1)/2.056(1) | 2.0599 |
| Ru-O _{aver} (\AA) | 1.9802 | 1.9723 | 1.975 | 1.977 |
| O(1)-O(1) \parallel a (\AA) | 2.7531(9) | 2.7310(11) | 2.750(4)/2.754(5) | 2.7372 |
| O(1)-O(1) \parallel b (\AA) | 2.7403(9) | " | 2.724(4)/2.724(4) | " |
| Vol RuO ₆ (\AA^3) | 10.34 | 10.22 | 10.27 | 10.29 |
| Θ -O(1) (deg) | 5.48(2) | / | 5.79(14)/5.08(12) | / |
| Θ -O(2) (deg) | 4.2(3) | / | 4.98(14)/3.61(16) | / |
| Φ (deg) | 13.12(2) | 13.554(8) | 13.80(9)/13.83(9) | / |

Table 4.1: Results of the single crystal structural analyses on $\text{Ca}_{1.85}\text{Sr}_{0.15}\text{RuO}_4$ at $T=295$ K and on $\text{Ca}_{1.8}\text{Sr}_{0.2}\text{RuO}_4$ at 295 and 20 K. The standard deviations are given in parentheses. R_w and R_{uw} denote the weighted and unweighted reliability values where $R_w = [\sum w_i \cdot (F_{obs}^2 - F_{calc}^2)^2 / \sum (w_i \cdot F_{obs}^4)]^{1/2}$ and $R_{uw} = \sum (F_{obs}^2 - F_{calc}^2) / \sum F_{obs}^2$; α is the twinning ratio (for any further notation cf. Table 4.3). For comparison we show also the results obtained for Sr_2RuO_4 [13].

The neutron diffraction measurement was performed on the four-circle diffractometer installed at the hot beam 5C.2 of the Orphée Reactor (experimental details

are given in section 3.2.3). The crystal was mounted on an aluminum pin with [001] parallel to the Φ axis of the diffractometer. At room temperature ($T=295\text{ K}$) a set of 2360 Bragg intensities was recorded with $\sin \Theta/\lambda < 0.76\text{ \AA}^{-1}$. Up to $2\Theta = 65^\circ$ all intensities allowed by P centering were measured, above only those allowed by F centering. The intensity data were numerically corrected for absorption corresponding to $\mu = 0.04\text{ cm}^{-1}$ and averaged according to the Laue symmetries $2/m$ for space group $P2_1/c$ and mmm for $Pbca$.

The lattice parameters in the metallic phase which were obtained by neutron powder diffraction in this work (Table 4.3) describe an unit cell which is markedly pseudotetragonal. The obtained values of ϵ , defining the orthorhombic strain, are in the high temperature phase smaller, by an order of magnitude, than values observed in the low temperature phase. However, one may expect even in orthorhombic lattices with marked pseudotetragonal symmetry, twinning of the crystal. To examine this possibility the intensity profiles obtained in ω scans for a number of Bragg peaks were carefully checked. But no evidence for extra reflections or split intensity maxima due to twinning of the crystal was found. This yields an upper limit for the orthorhombicity ϵ of 1×10^{-3} , supposing a twinned crystal. Though, no indication for twinning of the crystal was observed it should not be omitted in the structure factor calculation. Therefore, the crystal twinning was always taken into account through the performed refinement cycles, assuming a probable twin law which leaves the c -axis invariant and results in superposition of pairs of F_{hkl} and F_{khl} structure factors for the orthorhombic space group. Such a twinning mechanism is well known for isostructural compounds like $(\text{La}, \text{Sr})_2\text{CuO}_4$ and $(\text{La}, \text{Sr})_2\text{NiO}_4$ [50, 107]. In the case of the monoclinic space group $P2_1/c$ the measured intensities have been fitted by a fourfold superposition of the corresponding structure factors F_{hkl} , F_{khl} , $F_{h\bar{k}l}$, and $F_{k\bar{h}l}$.

First refinement cycles were performed for the structural model proposed by Braden *et al.* for $\text{Ca}_2\text{RuO}_{4.07}$ [6], in space group $P2_1/c$. In this model only one of the two O(1) sites has a nonzero z position, corresponding to a LTT like structure. In addition the number of free parameters was reduced by constraining most of the additional sites, which result from the reduced symmetry in $P2_1/c$ space group. These parameters were fixed corresponding to the symmetry relation $(0.5 - x, 0.5 + y, z)$ of $Pbca$, which is nonexistent in $P2_1/c$. Refinement of 26 parameters (scale factor, 3 twin fractions, an isotropic extinction parameter with a Lorentzian distribution of mosaicity, 9 atomic coordinates and 12 anisotropic temperature-factors) converged to $R_{uw}(F^2) = 5.62\%$ and $R_w = 8.72\%$. Even if this model leads to no physically unreasonable results the elevated R values compared to the internal agreement index $R_i = 2.65\%$ (for definition of R_i see [77]) indicate that this model is not well adapted for describing the crystal structure of the metallic phase.

In a next step refinement was performed by just omitting the constraint of $z\text{-O}(1) = 0$, yielding a significant improvement of the reliability values, with $R_{uw} = 3.59\%$ and $R_w = 4.35\%$. The two obtained $z\text{-O}(1)$ positions differ only by $5\sigma(I)$, clearly indi-

cating a LTO like tilt scheme. Finally, an unconstrained $P2_1/c$ structural model with the full number of free parameter was refined, resulting only in negligible improvement of the R values, with $R_{uw} = 3.58\%$ and $R_w = 4.34\%$. None of the atomic coordinates or temperature factors changes by more than $4\sigma(I)$ compared to the result of the previous model, implying furthermore no violation of the symmetry operator $(0.5 - x, 0.5 + y, z)$. Since $P2_1/c$ is a subgroup of $Pbca$, the description of Bragg reflection data must be better. However the observed extremely small improvement of the R values does not justify to ascribe the space group $P2_1/c$ to the metallic phase. Space group $Pbca$ was therefore adopted as the correct one for the room temperature structure of $\text{Ca}_{1.85}\text{Sr}_{0.15}\text{RuO}_4$.

The results of the refinements in space group $Pbca$ are reported in Table 4.1, for comparison we show also the values of related Sr_2RuO_4 [13]. The given bond distances and angles were calculated using the lattice constants, which have been determined on the two-axis diffractometer 3T.1, cf. Table 3.1. The site occupancies of each species were fixed to the corresponding stoichiometric value, since an individual refinement of these parameters leads to no statistically significant changes. The obtained results agree reasonably well with the equivalent neutron powder diffraction data, presented in Table 4.3. The single crystal analysis permits, however, a more precise determination of the atom coordinates, especially for z -values of the individual atoms, and the anisotropic temperature factors. One finds a RuO_6 octahedron, which is slightly elongated along c and resembles rather that of Sr_2RuO_4 than that of insulating Ca_2RuO_4 at room temperature. In addition, the tilt and rotation angles are much more similar to the values of the metallic phase in Ca_2RuO_4 than to the corresponding values of the insulating phase. One may therefore suppose that the characteristic structural differences between the metallic and insulating phase observed for Ca_2RuO_4 , can also be found in Sr doped samples.

The temperature-factor coefficients in Table 4.1, which can be determined by single crystal neutron diffraction with a sufficient reliability to allow a quantitative discussion, show pronounced anisotropy. At the Ca/Sr site the almost equal U_{11} and U_{22} are significantly larger than U_{33} . Compared to the equivalent values of Sr_2RuO_4 we find a largely enhanced amplitude in the a, b plane in the Ca doped sample, whereas the amplitude parallel c is reduced by the same relative amount. For isostructural $(\text{La}, \text{Sr})_2\text{CuO}_4$ it was shown that enhanced La- U_{11} and La- U_{22} parameters and a reduced La- U_{33} parameter clearly indicate a nearby tilt instability [51]. There is further evidence that $\text{Ca}_{1.85}\text{Sr}_{0.15}\text{RuO}_4$, though already strongly distorted, is in the vicinity of a structural phase transition. Both the thermal parameters at the in-plane, O(1), and apical oxygen, O(2), sites are strongly enhanced. At the O(2) site one finds, even in description by the long range distorted L - $Pbca$ -phase a U_{\perp} coefficient, denoting the mean-square atomic displacement perpendicular to the Ru-O(2) bond, which is significantly larger than for Sr_2RuO_4 . Also the thermal motion of the O(1) ion parallel to c , $U_{\text{long-axis}}$ is larger than in the stoichiometric compound. Through the L - $Pbca$ - S - $Pbca$ transition the O(1) site is displaced parallel to the c axis farther

away from the a, b plane, whereas the apical oxygen is further shifted perpendicular to the c axis. Hence, the characteristic enhancements of $\text{O}(2)\text{-U}_\perp$ and $\text{O}(1)\text{-U}_{\text{long-axis}}$ perfectly confirm the picture of a nearby tilt instability in $\text{Ca}_{1.85}\text{Sr}_{0.15}\text{RuO}_4$. Since $\text{Ca}_{1.85}\text{Sr}_{0.15}\text{RuO}_4$ shows still the metal-insulator transition one may suggest that, as in Ca_2RuO_4 , the structural changes related with the phase transition from $L\text{-Pbca}$ to $S\text{-Pbca}$ lead to the insulating phase. A study of this relation with the present sample was hampered, as already mentioned, by the fact that single crystals crack at the transition. The detailed analysis of the crystal structure of the insulating phase and of the corresponding metal-insulator transition is, hence, restricted to polycrystalline samples. The results of related neutron powder diffraction studies performed in this thesis will be discussed in detail in section 4.3. However, due to recent progress in the crystal growth of $\text{Ca}_{2-x}\text{Sr}_x\text{RuO}_4$ several untwinned single crystals of Ca_2RuO_4 have just become available, permitting additional diffraction studies (for example an electron density analysis of the insulating phase).

4.2.3 The pressure dependence of the crystal structure

In section 4.2 we have shown, that the metal insulator transition in Ca_2RuO_4 is associated with a first order structural phase transition from $L\text{-Pbca}$ to $S\text{-Pbca}$ phase. The pronounced structural changes at this transition may easily explain, within a Mott-Hubbard picture, the paramagnetic insulating state below T_S , due to a strongly reduced bandwidth and changed band filling. In order to confirm the importance of bandwidth control for the Mott-Insulator to metal transition we have investigated the effect of hydrostatic pressure on the crystal structure of Ca_2RuO_4 . Basically, the application of pressure reduces the electron correlation strength U/W , through the pressure induced increase of the bandwidth. This permits to study the correlation of structural and electronic properties of the transition.

Powder diffraction data of Ca_2RuO_4 were collected as a function of pressure at room temperature. The experiments were performed at three different diffractometers on the same stoichiometric sample used already for the temperature dependent study. The diffraction data up to 5.5 kbar, were collected on the two-axis diffractometer 3T.1 at the LLB using a helium gas pressure cell. This pressure cell provides hydrostatic pressure and the ability to vary pressure *in situ*. The data points between 7.0 and 29.2 kbar were measured by energy dispersive X-ray diffraction in a diamond anvil cell, at the Hamburger Synchrotron Strahlungslabor, beamline F3 (for experimental details see Ref. [108]). While these two powder diffraction experiments allow only determination of lattice parameters, Rietveld treatable data was obtained at ambient pressure, 7 and 10 kbar on D2B at the ILL, using a standard high pressure clamped cell with ZrTi anvils [109].

The pressure dependence of the orthorhombic lattice parameters a , b and c , the resulting orthorhombicity ϵ and the cell volume V at 300 K are shown in Fig. 4.6, combining the results from the three different pressure measurements. As can be eas-

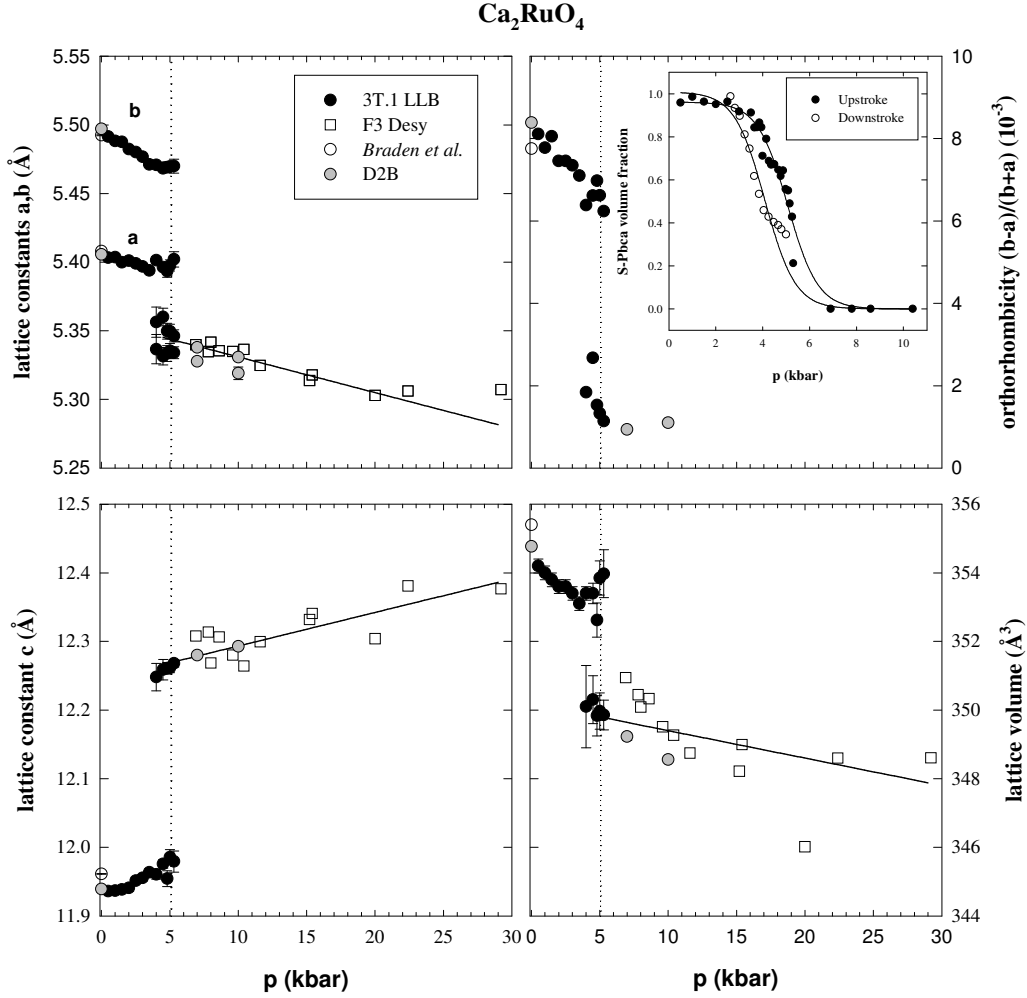


Figure 4.6: Lattice parameters a , b , and c , the orthorhombicity ϵ , and the lattice volume of Ca_2RuO_4 as function of pressure at 300 K, measured on upstroke. For the experimental details see text. The synchrotron data was refined only by a tetragonal cell, due to the reduced resolution and the quasitetragonality of the lattice. The inset shows the pressure dependence of the volume fraction of the insulating $S\text{-}Pbca$ phase in Ca_2RuO_4 through the upstroke and downstroke, measured on 3T.1 and the beamline F3.

ily deduced from the discontinuous changes in all lattice parameters, the structural transition occurs at $p_S = 5.5$ kbar in upstroke. The observed hysteresis of about 1.0 kbar (see inset in Fig. 4.6) confirms again the first order character of the transition. The lattice parameters exhibit the same anomaly as upon heating through the transition, with an increase of c and a decrease of a and b . The b -axis compressibility in the $S\text{-}Pbca$ is a factor of $\simeq 4.5$ larger than $\kappa_a(S\text{-}Pbca) = 2.1 \times 10^{-4} \text{ kbar}^{-1}$, resulting in a decrease of the orthorhombic strain ϵ with pressure (see Fig. 4.6). Above

the transition the mean in-plane compressibility $\kappa_{ab}(L\text{-}Pbca) = 5.5 \times 10^{-4} \text{ kbar}^{-1}$ is the same as in the $S\text{-}Pbca$ phase. It is interesting that the c -axis compressibility is negative in both phases, with $\kappa_c = -7.9 \times 10^{-4} \text{ kbar}^{-1}$ and $\kappa_c = -3.4 \times 10^{-4} \text{ kbar}^{-1}$ for the $S\text{-}Pbca$ and $L\text{-}Pbca$ phase, respectively. Though pressure should stabilize the low volume phase and hence the observed discontinuities in the cell parameters are not unexpected, the negative c -axis compressibilities are highly anomalous, indicating that at least one lattice distortion expands under pressure.

In addition to the determination of the cell parameters the data obtained on D2B were used for refining the structural model corresponding to the $L\text{-}Pbca$ phase of Ca_2RuO_4 for pressures larger than p_S . Contaminating reflections originating from the sample environment were treated as a secondary phase in the refinements. The results of the refinements are given in Table 4.2 on page 78. Similar to the pressure dependence of the cell parameters, we find the same characteristic structural changes at the phase transition as upon heating: a shrinking of the in-plane bond length and an increase in the Ru-O(2) distance together with a strongly reduced tilt distortion and a slightly enhanced rotational angle. We note that the observed splitting of the Ru-O(1) bond lengths (cf. Table 4.2) should be interpreted to be an artifact of the performed refinement, related to the more complicate background contribution under pressure, since similar splitting was observed for data recorded at ambient pressure but within the pressure cell (not given). Nevertheless one may conclude that the high pressure phase immediately above the transition is identical to the high-temperature metallic phase.

Concerning the related metal-insulator transition, Nakamura *et al.* have recently shown by resistivity measurements, that metallic Ca_2RuO_4 can be stabilized by pressure of $p_{MI} = 5 \text{ kbar}$ [110]. This matches perfectly with the observed structural phase transition at p_S and confirms again the strong correlation between the structural distortions and the metal-insulator transition. Furthermore the authors have found that the high pressure metallic phase of Ca_2RuO_4 exhibits ferromagnetic ordering at 7 kbar. The ferromagnetic T_c increases upon further pressure increase up to 50 kbar and then diminishes. Ferromagnetism seems to be completely suppressed at 150 kbar. According to electronic structure calculations by Fang and Terakura [111] the magnetic correlations in $\text{Ca}_{2-x}\text{Sr}_x\text{RuO}_4$ are strongly coupled to the tilt and rotational distortions. They have noted that the tilt stabilizes antiferromagnetic correlations in the metallic state, while rotations favor ferromagnetism. Hence, one may speculate that the ferromagnetic order in Ca_2RuO_4 is caused by the pressure dependence of the tilt and rotational distortions. An explanation of the magnetic effects observed in Ref. [110] could be given, if both rotational and tilt distortions decrease with pressure. While a vanishing tilt would enhance ferromagnetism, the decrease of the rotational distortion should lower ferromagnetism. Even if one might expect intuitively that compression would be accommodated by coordinated tilting of the octahedra, pressure studies of the isostructural system $(\text{La}, \text{Sr})_2\text{CuO}_4$ [112] have proven that just the opposite occurs; pressure suppresses the tilt. Unfortunately

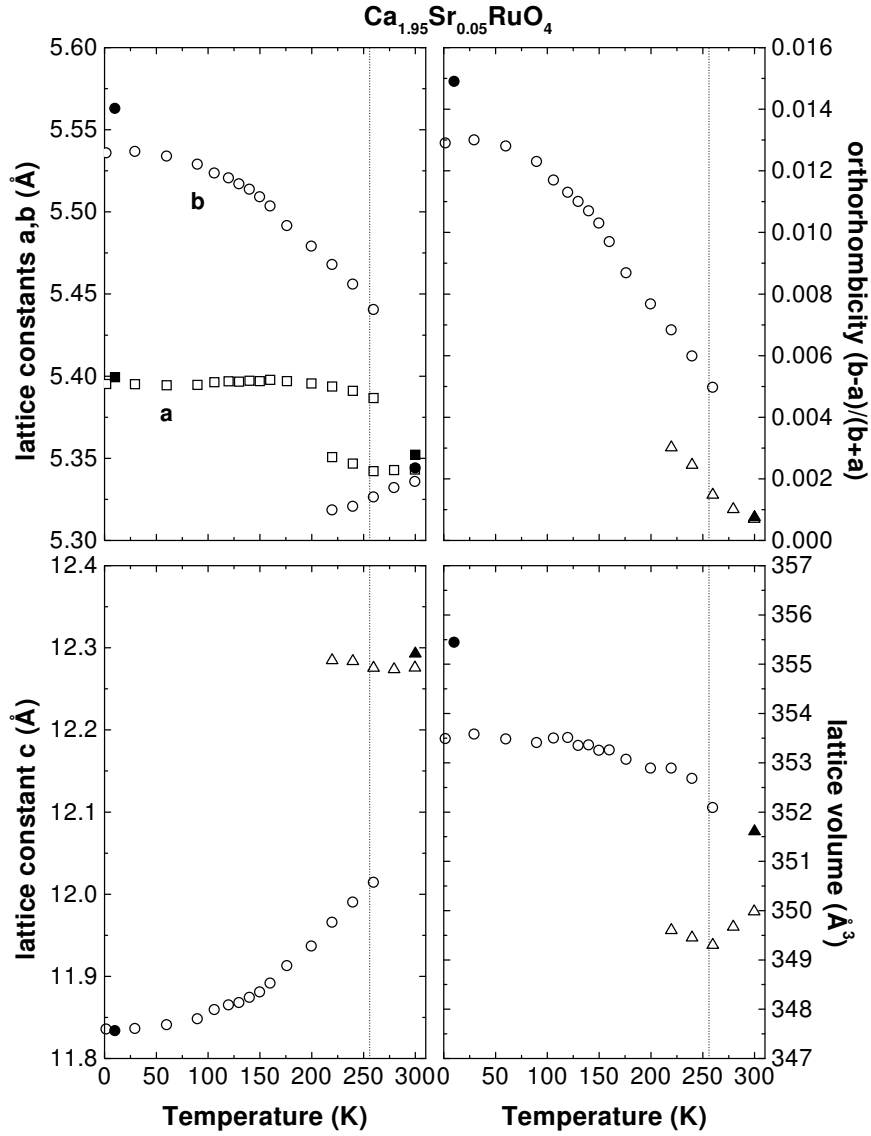


Figure 4.7: Temperature dependence of the lattice parameters in $\text{Ca}_{1.95}\text{Sr}_{0.05}\text{RuO}_4$. Open symbols designate the results obtained from the high-flux patterns and closed symbols those from the high resolution studies. $T_S = 256$ K is indicated by the dashed lines. The slight deviations between the high resolution and high flux results must be attributed to the insufficient extent in Q space of the latter data.

the limited number of pressure points of Rietveld treatable data makes it impossible to deduce conclusively $\partial\Phi/\partial p$ and $\partial\Theta/\partial p$ from our data. While $\Theta\text{-O}(2)$ decreases from 5.4° at 7kbar to 4.2° at 1kbar, $\Theta\text{-O}(1)$ shows just the inverse tendency and increases from 6.4° to 7.2° . Nevertheless, a decrease of the tilt angle could explain in a simple physical picture the negative c -axis compressibility, since a smaller value

of Θ is connected to a smaller buckling of the Ru-O(2)-Ca bond, which is parallel to the c -axis for $\Theta = 0$. But it should be mentioned that in the present case also some other type of lattice distortions, like for example the rotation of the RuO_6 -octahedra or the stretching of the Ru-O(2) bond distance, which is already slightly enhanced for $p = 10$ kbar (cf. Table 4.2), may contribute to an overall negative compressibility. It is obvious that further pressure diffraction studies are necessary to clarify the discussed correlation between ferromagnetism and lattice distortions in Ca_2RuO_4 . In the meantime structural studies at the high pressure facility of ISIS have become available and have demonstrated a clear correlation between the disappearance of the tilt distortion and the ferromagnetic order. Details will soon be presented elsewhere [113].

4.3 The Mott transition in $\text{Ca}_{2-x}\text{Sr}_x\text{RuO}_4$

In addition to the so far presented powder diffraction study of the temperature and pressure dependence of the metal-insulator transition in stoichiometric Ca_2RuO_4 , we have investigated the structural and magnetic aspects of this transition as function of Sr content x . Nakatsuji *et al.* and also Cao *et al.* reported a rather fast suppression of the metal-insulator transition with increasing Sr content x by resistivity measurements [2, 52, 80, 114]. From Ref. [2, 52] one can deduce a shift of $\Delta T_{MI}/\Delta x \simeq -39.7\text{K}/\%\text{Sr}$ of T_{MI} , leading to an extrapolated $x_c \simeq 0.18$ for which metallic conductivity should be retained down to lowest temperatures. Fukazawa *et al.* and independently Cao *et al.* [80, 115] observed a similar suppression by substituting the divalent Ca by the trivalent La, which has only a slightly larger ionic radius ($r_{ion}(\text{Ca}^{2+}) = 1.18 \text{ \AA} < r_{ion}(\text{La}^{3+}) = 1.22 \text{ \AA} < r_{ion}(\text{Sr}^{2+}) = 1.31 \text{ \AA}$ in ninefold coordination). While isovalent Sr substitution should influence the electronic properties of $\text{Ca}_{2-x}\text{Sr}_x\text{RuO}_4$ only by modifying the bandwidth (*bandwidth control*) the substitution of La for Ca changes also the electronic configuration of the t_{2g} bands by adding an extra electron (*filling control*). In this section we will concentrate on the effect of isovalent Sr substitution on the Mott transition and the correlated first-order structural phase transition in $\text{Ca}_{2-x}\text{Sr}_x\text{RuO}_4$, studied for the three different stoichiometric $x=0.05$, 0.10 , and 0.15 .

4.3.1 Structural aspects of the metal insulator transition

In $\text{Ca}_{1.95}\text{Sr}_{0.05}\text{RuO}_4$ and $\text{Ca}_{1.9}\text{Sr}_{0.1}\text{RuO}_4$ we find a structural transition similar to that found in Ca_2RuO_4 . For both samples this transition is of first order with a rather sharp temperature region where the $L\text{-Pbca}$ and $S\text{-Pbca}$ phases coexist and a hysteresis which amounts to about 50 K. The transition temperature T_S , obtained upon heating, shifts from 256 K for $x=0.05$ to 175 K for $x=0.10$. Since the transitions are rather sharp and there is no $L\text{-Pbca}$ phase remaining at low temperature it

has been possible to analyze the structural details in these compounds with the G4.1 data. Again high resolution patterns have been recorded at 300 and 11 K and additionally at 130 and 200 K for $x=0.1$. The results of the refinements are given in Table 4.3. The high flux patterns were measured in between 1.5 and 300 K upon heating.

Figure 4.7 presents the temperature dependence of the lattice parameters in $\text{Ca}_{1.95}\text{Sr}_{0.05}\text{RuO}_4$, showing similar discontinuities at the transition as for $x=0$ and 0.10 (for the latter specimen see Fig. 5 in Ref. [46], given in the appendix). In contrast to Ca_2RuO_4 the Sr doped samples show a strongly reduced thermal expansion of the b -axis within the $S\text{-}Pbca$ phase. Since the temperature dependence of the a as well as that of the c -axis show almost no changes as function of Sr content, the reduced stretching along b leads to a 33 and 76 % smaller orthorhombic strain ϵ at low temperatures for $x=0.05$ and 0.10, respectively. The pronounced decrease of the orthorhombic strain upon Sr substitution may be partially explained by the reduced tilt of the octahedron. The tilt angles $\Theta\text{-O}(1)$ [$\Theta\text{-O}(2)$] decrease from 12.04° [10.2°] for $x=0.05$ to 11.17° [9.4°] for $x=0.10$. However these changes are too small for explaining the total observed reduction of ϵ : assuming a direct coupling of the tilt angle and the orthorhombic strain, one expects according to Landau theory [116] a quadratical dependence of ϵ on Θ , which would lead to a corresponding decrease of ϵ of 15 and 35 %, respectively. The tilt can, hence, explain only half of the reduction of the orthorhombic strain upon substitution; in analogy to the pronounced temperature dependence of b in the stoichiometric sample [6], the other part results from smaller thermal expansion of the octahedron basal plane edge length parallel to b for higher Sr-contents.

Figure 4.8 shows the temperature dependent shape of the octahedra for the $\text{Ca}_{2-x}\text{Sr}_x\text{RuO}_4$ sample with $x=0.05$ (for the analogue figure of $\text{Ca}_{1.9}\text{Sr}_{0.1}\text{RuO}_4$ we refer to Ref. [46], given in the appendix). At first, one finds in the two Sr doped samples the same discontinuous changes at T_S as in Ca_2RuO_4 : (a) an increase in the $\text{RuO}(1)$ bond lengths and a shrinking of the $\text{Ru-O}(2)$ distance and (b) a discontinuous increase of the edge lengths of the octahedron basal plane. But in contrast to the stoichiometric compound the temperature dependence of these structural parameters below T_S is only small. Especially the thermal expansion of the $\text{Ru-O}(1)$ bond length and that of the octahedron basal plane edge length parallel to b decrease with increasing Sr content x . These two effects yield quite different octahedron shapes for $x=0.0, 0.05, \text{ and } 0.10$ at low temperatures. While in Ca_2RuO_4 the RuO_6 octahedron is flattened along c with $\lambda = \text{Ru-O}(2)/\overline{\text{Ru-O}(1)} = 0.978$, defining the degree of flattening, and has a rectangular basal plane elongated along b , in $\text{Ca}_{1.95}\text{Sr}_{0.05}\text{RuO}_4$ one obtains a smaller flattening of the octahedra with $\lambda = 0.987$ and an almost quadratical basal plane. Finally, for $x=0.1$ the octahedron is nearly regular with $\lambda = 1.002$ and has a slightly rectangular basal plane, which is in contrast to Ca_2RuO_4 elongated parallel to a . Nevertheless, the elongation of the octahedron along the a axis in the latter case may not be sufficient, due to the larger tilt, to overcompensate

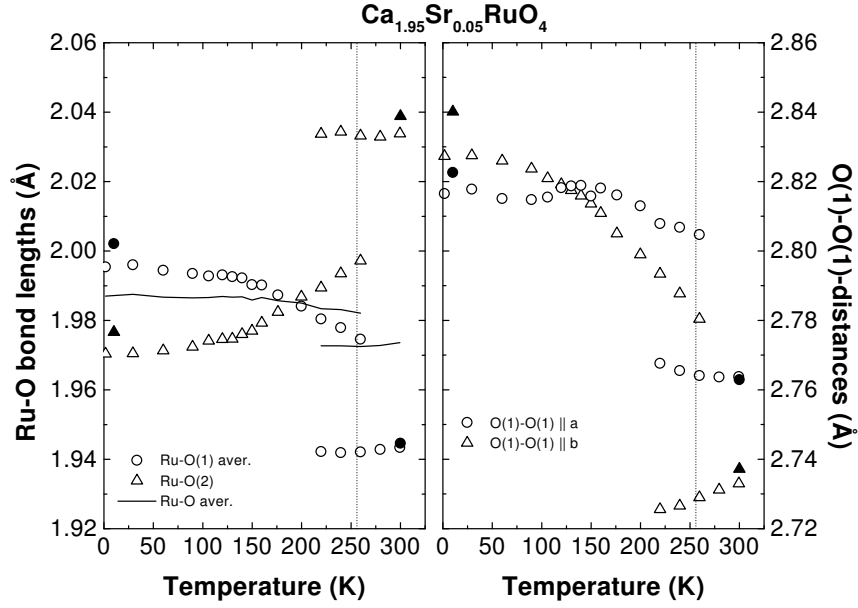


Figure 4.8: Temperature dependence of the Ru-O(1) bond distances and the edge lengths of the octahedron basal plane in $\text{Ca}_{1.95}\text{Sr}_{0.05}\text{RuO}_4$.

the lattice shrinking in the a direction; the orthorhombic lattice remains therefore longer along b .

In both samples we also find the jump of the tilt angles at T_S , which remain almost constant in the $S\text{-}Pbca$ phase, whereas one observes slight changes of $\Theta\text{-O}(1)$ and $\Theta\text{-O}(2)$ in the high-temperature phase. As in Ca_2RuO_4 , the rotation angle Φ decreases by about one degree through the structural phase transition from the $L\text{-}Pbca$ into the $S\text{-}Pbca$ phase and is constant over the whole studied temperature range in each of the two phases. In summary one may conclude that the structural transitions in $\text{Ca}_{1.95}\text{Sr}_{0.05}\text{RuO}_4$ and $\text{Ca}_{1.9}\text{Sr}_{0.1}\text{RuO}_4$ are identical to the one in the pure compound. However, the quite distinct octahedron shape below T_S as a function of Sr content x , as well as the different temperature dependence, seems to indicate some essential differences of the corresponding low-temperature phases.

In addition to so far described diffraction studies on $\text{Ca}_{2-x}\text{Sr}_x\text{RuO}_4$ with $x=0.05$ and 0.10 we have also analyzed a powder sample with $x=0.15$ by recording high resolution patterns at 300 and 10 K. While at room temperature we find, as expected, a single $L\text{-}Pbca$ phase, the powder pattern at $T = 10$ K indicates a mixture of $L\text{-}$ and $S\text{-}Pbca$ phases, with volume fractions of 63% and 37% , respectively. The coexistence of the two phases shows that still for $x=0.15$ the low temperature phase begins to nucleate, but the reduced transition temperature, due to the increased Sr content x , prevents a complete phase transformation. One may, hence, infer that the structural phase transition in $\text{Ca}_{2-x}\text{Sr}_x\text{RuO}_4$ should be completely suppressed slightly above

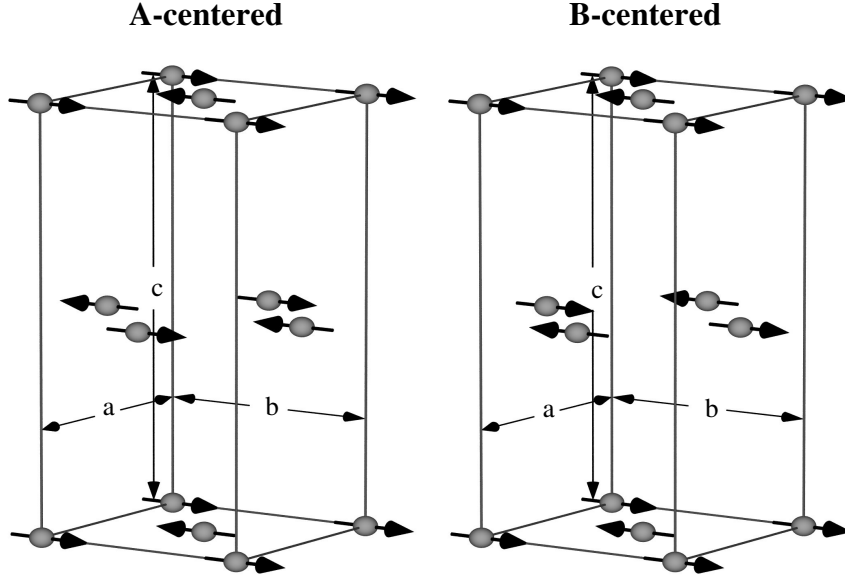


Figure 4.9: Schematic picture of the two antiferromagnetic ordered spin-structures in space group $Pbca$. Only the Ru-ions are shown and the canting of the spins was neglected. The A-centered structure is characterized by a propagation vector $\mathbf{k} = (100)$ of the magnetic mode (La_2CuO_4 -type), while that of the B centered mode is $\mathbf{k} = (010)$ (La_2NiO_4 -type).

$x=0.15$. The temperature dependence of the structure of $\text{Ca}_{1.85}\text{Sr}_{0.15}\text{RuO}_4$ is only little, as can be seen in Table 4.3 (the fit of the diffraction pattern at 10 K has been carried out using the two phases and constraining the structural parameters of the minority phase; therefore the fitted structural parameters have to be considered with caution). Only the tilt angles change significantly: $\Theta\text{-O}(1)$ [$\Theta\text{-O}(2)$] decreases from 6.5° [5.4°] at 10 K to 4.3° [1.7°] at 300 K. Supposing the tilt angle Θ as the order parameter of a transition from $L\text{-}Pbca$ phase into a non-tilted structure one roughly estimates a transition temperature of $T \simeq 530$ K.

Based on the presented neutron diffraction studies of $\text{Ca}_{2-x}\text{Sr}_x\text{RuO}_4$ powder samples, with $x=0.05$, 0.10 and 0.15 one can conclude that slight Sr substitution for Ca leads to rather fast suppression of the structural phase transition, comparable to the suppression of the metal-insulator transition upon Sr substitution. Furthermore, the observed structural changes at T_S are almost identical for the doped and pure compound. One might hence speculate that also for $\text{Ca}_{2-x}\text{Sr}_x\text{RuO}_4$ the metal-insulator transition is triggered by the structural phase transition at T_S . But the details of the coupling between structural, magnetic and electronic properties in $\text{Ca}_{2-x}\text{Sr}_x\text{RuO}_4$ are more subtle, as we will discuss in detail in the next sections.

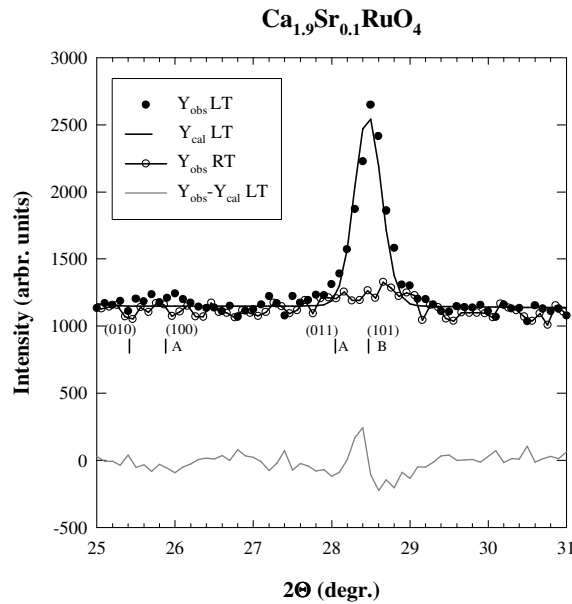


Figure 4.10: Parts of two diffraction patterns obtained with G4.1 at 1.5 K and room temperature on $\text{Ca}_{1.9}\text{Sr}_{0.1}\text{RuO}_4$, together with description via the Rietveld method. Vertical bars indicate the positions of magnetic reflections in the $S\text{-}Pbca$ phase. While an A-centered magnetic mode with moment parallel to the b -axis may lead to a (100) and (011) reflection, the observed (101) reflection corresponds to a B-centered mode.

4.3.2 Magnetic structure of $\text{Ca}_{2-x}\text{Sr}_x\text{RuO}_4$

The magnetic behavior of stoichiometric Ca_2RuO_4 is rather complicated, since there are two coexisting magnetic modes for static antiferromagnetic ordering in Ca_2RuO_4 , as reported in Ref. [6]: the A-centered and B-centered mode. For both types the magnetic moment is aligned along the b -axis and the spins order antiferromagnetically in the ab plane. The two magnetic modes differ only in the arrangement of the spins between neighboring RuO_2 planes, as shown in Fig. 4.9. While in the A-centered mode the spin of the Ru at (0 0.5 0.5) is equivalent to the spin of the Ru at (0 0 0) the B-centered mode corresponds to a spin arrangement with equivalent spins at (0.5 0 0.5) and (0 0 0). The latter spin structure, with propagation vector $\mathbf{k}=(0\ 1\ 0)$, is the same as in La_2CuO_4 , whereas the A-centered mode, with $\mathbf{k}=(1\ 0\ 0)$, has been found in the isostructural system La_2NiO_4 [117–119]. In Ca_2RuO_4 these two modes coexist, with the A-centered one as the majority phase even though its Néel temperature, $T_N \simeq 110\text{ K}$ is significantly lower than that of the B-centered mode, with $T_N \simeq 150\text{ K}$.

Both $\text{Ca}_{1.95}\text{Sr}_{0.05}\text{RuO}_4$ and $\text{Ca}_{1.9}\text{Sr}_{0.1}\text{RuO}_4$ exhibit antiferromagnetic order below just slightly different Néel temperatures of $T_N = 149\text{ K}$ and $T_N = 143\text{ K}$, see Fig. 4.11 and 4.12. Interestingly, we observe in both samples only one magnetic

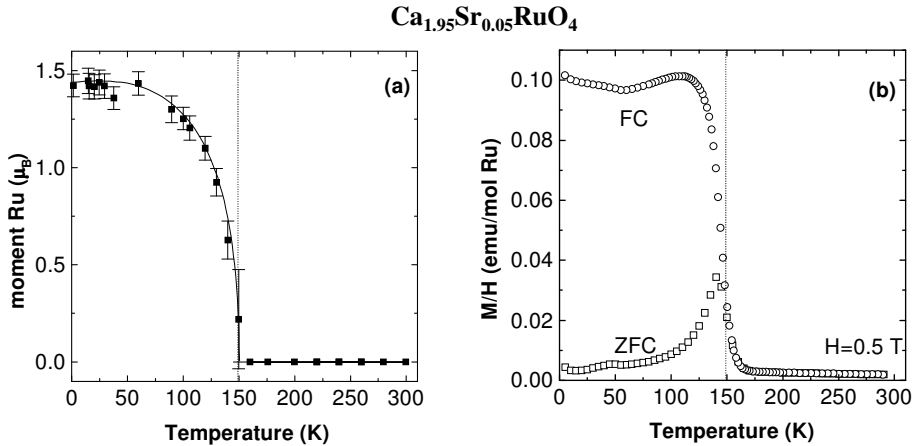


Figure 4.11: (a) Temperature dependence of ordered magnetic moment obtained by refinement of the B-centered antiferromagnetic structure of La_2NiO_4 -type in $\text{Ca}_{1.95}\text{Sr}_{0.05}\text{RuO}_4$ (the line is a guide to the eye); (b) temperature dependence of the field-cooled and zero-field-cooled magnetic susceptibility. The dashed line indicates T_N .

transition by neutron diffraction. Figure 4.10 shows, representatively, a part of the high-flux diffraction pattern obtained with $\text{Ca}_{1.9}\text{Sr}_{0.1}\text{RuO}_4$ at 1.5 K and room temperature. Similar to the observation in $\text{Ca}_2\text{RuO}_{4.07}$ [6], the diffraction patterns reveal a magnetic structure that is well described by the B-centered mode, with a magnetic moment parallel to the b -axis. No sizeable intensity can be found at positions according to the A-centered arrangement, as indicated by vertical bars in Fig. 4.10. The corresponding magnetic model was introduced in the structure refinement in order to get the value of the magnetic moment at different temperatures, as represented in Fig. 4.11 and 4.12. For the refinement we used the magnetic form factor of Ru^{1+} [120], since those for higher ionic states of Ru are not available. The obtained values of the magnetic moment, 1.42 ± 0.05 and $1.38 \pm 0.04 \mu_B$ for $x=0.05$ and 0.10 at low temperature, are within the error limits identical, but lower than the spin-only moment of $2 \mu_B$, expected for Ru^{4+} in the low spin state. This spin reduction is mainly due to the strong hybridization between the Ru-4d and O-2p orbitals, which is generally enhanced in 4d-ions (recent polarized neutron measurements on $\text{Ca}_{1.5}\text{Sr}_{0.5}\text{RuO}_4$ revealed an anomalously large magnetization at the O(1) sites with $\mu_{\text{Ru}} \simeq 4 - 5\mu_{\text{O}(1)}$ [121]).

Also for $\text{Ca}_{1.85}\text{Sr}_{0.15}\text{RuO}_4$ high-flux neutron diffraction patterns were recorded down to 1.5 K, but no evidence of long-range magnetic ordering has been detected. Furthermore, the magnetic susceptibility measured on the same powder sample does not reveal any anomaly, suggesting the disappearance of magnetic ordering already at $x=0.15$.

In agreement with the observation of just one magnetic mode for $x=0.05$ and 0.10

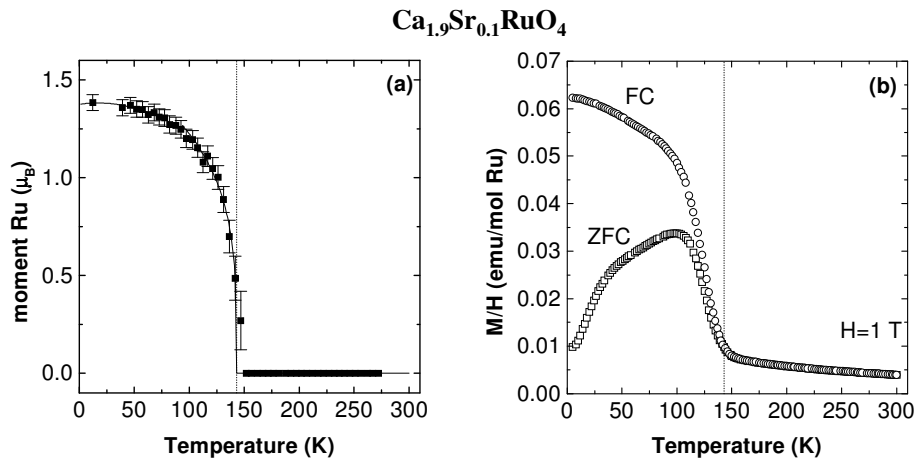


Figure 4.12: Temperature dependence of (a) the ordered magnetic moment (the line is intended as guide to the eye); (b) the field-cooled and zero-field-cooled magnetic susceptibility in $\text{Ca}_{1.9}\text{Sr}_{0.1}\text{RuO}_4$. The dashed lines indicate T_N .

the temperature dependence of the magnetic susceptibility (see Fig. 4.11 and 4.12) shows no extra splitting like for Ca_2RuO_4 . We also find no hysteresis behavior between zero-field-cooled and field-cooled sequences and between heating and cooling cycles, as shown in Fig. 4.11 (b) and in Fig. 4.12 (b). Furthermore, the low temperature susceptibility in both samples is clearly enhanced, compared to the value found in the stoichiometric compound. This enhancement agrees again nicely with a B-centered arrangement of the spins and should be attributed to Dzyaloshinski-Moriya interaction, as discussed in Ref. [6, 115]: Though the rotation of the RuO_6 octahedron would induce, by DM-interactions, for both types of magnetic ordering weak ferromagnetic moments along the a -axis in a single layer [122], these moments cancel out between neighboring RuO_2 planes in the A-centered mode, whereas they add up to a weak ferromagnetic component in the B-centered mode. Consequently, the B-centered order yields to a stronger ferromagnetic contribution in the magnetic susceptibility.

In contrast to Ca_2RuO_4 our neutron powder diffraction studies on $\text{Ca}_{2-x}\text{Sr}_x\text{RuO}_4$, with $x=0.05$ and 0.10 , does not reveal the pronounced changes of the lattice parameters associated with the magnetic ordering at T_N [6]. Furthermore, the reduced stretching of the octahedron edge length parallel to the b axis, which remains the direction of the ordered magnetic moment, seems to indicate some essential changes of spin-orbit coupling in $\text{Ca}_{2-x}\text{Sr}_x\text{RuO}_4$ upon slight substitution of Sr for Ca. The reduction or even complete suppression of spin-orbit coupling becomes also evident from the fact that despite of the almost regular shape of the RuO_6 octahedron for $x \neq 0$, which would favor an orbital and thus collinear spin moment along the c axis (see discussion in section 4.2.1), the spin-moment is still aligned along the b axis.

This rapid suppression of spin-orbit coupling may be easily explained if the chemical disorder introduced via the Sr substitution quenches largely the orbital momentum. However, recent polarized neutron diffraction for $\text{Ca}_{1.5}\text{Sr}_{0.5}\text{RuO}_4$ reveals still a sizeable orbital momentum for Ru [121], suggesting that the above picture is too simple. As the thermal expansion of the corresponding structural parameters, i.e. the Ru-O(1), Ru-O(2) bond lengths and the octahedron basal plane edge lengths, changes continuously with increasing Sr content x it could be otherwise possible that just slight structural differences tuned by the appropriate Ca/Sr content suppress the interaction between the spin and orbital fluctuations in the Mott regime of $\text{Ca}_{2-x}\text{Sr}_x\text{RuO}_4$, suggesting a quite complicated relationship between the electronic, spin and lattice degrees of freedom. Interestingly, calculations by Hotta and Dagotta [123] predict an orbital ordered state for Ca_2RuO_4 in the antiferromagnetic insulating phase, whose relative stability is quite sensitive to lattice effects. In order to further elucidate the correlation of spin- and orbital degrees of freedom in $\text{Ca}_{2-x}\text{Sr}_x\text{RuO}_4$, further works are required. The study of the isovalent alloy series $\text{Ca}_{2-x}\text{Mg}_x\text{RuO}_4$ ($r_{Mg} < r_{Ca}$) might for example help to test whether the orbital momentum is quenched by chemical disorder or not.

4.3.3 The metal-insulator transition in $\text{Ca}_{2-x}\text{Sr}_x\text{RuO}_4$

Up to now we have shown that the basic structural properties induced by the structural phase transition at T_S in $\text{Ca}_{2-x}\text{Sr}_x\text{RuO}_4$ and the pure compound are almost the same. In order to confirm that the metal to insulator transition coincides with the first-order structural phase transition from the $L\text{-}Pbca$ to the $S\text{-}Pbca$ phase, we have performed resistivity measurements on parts of the studied powder samples by a standard four probe technique.

The results of the resistivity measurements for $x=0.05$ and 0.10 are presented in Fig.4.13 (a) and (b). For $x=0.05$ the dramatic change of the temperature dependence below room temperature, clearly indicates the transition from a nearly metallic state to an insulating state. While $\rho(T)$ is almost constant above the transition, the resistivity increases by more than six orders of magnitude in the insulating phase. The observed strong thermal hysteresis of $\rho(T)$ clearly confirms the first order character of this transition. The inset in Fig. 4.13 (a) combines the resistivity data and the relative volume fraction of the $S\text{-}Pbca$ phase in the temperature range $200 \leq T \leq 300$ K. As seen from this inset, the two quantities scale perfectly with each other both upon heating and cooling, demonstrating that also for $\text{Ca}_{1.95}\text{Sr}_{0.05}\text{RuO}_4$ the metal to insulator transition coincides with the first-order structural phase transition. One should note that the metallic state for none of the samples in the $0 \leq x < 0.2$ composition range is fully realized above the transition; all samples show a temperature dependence with negative $d\rho/dT$. As discussed by Nakatsuji *et al.* [52] this weakly semiconducting behavior can be attributed, in addition to standard grain boundary effects, to the highly anisotropic transport properties in the 214 ruthenates.

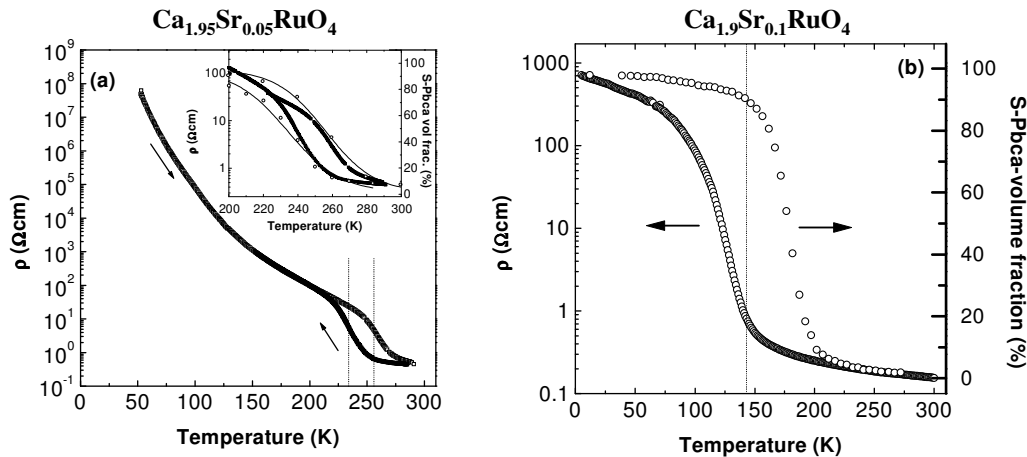


Figure 4.13: (a) Temperature dependence of the resistivity $\rho(T)$ on cooling and heating in $\text{Ca}_{1.95}\text{Sr}_{0.05}\text{RuO}_4$. The dashed line indicates the transition temperature T_S of the structural phase transition, obtained from the high-flux patterns upon cooling and heating. The inset shows the hysteresis in $\rho(T)$ together with that of the volume fraction of the *S-Pbca* phase. (b) The resistivity $\rho(T)$ together with the volume fraction of the *S-Pbca* phase in $\text{Ca}_{1.9}\text{Sr}_{0.1}\text{RuO}_4$ as a function of temperature. All dependencies were recorded upon heating. The dashed line indicates T_N .

With a further increase in Sr concentration T_{MI} ³ continues to decrease and drops from 356 K for $x=0$ to 148 K for $x=0.1$. Though the transition at T_{MI} for $x=0.10$ is characterized by the same abrupt rise in $\rho(T)$ at T_{MI} as for $x=0.05$, the transition from the nearly metallic state to the insulating state occurs at significant lower temperatures than the structural phase transition at $T_S \simeq 175$ K, but coincides with the antiferromagnetic ordering at T_N . In contrast to the transition sequence in Ca_2RuO_4 and $\text{Ca}_{1.95}\text{Sr}_{0.05}\text{RuO}_4$ from a paramagnetic metal (PM) to a paramagnetic insulator (PI) which orders antiferromagnetically at low temperatures (AFI), we find for $x=0.10$ a direct transition from a PM to an AFI, showing no intermediate paramagnetic insulating phase. Even though these two transition sequences are quite different they may be based on the same mechanism. In the case of Ca_2RuO_4 the insulating ground state has been explained within a Mott-scenario, resulting from the pronounced structural changes at the *L-Pbca-S-Pbca* transition. Following this argumentation one may infer that the smaller structural distortions in $\text{Ca}_{1.9}\text{Sr}_{0.1}\text{RuO}_4$ are not “sufficient” to open the insulating gap - the sample remains metallic - whereas the long-range order of the magnetic moments at the Néel temperature leads to the localization of the electrons and the insulating ground state. In this sense $\text{Ca}_{1.9}\text{Sr}_{0.1}\text{RuO}_4$ is also a Mott system, which differs from $x=0.0$ and

³The transition temperature T_{MI} was determined from the intersection of the high and low temperature $\log(\rho(T))$ curves.

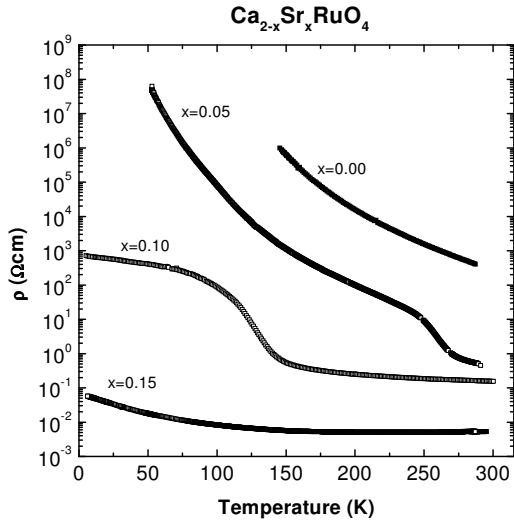


Figure 4.14: Temperature dependence of the resistivity $\rho(T)$ on heating of polycrystalline $\text{Ca}_{2-x}\text{Sr}_x\text{RuO}_4$, with $x=0.05, 0.10$, and 0.15 , measured upon heating. For comparison we show also the resistivity data from Ca_2RuO_4 , taken from Ref. [6]

0.05 only by the more itinerant character induced by the structural phase transition and demonstrates thereby nicely the important role of the Coulomb repulsion between electrons for the metal-insulator transition in $\text{Ca}_{2-x}\text{Sr}_x\text{RuO}_4$. We note, in this context, that band calculations neglecting the effects of onsite Coulomb interactions between d -electrons fail to reproduce the insulating ground state of Ca_2RuO_4 [124–126].

Figure 4.14 represents the temperature dependence of the electrical resistivity for the studied powder samples in the composition range $0.05 \leq x \leq 0.15$ together with the data for $x=0.0$, taken from Ref. [6]. For $x=0.05$ the electrical resistivity data follows reasonably well a Mott variable-range hopping type conduction law below T_{MI} , given by $\rho(T) = \rho_0 \exp(T_0/T)^{1/4}$ [102] with $T_0 = 2.7 \times 10^8$ K, indicating that strong localization dominates the conduction process. Similar resistivity characteristics have been reported for Ca_2RuO_4 by other groups [53, 81, 115] (cf. also Fig. 4.14). However the low temperature $\rho(T)$ for $x=0.10$ reflects a clear deviation in the conduction process from the variable-range hopping type mechanism showing only a weak temperature dependence. Such behavior suggests that delocalized electrons exist in the non-metallic region, which is consistent with the assumption made above that the smaller structural changes do not lead to a pure insulating phase in $\text{Ca}_{1.9}\text{Sr}_{0.1}\text{RuO}_4$. The $x=0.15$ sample exhibits a nearly temperature independent resistivity for $T > 100$ K, but below a slight upturn in $\rho(T)$ is encountered. Since the high resolution data for $x=0.15$ indicates that the structural phase transition still takes place, but remains even at lowest temperatures incomplete, this small increase in $\rho(T)$ should be attributed to remaining weak localization effects induced by the structural distortions.

4.3.4 Summary

The results presented above and in the previous sections lead to the following conclusions: The metal-insulator transition in $\text{Ca}_{2-x}\text{Sr}_x\text{RuO}_4$ involves, either by varying the substitution level x , the temperature or the external pressure, the first order structural transition from the $L\text{-}Pbca$ to the $S\text{-}Pbca$ phase. The distinction between metallic and insulating compounds appears to arise from an enhanced in-plane Ru-O bond distance and a larger tilt. This behavior suggests the interpretation as a Mott transition related to the lowering in energy of the d_{xy} band. Samples with strongly flattened octahedra are driven nonmetallic by the transition, whereas in a sample with a reduced flattening ($x=0.1$) the metal-insulator transition coincides with the magnetic ordering.

Below $T_N \simeq 145$ K the samples with $x=0.05$ and 0.10 exhibit long range antiferromagnetic order, with a propagation vector $\mathbf{k} = (010)$ and spins oriented parallel to the tilt axis. The tilt seems to play a key role in the magnetoelastic coupling since in all magnetically ordered structures of $\text{Ca}_{2-x}\text{Sr}_x\text{RuO}_4$ the spin direction is parallel to the tilt even though the shape of the octahedron is rather distinct [6].

4.4 Neutron diffraction study of $\text{Ca}_{2-x}\text{Sr}_x\text{RuO}_4$ in the magnetically correlated metallic state

Our experimental results presented above have shown that the Ca-rich region ($0 \leq x \leq 0.18$) of the $\text{Ca}_{2-x}\text{Sr}_x\text{RuO}_4$ phase diagram is characterized by a transition to an insulating antiferromagnetic ordered ground state, which is triggered by the change in the crystal structure. For higher Sr concentrations x ($0.2 \leq x < 0.5$) one finds a *metallic* region with magnetic properties which are dominated by a pronounced, but rather broad, maximum in the magnetic susceptibility at the characteristic temperature $T_P = T_{\max}(\chi)$ [2, 52, 127]. Nakatsuji *et al.* and Jin *et al.* have shown that the magnetic susceptibility above T_P obeys a Curie-Weiss law ($\chi(T) \sim (T - \Theta_W)^{-1}$) with a negative antiferromagnetic Weiss temperature Θ_W , which is comparable to T_P . Furthermore they observe strong magnetocrystalline anisotropy between the in-plane axes and the c -axis, as well as between the a and b directions of the orthorhombic lattice. At low temperature, strongly below T_P , the in-plane resistivity deviates clearly from the Fermi-liquid T^2 temperature dependence, observed for Sr_2RuO_4 [14, 16], indicating a non-Fermi-liquid ground state for $0.2 \leq x < 0.5$. In addition, a moderate magnetic field induces a metamagnetic transition below T_P . Based on these experimental results Nakatsuji *et al.* have speculated that the maximum in the susceptibility could be associated with antiferromagnetic *short range* order and is possibly linked to the three-dimensional Néel ordered state observed in the insulating Ca-rich region.

Interestingly the anisotropy of the in-plane susceptibility starts to develop already

far above T_P at a characteristic temperature T_O , accompanied by kinks in the c -axis electrical resistivity and in the temperature dependence of the specific heat. Moreover, $\chi(T)$ deviates from the Curie-Weiss behavior above T_O and tends to follow a simple Curie law ($\chi(T) \sim T^{-1}$), indicating a change of magnetic coupling mechanism at T_O . Based on their susceptibility measurements Nakatsuji *et al.* have speculated, that the appearance of the magnetic in-plane anisotropy below $T_O \gg T_P$ could be associated with a structural phase transition. They report furthermore a simultaneous decrease of T_O and T_P from $T_O \simeq 290$ K and $T_P \simeq 12$ K for $x = 0.2$ to absolute zero for $x_c \simeq 0.5$. In order to elucidate the origin of the maximum in the magnetic susceptibility and the relation of the magnetic crossover at T_O with structural changes we have analyzed a powder and single crystalline sample of composition $\text{Ca}_{1.8}\text{Sr}_{0.2}\text{RuO}_4$ by neutron diffraction.

4.4.1 Structural analysis of $\text{Ca}_{1.8}\text{Sr}_{0.2}\text{RuO}_4$ by single crystal neutron diffraction

Preliminary Details

Initially, the single crystal of $\text{Ca}_{1.8}\text{Sr}_{0.2}\text{RuO}_4$ was carefully examined on the two-axis diffractometer 3T.1 as function of temperature, by collecting data in the (100)/(001) and (210)/(001) diffraction plane. The $\lambda/2$ contamination was suppressed by the use of two pyrolytic graphite filters. While at room temperature the superstructure reflections ($10l$) and ($30l$) with l even, characteristic of a tilt distortion in the ideal K_2NiF_4 structure type, were not observed, a set of peaks of the type ($21\frac{1}{2}l$) with l odd were present. These superstructure reflections have intensities up to 6% of the strongest fundamental reflections and clearly indicate a long range deformation of the rotation-type with an unit cell which is doubled in the c -direction in respect to the $L\text{-}Pbca$ and $S\text{-}Pbca$ phases. These first observations demonstrate well that for $x=0.2$ only a rotational distortion is present at room temperature, while an additional tilt deformation, as found for stoichiometries with $x < 0.2$, can be excluded.

However, upon cooling superstructure reflections, indicating a long range deformation of the tilt type, appear below a characteristic temperature of $T_S = 284$ K. Figure 4.15 shows exemplarily the temperature dependence of the (304) reflection intensity scaled to that of the (200)-Bragg reflection. The transition into the low temperature phase with a nonvanishing tilt is continuous with only a minor first order contribution close to the transition, but no evidence for a hysteresis effect has been observed. As can be easily deduced from the l dependence of the distinct superstructure reflections – the tilt peaks ($h0l$) with h odd and l even and the rotational peaks ($hk\frac{1}{2}l$) with h even and k, l odd – the tilt and rotational distortions exhibit different stacking periods along the c -axis in the low temperature phase. While the periodicity of the rotation is still doubled, the tilt has a periodicity of just one c parameter ($c \sim 12.6 \text{ \AA}$). It is quite interesting that although the single

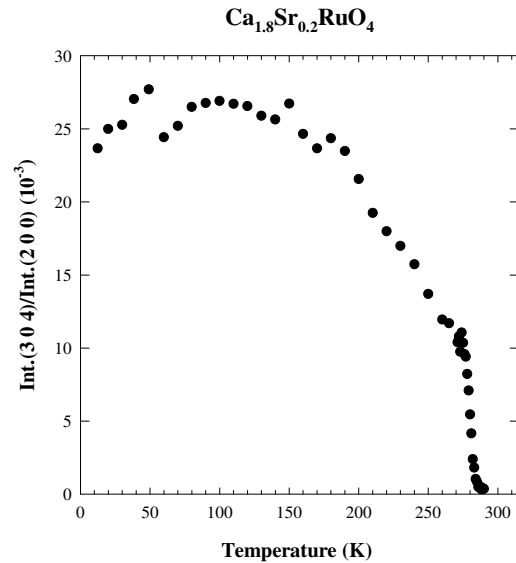


Figure 4.15: Dependence of the intensity of the (3 0 4) superlattice reflection due to the tilting of the RuO_6 -octahedron normalized to that of the (2 0 0) fundamental reflection as function of temperature for a $\text{Ca}_{1.8}\text{Sr}_{0.2}\text{RuO}_4$ single crystal. Indices are based on the $I4_1/acd$ unit cell.

crystal of $\text{Ca}_{1.8}\text{Sr}_{0.2}\text{RuO}_4$ exhibits at low temperature qualitatively the same characteristic structural deformations as observed for $0 \leq x \leq 0.18$ in the metallic phase, their stacking sequence is different. These differences might suggest a change of the interaction between the two order parameters, corresponding to different propagation vectors $\mathbf{q}_{\text{tilt}} = (0.5, 0.5, 0)$ and $\mathbf{q}_{\text{rotation}} = (0.5, 0.5, 0.5)$, as a function of Sr content. This will be discussed in more detail in the following sections together with the results of the structural analysis of the high and low temperature phase of $\text{Ca}_{1.8}\text{Sr}_{0.2}\text{RuO}_4$ performed on the four circle diffractometer 5C.2.

In order to determine the space groups of the high and low temperature phase, large sets of Bragg reflection intensities were collected in a $a_{\text{LTO}} \times a_{\text{LTO}} \times 2c$ lattice, with $a_{\text{LTO}} = \sqrt{2}a$, at 20 and 295 K on the four-circle diffractometer 5C.2. At 295 K a data set of 1056 Bragg reflection intensities was recorded with $\sin \Theta / \lambda \leq 0.85 \text{ \AA}^{-1}$, using a pure ω scan mode up to $2\Theta = 70^\circ$ and a $\omega - 2\Theta$ scan mode for higher diffraction angles. The experiment at 20 K was carried out with the same crystal mounted in a liquid helium cryostat. Due to the enhanced background of the cryostat, the low-temperature data collection had to be restricted to $\sin \Theta / \lambda \leq 0.76 \text{ \AA}^{-1}$; a total set of 2132 reflections were measured. The intensity data of the two sets were corrected for absorption numerically, though the absorption is almost negligible, $\mu = 0.04 \text{ cm}^{-1}$ (the resulting absorption correction factors varied only from 0.9776 to 0.9788).

The high temperature phase

Referring to the group-subgroup relations of the $I4/mmm$ structure, given in section 4.1, a rotational distorted modification of the K_2NiF_4 structure type may be described either by the tetragonal space group $I4_1/acd$ or by the orthorhombic space

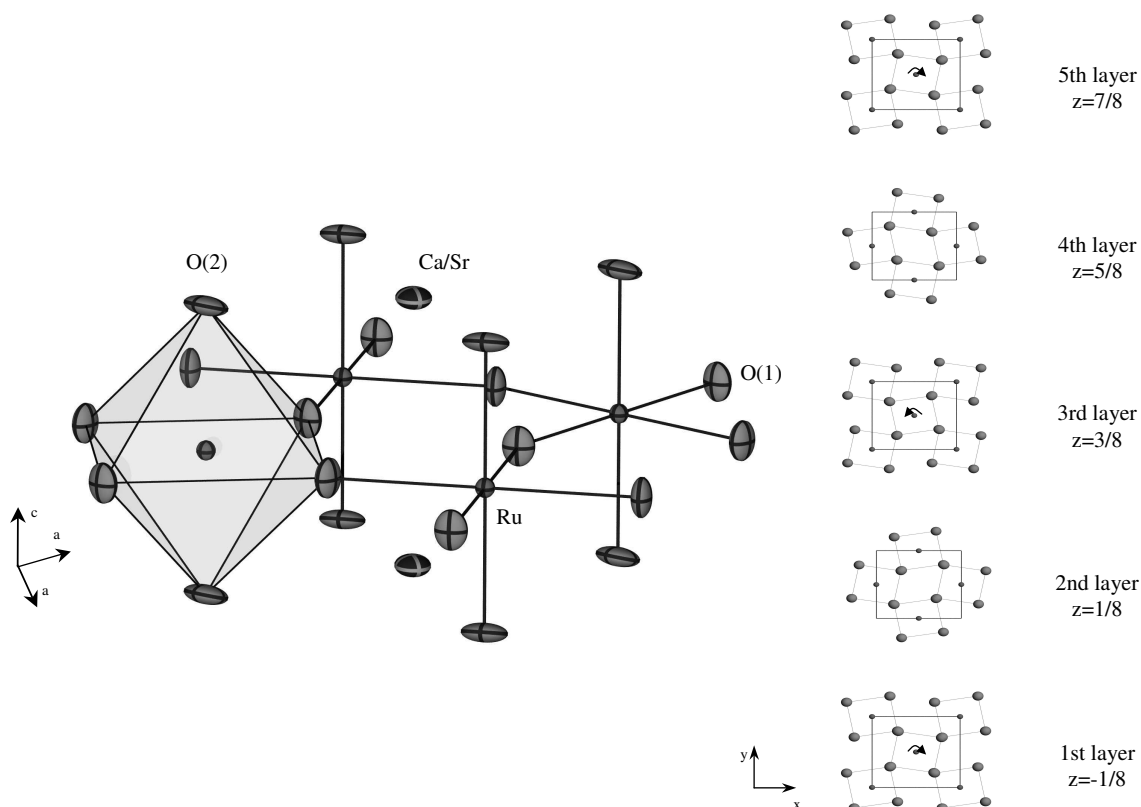


Figure 4.16: *Left:* A schematic plot of the RuO₆ octahedron, representing the results of the structural refinement of Ca_{1.8}Sr_{0.2}RuO₄ at 295 K. The ellipsoids correspond to a probability density of 80%. *Right:* Schematic representation of the stacking of the RuO₂ planes which are distorted by the rotation of the RuO₆ octahedron around the *c*-axis. The *z* coordinates in respect to the $I4_1/acd$ unit cell are indicated and the *c* axis is perpendicular to the page.

group $Acam$. If one assumes a rigid rotation of the RuO₆ octahedra about a direction parallel to the *c*-axis, the atomic arrangement of the RuO₂ planes is defined only by the displacement of the O(1) atoms in the *ab* plane. Since the rotation of two RuO₆ octahedra separated along [001] by one *c* parameter may be clockwise or counterclockwise, the RuO₂ plane at $z = 0$ is identical either to that at $z = 1.0$ or to that at $z = 2.0$. While the first configuration, with space group $Acam$, implies no doubling of the *c* parameter, the latter configuration, with space group $I4_1/acd$, generates the observed doubling of the unit cell in *c* direction. The corresponding rotation scheme is shown in the right part of Fig. 4.16.

Based on the preliminary investigation on 3T.1 space group $I4_1/acd$ was used for the structure refinement. The intensity data recorded at 295 K were averaged according to the Laue-group $4/mmm$ to provide a set of 485 independent reflections.

In the refinement we applied an isotropic extinction correction according to the Becker-Coppens model for secondary extinction of type I. However, due to strong extinction effects in this rather perfect crystal, 19 reflections with extinction stronger than 70 % were excluded. The refinement of 16 parameters (scale factor, 3 coordinates, 11 anisotropic temperature-factor coefficients and an extinction parameter) converged to low disagreement indices, with $R_w = 2.88\%$ and $R_{uw} = 1.77\%$. At this stage the site occupancies were individually refined for each species. As no statistically significant deviation of the occupancies was indicated, the parameters were restored to unity. The final structure parameters are listed in Table 4.1 on page 31 and are shown in a schematic plot in the left part of Fig. 4.16. Because of the low precision of the lattice parameters obtained by the four circle diffractometer, we used the values obtained with the two-axis diffractometer 3T.1, presented in Table 3.1, for calculating the bond distances and angles.

The refined structure parameters for $\text{Ca}_{1.8}\text{Sr}_{0.2}\text{RuO}_4$ in space group $I4_1/acd$ can be compared to the neutron diffraction study on a single crystal of Sr_2RuO_4 [13], with its undistorted K_2NiF_4 structure. Basically, these closely related structures differ only in the positions of the O(1) oxygen atoms, due to the rotation of the RuO_6 octahedra around the c axis in space group $I4_1/acd$. More specifically, the rotation shifts the O(1) oxygen atoms located in the RuO_2 planes from the positions $(\frac{1}{4}, \frac{1}{2}, \frac{1}{8})$, which they would occupy if the symmetry were $I4/mmm$, to $(x, \frac{1}{4} + x, \frac{1}{8})$. The value of x found at room temperature for $\text{Ca}_{1.8}\text{Sr}_{0.2}\text{RuO}_4$ corresponds to a rotation angle $\Phi = 13.55^\circ$ as indicated in Fig. 4.16. It is quite interesting that the rotation angle Φ adjusts in such a way that in spite of the 3 % smaller tetragonal lattice parameter a for $x=0.2$ the Ru-O(1) bond-lengths are almost the same in the stoichiometric and Ca substituted sample. Furthermore, one finds in both compounds nearly identical Ru-O(2) bond lengths, though the insertion of the smaller Ca-ion leads also to a shrinking of the lattice parameter c of 2 %. Since the Ru-O(2) distance is determined just by the c parameter and the z -position of the O(2) site, the shortening of c is compensated independently of the rotation of the RuO_6 octahedron, by displacing the O(2) site parallel to c towards the Ca/Sr site. This displacement avoids a flattening of the RuO_6 octahedron but reduces the Ca-O(2) bond parallel to the c -axis, which is already significantly shorter than all others Ca-O bonds. Nevertheless, the Ca/Sr atom does not evade this proximity to the O(2) atom, but gets even closer to the O(2) layer, as indicated by the smaller z -position of the Ca site compared to that of Sr_2RuO_4 . As a consequence the Ca-O(2) bond along the c -axis amounts to only 2.2914(4) Å, which is $\sim 24\%$ smaller than the longest Ca-O bond. But on the other hand the shift of the Ca-atoms toward the O(2) layer moves the Ca further away from the RuO_2 plane and its O(1) nearest neighbors. This displacement permits the system to maintain an almost unchanged (averaged) Ca-O(1) bond, with 2.688 Å, despite of the significant compression of the unit cell. Thus, one may conclude that the three positional parameters of the $I4_1/acd$ structure of $\text{Ca}_{1.8}\text{Sr}_{0.2}\text{RuO}_4$ adjust in order to reproduce exactly the arrangement of the Ru-O and Sr-O bonds found in

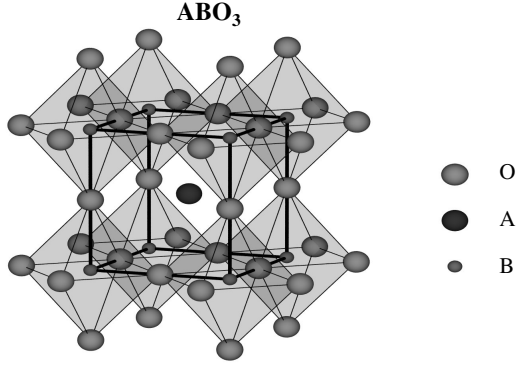


Figure 4.17: Crystal structure of cubic perovskite ABO_3

Sr_2RuO_4 . However, in view of the two rotational modifications of the K_2NiF_4 structure, the interesting question arises why the system favors the $I4_1/acd$ symmetry ($2c$ rotation) rather than the $Acam$ symmetry ($1c$ rotation). A possible reason for this could be the reduced Coulomb repulsion between the basal oxygen ions of two RuO_2 planes separated by one c parameter in the former symmetry. While in space group $Acam$ the corresponding planes are identical the distinct rotation scheme in space group $I4_1/acd$ results in an increased O(1) interlayer distance ($\simeq 0.3\%$) and thus in a reduced Coulomb repulsion. However, the phonon branch in Sr_2RuO_4 which corresponds to the rotation of the RuO_6 octahedra around the c -axis has practically no dispersion in $[001]$ direction, indicating that there is very little coupling between rotations in different layers [47]. Nevertheless, the decrease of the lattice constant c with decreasing Sr content x , may enhance the interlayer coupling.

Before going into a detailed discussion of the underlying mechanism of the $I4/mmm$ to $I4_1/acd$ transition in $Ca_{2-x}Sr_xRuO_4$, we complete the discussion of the results of the structural refinement at room temperature with the observed thermal parameters (Table 4.1 and Fig. 4.16). As in $Ca_{1.85}Sr_{0.15}RuO_4$ (see section 4.2.2) the thermal ellipsoids show a pronounced anisotropy, with characteristically enhanced temperature-factor coefficients compared to the equivalent values in Sr_2RuO_4 . Both, the largely enhanced amplitude in the a, b plane at the Ca/Sr site and significant larger O(1)- $U_{\text{long-axis}}$ and O(2)- U_{\perp} coefficients, clearly indicate the nearby tilt instability. The remaining thermal parameters are in general agreement with the corresponding results for $Ca_{1.85}Sr_{0.15}RuO_4$ and Sr_2RuO_4 and give for example no indication of static disorder due to the mixing of Ca and Sr.

Bond-length mismatch

Octahedral tilting and rotational distortions are common in perovskite related structures, which can be derived basically from the Ruddlesden-Popper series $A_{n+1}B_nO_{3n+1}$. These distortions reduce the symmetry of the A and B-site coordination environment and result in a change in A-O and B-O bond lengths. The reduction of symmetry reflects the response of the system to a bond-length mismatch for the coordination

polyhedra around the A and B cations, imposed by the higher symmetry. This can be easily seen in the cubic perovskite structure ($n=\infty$), which imposes that the A-O distance corresponds to exactly $\sqrt{2}$ times the B-O distance (see Fig. 4.17). A measure of the stability of such a structure is the so-called Goldschmidt tolerance factor [128]

$$t = \frac{R_A + R_O}{\sqrt{2}(R_B + R_O)} ,$$

where $R_A + R_O$ and $R_B + R_O$ are the optimum cation-oxygen bond lengths. A perfect matching of the bonds occurs for $t = 1$. In ionic solids the length $R_A + R_O$ and $R_B + R_O$ are commonly taken as the sums of the empirically determined room-temperature ionic radii [82]. The internal stresses associated with $t \neq 1$ may be relieved by a cooperative tilting or rotating of the BO_6 octahedra. For the parent perovskite compounds SrRuO_3 and CaRuO_3 one calculates $t = 0.95$ and $t = 0.90$, indicating the instability of the cubic perovskite structure for the ions Sr^{2+} , Ca^{2+} and Ru^{4+} . And indeed both compounds do not adopt the cubic structure at room temperature, but have an orthorhombically distorted perovskite structure, with $Pbnm$ symmetry [96, 97].

For the studied K_2NiF_4 -type structure ($n=2$) of $\text{Ca}_{2-x}\text{Sr}_x\text{RuO}_4$ the discussion of the bond-length mismatch by means of the tolerance factor is inappropriate, since the higher degrees of freedom of the layered perovskite structure allow the system already to relieve the strain without reducing symmetry. This can be accomplished by distorting the two coordination polyhedra – the RuO_6 octahedron and the CaO_9 polyhedron which are depicted in Fig. 4.18 – in the c -direction. Therefore, it appears more convenient to analyze the stability of the structure using the bond valence sum method. The bond valence sum method developed by Brown and Altermatt [129, 130] describes the correlation between the bond length and the bond valence. The bond valence s_{ij} of an i - j bond is calculated from an empirically determined parameter R_{ij}^0 , specific for each i - j pair, and from the experimental bond length R_{ij} (in Å) as $s_{ij} = \exp((R_{ij}^0 - R_{ij})/0.37)$. Summing over the bond valences from all the nearest-neighboring ions j gives the bond valence sum of an ion i as

$$V_i = \pm \sum_j s_{ij} = \pm \sum_j \exp\left(\frac{R_{ij}^0 - R_{ij}}{0.37}\right) .$$

The bond valence method allows, usually, an estimation of the oxidation state of an ion based on the structural environment, i.e. the coordination sphere and the nearest-neighboring atoms. In the present case of a layered perovskite-type structure the bond valence sum calculations can also be used for indicating tensile or compressive strain directed to an atom in a structure. Without internal strain the calculated bond valence sums should correspond exactly to the formal valence (equal to its oxidation state) of each ion. Any internal strain caused by the symmetry can then be quantified by the difference between the calculated bond valence sum of an ion

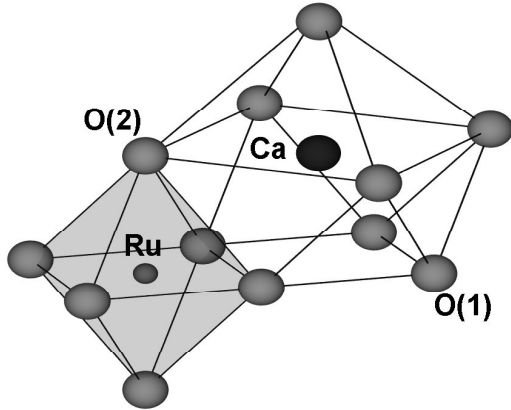


Figure 4.18: A schematic plot of the RuO_6 octahedron and the CaO_9 polyhedron, which form the K_2NiF_4 -structure of $\text{Ca}_{2-x}\text{Sr}_x\text{RuO}_4$.

and its formal valence. Such an analysis is perfectly adapted to describe the phase transitions in the $(\text{La}, \text{Sr})_2\text{CuO}_4$ family [51, 131].

For stoichiometric Sr_2RuO_4 at room temperature one calculates, utilizing the empirical values of R_{ij}^0 , given in literature [129, 132], +4.127 for Ru^{4+} and +2.005 for Sr^{2+} [13]. While the value for the ninefold coordinated Sr-site is rather close to the expected valence of +2.0 and indicates a perfect equilibrium of the bond distances in the SrO_9 polyhedron, the slightly enhanced valence sum for the Ru-site reflects the internal strain caused by the elongation of the RuO_6 octahedron. In the case of $\text{Ca}_{1.8}\text{Sr}_{0.2}\text{RuO}_4$ it is quite illustrative to calculate at first the bond valence sum by neglecting the rotational distortion. Under this assumption one determines +4.660 for Ru^{4+} and +1.699 for $\text{Ca}^{2+}/\text{Sr}^{2+}$, clearly indicating that the Ru-O bonds would be under compression, while the Ca-O bonds would be under tension in an undistorted K_2NiF_4 structure. Though in $I4/mmm$ symmetry a significant distortion of the polyhedra corresponding to the free parameters $z\text{-O}(2)$, $z\text{-Ca/Sr}$ and $c \neq a = b$ is possible, these distortions are obviously not sufficient to compensate the strong internal misfit caused by the Ca ion. The smaller Ca needs a smaller polyhedron, therefore, it exerts a higher pressure on the Ru-O bonds, as indicated by the strongly enhanced bond valence sum of Ru^{4+} . In the $I4/mmm$ symmetry it is impossible to reduce the $(\text{Ca}, \text{Sr})\text{O}_9$ polyhedron volume without simultaneously increasing the pressure on the Ru-O bonds. Lowering the symmetry by a cooperative rotation of the ruthenium-centered octahedra in $I4_1/acd$ symmetry, allows the system to adjust the volumes of the $(\text{Ca}, \text{Sr})\text{O}_9$ polyhedron and the RuO_6 octahedron separately, via the new degree of freedom. Due to the rotation of the RuO_6 octahedra in the $I4_1/acd$ phase around the c -axis the Ru-O(1) and Ca/Sr-O(2) in-plane distances become independent. Consistently, the observed bond valence sums in the $I4_1/acd$ phase are significantly closer to the expected values, with +4.179 for Ru^{4+} and +1.896 for $\text{Ca}^{2+}/\text{Sr}^{2+}$. Hence, the bond-valence analysis confirms the model of the bond mismatch quantitatively for $\text{Ca}_{1.8}\text{Sr}_{0.2}\text{RuO}_4$.

Apart from the rotation of the RuO_6 octahedra, which is by far the largest distor-

tion in $\text{Ca}_{1.8}\text{Sr}_{0.2}\text{RuO}_4$ at room temperature, the additional parameter $z\text{-O}(2)$ and $z\text{-Ca/Sr}$ adjust in such a way that the $\text{Ru-O}(2)$ and (averaged) $\text{Ca/Sr-O}(1)$ distances are independently of the Sr concentration x almost identical. As a consequence, the $\text{Ca/Sr-O}(2)$ bond length parallel to the c -direction becomes very short. One might speculate that this strongly compressed bond, which is even shorter than the sum of the corresponding ionic radii, provides the driving force of the adjacent tilt instability. However, this hypothesis contradicts the general observation of a negative thermal expansion of the lattice parameter c in $I4_1/acd$ symmetries [89–93, 100], which would lead to more relaxed $\text{Ca/Sr-O}(2)$ bond length on lowering the temperature. Yet, another possible mechanism to explain the transition into the tilt distorted phase could be the fact that the rotation of the RuO_6 octahedra and the simultaneous shrinking of the lattice parameter a , with decreasing Sr content x as well as with decreasing temperature, results in a considerably shortened $\text{O}(1)\text{-O}(1)$ distance of two opposite oxygen ions, of distinct RuO_4 plaquettes. In $\text{Ca}_{1.8}\text{Sr}_{0.2}\text{RuO}_4$ the shortest of these $\text{O}(1)\text{-O}(1)$ distance, 2.8495 \AA is much shorter than that observed in Sr_2RuO_4 , with $\text{O}(1)\text{-O}(1)=3.8710 \text{ \AA}$ [13] and is furthermore close to the doubled ionic radius of an oxygen ion (2.80 \AA). Within this instructive scenario the tilt of the octahedra would allow the system to reequilibrate the internal pressure, without further reducing the corresponding $\text{O}(1)\text{-O}(1)$ distance and, therefore, without further enhancing the anion repulsion between these two opposite oxygen ions. Although the foregoing discussion gives a simple physical picture of the tilt transition, an intrinsic bond length mismatch might not be the only cause for the structural phase transition. As discussed by Nakatsuji *et. al* [3] one could associate the tilt transition also with a Jahn-Teller-type effect. We will come back to this point in more detail together with the discussion of the low temperature phase in the forthcoming section. Completing the discussion of the bond length mismatch and its relationship to the structural phase transitions in $\text{Ca}_{2-x}\text{Sr}_x\text{RuO}_4$ we note that the interpretation of the $L\text{-Pbca-S-Pbca}$ phase transition, discussed in section 4.2 and 4.3, alone on the basis of the bond-length mismatch is impossible, since this transition is primarily driven by the coupled elastic and electronic energies, associated with the structural changes.

The low temperature phase

As we have already mentioned, the study of the $\text{Ca}_{1.8}\text{Sr}_{0.2}\text{RuO}_4$ single crystal on the two-axis diffractometer 3T.1 revealed the appearance of several additional superlattice reflections, which are forbidden in $I4_1/acd$ symmetry. The type of the observed reflections clearly indicates that the low temperature phase possesses a nonvanishing tilt. In addition, the symmetry reduction at the phase transition leads to the occurrence of twin domains, indicated by a pronounced broadening and splitting of the intensity profiles below $T_S = 284 \text{ K}$. In comparison to the well understood twin rule of the orthorhombic LTO-phase in $\text{La}_{2-x}\text{Sr}_x\text{CuO}_4$ [50], the twinning in $\text{Ca}_{1.8}\text{Sr}_{0.2}\text{RuO}_4$

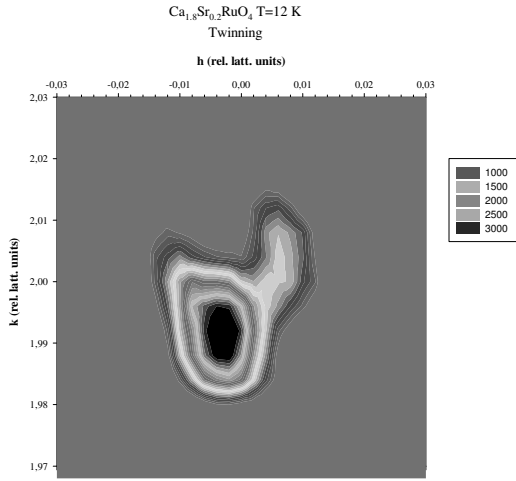


Figure 4.19: Mapping of the (020) reflection in twinned Ca_{1.8}Sr_{0.2}RuO₄ at 12 K.

is more complex. The situation is illustrated in Fig. 4.19, which shows the mapping of the (020) reflection in the $(hk0)$ -plane at 12 K. One sees clearly a splitting of the (020) reflection in a central peak with one satellite, which has half the intensity of the central component. For both peaks a pronounced anisotropic broadening along [010] is observed. Also for (220) there is a splitting into two peaks with different intensities. The intensity of the central peak is about five times larger than that of the other peak, suggesting that at least one twin domain is dominant in the present crystal. Apart from these pronounced changes of the peak profiles for (020) and (220), several scanned (00 l) reflections show no change in shape, upon cooling.

The most likely explanation for the observed twinning can be given by the formation of twin domains due to two different twin laws. One kind of twin domains is related to twin orientations which share the (110)-plane, similar to that found in La_{2-x}Sr_xCuO₄. A second family of domains, which has as common axis for the twinning $\langle 100 \rangle$, corresponds to a formation of two twin orientations by a 90° rotation of the reciprocal lattice around [001]. Figure 4.20 displays the effect of superimposing the reciprocal lattice of a pair of domains by these two twin laws. While the twinning by 90° rotation explains qualitatively the splitting of the (220) reflection and the anisotropic broadening for (020), the twinning by reflection, with a pair of twin domains having (110) as a common plane, leads to the splitting of the (020) peak. For both twin laws the angle Δ between the different lattices results from the orthorhombic distortion by $\Delta = 2 \arctan(b/a) - 90^\circ$. For (020) one finds, $\Delta = 0.47 \pm 0.06^\circ$ and at (220), $\Delta = 0.57 \pm 0.06^\circ$, which are in good agreement with each other. From these values one calculates $\epsilon = 4.1 \dots 5.0 \times 10^{-3}$ for the orthorhombic strain. However, these values are not completely consistent with the data, since the determined ϵ would lead to a somewhat larger broadening of the (020) reflections. It is worth pointing out in this context that the twin domains connected by a 90° rotation imposes strong disturbances to the crystal lattice. The presence of 90° rotation twins implies that the orthorhombic long and short axes

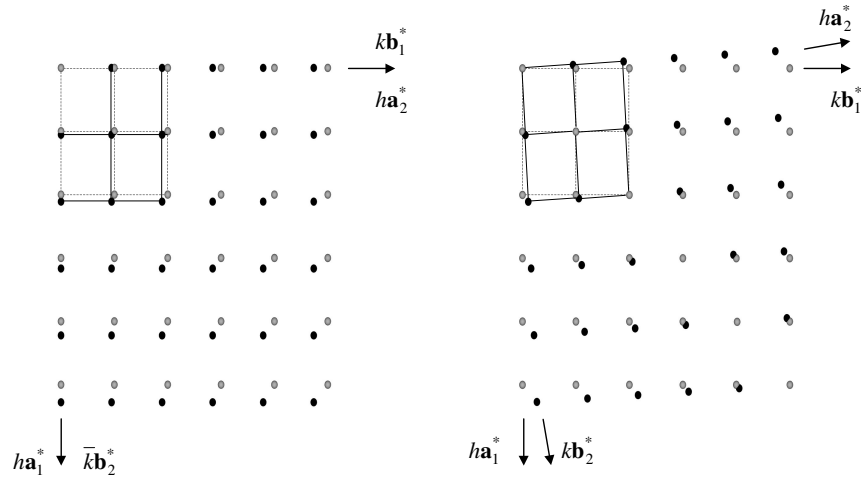


Figure 4.20: Relative positions of reciprocal-lattice points from domains twinned by 90° (left) and by reflection (right).

of the low temperature phase alternate from one domain to another. Hence, the corresponding boundary imposes a strong misfit between two lattices in neighboring domains, which increases with the length of the boundary. As a consequence the domain interfaces are particularly disturbed. Therefore it can not be ruled out that some puzzling microstructural effects are involved, which would allow the crystal lattice to reduce the strain imposed by the 90° rotation twins. It would be helpful for the complete understanding of the nature of the twins to study the sample by high-resolution electron microscopy and electron diffraction. A possible monoclinic distortion of the orthorhombic lattice can not be excluded but has to be smaller than $|90^\circ - \gamma| < 0.06^\circ$, since longitudinal scans on the strong component of (220) and $(2\bar{2}0)$ revealed identical 2Θ values, corresponding to the diffractometer resolution.

For the detailed structural analysis of $\text{Ca}_{1.8}\text{Sr}_{0.2}\text{RuO}_4$ on the four-circle diffractometer 5C.2 at 20 K the twinning of the crystal was taken into account by adapting the entire scan width, ensuring that the integrated intensities correspond to the integration over all domains. However, this adaptation of the scan width provoked a contamination of several reflections by adjacent Bragg peaks, which had to be removed from the data set. Referring to our discussion in section 4.1 one may consider for the low temperature phase two possible orthorhombic space groups: $Pbca$ and $P2_12_12_1$. In the case of the orthorhombic space group $Pbca$, associated with a tilt around an axis close to $[010]$ and a rotation around $[001]$, with different stacking schemes along the c -axis, the Ca, O(1), and O(2) sites are split in two independent positions in respect to the L - $Pbca$ and S - $Pbca$ phases discussed in section 4.2. We want to emphasize that even if the above distortion scheme of the low temperature phase of $\text{Ca}_{1.8}\text{Sr}_{0.2}\text{RuO}_4$ can be described by the same space group as the L - $Pbca$ and S - $Pbca$ phases, these $Pbca$ a continuous transition between these phases is not

symmetry-allowed as can be easily deduced from the different propagation vectors of the rotational distortion (see also Fig. 4.2). Concerning the twinning of the crystals we assumed for the refinement cycles a twin law which leaves the c -axis invariant. Because of the mmm Laue symmetry, a distinction between a twinning by 90° , which results in a superposition of F_{hkl} and $F_{k\bar{h}l}$ structure factors, and twinning by reflection, which superposes F_{hkl} and F_{khl} , is not necessary. Therefore, the measured intensities have been analyzed by $Int_{hkl} = scale \cdot [\alpha F_{hkl}^2 + (1 - \alpha) F_{khl}^2]$, where α designates the twinning ratio. First refinements, with 944 averaged reflections, of the full number of free parameters (scale factor, one twin fraction, an isotropic extinction parameter with a Lorentzian distribution of mosaicity, 21 atomic coordinates and 10 anisotropic temperature-factors), indicated strong correlation of the Ca- z positions and the O(2)- z positions, which were therefore constrained. Furthermore, the Ru- x and Ru- z positions were fixed to 0 and $3/8$, respectively, since no deviation of these parameters from their high symmetry positions larger than their statistical error, was obtained. The final results of the refinements and the corresponding residuals are presented in Table 4.1 on page 31. Whereas the determined parameters show no physically unreasonable results, with realistic temperature factors, the final disagreement factors $R_w = 7.10\%$ and $R_{uw} = 5.63\%$ are relatively high and less satisfying than those of the room temperature data set. Therefore we performed additional refinements in the acentric orthorhombic $P2_12_12_1$ space group, which represents the combination of the $2c$ periodical $I4_1/acd$ rotation with the $1c$ periodical octahedron tilt of $Pccn$ -type. Though the number of free parameters increases considerably in this structure (42 atomic coordinates), the refinements lead to no significant improvement in the fit. Furthermore we observe no intensities inconsistent with the $Pbca$ symmetry (note the lower symmetry space group $P2_12_12_1$ allows additional reflections in respect to $Pbca$). As additionally the observed twinning may affect adversely the quality of the data set, we do not feel justified in adding further structural parameters to our refinement and adopt, therefore, $Pbca$ as the most likely space group for the low temperature phase of $Ca_{1.8}Sr_{0.2}RuO_4$, which we will refer to as $D-Pbca$.

For calculating the bond distances and bond angles given in Table 4.1, the temperature dependence of the lattice parameters has been determined by powder X-ray diffraction using Cu- K_α radiation on a nominally equivalent single crystal. The obtained values at lowest temperature ($T=25\text{ K}$) are $a = 5.333\text{ \AA}$, $b = 5.303\text{ \AA}$, and $c = 24.866\text{ \AA}$ [113]. In comparing the determined Ru-O(1) and Ru-O(2) distances to our previous results, it becomes again evident that these values reproduce almost exactly the regular octahedron shape found in Sr_2RuO_4 [13]. The averaged tilt and rotation angle of the octahedra, which amount to $\Theta\text{-O(1)}=5.4^\circ$ [$\Theta\text{-O(2)}=4.3^\circ$] and $\Phi=13.8^\circ$ are comparable in magnitude to those found for the metallic $L-Pbca$ phase of the $Ca_{1.85}Sr_{0.15}RuO_4$ single crystal at room temperature and the corresponding powder samples (see Table 4.3). From this we conclude that even if the stacking sequences of the rotational distortions are quite different for the $L-Pbca$ phase ($x < 0.2$)

and the $D\text{-}Pbca$ phase ($x \geq 0.2$), derived from $I4_1/acd$, the distortion pattern of the RuO_6 octahedra within a particular RuO_2 plane is similar in the two phases.

Additionally, we have tried to observe magnetic order in $\text{Ca}_{1.8}\text{Sr}_{0.2}\text{RuO}_4$ by elastic neutron scattering. In order to search for the development of long-range magnetic order, we performed a diffraction experiment in the temperature range from 1.5 to 100 K, using the 1T.1 triple-axis spectrometer. Diffraction data were obtained within the two scattering planes spanned by $(1, 0, 0)$, $(0, 1, 0)$ and $(1, 1, 0)$, $(0, 0, 1)$, respectively. At a series of temperatures we tried to detect the occurrence of new Bragg peaks, or to observe an increase in the nuclear Bragg peaks that might be associated with possible ferromagnetic ordering. No evidence was found for any long-range magnetic ordering, either ferromagnetic or antiferromagnetic, with an estimated upper limit of about $0.10 \mu_B$ for any possible ordered moment.

Finally, let us try to bring our results in agreement with the experimental findings by Nakatsuji *et al.* and Jin *et al.* [2, 52, 127]. Both authors reported kinks in the electric resistivity with a clear changeover from nonmetallic to metallic behavior in ρ_c , at the temperature T_O on cooling. At the same time the magnetic anisotropy starts to appear at T_O and the temperature dependence of the magnetic susceptibility $\chi(T)$ changes. Nakatsuji and co workers find for $x = 0.2$ $T_O \simeq 290$ K consistent with the transition temperature $T_S = 284$ K of the structural phase transition into the tilt distorted phase. As already discussed by both authors the nonmetallic-metallic transition in ρ_c can be easily explained by the occurrence of the tilt distortion, since the tilting of the RuO_6 octahedra shortens the lattice parameter c , yielding a subsequently enhancement of the interlayer coupling below T_S and thus to the more metallic behavior of ρ_c . Even if it is obvious that the change of magnetic coupling at T_O is also driven by the tilting of the octahedra, the underlying mechanism is still unclear. At the present time the physical properties of $\text{Ca}_{1.8}\text{Sr}_{0.2}\text{RuO}_4$ suggest two scenarios: (i) *Fermi surface nesting* - Mazin and Singh and also Fang and Terakura [45, 111, 126] argue that the reduction of next-nearest-neighbor hopping, induced in $\text{Ca}_{1.8}\text{Sr}_{0.2}\text{RuO}_4$ below T_S by the tilting of the octahedra, enhances the Fermi surface nesting and stabilizes the antiferromagnetic state [111, 126]. The experimental test of this scenario via neutron scattering techniques has not been possible so far, because of the insufficient size of the available single crystals. (ii) *Partial localization* - Anisimov *et al.* propose, based on their band structure calculations, that the narrowing and the crystal field splitting of the (xz, yz) bands, controlled by the tilting and rotation of the RuO_6 octahedra, cause a partial localization of 3 electrons in these bands, while the remaining electron is in the broader and still itinerant xy -band [104]. Within this picture the localized 3 electrons produce a net local moment of $S = 1/2$, in agreement with the susceptibility data which reveals $S = 0.55 \dots 0.66$ [2, 52, 127]. The metallic character of the sample can be attributed to the remaining electron in the itinerant xy -band. Based on this idea, it is tempting to argue that the elongation of the octahedron basal plane, as can be seen in Table 4.1, is related to a Jahn-Teller effect which lifts the degeneracy of the d_{xz} - and d_{yz} -bands. However, the

tilt may explain this elongation already in a purely structural way, as discussed in Section 4.2.1. Therefore, it is still unclear whether the structural phase transition at T_S and the corresponding changeover of magnetic coupling mechanism is driven by a Jahn-Teller effect, as discussed by Nakatsuji *et al.*, or can be simply understood by purely structural arguments.

Independent of the different approaches to explain the magnetic correlation in $\text{Ca}_{1.8}\text{Sr}_{0.2}\text{RuO}_4$, it is obvious that the tilt plays a key role in the magnetoelastic coupling in this concentration regime. Furthermore, it appears most likely that the tilt axis is the cause of the strong magnetic anisotropy, observed by Nakatsuji *et al.* between the a and b directions of the orthorhombic lattice. One should note that although our single-crystal study suggests a strong tendency of twinning, the combination of domains twinned by reflection and by 90° rotation with quite distinct volume fractions should lower the anisotropy to a lesser extent than generally expected.

4.4.2 Neutron powder diffraction study on structural properties of $\text{Ca}_{1.8}\text{Sr}_{0.2}\text{RuO}_4$

In addition to the detailed structural analysis of $\text{Ca}_{1.8}\text{Sr}_{0.2}\text{RuO}_4$ by single crystal neutron diffraction we have investigated the temperature dependence of the crystal structure of a powder sample with nominally the same stoichiometry, in the temperature range from 1.5 to 900 K on G4.1 and by recording high resolution patterns at 10, 300, and 520 K on 3T.2. Unlike single crystal, which shows a single $I4_1/acd$ phase at room temperature, the powder sample is found to consist of two coexisting phases at all temperatures. The high resolution powder patterns at $T = 300$ and 10 K indicate a mixture of the $L\text{-}Pbca$ phase with a minor and temperature independent contribution of about 16 vol% of a $I4_1/acd$ phase. One should note that the $I4_1/acd$ and $L\text{-}Pbca$ phases may be easily distinguished by neutron powder diffraction, since the superstructure reflections related to the rotation occur at different l values due to the distinct stacking, see for example the positions of the $(2\ 1\ l)$ reflections in Fig. 4.21. Furthermore, we can unambiguously exclude a unique structure based on the low temperature $D\text{-}Pbca$ phase found for the single-crystal, because by applying this model we were not able to fit properly the diffraction pattern. However, in agreement with our single crystal study no indication for long range magnetic ordering has been observed in the high flux patterns down to lowest temperatures.

In Table 4.3 we give the obtained structural parameters of the majority phase, using the two-phase mixture fit. Similar to the temperature dependence of the crystal structure of $\text{Ca}_{1.85}\text{Sr}_{0.15}\text{RuO}_4$ one observes the most pronounced changes as function of temperature for the tilt angles: $\Theta\text{-O}(1)$ [$\Theta\text{-O}(2)$] decreases from 6.6° [5.6°] at 10 K to 3.9° [2.9°] at 300 K. Assuming, based on the phenomenological Landau theory [116], that the square of the tilt angle varies linearly with temperature, one expects

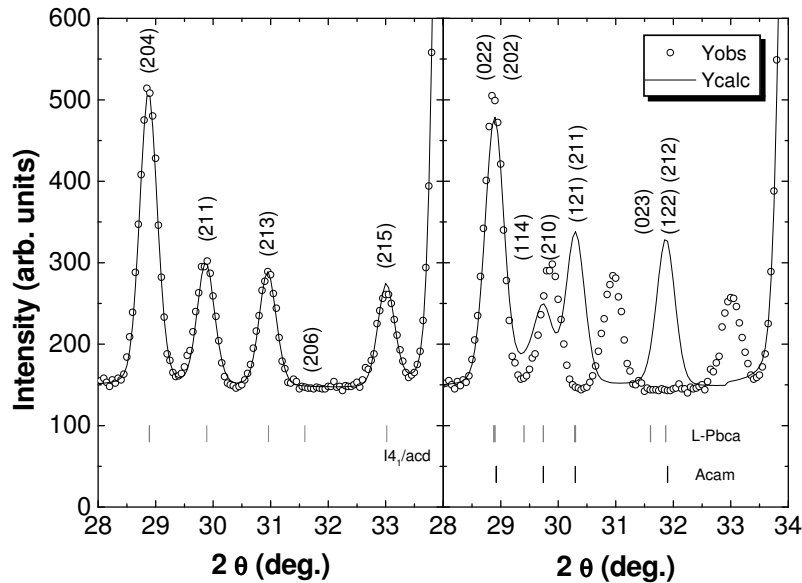


Figure 4.21: Comparison of the powder diffraction patterns calculated for the rotational distortion in space group $I4_1/acd$ ($c \sim 24 \text{ \AA}$; *left*) and in space group $Pbca$ ($c \sim 12 \text{ \AA}$; *right*). Also shown are the positions of the nuclear reflections in the $Acam$ lattice, indicated by the black vertical bars. The calculated patterns are compared to high resolution data observed for $\text{Ca}_{1.5}\text{Sr}_{0.5}\text{RuO}_4$.

the disappearance of the tilt-distortion above $T_S = 431 \text{ K}$. In good agreement with this rather roughly estimated value, an initial refinement for the high resolution pattern recorded at 520 K using the two phases ($L\text{-}Pbca$ and $I4_1/acd$) indicates that the static displacements $z(\text{O}(1))$ and $x, y(\text{O}(2))$, characteristic for the tilt of the RuO_6 octahedra, converge toward zero. For $z(\text{O}(1))=0$ and $x, y(\text{O}(2))=0$ the $Pbca$ space group becomes equivalent to the $Acam$ space group (note that the standard convention space group is $Cmca$). Consistently with the initial refinement the 520 K data can be described reasonably well in space group $Acam$, without no significant difference of the R values compared to the use of the $L\text{-}Pbca$ model. Therefore it appears most likely that the majority phase shows a phase transformation from orthorhombic $L\text{-}Pbca$ to orthorhombic $Acam$, corresponding to a disappearance of the tilt of the still rotational distorted RuO_6 octahedra. The final refinements within this symmetry and the coexisting $I4_1/acd$ phase were done by constraining the in-plane lattice constants to $a = b$, because no indication of orthorhombic splitting could be resolved. The refined parameters are included in Table 4.3. Comparing them to the values obtained at lower temperatures one observes no drastic changes, suggesting a continuous transition (second-order), as it could be expected due to the group-subgroup relationship of the two symmetries ($Acam \supset Pbca$).

Further evidence for the successive transition of the majority phase from $L\text{-}Pbca$

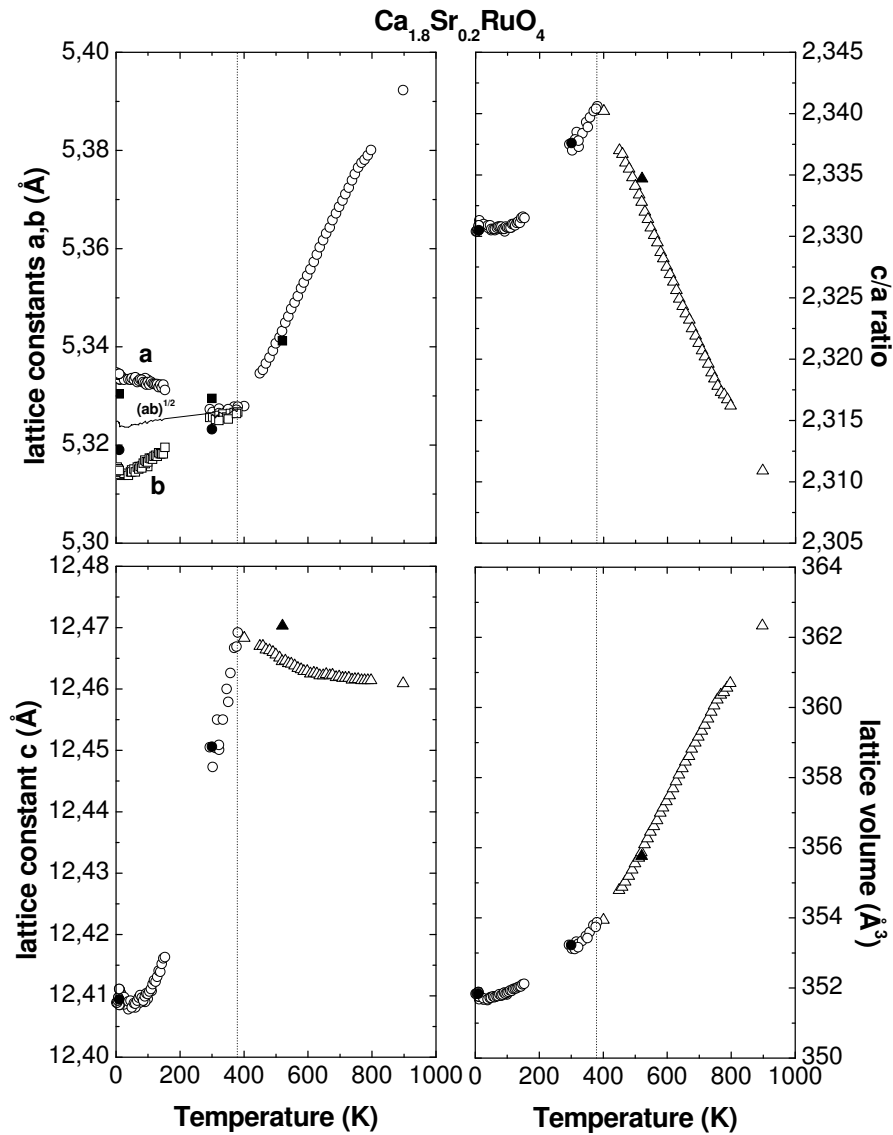


Figure 4.22: Lattice parameters a, b , and c , the c/a ratio, and the lattice volume of $\text{Ca}_{1.8}\text{Sr}_{0.2}\text{RuO}_4$ as a function of temperature. Open symbols designate the results obtained from the high-flux patterns and closed symbols those from the high resolution studies.

to $Acam$ upon heating can be deduced from the temperature dependence of the lattice constants, which are shown in Fig. 4.22. Since the data obtained on G4.1 are insufficient for a full structure determination in the two phase assemblage, the corresponding structural and thermal parameters were constrained to the values extrapolated from the high-resolution data and only the cell parameters of the majority phase and the scale factors of both phases were fitted. While below room

temperature the temperature dependence of the lattice parameters changes continuously without any anomaly, clear kinks without discontinuity at about 380 K in all cell constants are visible. These kinks can be attributed to drastic changes of the thermal expansion of the lattice parameters in conjunction with the transition from $L-Pbca$ to $Acam$ phase. The thermal expansion of the (a, b) -plane in the high-temperature phase is considerably larger than in the low temperature phase, while the occurrence of the tilt distortion below 380 K leads for the c parameter even to a change from an overall negative to a positive thermal expansion. Almost similar characteristics have been observed for the equivalent $HTT \rightarrow LTO$ transition in the apparent compounds $(La, Sr)_2CuO_4$ and $(La, Sr)_2NiO_4$ [88, 133–135] and were explained in the framework of Landau's phenomenological theory of phase transitions [49, 112]. Based on this theory the structural changes at the phase transition can be ascribed to the coupling between the spontaneous strain and the structural order parameter. In the case of the $HTT \rightarrow LTO$ transition the magnitude of the order parameter can be parameterized by the tilt angle Θ . For the spontaneous strain in the low-symmetry phase Landau theory predicts a proportionality to the square of the tilt angle [116]. It is apparent that the observed kinks in the temperature dependence of the lattice constants in $Ca_{1.8}Sr_{0.2}RuO_4$ can be attributed in an identical manner to the coupling between the tilt and the strain field. However, a detailed and complete analysis of the present structural phase transition in the frame of the phenomenological Landau theory has to be extended in comparison to the $HTT \rightarrow LTO$ transition to include more complicated details of symmetry and to account for different vector components of the order parameter and will not be given here.

Finally, a few comments have to be made about the differences in the crystal structure of the single crystal and the powder sample. Though, both samples show that the structure needs a tilt distortion in this concentration regime, the coupling of the tilting- and rotation schemes of the appropriate phases along the c axis are different. While for the single crystal the tilt distortion in the low temperature phase exhibits a different period along the c axis than the rotational distortion, the stacking sequence of the tilt and the rotation observed in the powder sample is identical. These structural differences should be interpreted by the fact that the first order phase boundary between $Acam/L-Pbca$ (corresponding to a $1c$ rotation scheme) and $I4_1/acd/D-Pbca$ ($2c$ rotation scheme) is close to $x=0.2$ and that just minor deviations of the nominal stoichiometry or subtle influence in the real structure are sufficient to tune the structural balance between the different tilt- and rotation schemes. Our initial speculation [46] that the stronger tilt near $x=0.2$ forces the rotational distortion whose stacking sequence is much less defined [6], into the same one c period has to be excluded, since up to 900 K the relative fraction of the minority $I4_1/acd$ phase remains almost constant within the experimental error, although the tilt already disappears near 380 K. A further study of the structural characteristics in the vicinity of the first order phase boundary at $x \simeq 0.2$ has not been possible since the synthesis of samples with a sufficient size for neutron diffraction has so

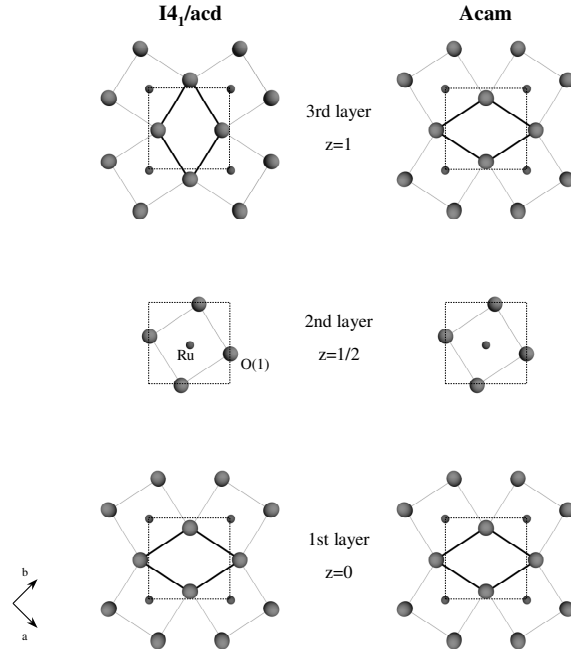


Figure 4.23: Comparison of the rotation scheme on each layer containing RuO₂ plane for the symmetry of $I4_1/acd$ ($2c$ rotation) and $Amca$ ($1c$ rotation). The dashed line indicate the unit cell of the $I4_1/mmm$ phase and the z coordinate of each layer is indicated in respect to this unit cell. Also shown are the directions of the principal axes in the larger $\sqrt{2}a \times \sqrt{2}a$ cell.

far proven unsuccessful. In view of the physical properties one might argue at first sight that the discussed structural differences does not lead to any profound influences, since the structural arrangement within a single RuO₂ is identical for the $Amca/L-Pbca$ and the $I4_1/acd/D-Pbca$ phases. But one may speculate that for the rotational distorted structures the quite distinct configurations of the RuO₂ layers in respect to each other provide an indication of orbital ordering. This becomes clear when considering the deformations of adjacent layers along c for a particular RuO₂ plane as indicated in Fig. 4.23. While in $Amca$ the atomic arrangement of these layers are identical, and in particular the deformation of the corresponding oxygen plaquettes (thick lines in Fig. 4.23) above and below a Ru ion, in $I4_1/acd$ symmetry these layers form different distortion configurations for the interjacent Ru ions. In view of an orbital ordered configuration of the t_{2g} electrons this means that $Amca$ symmetry would be in general consistent with an antiferroorbital ordering of the d_{xz} and d_{yz} orbitals, whereas for $I4_1/acd$ this can be excluded from the outset. Furthermore, the possibility of orthorhombic splitting in $Amca$ may account for the required deformation of the octahedron resulting from an antiferroorbital ordering. However, in order to clarify this scenario in more details further structural studies

of the *Acam* phase are needed.

4.4.3 The second order structural phase transition as function of Strontium content x

As we have already mentioned above, Nakatsuji *et al.* have reported that the characteristic temperature T_O of the anomalies of the electronic and magnetic properties, corresponding with the structural phase transition decreases continuously with increasing Sr content x and finally goes down to zero at $x \simeq 0.5$. It is also at this concentration, that the peak temperature T_P of the maximum in the magnetic susceptibility approaches $T=0$ K and that the low temperature susceptibility $\chi(0)$ becomes strongly enhanced. In order to confirm the strong coupling of the magnetism and the tilt distortion several single crystals ($x=0.50, 0.52, 0.62$, and 1.00) have been studied on the 3T.1 thermal neutron diffractometer as function of temperature.

The temperature dependence of the characteristic superstructure reflections corresponding to a deformation of the tilt type shown in Fig. 4.24 (a), indicates a second order phase transition similar to the one observed for $x=0.2$ (see Fig. 4.15). In agreement with the second order character of the phase transition the measurements upon cooling and upon heating did not reveal any hysteresis for all studied single crystals. The higher Sr content causes a reduced transition temperature and a weaker tilt at low temperature, as can be deduced from the smaller relative superstructure intensities for the crystals shown in Fig. 4.24 (a) in comparison to the one for $x=0.2$. In the case of $x=0.62$ the transition is sluggish, rendering the determination of a transition temperature impossible. Figure 4.24 (b) shows the temperature dependence of the correlation length of scans through the superstructure intensity for this sample, performed on the triple axis spectrometer 4F.1. Even at lowest temperature the reflections are still strongly broadened, with corresponding correlation lengths of about $\zeta_{ab} \simeq 27 \text{ \AA}$ and $\zeta_c \simeq 21 \text{ \AA}$. Furthermore, the correlation lengths decrease rapidly as the temperature is increased. Obviously, the continuous tilt transition in $\text{Ca}_{1.38}\text{Sr}_{0.62}\text{RuO}_4$ is of strong disorder character. This means that the low temperature structure should be thought of as a composition of local domains in which the RuO_6 octahedra tilts are ordered, but the domains themselves are disordered in respect to another. As can be inferred from the extremely small correlation lengths, the size of the domains over which the tilts of the octahedra are ordered is not bigger than a few lattice constants. This clearly indicates, that the continuous phase transition from the $I4_1/acd$ to the $D-Pbca$ in $\text{Ca}_{2-x}\text{Sr}_x\text{RuO}_4$ phase evolves from a purely displacive phase transition for $x=0.2$ to a transition with pronounced order-disorder character with increasing Sr substitution level.

For $x_c=0.5$, Nakatsuji *et al.* report a drastic enhancement of the low-temperature susceptibility, suggesting that the system is on the verge of ferromagnetic ordering. In order to search for the development of long range magnetic order, we have performed

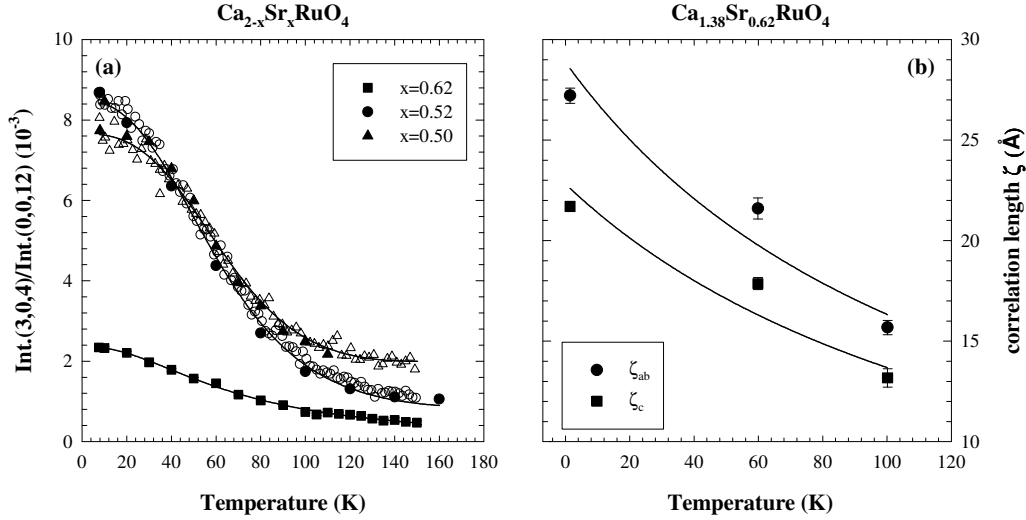


Figure 4.24: (a) Comparison of the temperature dependence of the intensity of the (3 0 4) superstructure reflection normalized to that of the (0 0 12) fundamental reflection, for three single crystals, with $x=0.50$, 0.52 and 0.62 . The open symbols for $x=0.50$ and 0.52 denote data, which have been collected upon heating continuously with a rate of 0.5 K/min , while all other data have been recorded at stabilized temperatures. (b) Temperature dependence of the correlation length ζ of the (304) superstructure reflections in $\text{Ca}_{1.38}\text{Sr}_{0.62}\text{RuO}_4$. ζ was determined by fitting our data to simple Lorentzians, convoluted with the experimental resolution function. The scans were performed along the [100] and the [001] orthorhombic directions on the triple axis spectrometer 4F1. The lines are guides to the eye.

additional elastic neutron scattering experiments on the $x=0.5$ single crystal, using the 1T.1 triple-axis spectrometer. Equivalent to our attempts to observe magnetic order in $\text{Ca}_{1.8}\text{Sr}_{0.2}\text{RuO}_4$ (see above), we looked for the development of new Bragg peaks and for intensity changes of several nuclear peaks by varying temperature. Despite our careful investigation we did not observe any indication for long range magnetic ordering down to $T=1.5\text{ K}$.

Summing up, the presented results show that near the critical concentration $x_c \simeq 0.5$, at which T_P goes down to zero the tilt distortion vanishes. Hence one may expect near $x_c \simeq 0.5$ the instability point of the continuous tilt transition at absolute zero, or in other words, the quantum critical point of the second order structural phase transition. Note, however, that there is a gradual crossover to short range order. Since the system reaches at x_c an incipient ferromagnetic instability, as indicated by the strongly enhanced $\chi(0)$, it becomes evident that the emergence of the tilt distortion at x_c suppresses these ferromagnetic ordering tendencies and drives the system to the unusual magnetic state between $x=0.2$ and $x=0.5$. This shows that the structural phase transition in the intermediate metallic region $0.2 \leq x \leq 0.5$.

induces a change of magnetic coupling as function of temperature as well as function of concentration, demonstrating again the crucial role of the tilt distortion in the magnetoelastic coupling. However, in this concentration regime many interesting questions are still to be answered, e.g., the magnetic origin of the peak in $\chi(T)$ and the correlation of the tilt distortion and the magnetic and electronic properties as a function of hydrostatic pressure and magnetic field, namely in light of the metamagnetic transition reported by Nakatsuji *et al.* [84].

4.5 The ferromagnetic instability and the rotational distortion

The following sections will deal with the structural properties of $\text{Ca}_{2-x}\text{Sr}_x\text{RuO}_4$ as determined by neutron powder diffraction, for the composition range $0.5 \leq x \leq 2.0$. First, the temperature dependence of the crystal structure of $\text{Ca}_{1.5}\text{Sr}_{0.5}\text{RuO}_4$ is presented. Second, the influence of the Sr substitution on the rotational distortion is presented, based on the results of the diffraction experiments for samples with $x=1.0, 1.5$, and 1.8 . Finally we will discuss the possible correlation between the RuO_6 rotation and the tendency to ferromagnetic ordering near $x_c = 0.5$.

4.5.1 The crystal structure of $\text{Ca}_{1.5}\text{Sr}_{0.5}\text{RuO}_4$

Neutron diffraction experiments were carried out on $\text{Ca}_{1.5}\text{Sr}_{0.5}\text{RuO}_4$, using the powder diffractometers 3T.2 ($T=10$ and 300 K) and G4.1 ($1.5 \leq T \leq 270$ K). The obtained high resolution data can be reasonably well described in an unique $I4_1/acd$ phase. The corresponding refined structural parameters are reported in Table 4.3, and show only little temperature dependence. In contrast to the superstructure reflections observed on the single crystal with nominal the same stoichiometry, which are forbidden in $I4_1/acd$ symmetry, our raw neutron powder diffraction data did not reveal any indication for additional Bragg peaks down to lowest temperatures. As may be seen in Fig. 4.24 the superstructure intensities are very weak and thus not strong enough to be detected by powder neutron diffraction. Nevertheless, the determined structural parameters analyzed in space group $I4_1/acd$ give some indications which suggest that the structural phase transition occurs also in the polycrystalline sample. First, one obtains at 10 K very large values for the thermal parameter of the O(1) and O(2) sites in the direction of the displacement by the tilt $U_{\text{long-axis}}=U_{33}(\text{O}(1))=0.0152(6) \text{ \AA}^2$ and $U_{\perp}=U_{11}=U_{22}(\text{O}(2))=0.0084(3) \text{ \AA}^2$ corresponding to a root mean square tilt of 0.7° . In order to take account of local disorder and phononic contributions we have subtracted the appropriate thermal parameters of Sr_2RuO_4 given in Ref. [13], so that the estimated angle represents mainly the *static* tilt deformation. However, one should note that also the Ca/Sr mixing in $\text{Ca}_{2-x}\text{Sr}_x\text{RuO}_4$ may lead to local tilt distortions, which would contribute to the

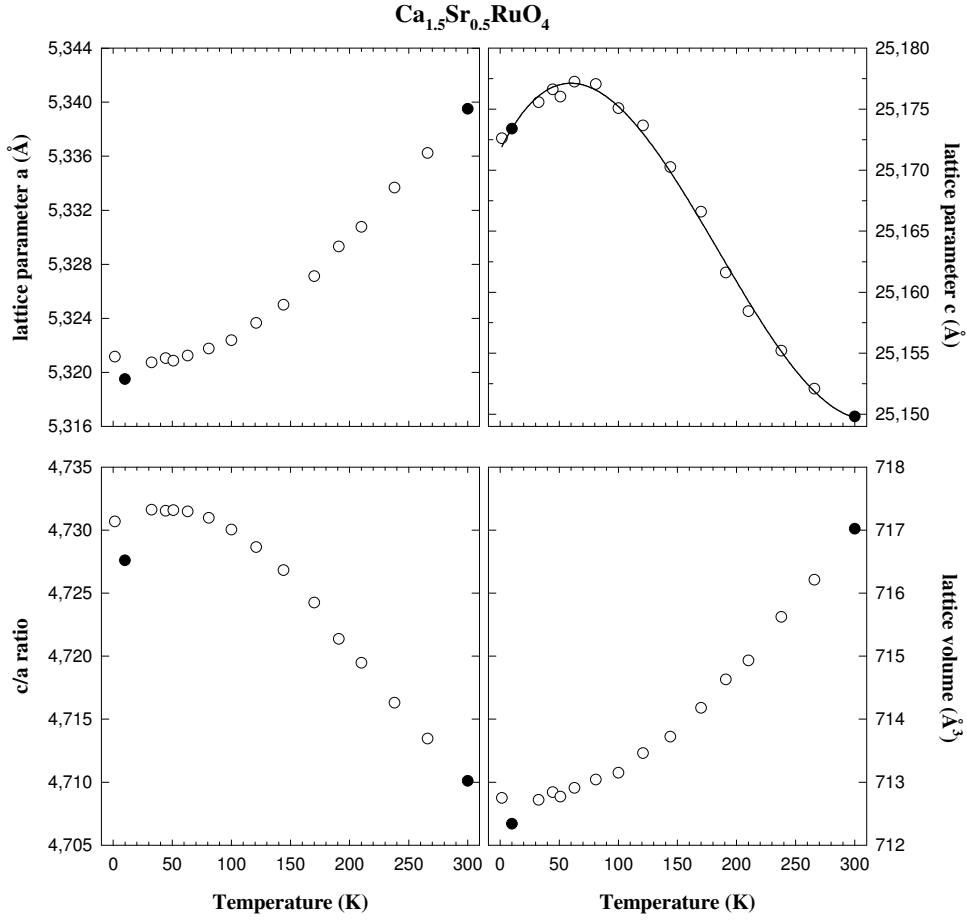


Figure 4.25: Temperature dependence of lattice parameters of $\text{Ca}_{1.5}\text{Sr}_{0.5}\text{RuO}_4$. The open symbols denote the results obtained on G4.1 and the filled ones correspond to data from 3T.2.

enhancement of the thermal parameters, as for example observed in the related systems $\text{La}_{2-x}\text{Sr}_x\text{CuO}_4$ and $\text{Ba}_{1-x}\text{K}_x\text{BiO}_3$ [136, 137]. Although, one may ascribe these enhanced parameters to the neglect of the tilt distortion in our tetragonal treatment, a reliable analysis by powder diffraction of the low temperature phase is not possible since the corresponding tilt distortion is too small.

Another indication for a continuous transition from the $I4_1/acd$ structure to a tilt distorted phase occurs also in the powder sample, can be derived from the temperature dependence of the lattice parameters which are shown in Fig. 4.25. While the a parameter and the volume of the unit cell decrease upon cooling, showing the usual thermal expansion, the c parameter and the c/a ratio increase at first, before decreasing below $T \simeq 65$ K. As already discussed for $\text{Ca}_{1.8}\text{Sr}_{0.2}\text{RuO}_4$ in section 4.4.2 this anomaly in the temperature dependence of the c lattice parameter can be at-

tributed to the occurrence of the tilt distortion. This can be understood not only in the frame of the phenomenological Landau theory, but also qualitatively, since the projection of the octahedra along c varies with the cosine of the tilt angle. Consistently with this anomaly in the powder sample, the thermal expansion coefficient of the single crystal with nominally the same stoichiometry measured along the $[001]$ direction in a capacitive dilatometer, changes sign from negative to positive values at $T=68$ K with decreasing temperature (not shown). Therefore one may conclude that, in perfect agreement with the performed single crystal study, also the studied powder sample with $x=0.5$ exhibits a continuous phase transition from $I4_1/acd$ into a low temperature phase, which is characterized by an additional tilt distortion. The weakness of the observed superstructure reflections in the single crystal study and the fact that $x=0.5$ is close to the instability point of the structural phase transition renders a more detailed study of the low temperature phase by neutron powder diffraction in this concentration regime almost impossible.

Let us now move back to the main purpose of this section, the characteristics of the rotational distortion. Beside the observed decrease of the lattice parameter c below $T \simeq 65$ K the most striking feature of the structural properties of $\text{Ca}_{1.5}\text{Sr}_{0.5}\text{RuO}_4$ is the negative thermal expansion of the c axis between 100 and 300 K. It is rather peculiar for a layered oxide with K_2NiF_4 structure that the c parameter expands upon cooling and it seems to be a characteristic property of the rotational distorted modification of this structure type (cf. Fig. 4.22) [89, 91, 93]. At first sight this anomalous feature might be attributed to the increase of the octahedron rotation angle Φ upon cooling (between 300 and 10 K, Φ increases from $12.43(4)^\circ$ to $12.78(4)^\circ$, analyzed in space group $I4_1/acd$), since of the free positional parameters in the $I4_1/acd$ structure only the x position of the oxygen in the RuO_2 planes changes significantly. However, the small temperature dependence of the rotation angle Φ excludes this as an explanation of the total effect occurring in c . Already pure Sr_2RuO_4 shows, in comparison with apparent layered K_2NiF_4 type structures like $(\text{La}, \text{Sr})_2\text{CuO}_4$ and $(\text{La}, \text{Sr})_2\text{NiO}_4$, an unusual small thermal expansion of the c axis, i.e., on cooling from 295 to 10 K the decrease of the a axis is twice as large as that of the c axis [11]. Since Sr_2RuO_4 remains undistorted down to lowest temperatures and is, furthermore, very close to the rotational instability, the observed negative thermal expansion of the c axis in the only rotationally distorted phase of $\text{Ca}_{1.5}\text{Sr}_{0.5}\text{RuO}_4$ and $\text{Ca}_{1.8}\text{Sr}_{0.2}\text{RuO}_4$ and the small contraction in pure Sr_2RuO_4 may instead have a dynamical origin rather than a static one. Therefore we conclude that some phonon mode Grüneisen parameters are negative, most likely those of the rotational modes.

4.5.2 The evolution of the rotational distortion

The compound with $x=1.0$ was studied at room temperature and at 11 K by high resolution diffraction. The initial model of its structure was assumed to be similar to that of $\text{Ca}_{1.5}\text{Sr}_{0.5}\text{RuO}_4$ and first refinements were carried out adopting the symmetry

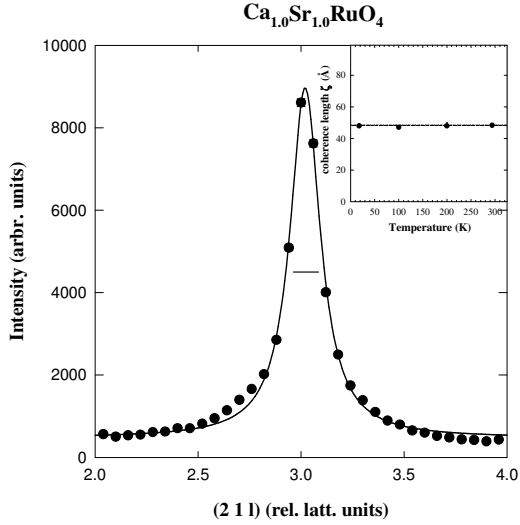


Figure 4.26: Profile of the $(2\ 1\ 3)$ ($I4_1/acd$ notation) superlattice reflection measured along the $[001]$ direction at $T=18\text{ K}$ for $\text{Ca}_{1.0}\text{Sr}_{1.0}\text{RuO}_4$. The measurements were performed on the triple axis spectrometer 4F.2. The solid line represents a fit by a Lorentzian scattering function convoluted with the experimental resolution (indicated by the horizontal bar). The inset shows the temperature dependence of the corresponding correlation length ξ .

of space group $I4_1/acd$. These refinements gave acceptable R values, but we obtained only poor agreement of the observed and calculated intensities for the superstructure reflections, which characterize the rotational distortion. This observation indicates that some structural disorder is present in the rotation scheme. In order to explore this possibility in more detail we have carried out a neutron diffraction study of a nominally equivalent single crystal with $x=1.0$ on the triple axis spectrometer 4F.2. While scans performed along the $[100]$ direction through the corresponding superstructure reflections reveal no significant peak broadening within the experimental resolution, we observed strong diffuse scattering in scans along the $[001]$ direction. Representative data are shown in Fig. 4.26. The reason for the diffuse scattering can be found in the disordering of the rotation scheme of the RuO_6 octahedra parallel to the c axis. This means that independent of the $I4_1/acd$ symmetry successive RuO_2 layers are uncorrelated, allowing the RuO_6 octahedra in different layers to be rotated with an arbitrary phase. From the intrinsic peak width of the performed scans, we infer an out of plane correlation length for the rotational distortion of $\xi_c \simeq 48\text{ \AA}$ which shows almost no temperature dependence on cooling down to 1.5 K .

Concerning the powder diffraction data the disordering of the atomic arrangement of the RuO_2 layers has been included in the refinement by splitting the $\text{O}(1)$ positions into two sets of positions $(x, |x| + \frac{1}{4}, \frac{1}{8})$ with $x = \pm\delta$ and a constrained occupancy of $n(\text{O}(1)_{+\delta}) + n(\text{O}(1)_{-\delta}) = 1$, similar to the observation in Ref. [91, 138] for Sr_2IrO_4 and $\text{Sr}_3\text{Ru}_2\text{O}_7$. By applying this model the refinement was significantly improved and we were able to fit properly the diffraction pattern in the tetragonal space group. The final structural parameters are given in Table 4.3 for the two temperatures at which data were taken. There is only little temperature dependence in the structure of $\text{Ca}_{1.0}\text{Sr}_{1.0}\text{RuO}_4$ similar to the behavior observed for $x=0.5$. From the three positional parameters $z\text{-Ca}$, $z\text{-O}(2)$, and $x\text{-O}(1)$ in $I4_1/acd$ symmetry only the latter changes

significantly, related to the increase of the average octahedron rotation angle by about 4% between 300 and 10 K, from $10.71(3)^\circ$ to $11.13(3)^\circ$. The refined value of the occupancy at the splitted O(1) site found for both temperature amounts to $n(\text{O}(1)_{\pm\delta}) = 0.88$ and may serve as degree of disorder of the rotational stacking scheme.

Combining the above results with those obtained for $\text{Ca}_{1.5}\text{Sr}_{0.5}\text{RuO}_4$ one estimates the critical concentration for the appearance of the pure rotation distortion near $x=2.5$, by assuming, according to Landau theory [116], that the square of the rotational angle varies linearly with the concentration. From this consideration one would expect pure Sr_2RuO_4 to exhibit the same rotational distortion in obvious contradiction with the observation that it remains undistorted till low temperature [12]. Also the single crystal diffraction studies on pure Sr_2RuO_4 [13], which are more sensitive to diffuse scattering than powder diffraction, did not reveal any indication for a local rotational distortion. Moreover, for a Sr concentration of $x=1.5$ we already do not find any long range order in the powder sample. However, there is sizeable diffuse scattering - strong enough to be detected by powder diffraction, as may be seen in the pattern plotted in Fig. 4.27 - indicating that the rotation distortion still exists on a short range scale. Another point that supports the existence of structural deformations is the fact that the c axis in $\text{Ca}_{0.5}\text{Sr}_{1.5}\text{RuO}_4$ exhibits still a negative thermal expansion (not shown), which may be considered, although not obvious, as a general feature of structures in which the RuO_6 octahedra are rotated about the c axis. Finally for $x=1.8$ the high resolution powder pattern at 10 K indicates an unique $I4/mmm$ phase, with no additional peaks or diffuse contributions which would suggest $I4_1/acd$. But as one expects due to the enhanced temperature factors in pure Sr_2RuO_4 [13], we find also in this Ca substituted sample a rather large value of the $U_\perp(\text{O}(1))$ parameter which is directly related to the rotation transition (see Table 4.3). Summing up, we conclude that the transformation from $I4/mmm$ to $I4_1/acd$ symmetry in $\text{Ca}_{2-x}\text{Sr}_x\text{RuO}_4$ upon substitution of Sr which is allowed via a second-order structural phase transition exhibits pronounced order-disorder character.

In view of the magnetic properties of $\text{Ca}_{2-x}\text{Sr}_x\text{RuO}_4$ for Sr concentrations $x \geq 0.5$, the interesting question arises what effect does the RuO_6 octahedron rotation have on the enhancement of the ferromagnetic instability toward $x_c=0.5$. It is quite obvious that the increasing rotation occurring in the metallic phase with decreasing Sr content and the simultaneous enhancement of the low-temperature susceptibility which for $x=0.5$ is about 150 times larger than that of pure Sr_2RuO_4 (see Fig. 4.1) are strongly correlated. We cite two band-structure calculations which reinforce this consideration. Fang and Terakura observe by ab-initio calculations based on the local density approximation that the rotation of the octahedra narrows and lowers the γ band [111]. Both effects enhance the influence of the Van Hove singularity and push the system closer to the ferromagnetic instability. On the other hand Anisimov *et al.* use an additional Hubbard-U which causes together with the rotation

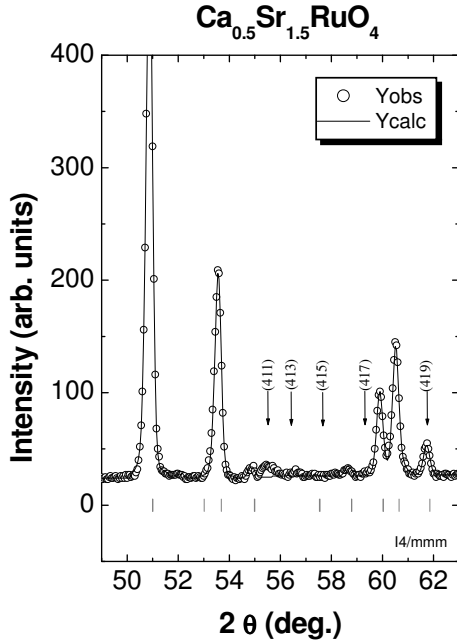


Figure 4.27: Part of the powder neutron diffraction pattern and Rietveld refinement in space group $I4/mmm$ for $\text{Ca}_{0.5}\text{Sr}_{1.5}\text{RuO}_4$ at room temperature. The arrows indicate superlattice reflections due to the RuO_6 rotational distortion.

of the octahedra a partial localization in the d_{xz}, d_{yz} bands [104]. The same effect may probably account for the anomalous magnetic behavior observed for $0.2 \leq x < 0.5$ as we have already mentioned in section 4.4.1. According to the authors the orthorhombic distortion for $x < 0.5$ explains via some additional orbital degrees of freedom the quite different magnetic properties in these regions. Though the observation of a Curie-Weiss behavior corresponding to a spin $S = \frac{1}{2}$ supports the Anisimov scenario, a polarized neutron diffraction study on $\text{Ca}_{1.5}\text{Sr}_{0.5}\text{RuO}_4$ which reveals that the main part of the spin-density arises from the γ band clearly contradict it [121]. Particularly with regard to our inelastic studies for x close to 0.5 (see chapter 6), we conclude that one may well explain the magnetic behavior for metallic $\text{Ca}_{2-x}\text{Sr}_x\text{RuO}_4$ with $x \geq 0.5$ without localization just by the enhanced magnetic contribution of the d_{xy} -band, as it is proposed in Ref. [111].

4.6 Conclusion

According to the studies presented in this chapter the structural and magnetic phase diagram of $\text{Ca}_{2-x}\text{Sr}_x\text{RuO}_4$ is rather complicated, a schematic picture is given in Fig. 4.28, which also presents the results of the magnetic studies by S. Nakatsuji *et al.* [2, 3]. In addition, the tilt and rotation angles together with the deformation of the octahedron basal plane are depicted in Fig. 4.29. At low temperature and for decreasing Sr-concentration, one passes from the undistorted K_2NiF_4 structure in pure Sr_2RuO_4 , space group $I4/mmm$, to a simple rotation $I4_1/acd$ in agreement to the low lying rotation mode in the pure compound [47]. This rotational distortion can

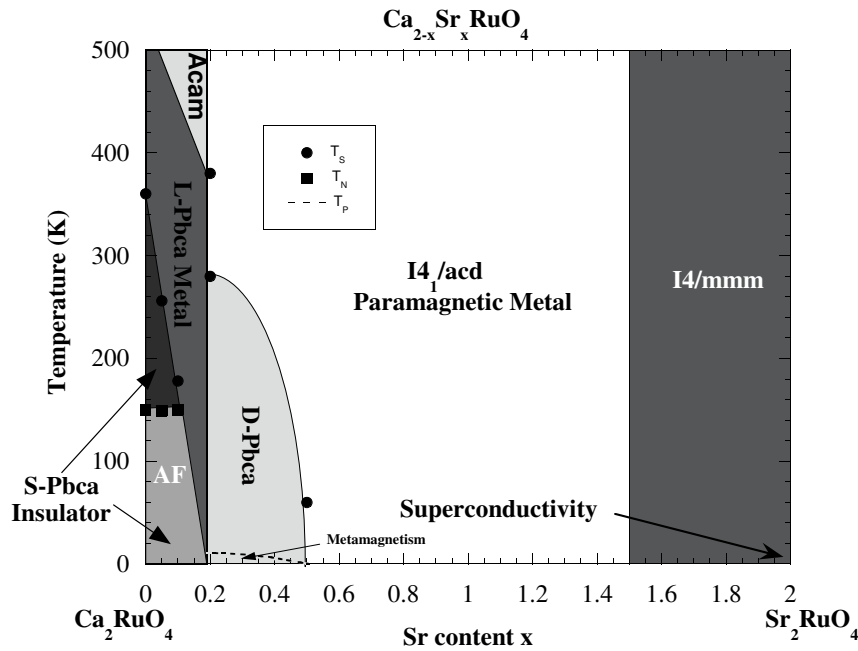


Figure 4.28: Phase diagram of $\text{Ca}_{2-x}\text{Sr}_x\text{RuO}_4$ including the different structural and magnetic phases and the occurrence of the maxima in the susceptibility (Ref. [2, 3]).

be considered as the purely structural consequence of the smaller ionic radius of the Ca. An estimated boundary is included in the diagram in Fig. 4.28, though the transition is found to exhibit order-disorder character. For a Sr-concentration of $x=1.5$ only diffuse scattering representative of a short range rotational distortion is present. For $x=1.0$ the rotational angle already amounts to 11.13° ; the rapid suppression of the structural distortion in Sr-rich samples appears to be extraordinary it might hide some further effect. For much smaller Sr-content, near $x=0.5$, a combination of rotation and small tilt is found. This is realized either in a subgroup of $I4_1/acd$ or in $L-Pbca$. Further decrease of the Sr-content leads finally to the combination of the rotation and the large tilt in the insulating $S-Pbca$ phase. The Sr-dependence of the tilt and rotation angles is resumed in Fig. 4.30. Most interestingly all these structural transitions are closely coupled to the physical properties.

The purely rotational distortion should be related to the continuous increase of the low-temperature susceptibility upon Sr substitution in $\text{Ca}_{2-x}\text{Sr}_x\text{RuO}_4$. This rotation phase becomes unstable against the tilt for Sr concentrations lower than 0.5, since in the single crystal with $x=0.5$ only a minor distortion has been observed, which remained undetectable in the powder sample. In this concentration regime the corresponding phase transition is smeared out due to strong disorder. For the Sr-concentration of $x=0.2$ we already find tilt angles of about 6.6° at low temperature by powder neutron diffraction. Hence, one may identify the concentration $x=0.5$

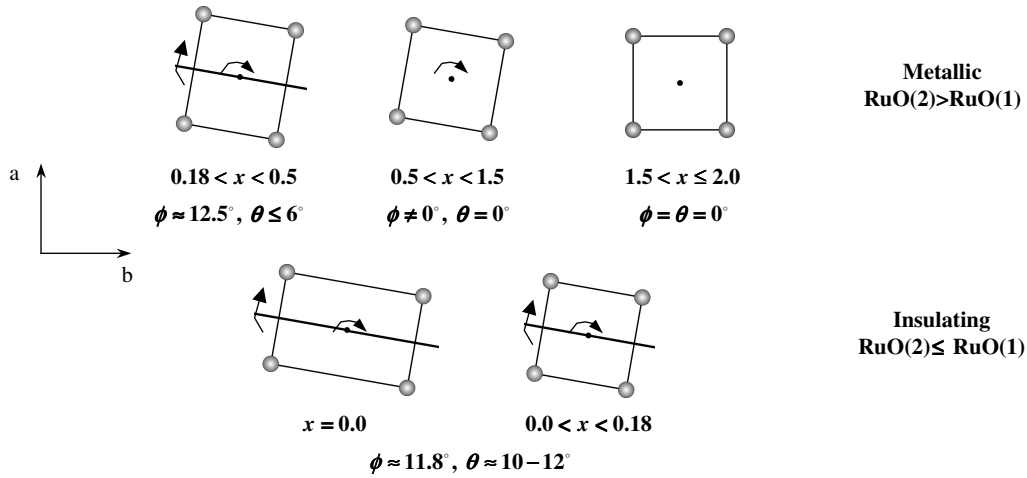


Figure 4.29: Schematic representation of the tilt and rotational distortion of the octahedra, together with the elongation of the basal planes. Only the basal square consisting of the Ru (black points) and the O(1) (grey points) is shown.

with the quantum critical point of the continuous tilt transition which coincides with a maximum in the low temperature magnetic susceptibility. For $x=0.5$, Nakatsuji et al. report a low temperature magnetic susceptibility about 150 times larger than that of pure Sr_2RuO_4 [2]. This suggests that the low-lying tilt modes are strongly coupled to the magnetism. This interpretation is further supported by the fact that in all magnetically ordered structures, $x=0.0 \dots 0.1$ and in $\text{Ca}_2\text{RuO}_{4.07}$, the spin-direction is parallel to the tilt axis in spite of a different octahedron shape as it is schematically drawn in Fig. 4.28. Decrease of the Sr-content below $x=0.5$ stabilizes the tilt and causes a maximum in the temperature dependence of the susceptibility at $T = T_P$, indicated in Fig. 4.28 [2]. T_P , however, does not coincide with the structural transition from $I4_1/acd$ to the tilted phase but is much lower. We speculate that the susceptibility maximum arises from an increase of antiferromagnetic fluctuations induced through the tilt.

There is another anomalous feature in the temperature dependent susceptibility of samples with $0.2 \leq x < 0.5$: Nakatsuji et al. find a strong magnetic anisotropy between the a and b -directions of the orthorhombic lattice [2, 3]. In relation to the magnetic order in the insulating compounds it appears again most likely that the tilt axis, which is parallel b , is the cause of the huge anisotropy. However, there might be an additional more complex effect related to orbital ordering of spin-orbit coupling, as discussed in [3, 104].

For Sr concentrations lower than 0.2 we find the $L\text{-}Pbca$ symmetry and the first order phase transition leading to the insulating $S\text{-}Pbca$ phase. The metal-insulator transition is hence observed as a function of concentration as well as a function of temperature. The experimental results concerning the structural behavior of samples

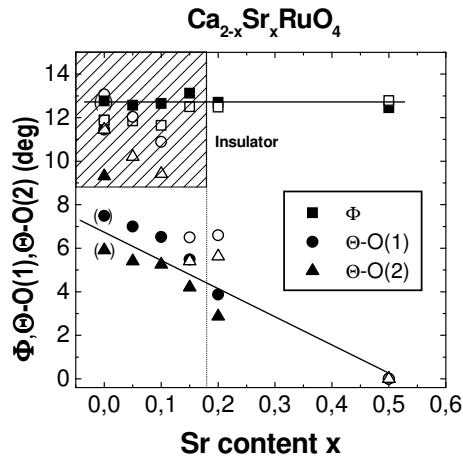


Figure 4.30: The Sr concentration dependence of the tilt $\Theta\text{-O}(1)$ and $\Theta\text{-O}(2)$ and rotation angle Φ in $\text{Ca}_{2-x}\text{Sr}_x\text{RuO}_4$. The filled symbols denote the results obtained at $T=300\text{ K}$ (those with brackets are obtained at $T=400\text{ K}$) and the open symbols are those at $T=10\text{ K}$, the dashed line indicates the critical concentration below which one observes the insulating $S\text{-Pbca}$ phase at low temperature. The lines are intended as guides to the eye.

in this regime show a second phase transition above room temperature into a purely rotational distorted phase, with space group $Acam$. In a first view this space group differs only by the stacking of the rotation distortion from the adjacent $I4_1/acd$ phase.

In the Sr range $0.2 \leq x \leq 2$ all samples are found to be metallic at low temperature and there is little variation of the octahedron shape and in particular of the in-plane Ru-O bond lengths when compared to that observed in Sr_2RuO_4 [12, 13]. The concentration dependent octahedron shape is shown in Fig. 4.31. Metallic 214-ruthenates appear to be identical at least concerning their Ru-O-bond distances. The minor deviation near $x=0.2$ may be explained by the relaxed constraint in the tilted structure. For smaller Sr-content the metal insulator transition occurs, but one may still compare to the Ru-O(1)-bonds in the metallic high temperature phase. For this purpose we have scaled the high resolution results in the metallic phase of the samples presenting the metal insulator transition, by the thermal expansion of Sr_2RuO_4 [12]. The scaling by the thermal expansion of pure Sr_2RuO_4 is not fully justified, since the temperature dependent tilt and rotation should alter the thermal expansion. This and the insertion of additional oxygen should explain the minor deviations. Also the scaled values for samples which are insulating at low temperature are comparable to pure Sr_2RuO_4 . This demonstrates the equivalence of the metal insulator transition as a function of temperature and as a function of concentration.

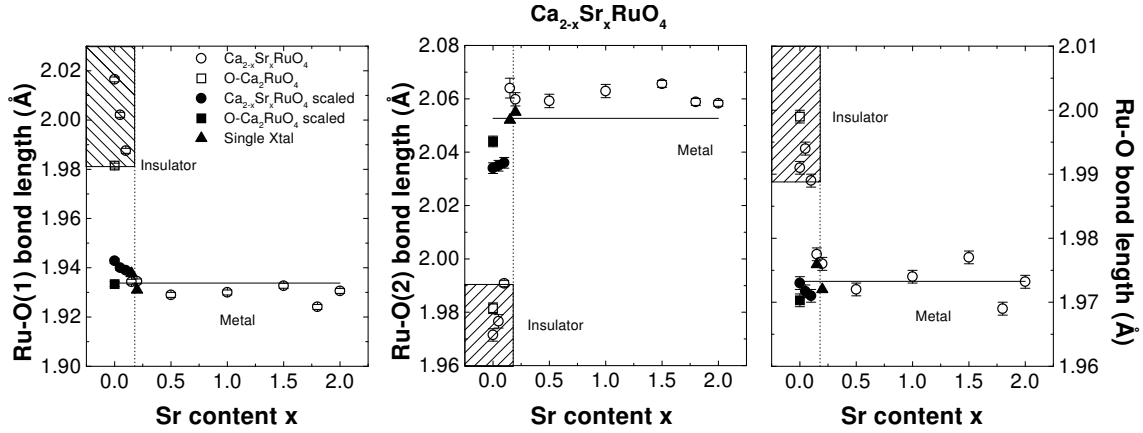


Figure 4.31: Composition dependence of the Ru-O(1)-, Ru-O(2)-, and averaged Ru-O bond distances in $\text{Ca}_{2-x}\text{Sr}_x\text{RuO}_4$ at 10 K, open symbols. Filled symbols were obtained by extrapolating the distances obtained in the high temperature metallic phase to 10 K using the thermal expansion of Sr_2RuO_4 ; the dashed line designates the critical concentration for the metal insulator transition. The other lines are intended as guides to the eye.

Concerning the metal insulator transition it appears necessary to separate two effects. In all samples exhibiting an insulating low temperature phase there is an increase of the in-plane bond lengths and a reduction of the Ru-O(2)-distance accompanied with the increase of the tilt angle. This effect has to account for the non-metallic behavior. Within a Mott-scenario [102] one may phenomenologically explain the effect, since both tilting and increase of the in-plane distances should strongly reduce the band-width. In particular the band corresponding to the d_{xy} -orbital should become more localized and lower in energy. The second effect is found only in the stoichiometric compound where the transition is not complete immediately below T_S ; instead the octahedron becomes flattened mainly due to the elongation of the basal plane along the b -axis which is the direction of the spins in the antiferromagnetic ordered structure. We do not think that this rather peculiar behavior can be explained by simple structural arguments. It appears likely that spin-orbit coupling in the non-metallic phase causes these low temperature structural anomalies. The reason why similar effects do not occur in $\text{Ca}_2\text{RuO}_{4.07}$ and in $\text{Ca}_{1.9}\text{Sr}_{0.1}\text{RuO}_4$ might be found in their remaining itinerant character. Spin-orbit coupling also forces the spin direction parallel to the tilt-axis, which will strongly reduce the weak ferromagnetism along the c -direction.

4.A Results of the high resolution powder diffraction analyses on $\text{Ca}_{2-x}\text{Sr}_x\text{RuO}_4$

Table 4.2 and 4.3 presents the Rietveld refinement results from the high-resolution neutron powder diffraction studies of $\text{Ca}_{2-x}\text{Sr}_x\text{RuO}_4$ carried out on D2B at the Institut Laue-Langevin in Grenoble, in collaboration with the Cavendish Laboratory of the University of Cambridge, and on 3T.2 at the Laboratoire Léon Brillouin in Saclay. In order to facilitate the comparison of the structural data we repeat also the results of the single crystal structural analyses, already given in table 4.2.

| Pressure | 1 atm | 7 kbar | 10 kbar |
|--|---------------|-------------------------|-------------------------|
| Space group | <i>S-Pbca</i> | <i>L-Pbca</i> | <i>L-Pbca</i> |
| <i>a</i> (Å) | 5.4056(3) | 5.3387(10) | 5.3307(5) |
| <i>b</i> (Å) | 5.4971(2) | 5.3266(11) | 5.3191(5) |
| <i>c</i> (Å) | 11.9392(6) | 12.2805(12) | 12.2923(9) |
| Vol (Å ³) | 354.77(3) | 349.22(11) | 348.54(5) |
| ϵ | 0.0084 | 0.0011 | 0.0011 |
| R_{wp} (%) | 6.99 | 10.80 | 9.79 |
| Ca <i>x</i> | 0.0073(6) | 0.0110(42) | 0.0199(31) |
| <i>y</i> | 0.0465(6) | 0.0213(32) | 0.0259(24) |
| <i>z</i> | 0.3509(2) | 0.3479(7) | 0.3458(5) |
| U_{iso} (Å ²) | 0.0030(8) | 0.0154(27) | 0.0140(25) |
| Ru U_{iso} (Å ²) | 0.0020(8) | 0.0057(23) | 0.0068(21) |
| O(1) <i>x</i> | 0.1976(5) | 0.1832(20) | 0.1817(14) |
| <i>y</i> | 0.3017(5) | 0.2952(19) | 0.2927(13) |
| <i>z</i> | 0.0240(2) | 0.0124(11) | 0.0138(8) |
| $U_{\perp\text{-plane}}$ (Å ²) | 0.0113(14) | | |
| $U_{\parallel\text{-plane}}$ (Å ²) | 0.0034(5) | 0.0158(26) ^a | 0.0105(23) ^a |
| $U_{\text{long-axis}}$ (Å ²) | 0.0059(7) | | |
| O(2) <i>x</i> | -0.0580(4) | -0.0308(23) | -0.0238(18) |
| <i>y</i> | -0.0166(6) | -0.0193(33) | -0.0156(25) |
| <i>z</i> | 0.1641(2) | 0.1659(5) | 0.1694(5) |
| U_{\perp} (Å ²) | 0.0071(6) | 0.0210(37) ^a | 0.0218(32) ^a |
| U_{\parallel} (Å ²) | 0.0057(5) | | |
| Ru-O(1) (Å) | 1.993(3) | 1.858(10) | 1.841(7) |
| | 1.986(3) | 2.018(11) | 2.031(7) |
| Ru-O(2) (Å) | 1.986(3) | 2.047(7) | 2.088(6) |
| Ru-O _{aver} (Å) | 1.988 | 1.974 | 1.987 |
| O(1)-O(1) _a (Å) | 2.821(2) | 2.729(5) | 2.725(3) |
| O(1)-O(1) _b (Å) | 2.806(1) | 2.757(6) | 2.757(4) |
| Vol RuO ₆ (Å ³) | 10.48 | 10.27 | 10.46 |
| Θ -O(1) (deg) | 11.71(11) | 6.4(6) | 7.2(4) |
| Θ -O(2) (deg) | 9.5(6) | 5.4(2.9) | 4.2(3.3) |
| Φ (deg) | 11.76(9) | 12.6(4) | 12.54(6) |

^a Value represents isotropic mean-square atomic displacement U_{iso} .

Table 4.2: Refined structural parameters from neutron powder diffraction for Ca_2RuO_4 at different pressures. Numbers in parentheses are standard deviations from Rietveld refinement. For the notations see Table 4.3.

4.A Results of the high resolution powder diffraction analyses on $\text{Ca}_{2-x}\text{Sr}_x\text{RuO}_4$

| Composition | x=0.0 | | x=0.0 | | x=0.0 | | x=0.05 | | x=0.05 | | x=0.1 | | x=0.1 | |
|--|--|---------------|---------------|---------------|---------------|---------------|---------------|---------------|---------------|---------------|---------------|---------------|---|---------------|
| | 11 K | 180 K | 300 K | 400 K | 300 K | 400 K | 300 K | 10 K | 300 K | 10 K | 10 K | 10 K | 130 K | 130 K |
| Space group | <i>S-Pbca</i> | <i>S-Pbca</i> | <i>S-Pbca</i> | <i>L-Pbca</i> | <i>S-Pbca</i> | <i>L-Pbca</i> | <i>L-Pbca</i> | <i>S-Pbca</i> | <i>L-Pbca</i> | <i>S-Pbca</i> | <i>S-Pbca</i> | <i>S-Pbca</i> | <i>S-Pbca</i> | <i>S-Pbca</i> |
| <i>a</i> (Å) | 5.3877(2) | 5.3945(2) | 5.4097(3) | 5.3606(3) | 5.3994(7) | 5.3522(4) | 5.4207(4) | 5.3994(7) | 5.3522(4) | 5.4207(4) | 5.4108(3) | 5.4108(3) | 5.4108(3) | 5.4108(3) |
| <i>b</i> (Å) | 5.6323(3) | 5.5999(3) | 5.4924(4) | 5.3507(3) | 5.5629(7) | 5.3441(4) | 5.4802(6) | 5.5629(7) | 5.3441(4) | 5.4802(6) | 5.4842(4) | 5.4842(4) | 5.4842(4) | 5.4842(4) |
| <i>c</i> (Å) | 11.7463(5) | 11.7653(3) | 11.9613(6) | 12.2637(4) | 11.8338(9) | 12.2927(5) | 11.9395(6) | 11.8338(9) | 12.2927(5) | 11.9395(6) | 11.9705(6) | 11.9705(6) | 11.9705(6) | 11.9705(6) |
| Vol (Å ³) | 356.44(3) | 355.41(3) | 355.40(4) | 351.76(2) | 355.44(7) | 351.61(4) | 354.68(5) | 355.44(7) | 351.61(4) | 354.68(5) | 355.21(4) | 355.21(4) | 355.21(4) | 355.21(4) |
| ϵ | 0.0222 | 0.0187 | 0.0008 | 0.0009 | 0.0149 | 0.0008 | 0.0054 | 0.0149 | 0.0008 | 0.0054 | 0.0067 | 0.0067 | 0.0067 | 0.0067 |
| R_{exp} (%) | Ref. [6] | 5.81 | Ref. [6] | 5.39 | 6.64 | 6.17 | 5.16 | 6.64 | 6.17 | 5.16 | 4.87 | 4.87 | 4.87 | 4.87 |
| Ca/Sr <i>x</i> | 0.0021(5) | 0.0042(4) | 0.0086(6) | 0.0110(5) | 0.0086(6) | 0.0110(7) | 0.0083(4) | 0.0086(6) | 0.0110(7) | 0.0083(4) | 0.0086(4) | 0.0086(4) | 0.0086(4) | 0.0086(4) |
| <i>y</i> | 0.0593(4) | 0.0559(4) | 0.0474(6) | 0.0269(5) | 0.0504(6) | 0.0256(7) | 0.0425(4) | 0.0504(6) | 0.0256(7) | 0.0425(4) | 0.0418(1) | 0.0418(1) | 0.0418(1) | 0.0418(1) |
| <i>z</i> | 0.3525(2) | 0.3524(2) | 0.3518(2) | 0.3479(1) | 0.3524(2) | 0.3479(2) | 0.3505(2) | 0.3524(2) | 0.3479(2) | 0.3505(2) | 0.3504(2) | 0.3504(2) | 0.3504(2) | 0.3504(2) |
| U_{iso} (Å ²) | 0.0040(6) | 0.0052(5) | 0.0093(9) | 0.0112(4) | 0.0093(9) | 0.0112(4) | 0.0039(5) | 0.0093(9) | 0.0112(4) | 0.0039(5) | 0.0050(5) | 0.0050(5) | 0.0050(5) | 0.0050(5) |
| Ru U_{iso} (Å ²) | 0.0033(6) | 0.0025(4) | 0.0038(6) | 0.0050(4) | 0.0038(6) | 0.0050(4) | 0.0024(6) | 0.0038(6) | 0.0050(4) | 0.0024(6) | 0.0023(4) | 0.0023(4) | 0.0023(4) | 0.0023(4) |
| O(1) <i>x</i> | 0.1952(4) | 0.1961(3) | 0.1961(4) | 0.1939(4) | 0.1961(4) | 0.1939(4) | 0.1974(3) | 0.1961(4) | 0.1939(4) | 0.1974(3) | 0.1974(3) | 0.1974(3) | 0.1974(3) | 0.1974(3) |
| <i>y</i> | 0.3005(4) | 0.3018(4) | 0.3013(5) | 0.3064(4) | 0.3013(5) | 0.3064(4) | 0.3016(3) | 0.3013(5) | 0.3064(4) | 0.3016(3) | 0.3012(4) | 0.3012(4) | 0.3012(4) | 0.3012(4) |
| <i>z</i> | 0.0272(2) | 0.0264(2) | 0.0234(2) | 0.0147(2) | 0.0234(2) | 0.0147(2) | 0.0229(1) | 0.0234(2) | 0.0147(2) | 0.0229(1) | 0.0229(2) | 0.0229(2) | 0.0229(2) | 0.0229(2) |
| U_{\perp} -plane (Å ²) | 0.0047(10) | 0.0047(5) | 0.0140(14) | 0.0116(6) | 0.0047(5) | 0.0116(6) | 0.0024(6) | 0.0047(5) | 0.0116(6) | 0.0024(6) | 0.0011(7) | 0.0011(7) | 0.0011(7) | 0.0011(7) |
| U_{\parallel} -plane (Å ²) | 0.0014(9) | 0.0055(5) | 0.0060(6) | 0.0033(5) | 0.0060(6) | 0.0033(5) | 0.0020(6) | 0.0060(6) | 0.0033(5) | 0.0020(6) | 0.0031(6) | 0.0031(6) | 0.0031(6) | 0.0031(6) |
| $U_{\text{long-axis}}$ (Å ²) | 0.0080(15) | 0.0112(10) | 0.0144(14) | 0.0205(8) | 0.0144(14) | 0.0205(8) | 0.0245(12) | 0.0144(14) | 0.0205(8) | 0.0245(12) | 0.0171(9) | 0.0171(9) | 0.0171(9) | 0.0171(9) |
| O(2) <i>x</i> | -0.0692(3) | -0.0673(3) | -0.0576(3) | -0.0386(3) | -0.0576(3) | -0.0386(3) | -0.0622(4) | -0.0576(3) | -0.0386(3) | -0.0622(4) | -0.0583(2) | -0.0583(2) | -0.0583(2) | -0.0583(2) |
| <i>y</i> | -0.0212(4) | -0.0218(4) | -0.0154(5) | -0.0067(4) | -0.0154(5) | -0.0067(4) | 0.0179(5) | -0.0154(5) | -0.0067(4) | 0.0179(5) | -0.0141(4) | -0.0141(4) | -0.0141(4) | -0.0141(4) |
| <i>z</i> | 0.1645(2) | 0.1645(2) | 0.1646(2) | 0.1656(1) | 0.1646(2) | 0.1656(1) | 0.1644(2) | 0.1646(2) | 0.1656(1) | 0.1644(2) | 0.1645(1) | 0.1645(1) | 0.1645(1) | 0.1645(1) |
| U_{\perp} (Å ²) | 0.0045(9) | 0.0093(5) | 0.0125(10) | 0.0169(6) | 0.0045(9) | 0.0125(10) | 0.0169(6) | 0.0045(9) | 0.0125(10) | 0.0169(6) | 0.0070(5) | 0.0070(5) | 0.0070(5) | 0.0070(5) |
| U_{\parallel} (Å ²) | 0.0002(10) | 0.0042(8) | 0.0093(9) | 0.0117(8) | 0.0093(9) | 0.0117(8) | 0.0079(7) | 0.0093(9) | 0.0117(8) | 0.0079(7) | 0.0053(9) | 0.0053(9) | 0.0053(9) | 0.0053(9) |
| Ru-O(1) (Å) | 2.018(2) | 2.004(2) | 1.986(3) | 1.949(2) | 1.986(3) | 1.949(2) | 1.946(3) | 1.986(3) | 1.949(2) | 1.946(3) | 1.988(2) | 1.988(2) | 1.988(2) | 1.988(2) |
| Ru-O(2) (Å) | 2.015(2) | 2.018(2) | 1.993(2) | 1.950(2) | 1.993(2) | 1.950(2) | 1.943(3) | 1.993(2) | 1.950(2) | 1.943(3) | 1.986(2) | 1.986(2) | 1.986(2) | 1.986(2) |
| Ru-O _{aver} (Å) | 1.972(2) | 1.973(1) | 1.995(2) | 2.042(1) | 1.995(2) | 2.042(1) | 2.039(2) | 1.977(3) | 2.039(2) | 1.991(1) | 1.997(1) | 1.997(1) | 1.997(1) | 1.997(1) |
| O(1)-O(1) _a (Å) | 2.002 | 1.998 | 1.991 | 1.980 | 1.991 | 1.980 | 1.976 | 1.994 | 1.976 | 1.989 | 1.990 | 1.990 | 1.990 | 1.990 |
| O(1)-O(1) _b (Å) | 2.826(1) | 2.828(1) | 2.819(2) | 2.771(1) | 2.819(2) | 2.771(1) | 2.823(2) | 2.819(2) | 2.771(1) | 2.823(2) | 2.822(1) | 2.822(1) | 2.822(1) | 2.822(1) |
| O(1)-O(1) _c (Å) | 2.877(1) | 2.860(1) | 2.807(1) | 2.742(1) | 2.807(1) | 2.742(1) | 2.737(1) | 2.840(1) | 2.737(1) | 2.737(1) | 2.799(1) | 2.799(1) | 2.799(1) | 2.799(1) |
| Vol RuO ₆ (Å ³) | 10.69 | 10.64 | 10.53 | 10.34 | 10.53 | 10.34 | 10.28 | 10.56 | 10.28 | 10.48 | 10.50 | 10.50 | 10.50 | 10.50 |
| Θ -O(1) (deg) | 13.07(9) | 12.69(9) | 11.45(10) | 7.49(10) | 11.45(10) | 7.49(10) | 7.00(12) | 12.04(10) | 7.00(12) | 11.17(5) | 11.22(9) | 11.22(9) | 11.22(9) | 11.22(9) |
| Θ -O(2) (deg) | 11.5(5) | 11.2(5) | 9.3(6) | 5.9(5) | 9.3(6) | 5.9(5) | 5.4(9) | 10.2(6) | 5.4(9) | 9.4(3) | 9.1(3) | 9.1(3) | 9.1(3) | 9.1(3) |
| Φ (deg) | 11.88(7) | 11.93(5) | 11.88(7) | 12.77(8) | 11.88(7) | 12.77(8) | 12.57(10) | 11.85(8) | 12.57(10) | 11.77(5) | 11.73(5) | 11.73(5) | 11.73(5) | 11.73(5) |
| Sample Preparation | Dr. S. Nakatsuji, Ref. [52] University of Kyoto | | | | | | | | | | | | Dr. P. Adelmann Forschungszentrum Karlsruhe, IFP | |
| | | | | | | | | | | | | | Dr. P. Adelmann Forschungszentrum Karlsruhe, IFP | |

Table 4.3: Results of the high resolution powder diffraction analyses on $\text{Ca}_{2-x}\text{Sr}_x\text{RuO}_4$. O(1) denotes the oxygen in the RuO_2 -planes and O(2) the apical one. The rotation angle is unique and designed by Φ whereas the tilt angle may be determined at the two oxygen sites, Θ -O(1) and Θ -O(2) (*continued on next page*).

| Composition | x=0.1 | x=0.1 | x=0.15 | x=0.15 | x=0.2 ^a | x=0.2 ^a | x=0.2 ^a |
|--|----------------------------------|----------------------------------|----------------------------------|----------------------------------|-----------------------------|-----------------------------|-----------------------------|
| Temperature | 200 K | 300 K | 10 K | 300 K | 10 K | 300 K | 520 K |
| Space group | <i>L-Pbca</i> | <i>L-Pbca</i> | <i>L-Pbca</i> | <i>L-Pbca</i> | <i>L-Pbca</i> | <i>L-Pbca</i> | <i>Acmm</i> |
| <i>a</i> (Å) | 5.3488(2) | 5.3494(3) | 5.3301(9) | 5.3373(11) | 5.3304(4) | 5.3295(5) | 5.3412(1) |
| <i>b</i> (Å) | 5.3345(2) | 5.3420(3) | 5.3170(8) | 5.3273(11) | 5.3190(5) | 5.3232(4) | " |
| <i>c</i> (Å) | 12.3300(4) | 12.3219(4) | 12.3721(12) | 12.3800(12) | 12.4094(7) | 12.4506(7) | 12.4703(1) |
| Vol (Å ³) | 351.81(2) | 352.12(3) | 350.63(9) | 352.01(11) | 351.84(5) | 353.22(5) | 355.76(1) |
| ϵ | 0.0013 | 0.0007 | 0.0012 | 0.0009 | 0.0011 | 0.0006 | 0 |
| R_{wip} (%) | 5.59 | 5.84 | 6.91 | 6.21 | 5.95 | 5.48 | 5.82 |
| Ca/Sr <i>x</i> | 0.0099(5) | 0.0099(6) | 0.0114(11) | 0.0112(18) | 0.0133(7) | 0.0103(15) | 0 |
| <i>y</i> | 0.0221(6) | 0.0214(6) | 0.0148(15) | 0.0248(13) | 0.0169(9) | 0.0157(12) | 0 |
| <i>z</i> | 0.3479(1) | 0.3481(1) | 0.3474(3) | 0.3476(3) | 0.3475(2) | 0.3482(2) | 0.3486(2) |
| U_{iso} (Å ²) | 0.0056(4) | 0.0053(4) | 0.0013(8) | 0.0042(10) | 0.0073(4) | 0.0138(9) | 0.0135(6) |
| Ru U_{iso} (Å ²) | 0.0026(4) | 0.0045(4) | 0.0008(6) | 0.001(9) | 0.0007(4) | 0.0029(5) | 0.0096(6) |
| O(1) <i>x</i> | 0.1932(4) | 0.1934(4) | 0.1953(10) | 0.1953(10) | 0.1958(6) | 0.1944(6) | 0.1938(7) |
| <i>y</i> | 0.3055(4) | 0.3056(4) | 0.3064(9) | 0.3038(10) | 0.3064(6) | 0.3070(6) | 0.3050(7) |
| <i>z</i> | 0.0135(2) | 0.0127(2) | 0.0125(4) | 0.0082(9) | 0.0126(3) | 0.0075(6) | 0 |
| U_{\perp} -plane (Å ²) | 0.0068(6) | 0.0100(5) | 0.0104(8) | 0.0104(8) | 0.0023(6) | 0.0088(8) | 0.0148(5) |
| U_{\parallel} -plane (Å ²) | 0.0035(6) | 0.0020(6) | 0.0047(8) ^b | 0.0044(5) | 0.0005(2) | 0.0054(5) | 0.0072(5) |
| $U_{\text{long-axis}}$ (Å ²) | 0.0195(8) | 0.0245(12) | 0.0213(20) | 0.0213(20) | 0.0166(16) | 0.0228(18) | 0.0348(7) |
| O(2) <i>x</i> | -0.0370(3) | -0.0340(4) | -0.0359(7) | -0.0099(20) | -0.0368(5) | -0.0187(14) | 0 |
| <i>y</i> | -0.0085(5) | -0.0079(6) | -0.0034(12) | -0.0055(20) | -0.0078(5) | -0.0051(10) | 0 |
| <i>z</i> | 0.1650(1) | 0.1649(1) | 0.1661(3) | 0.1659(3) | 0.1652(2) | 0.1644(2) | 0.1645(2) |
| U_{\perp} (Å ²) | 0.0098(5) | 0.0151(5) | 0.0151(5) | 0.0150(10) | 0.0044(7) | 0.0162(10) | 0.0301(6) |
| U_{\parallel} (Å ²) | 0.0058(7) | 0.0079(7) | 0.0015(9) ^b | 0.0081(10) | 0.0035 | 0.0051(10) | 0.0059(7) |
| Ru-O(1) (Å) | 1.937(2) | 1.939(2) | 1.940(5) | 1.929(5) | 1.942(3) | 1.937(3) | 1.930(4) |
| Ru-O(2) (Å) | 1.949(2) | 1.948(2) | 1.929(5) | 1.934(5) | 1.927(3) | 1.928(3) | 1.939(4) |
| Ru-O _{aver} (Å) | 2.044(1) | 2.040(1) | 2.064(4) | 2.055(4) | 2.060(3) | 2.050(3) | 2.051(3) |
| O(1)-O(1) _a (Å) | 1.977 | 1.976 | 1.978 | 1.973 | 1.976 | 1.972 | 1.974 |
| O(1)-O(1) _b (Å) | 2.759(1) | 2.758(1) | 2.749(2) | 2.737(3) | 2.750(2) | 2.739(2) | 2.735(2) |
| Vol RuO ₆ (Å ³) | 2.736(1) | 2.739(1) | 2.722(2) | 2.727(2) | 2.722(1) | 2.727(2) | 2.737(2) |
| Vol RuO ₆ (Å ³) | 10.29 | 10.27 | 10.30 | 10.22 | 10.28 | 10.21 | 10.24 |
| Θ-O(1) (deg) | 6.93(10) | 6.52(10) | 6.5(2) | 4.3(4) | 6.6(2) | 3.9(3) | / |
| Θ-O(2) (deg) | 5.7(5) | 5.2(5) | 5.4(1.6) | 1.7(5.1) | 5.6(1.0) | 2.9(1.9) | / |
| Φ (deg) | 12.66(8) | 12.65(6) | 12.5(2) | 12.2(2) | 12.47(11) | 12.69(12) | 12.54(14) |
| Sample Preparation | Dr. P. Adelmann | Dr. P. Adelmann | Dr. P. Adelmann | Dr. P. Adelmann | Dr. S. Nakatsuji, Ref. [52] | Dr. S. Nakatsuji, Ref. [52] | Dr. S. Nakatsuji, Ref. [52] |
| | Forschungszentrum Karlsruhe, IFF | Forschungszentrum Karlsruhe, IFF | Forschungszentrum Karlsruhe, IFF | Forschungszentrum Karlsruhe, IFF | University of Kyoto | University of Kyoto | University of Kyoto |

^a With minor contribution of $I4_1/acd$ phase; for details see text.
^b Value represents isotropic mean-square atomic displacement U_{iso}

Table 4.3: (continued from previous page) U_{\parallel} and U_{\perp} denote the mean-square atomic displacements parallel and perpendicular to the Ru-O bonds. O(1)-O(1)_a, b denote the length of the edge of the octahedron basal plane along a, b respectively (continued on next page).

4.A Results of the high resolution powder diffraction analyses on $\text{Ca}_{2-x}\text{Sr}_x\text{RuO}_4$

| Composition | x=0.5 | x=0.5 | x=1.0 | x=1.0 | x=1.5 | x=1.8 | x=2.0 | x=2.0 |
|--|---|---|---|---|---------------|------------|-----------|-----------|
| Temperature | 10 K | 300 K | 10 K | 300 K | 300 K | 10 K | 20 K | 295 K |
| Space group | $I4_1/acd$ | $I4_1/acd$ | $I4_1/acd + \text{Dis.}$ | $I4_1/acd + \text{Dis.}$ | $F4/mmm$ | $F4/mmm$ | $F4/mmm$ | $F4/mmm$ |
| a (Å) | 5.3195(1) | 5.3395(1) | 5.3622(1) | 5.3830(1) | 5.4259(2) | 5.4422(1) | 5.4609 | 5.4744 |
| b (Å) | " | " | " | " | " | " | " | " |
| c (Å) | 2 · 12.5867(3) | 2 · 12.5749(3) | 2 · 12.6868(3) | 2 · 12.6757(3) | 12.7289(5) | 12.7321(2) | 12.7217 | 12.7397 |
| Vol (Å ³) | 2 · 356.17(1) | 2 · 358.51(1) | 2 · 364.78(2) | 2 · 367.30(2) | 374.74(2) | 377.09(1) | 379.38 | 381.80 |
| $ e $ | / | / | / | / | / | / | / | / |
| R_{wp} (%) | 5.15 | 4.26 | 6.57 | 5.07 | 6.67 | 7.24 | Ref. [13] | Ref. [13] |
| Ca/Sr x | 0 | 0 | 0 | 0 | 0 | 0 | 0 | 0 |
| y | 1/4 | 1/4 | 1/4 | 1/4 | 0 | 0 | 0 | 0 |
| z | 0.5492(1) | 0.5494(1) | 0.5497(1) | 0.5500(1) | 0.3513(1) | 0.3522(1) | 0.35306 | 0.35316 |
| U_{iso} (Å ²) | 0.0022(3) | 0.0090(3) | 0.0025(3) | 0.0081(3) | 0.0074(3) | 0.0025(2) | 0.0029 | 0.0061 |
| Ru U_{iso} (Å ²) | 0.0014(3) | 0.0042(3) | 0.0038(3) | 0.0065(3) | 0.0023(3) | 0.0024(2) | 0.0019 | 0.0026 |
| O(1) x | 0.1933(2) | 0.1949(2) | 0.2008(2) | 0.2027(2) | 1/4 | 1/4 | 1/4 | 1/4 |
| y | $x+1/4$ | $x+1/4$ | $x+1/4$ | $x+1/4$ | 1/4 | 1/4 | 1/4 | 1/4 |
| z | 1/8 | 1/8 | 1/8 | 1/8 | 0 | 0 | 0 | 0 |
| U_{\perp} -plane (Å ²) | 0.0052(16) | 0.0092(16) | 0.0157(8) | 0.0156(5) | 0.0967(20) | 0.0389(17) | 0.0051 | 0.0110 |
| U_{\parallel} -plane (Å ²) | 0.0024(8) | 0.0040(7) | 0.0014(1) | 0.0022(2) | 0.0041(5) | 0.0034(4) | 0.0030 | 0.0031 |
| $U_{\text{long-axis}}$ (Å ²) | 0.0152(6) | 0.0211(6) | 0.0149(7) | 0.0217(7) | 0.0078(6) | 0.0085(7) | 0.0049 | 0.0107 |
| O(2) x | 0 | 0 | 0 | 0 | 0 | 0 | 0 | 0 |
| y | 1/4 | 1/4 | 1/4 | 1/4 | 0 | 0 | 0 | 0 |
| z | 0.4568(1) | 0.4568(1) | 0.4563(1) | 0.4563(1) | 0.1616(1) | 0.1617(1) | 0.16180 | 0.16169 |
| U_{\perp} (Å ²) | 0.0084(3) | 0.0142(3) | 0.0086(3) | 0.0143(3) | 0.0113(3) | 0.0057(4) | 0.0059 | 0.0096 |
| U_{\parallel} (Å ²) | 0.0050(7) | 0.0080(7) | 0.0052(6) | 0.0078(6) | 0.0043(7) | 0.0048(6) | 0.0025 | 0.0050 |
| Ru-O(1) (Å) | 1.929(1) | 1.933(1) | 1.932(1) | 1.937(1) | 1.9183(1) | 1.9241(1) | 1.9307 | 1.9355 |
| Ru-O(2) (Å) | / | / | / | / | / | / | / | / |
| Ru-O _{aver} (Å) | 2.059(3) | 2.057(3) | 2.063(3) | 2.061(3) | 2.057(1) | 2.058(1) | 2.0584 | 2.0599 |
| O(1)-O(1) _a (Å) | 1.972 | 1.975 | 1.976 | 1.978 | 1.965 | 1.969 | 1.973 | 1.977 |
| O(1)-O(1) _b (Å) | 2.727(2) | 2.734(5) | 2.733(1) | 2.739(1) | 2.7130(1) | 2.7211(1) | 2.7305 | 2.7372 |
| Vol RuO ₆ (Å ³) | 10.21 | 10.25 | 10.27 | 10.31 | 10.09 | 10.16 | 10.23 | 10.29 |
| Θ -O(1) (deg) | / | / | / | / | / | / | / | / |
| Θ -O(2) (deg) | / | / | / | / | / | / | / | / |
| Φ (deg) | 12.78(4) | 12.43(4) | 11.13(3) | 10.71(3) | / | / | / | / |
| Sample Preparation | Dr. S. Nakatsuji University of Kyoto | Dr. S. Nakatsuji University of Kyoto | Dr. S. Nakatsuji University of Kyoto | Dr. P. Adelmann Forschungszentrum Karlsruhe, IFP | see Ref. [13] | | | |

Table 4.3: (continued from previous page) Errors are given in parentheses and result from the least square fitting; therefore they do not take account of systematic errors and underestimate effects of correlations. R_{wp} is the 'R-weighted pattern' value, where $R_{wp} = [\sum w_i(y_i(obs) - y_i(calc))^2 / \sum w_i(y_i(obs))^2]^{1/2}$ and $w_i = 1/\sigma(y_i^2(obs))$. For comparison we show also the structural parameters for Sr_2RuO_4 and Ca_2RuO_4 [6, 13].

| Composition | x=0.15 | x=0.2 | x=0.2 | x=2.0 |
|---|---------------|---------------------------|---------------------------|---------------|
| Temperature | 295 K | 295 K | 20 K | 295 K |
| Space group | <i>L-Pbca</i> | <i>I4₁/acd</i> | <i>D-Pbca</i> | <i>F4/mmm</i> |
| Ref. | 613 | 466 | 944 | |
| R_w (%) | 3.73 | 2.88 | 7.10 | Ref. [13] |
| R_{uw} (%) | 3.08 | 1.77 | 5.63 | |
| α (%) | 79.1 | / | 55.2 | / |
| Ca/Sr x | 0.0081(2) | 0 | 0.0081(11)/-0.0101(11) | 0 |
| y | 0.0176(2) | 1/4 | 0.2407(5)/0.2265(5) | 0 |
| z | 0.34824(4) | 0.54902(1) | 0.54908(3)/(3/4 - z_1) | 0.35316(2) |
| U_{11} (\AA^2) | 0.0093(3) | 0.0118(1) | 0.0020(7) | 0.00678(8) |
| U_{22} (\AA^2) | 0.0104(3) | = U_{11} | 0.0065(8) | = U_{11} |
| U_{33} (\AA^2) | 0.0037(1) | 0.0049(1) | 0.0016(3) | 0.00488(9) |
| U_{13} (\AA^2) | -0.0017(3) | 0.0014(2) | 0 | / |
| Ru x | 0 | 0 | 0 | 0 |
| y | 0 | 1/4 | 0.2434(3) | 0 |
| z | 0 | 3/8 | 3/8 | 0 |
| $U_{11} = U_{22}$ (\AA^2) | 0.00134(5) | 0.00300(9) | 0.0018(2) | 0.00227(9) |
| U_{33} (\AA^2) | 0.0031(1) | 0.0040(1) | 0.0015(2) | 0.00357(12) |
| O(1) x | 0.1918(1) | 0.18973(5) | 0.1916(6)/0.6912(6) | 1/4 |
| y | 0.3083(1) | $x+1/4$ | 0.4341(5)/0.5528(5) | 1/4 |
| z | 0.01058(5) | 1/8 | 0.1300(1)/0.1196(1) | 0 |
| $U_{\perp\text{-plane}}$ (\AA^2) | 0.0072(1) | 0.0087(1) | 0.0053(3) | 0.0110(1) |
| $U_{\parallel\text{-plane}}$ (\AA^2) | 0.0024(1) | 0.0035(1) | 0.0023(3) | 0.0031(1) |
| $U_{\text{long-axis}}$ (\AA^2) | 0.0134(3) | 0.0172(2) | 0.0065(4) | 0.0107(1) |
| O(2) x | -0.0275(1) | 0 | -0.0340(9)/0.0233(8) | 0 |
| y | -0.0060(1) | 1/4 | 0.2380(4)/0.2506(4) | 0 |
| z | 0.16491(3) | 0.45727(1) | 0.45737(2)/(3/4 - z_1) | 0.16169(2) |
| U_{\perp} (\AA^2) | 0.0123(2) | 0.0153(1) | 0.0061(7) | 0.00969(10) |
| U_{\parallel} (\AA^2) | 0.0040(1) | 0.0049(1) | 0.0025(2) | 0.00458(12) |
| Ru-O(1) (\AA) | 1.9426(6) | 1.9311(12) | 1.936(3)/1.936(3) | 1.9355 |
| | 1.9418(6) | / | 1.935(3)/1.937(3) | / |
| Ru-O(2) (\AA) | 2.0561(5) | 2.0545(4) | 2.052(1)/2.056(1) | 2.0599 |
| Ru-O _{aver} (\AA) | 1.9802 | 1.9723 | 1.975 | 1.977 |
| O(1)-O(1) _a (\AA) | 2.7531(9) | 2.7310(11) | 2.750(4)/2.754(5) | 2.7372 |
| O(1)-O(1) _b (\AA) | 2.7403(9) | " | 2.724(4)/2.724(4) | " |
| Vol RuO ₆ (\AA^3) | 10.34 | 10.22 | 10.27 | 10.29 |
| Θ -O(1) (deg) | 5.48(2) | / | 5.79(14)/5.08(12) | / |
| Θ -O(2) (deg) | 4.2(3) | / | 4.98(14)/3.61(16) | / |
| Φ (deg) | 13.12(2) | 13.554(8) | 13.80(9)/13.83(9) | / |

Table 4.3: Results of the single crystal structural analyses on $\text{Ca}_{1.85}\text{Sr}_{0.15}\text{RuO}_4$ at $T=295\text{ K}$ and on $\text{Ca}_{1.8}\text{Sr}_{0.2}\text{RuO}_4$ at 295 and 20 K. The standard deviations are given in parentheses. R_w and R_{uw} denote the weighted and unweighted reliability values where $R_w = [\sum w_i \cdot (F_{obs}^2 - F_{calc}^2)^2 / \sum (w_i \cdot F_{obs}^4)]^{1/2}$ and $R_{uw} = \sum (F_{obs}^2 - F_{calc}^2) / \sum F_{obs}^2$; α is the twinning ratio (for any further notation cf. Table 4.3). For comparison we show also the results obtained for Sr_2RuO_4 [13].

Chapter 5

Lattice Dynamics of $\text{Ca}_{2-x}\text{Sr}_x\text{RuO}_4$

5.1 Introduction

From the lattice-dynamical point of view the structural phase transitions, observed in numerous layered perovskites which crystallize like the $\text{Ca}_{2-x}\text{Sr}_x\text{RuO}_4$ system in the K_2NiF_4 -type structure, are associated with an unstable optical phonon, whose frequency falls to zero on cooling towards the transition temperature. A vanishing frequency implies a vanishing restoring force against the corresponding deformation, therefore this vibration is called a *soft mode*. The atomic displacements associated with the soft mode are the same as the structural distortions in the low-temperature phase. The soft mode concept has achieved considerable success in the description and understanding of structural phase transitions in solids. In order to present this concept we consider in this introduction two representative examples, the displacive phase transition in the ferroelectric perovskite titanates (e. g., SrTiO_3 or BaTiO_3) and the tetragonal-to-orthorhombic phase transition in La_2CuO_4 , emphasizing those features relevant to our experimental data. For further reading we refer to the following references [139–143].

The soft mode concept has been widely applied to structural phase transitions in solids. The central idea of this concept is that the structural phase transition is caused by a lattice dynamical instability, for which the frequency of a particular phonon mode tends to zero when approaching the phase transition. The polarization pattern of this soft-mode corresponds to the deformation of the structure in the low-temperature phase. The most known example for such a transition can be found amongst the ferroelectric perovskite titanates. At high temperature these all share the simple-cubic perovskite structure ATiO_3 : metal A at the cube corners, the Ti cation at the cube center, and O atoms at the cube faces. The structural instabilities in these compounds can be divided into two groups by the location of the soft modes, either at the zone center (*ferrodistortive* instabilities) or at the zone boundary (*antiferrodistortive* instabilities). In both cases a displacive phase transition results, when the phonon frequency of this mode tends towards zero upon cooling. At the transition temperature the atomic displacement associated with the soft mode freezes into the structure in the low temperature phase. The displacive phase transition which is related with a soft mode at $q = 0$ leads to a displacement pattern, for which the

A and Ti cations move off-center with respect to the surrounding oxygen anions, so that the material develops a spontaneous macroscopic dielectric polarization (e. g. PbTiO_3). On the other hand the condensation of a soft mode at the zone boundary causes a deformation where equivalent atoms in neighboring cells are not displaced identically and implies thus an enlargement of the unit cell. Such a transition is seen for examples in SrTiO_3 , involving rotations of adjacent TiO_6 octahedra, which are connected with the softening of the related zone boundary mode.

Another important example of soft mode behavior is the $\text{La}_{2-x}\text{Sr}_x\text{CuO}_4$ system. At high temperatures this system shares the K_2NiF_4 structure in its undistorted high-temperature tetragonal (HTT) form. As the temperature is reduced, the structure transforms from the HTT phase to a low-temperature orthorhombic phase (LTO) via a continuous phase transition [144–148]. This transition is characterized by tilts of the CuO_6 octahedron (cf. chapter 4), involving characteristic soft-phonon behavior at the zone boundary: The phonon frequency of this mode at the X point of the HTT phase goes to zero upon approaching the phase transition. In addition the structural instability is reflected in the dispersion of the corresponding optical branch with Σ_4 symmetry. In La_2CuO_4 the soft mode in the high-temperature phase is twofold-degenerate, corresponding to two equivalent displacement wave vectors $\mathbf{Q}_1 = (\frac{1}{2}, \frac{1}{2}, 0)$ and $\mathbf{Q}_2 = (\frac{1}{2}, -\frac{1}{2}, 0)$ with amplitudes Q_1 and Q_2 , which describes a tilt around $[1 - 10]$ and $[110]$, respectively. Below the transition temperature the degeneracy is lifted, so that in the low-temperature phase two modes with different frequencies can be observed. Identifying the amplitudes Q_1 and Q_2 as the two components of the order parameter of the phase transition one may easily discuss the phase transformations in the La_2CuO_4 system: The LTO phase corresponds to $Q_1 \neq 0$ and $Q_2 = 0$, or $Q_1 = 0$ and $Q_2 \neq 0$, while the LTT, and $Pccn$ phase, correspond to $Q_1 = Q_2 \neq 0$ and $Q_1 \neq Q_2 \neq 0$, respectively. Furthermore, a more quantitative discussion of the phase transformations is simply provided within the framework of Landau theory, which is an expansion of the free energy in terms of the order parameter, together with terms that couple the order parameter with the strain [49, 116, 139, 140].

In the case of Sr_2RuO_4 , which is stable in the tetragonal $I4/mmm$ structure down to lowest temperatures, the phonon dispersion curves indicate also a close structural instability: inelastic neutron scattering measurements observe a steep dispersion near the rotational phonon mode belonging to the Σ_3 representation [47]. As may be seen in Fig. reffig:5.1 this branch is softening continuously in the Brillouin zone, with an extremely steep negative slope for wave vectors approaching the zone boundary. In contrast, the tilt mode which drives the displacive phase transition in La_2CuO_4 does not exhibit any anomalous behavior in Sr_2RuO_4 , as can be inferred from the dispersion of the lowest optic Σ_4 branch in Fig. 5.1. While in La_2CuO_4 a drastic drop of this branch is observed in the phonon dispersion curves towards the zone-boundary, in Sr_2RuO_4 the frequency of this branch decreases only slightly from 3.7 THz at the zone center to 3.4 THz to the X point. These observations demonstrate that Sr_2RuO_4

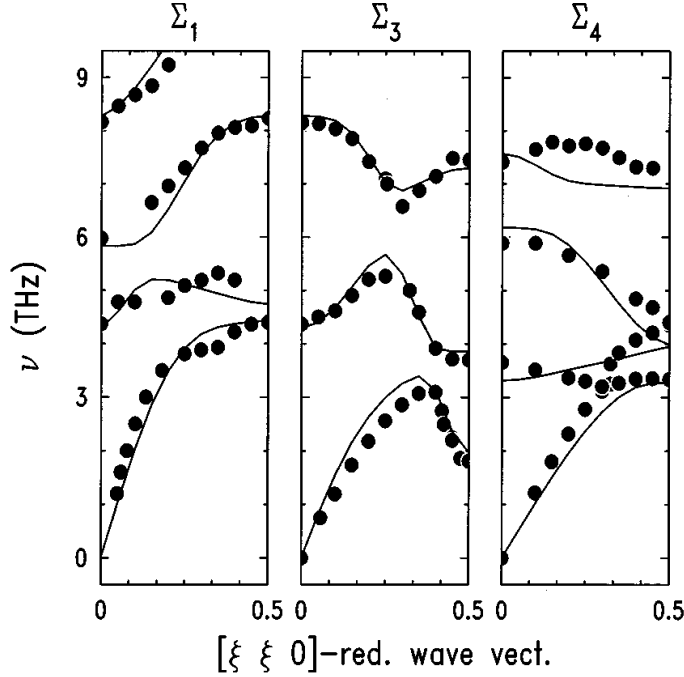


Figure 5.1: Experimentally determined and calculated low frequency part of the phonon dispersion along [110] in Sr_2RuO_4 , taken from Ref. [47]. Only the phonons with Σ_1 , Σ_3 , and Σ_4 symmetry are shown.

also appears to be close to a structural instability which, however, does not involve a tilt of the octahedron as for La_2CuO_4 , but corresponds to a rotation of RuO_6 octahedra about the [001] axis. This is well in accordance with our observations of a pure $I4_1/acd$ -phase for $\text{Ca}_{1.0}\text{Sr}_{1.0}\text{RuO}_4$ and $\text{Ca}_{1.5}\text{Sr}_{0.5}\text{RuO}_4$ and our detection of sizeable diffuse scattering in $\text{Ca}_{0.5}\text{Sr}_{1.5}\text{RuO}_4$ due to local rotational distortions. Although the dispersion in Sr_2RuO_4 shows the signature of a close structural instability, the temperature dependence of the rotational mode does not exhibit the expected phonon softening upon cooling. In addition anomalous broadening of the rotational mode upon heating has been observed and can be most probably attributed to electron-phonon interaction. As discussed by the authors of Ref. [47] these results suggest that the rotational instability and the related phase transition is presumably not only caused by purely structural features, but involves also a more complex electron phonon coupling mechanism.

Despite of any anomalous behavior of the tilt-mode in Sr_2RuO_4 our structural studies have revealed that the rotation phase becomes unstable against the tilt deformation for Sr concentrations lower than $x \simeq 0.5$. In order to study the dynamic aspects of the corresponding structural phase transition in $\text{Ca}_{2-x}\text{Sr}_x\text{RuO}_4$, we have investigated the stability of the low-lying phonon modes using inelastic neutron scat-

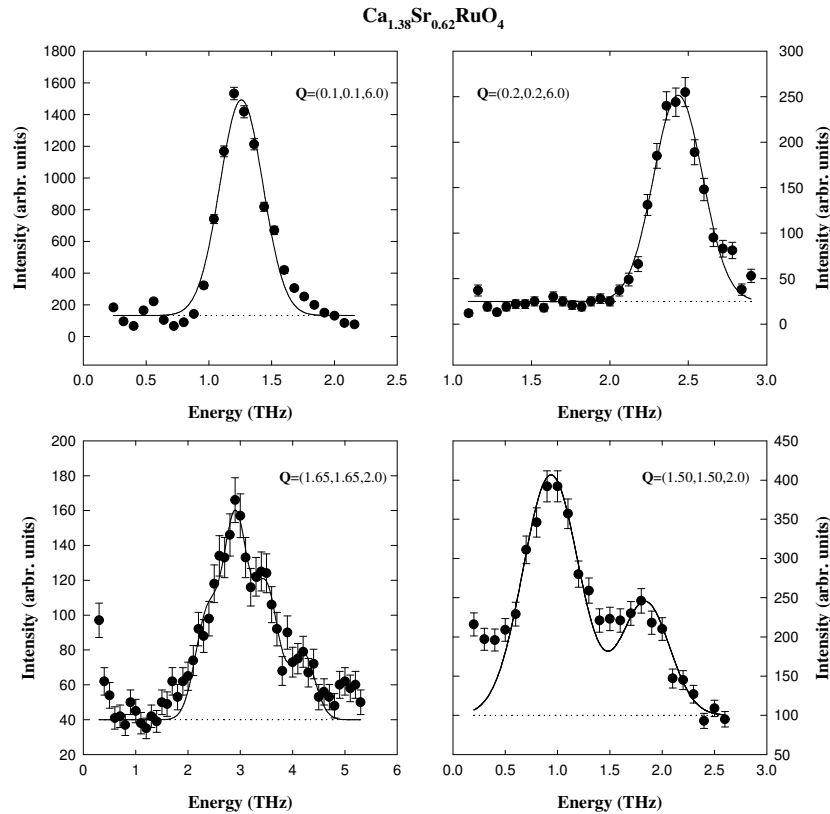


Figure 5.2: Raw energy scans showing phonons peak in $\text{Ca}_{1.38}\text{Sr}_{0.62}\text{RuO}_4$, measured at $T=295$ K. *Upper row:* Spectra of transverse acoustic phonons with Σ_4 symmetry, measured along $[110]$. *Lower row:* Soft phonons at $(1.65/1.50, 1.65/1.50, 2.0)$ corresponding to $(0.35/0.50, 0.35/0.50, 0)$.

tering techniques. Single crystals with Sr concentrations of $x=0.62$, 0.50 , and 0.20 were studied. Although the latter two crystals are rather small in volume (cf. Tab. 3.1) the measurements of the phonon dispersion curves lead to satisfactory results, which are presented in the following sections.

5.2 Soft Mode character of the tilt transition in $\text{Ca}_{2-x}\text{Sr}_x\text{RuO}_4$

The neutron scattering experiments devoted to the study of the lattice dynamics in $\text{Ca}_{2-x}\text{Sr}_x\text{RuO}_4$ were performed on the triple-axis spectrometer 1T.1 at the Orphée Reactor (experimental details are given in section 3.2.3). For simplicity we use in this chapter the tetragonal $I4/mmm$ unit cell. Since our experiments were focussed on the modes related to the structural phase transition involving the tilt of the RuO_6

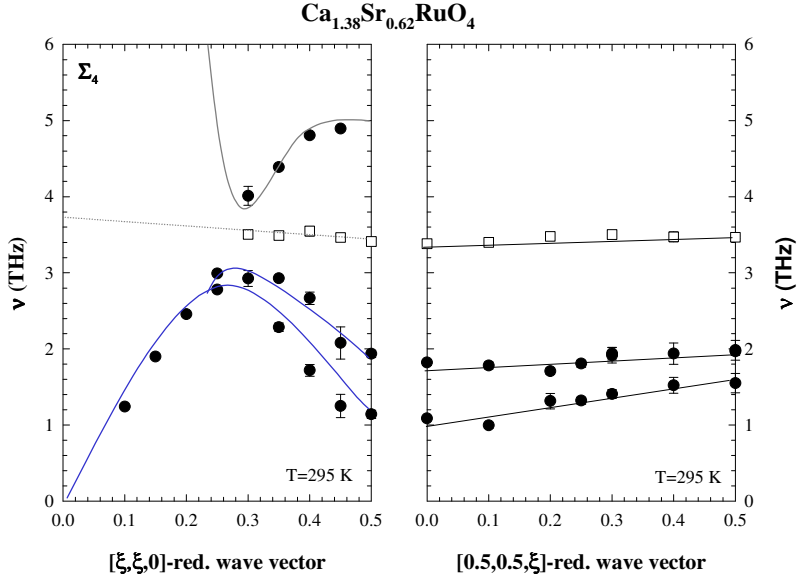


Figure 5.3: *Left:* Low frequency part of the phonon dispersion in the [110] direction (Σ_4 symmetry) in $\text{Ca}_{1.38}\text{Sr}_{0.62}\text{RuO}_4$. *Right:* Dependence of the tilt mode frequency on the q_c component. For details refer to Fig. 5.5 and the text. In both panels the lines are intended as guides to the eye.

octahedra, our efforts were centered on modes belonging to the Σ_4 representation (note in $I4/mmm$ this representation contains 6 of the 21 possible branches along [110], including especially the transverse acoustic modes polarized parallel to the c axis and the optical phonon mode whose vibration pattern corresponds to the tilt deformation). For this purpose the crystals were investigated in the (110)/(001) scattering plane, permitting the measurement of the phonon dispersion curves of the soft X -point modes and of the out-of-plane transversal acoustic modes, starting from the $(\frac{3}{2}, \frac{3}{2}, 2)$ and the (006) reciprocal lattice points, respectively. These positions have been chosen for this study because of their favorable dynamical structure factors. Figure 5.2 shows typical constant- Q energy scans of these modes in $\text{Ca}_{1.38}\text{Sr}_{0.62}\text{RuO}_4$ at room temperature for different wave vectors.

The measured phonon frequencies of the acoustic and lowest lying optical branches obtained from these scans are plotted in Fig. 5.3. Compared to those reported for Sr_2RuO_4 , given in Fig. 5.1, one recognizes a significant change of the dispersion near the transversal acoustic modes (hereinafter referred to as TA) at low frequencies. When following this branch from the Γ point toward the zone boundary, one observes at first the conventional behavior of a TA phonon, i.e., the phonon frequency increases monotonically with increasing Q . But beyond $\xi \sim 0.25$ this branch exhibits a pronounced dip. This is quite a standard case of soft phonon behavior: The TA mode has the same symmetry as the optical soft mode, and, hence, they should repel

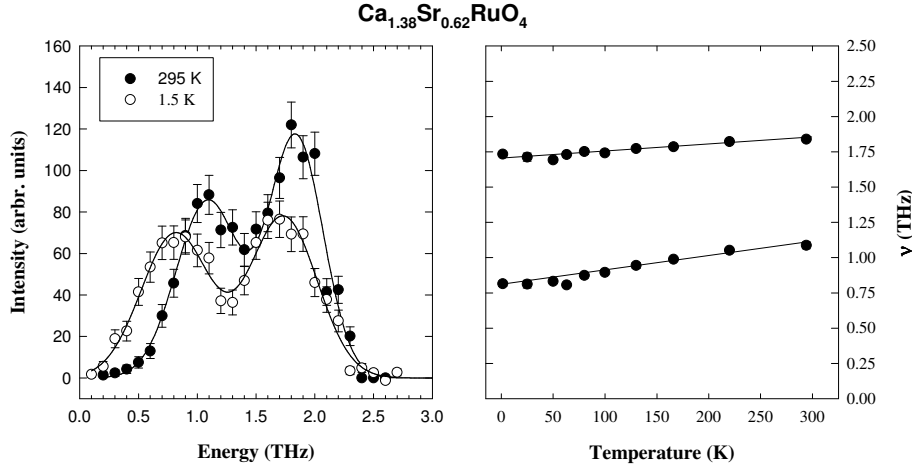


Figure 5.4: *Left:* The soft phonon at the superlattice position $\mathbf{Q}=(\frac{3}{2}, \frac{3}{2}, 2)$, at $T=1.5$ and 295 K in $\text{Ca}_{1.38}\text{Sr}_{0.62}\text{RuO}_4$. Note the splitting and the decrease in energy with decreasing temperature. For the sake of clarity, the background has been subtracted and the data has been corrected by the Bose factor, $(n(\omega) + 1)$; lines are fit by gaussian peaks. *Right:* The temperature dependence of the soft-mode phonon frequency in $\text{Ca}_{1.38}\text{Sr}_{0.62}\text{RuO}_4$. The lines are guides to the eye.

each other and exhibit anticrossing behavior. This means that the steep softening of the optical soft mode branch in the Brillouin zone, which starts at a frequency at the Γ point somewhat higher than the covered energy range, leads to successive interactions with the lower lying, symmetry equivalent phonon branches with a transfer of character. On the other hand the lowest optic Σ_4 branch stays flat beyond $\xi \sim 0.25$ up to the zone boundary tilt mode (3.4 THz), indicating that in this case the interaction due to softening is negligible. In addition to the reported softening of the low lying phonon branches at the zone boundary, a clear splitting of the related modes is observed. Though the zone boundary modes are doubly degenerated, corresponding to the two tilts around $[010]$ and $[100]$, this degeneracy should not be lifted by the rotational distortion in $\text{Ca}_{1.38}\text{Sr}_{0.62}\text{RuO}_4$. However, the structural transition in $\text{Ca}_{1.38}\text{Sr}_{0.62}\text{RuO}_4$ result in a doubling of the c -lattice parameter, so that the rotational deformation present in $I4_1/acd$ symmetry imposes a specific stacking sequence on the tilt distortion. Therefore, the observed splitting of the tilt modes at $(\frac{1}{2}, \frac{1}{2}, 0)$ might be possibly due to the different stacking periods of the tilt and rotational distortions along the c -axis and their possible interaction.

The splitted X -point phonon in $\text{Ca}_{1.38}\text{Sr}_{0.62}\text{RuO}_4$ was investigated as a function of temperature. As shown in Fig. 5.4 the phonons are well defined down to lowest temperature. On cooling down to 1.5 K the frequency of the two peaks of the soft mode decreases by 23 % and 8 %, for the lower and higher lying modes, respectively (see Fig. 5.4). The relatively low frequency of this mode (0.82 THz) and the

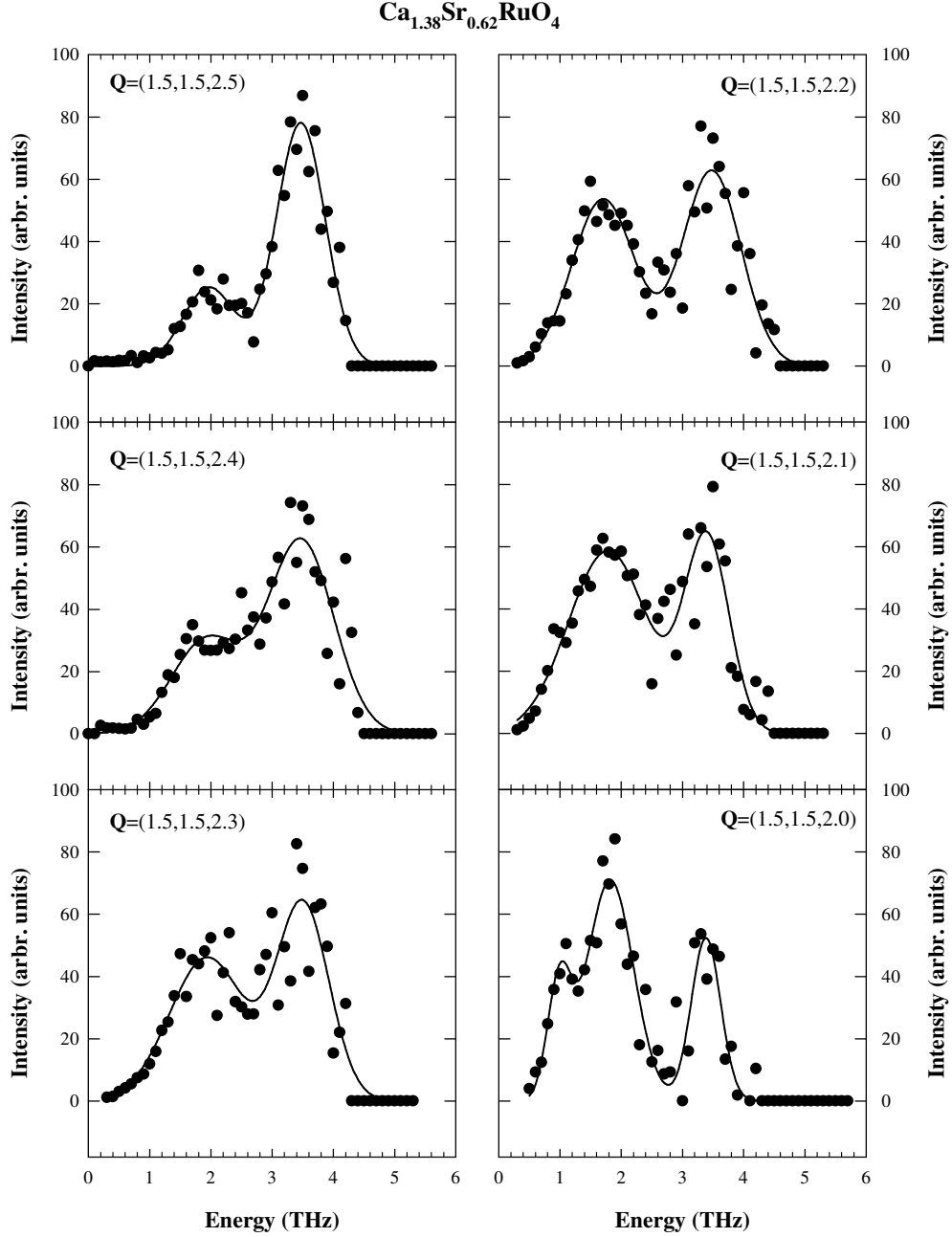


Figure 5.5: Typical energy scans of the tilt mode measured in the [001] direction around the superlattice peak position $(\frac{3}{2}, \frac{3}{2}, 2)$ at room temperature. Note the intensity crossover for the two branches on approaching $(\frac{1}{2}, \frac{1}{2}, \frac{1}{2})$. For clarity the background has been subtracted and the data has been corrected by the Bose factor. The lowest lying phonons, which are at $(\frac{3}{2}, \frac{3}{2}, 2)$ clearly splitted, have been fitted for all positions with two gaussian peaks with widths fixed to those determined at the zone boundary.

softening towards low temperatures indicates that the tetragonal $I4_1/acd$ phase of $\text{Ca}_{1.38}\text{Sr}_{0.62}\text{RuO}_4$ is inherently unstable against the tilt deformation, in good agreement with our former results (cf. section 4.4.3). The considerably different frequency softening on cooling of the two modes at the X point may be taken as evidence for the quite distinct character of these modes, as discussed above.

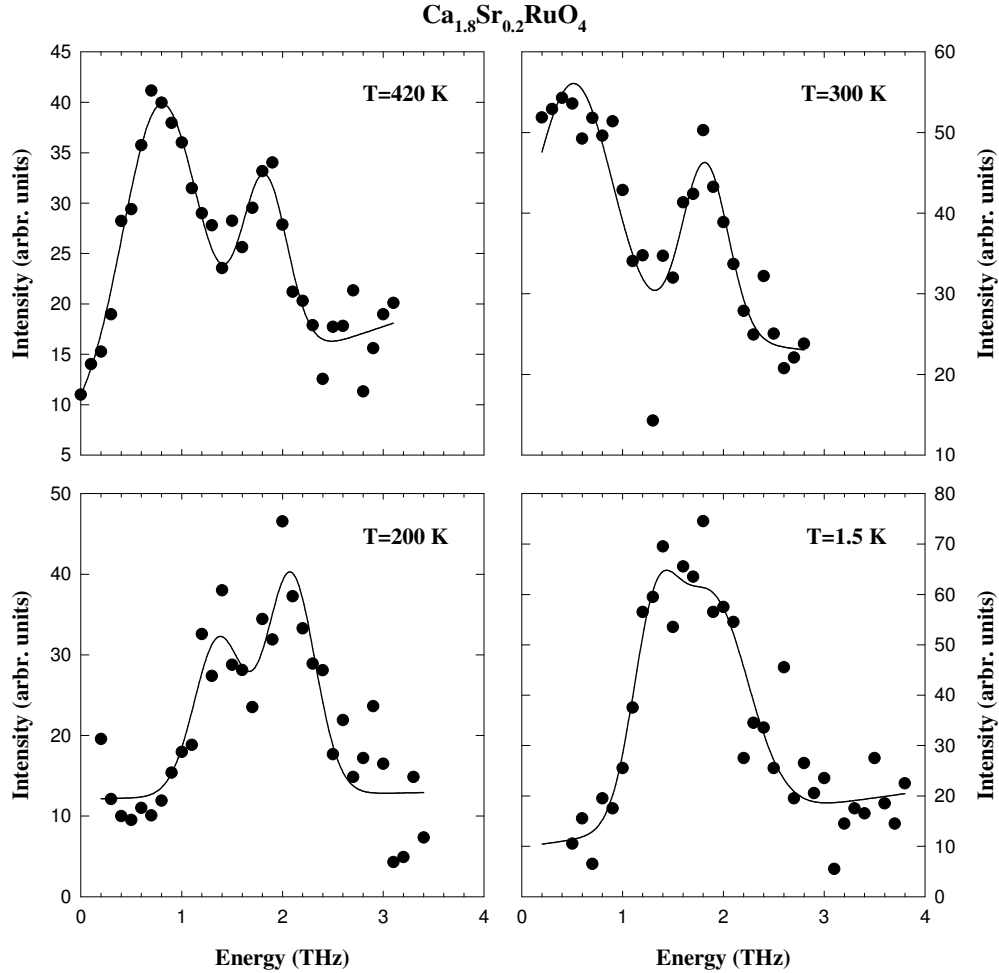


Figure 5.6: Energy scans at the superstructure reflection $\mathbf{Q}=(\frac{3}{2}, \frac{3}{2}, 2)$, in $\text{Ca}_{1.8}\text{Sr}_{0.2}\text{RuO}_4$. Our elastic intensity measurements have revealed a transition temperature of $T_O = 285$ K for this single crystal (cf. Fig. 4.15). For clarity the background has been subtracted and the data has been corrected by the Bose factor.

Finally, we studied the dispersion of the tilt branch in $\text{Ca}_{1.38}\text{Sr}_{0.62}\text{RuO}_4$ along the c -axis. In general one might expect a finite dispersion of the tilt-phonon-modes, fixing the stacking sequence. Some typical constant \mathbf{Q} scans of the tilt mode measured along the $[001]$ direction at room temperature are plotted in Fig. 5.5. The frequencies of the modes exhibits no distinct changes when approaching $(\frac{1}{2}, \frac{1}{2}, \frac{1}{2})$, yielding an almost

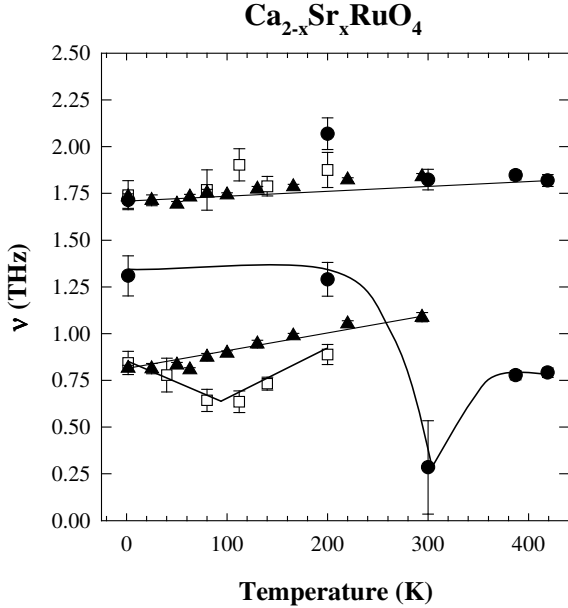


Figure 5.7: Summary of the soft phonon frequency, measured at $\mathbf{Q}=(\frac{3}{2}, \frac{3}{2}, 2)$, in all three samples of $\text{Ca}_{2-x}\text{Sr}_x\text{RuO}_4$ studied here, with $x=0.62$ (\blacktriangle), 0.50 (\square), and 0.20 (\bullet). The lines are intended as guides to the eye.

flat dispersion (see Fig. 5.3). It is tempting to interpret the absence of dispersion of the tilt mode along c as an indication for the lack of interlayer coupling of the octahedron tilt due to the small interionic forces for the $\text{Ca}^{2+}/\text{Sr}^{2+}$ ion and the two-dimensional character of the structure. However, close to $(\frac{1}{2}, \frac{1}{2}, \frac{1}{2})$ one observes a pronounced change of intensity, with a transfer of character between the higher lying phonon mode and the lower lying ones. Furthermore, the observed characteristics are quite unusual compared to the soft mode behavior in $(\text{La}, \text{Sr})_2\text{CuO}_4$, for which an almost isotropic dispersion in the $[110]$ and $[001]$ directions has been reported [146, 148]. We think that these differences might be understood in terms of the structural distortion already present in $\text{Ca}_{1.38}\text{Sr}_{0.62}\text{RuO}_4$ (note that the rotational angle Φ amounts for $x=1.0$ to 10.7°). Due to the rotational distortion $(\frac{1}{2}, \frac{1}{2}, \frac{1}{2})$ does not lie any more on the boundary of the Brillouin zone, but is folded back forming a new zone-center in $I4_1/acd$ symmetry. Therefore, the structural deformation might have an important impact on the corresponding branches as indicated by the intensity crossover, and might hide presumably a frequency hardening of the tilt mode along $(\frac{1}{2}, \frac{1}{2}, \xi)$. Furthermore, the structural disorder introduced by the Ca/Sr mixing might have a non-negligible influence on the phonon modes, which might further attenuate the softening along c . Model calculations would be quite helpful to analyze our experimental data in more detail, *(i)* by simulating the effect of disorder induced by the mixing of Ca and Sr ions on the dispersion curves and *(ii)* by describing the data by an adequate lattice dynamical model based on the distorted $I4_1/acd$ structure.

So far we discussed the characteristics of the tilt mode only for $\text{Ca}_{1.38}\text{Sr}_{0.62}\text{RuO}_4$ which is just prone to undergo the structural phase transition from tetragonal $I4_1/acd$ into the tilt distorted low temperature phase. Let us now turn to the results

of our investigation of the soft mode behavior in $\text{Ca}_{2-x}\text{Sr}_x\text{RuO}_4$ for two small single crystals ($V \simeq 14 \dots 20 \text{ mm}^3$, see Table 3.1), with $x=0.5$, and 0.2 , which exhibit the tilt transition near $T_O \simeq 80 \text{ K}$ and at $T_O = 285 \text{ K}$, respectively. In Fig. 5.6 we present typical constant Q scans at the point $(\frac{3}{2}, \frac{3}{2}, 2)$ for $\text{Ca}_{1.8}\text{Sr}_{0.2}\text{RuO}_4$ at different temperatures, above and below T_O , respectively. It is evident that the lower lying modes, become soft on cooling to T_O , while below the transition temperature the frequency of the soft modes stiffens (Fig. 5.7). Similar to our observations in $\text{Ca}_{1.38}\text{Sr}_{0.62}\text{RuO}_4$ the lowest lying X point mode is clearly splitted in two peaks, both above and below T_O . While the lower lying phonon exhibits the clear soft mode behavior, the frequency of the other one decreases only slightly on cooling, as may be seen in Fig. 5.7. Although one may expect that the twofold degeneracy of the tilt mode is lifted below T_O , the observed splitting of the modes is most likely due to the different stacking periods of the tilt and rotational distortions, as discussed above, and should not be mistaken as the mode associated with the non-condensed component of the order parameter. The reason why we did not observe on the other hand the expected splitting below T_O can be explained in a plausible way by the fact that the mode, which condensates in the low-temperature phase, strongly hardens below T_O . Therefore, the temperature dependence of the observed low frequency mode possibly reflects the behavior of the soft mode, which corresponds to the tilt perpendicular to the tilt which condensates, whereas the frequency of the other mode shows a steep increase and lies already at $T = 200 \text{ K}$ above the highest studied energy transfer of 3.5 THz . This is furthermore supported by the fact that the frequency for the tilt mode in apparent La_2CuO_4 at lowest temperature, amounts already to 3.8 THz , even though the structural deformation is significantly smaller compared to that in $\text{Ca}_{1.8}\text{Sr}_{0.2}\text{RuO}_4$ [51, 149].

While for $x=0.2$ the soft mode condensates almost completely on cooling towards T_O and hardens in the tilt distorted phase, the phase transition in $\text{Ca}_{1.5}\text{Sr}_{0.5}\text{RuO}_4$ leads to only slight changes in the temperature dependence of the tilt mode frequency. Though one observes the expected frequency-softening of this mode with decreasing temperature ($T > T_O$), the frequency does not vanish near the transition temperature but increases upon further cooling. Since $x=0.5$ is close to the critical concentration x_c of the continuous tilt transition, the observed anomalous damping of the soft mode might be caused by related order-disorder effects. This means that under the influences of the formation of only small domains, instead of a long-range distorted structure, the soft-phonon evolves into its low temperature counterpart without exhibiting a complete softening. It is then also plausible that for $\text{Ca}_{1.38}\text{Sr}_{0.62}\text{RuO}_4$ there is no indication of a structural phase transition in the temperature dependence of the phonon modes, although one observes below 100 K the occurrence of tilt superstructure reflections. Furthermore, this agrees with our observation that these reflections are strongly broadened, corresponding to coherence lengths of just a few lattice parameters (see Section 4.4.3). Alternatively, one might argue that the disorder due to Ca-Sr mixing on the same site influences the

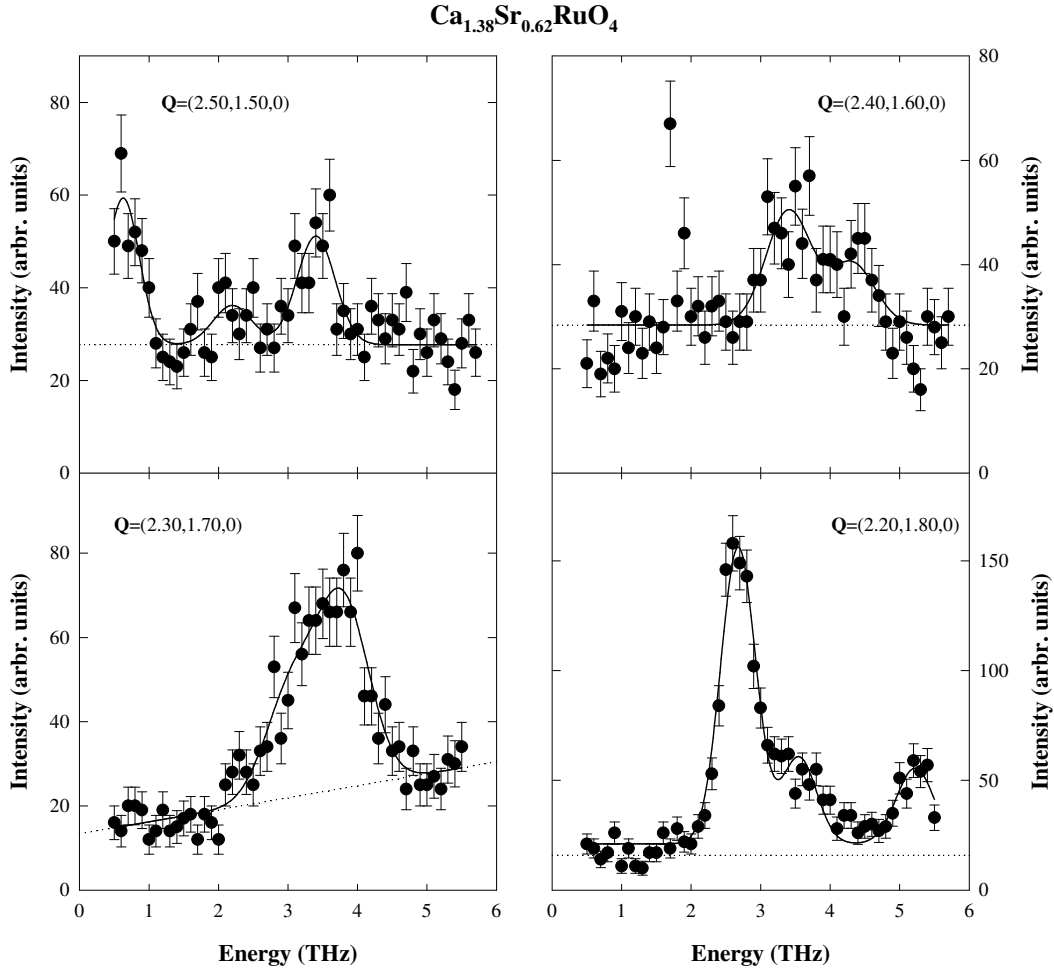


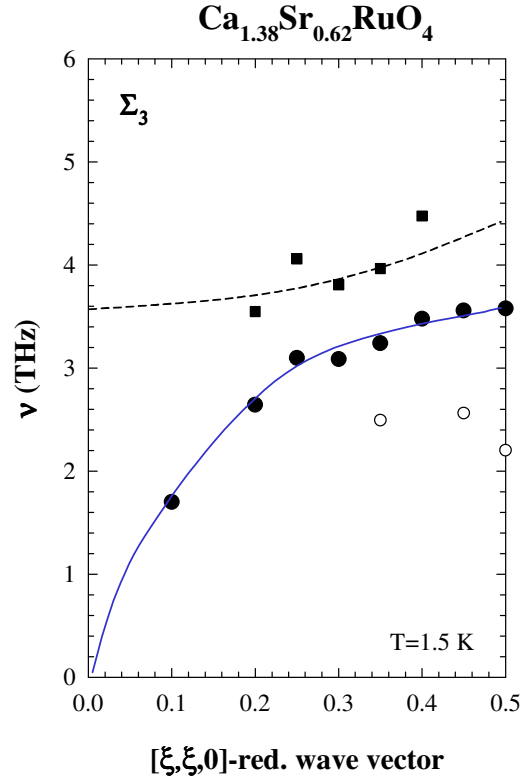
Figure 5.8: Raw energy scans on the rotational modes measured along $[110]$ near the superlattice position $(\frac{5}{2}, \frac{3}{2}, 0)$ in $\text{Ca}_{1.38}\text{Sr}_{0.62}\text{RuO}_4$ at $T = 1.5$ K; lines are fit by gaussian peaks.

tilt transition generating some order disorder character, as observed for the apparent tilt transition in K-doped BaBiO_3 [136]. There, however, the pronounced disorder completely smears out the transition, so that the corresponding critical scattering can be followed up to twice the transition temperature.

5.3 The rotational mode

In addition to the detailed analysis of the soft mode behavior in $\text{Ca}_{2-x}\text{Sr}_x\text{RuO}_4$ which is related to the $I4_1/acd$ to $D\text{-}Pbca$ phase transition we spent some time mapping out the Σ_3 branch in $\text{Ca}_{1.38}\text{Sr}_{0.62}\text{RuO}_4$. In the $I4/mmm$ unit cell this

Figure 5.9: Dispersion of the low lying phonon branches with Σ_3 symmetry in $\text{Ca}_{1.38}\text{Sr}_{0.62}\text{RuO}_4$ at $T = 1.5$ K. The lines are guides to the eye. The corresponding modes can be identified as the transverse acoustic (\bullet) and optical modes (\blacksquare), by comparing their frequencies to the results presented in Fig. 5.1. The open symbols refer to a small signal, which cannot be attributed to any of the phonon branches.



branch ends at the $(\frac{1}{2}, \frac{1}{2}, 0)$ zone boundary in the mode corresponding to the rotation of the RuO_6 octahedra around the c axis. As mentioned in the introduction, the rotational instability in Sr_2RuO_4 is reflected in the softening of these modes. For $\text{Ca}_{1.38}\text{Sr}_{0.62}\text{RuO}_4$ the lowest lying acoustic and optic branches were both obtained from the $(2.5, 1.5, 0)$ reciprocal lattice point at $T=1.5$ K in the $(\zeta, \zeta, 0)$ symmetry direction. The crystal was mounted with the (001) axis horizontal. Some typical constant Q -scans accessible with this configuration are displayed in Fig. 5.8.

The corresponding dispersion curve measured from $(2.50, 1.50, 0)$ to $(2.10, 1.90, 0)$ is shown in Fig. 5.9. At first sight, the transverse acoustic mode and the lowest lying optical mode exhibit conventional behavior with no indication of a steep dispersion as observed for Sr_2RuO_4 , see Fig. 5.1. This is actually expected, because of the rotational distorted structure of $\text{Ca}_{1.38}\text{Sr}_{0.62}\text{RuO}_4$ and the related hardening of the soft mode. However, we detected some additional weak intensity near 2 THz in several scans, which cannot be attributed to any of the phonon branches. It is quite interesting that the character of this contribution is somewhat reminiscent of the softening of the rotational mode in Sr_2RuO_4 towards the zone boundary, as may be seen in Fig. 5.9. The intrinsic nature of this peak was demonstrated by the observation of a signal of similar intensity around symmetry-equivalent points in reciprocal space (e.g., at $(2.5, 1.5, 0)$ and $(1.5, 2.5, 0)$). However, we emphasize that the intensity of this signal is extremely small, so that it seems possible that one deals here with

scattering caused by the substitutional disorder due to the Ca/Sr mixing or it could be possible that the distorted structure of $\text{Ca}_{1.38}\text{Sr}_{0.62}\text{RuO}_4$ accounts for this intensity. Therefore, it seems reasonable to conclude that the shape of the Σ_3 branch in $\text{Ca}_{1.38}\text{Sr}_{0.62}\text{RuO}_4$ is in principle typical of a classical hardening of a phonon spectrum at low energies in connection with a structural phase transition.

Finally, it is worth noting that the absence of any indication of the substitution induced phase transition from $I4_1/acd$ phase ($2c$ rotation) to $Acam$ phase ($1c$ rotation), in the lowest Σ_3 branches is from purely structural considerations fully understandable: Since this transition is expected to be of first order, the corresponding phase transformation might consist in a discontinuous jump of the soft mode, as observed in Pr_2NiO_4 for the first order LTO \rightarrow LTT phase transition [150].

5.4 Summary

The structural phase transition from the tetragonal ($I4_1/acd$) to the orthorhombic structure in $\text{Ca}_{2-x}\text{Sr}_x\text{RuO}_4$ with $0.2 \leq x \leq 0.5$, characterized by the appearance of a tilt of the RuO_6 octahedra, is caused by a typical soft phonon transition at the X point similar to that observed in many perovskite compounds [141, 142, 144–148, 151]. The transition in $\text{Ca}_{1.8}\text{Sr}_{0.2}\text{RuO}_4$ has been clearly observed as an almost complete softening of the tilt phonon on cooling towards T_O , in agreement with a continuous character of the tilt transition. For $x=0.5$, which is close to the composition where the tilt distortion vanishes, the soft phonon does not condensate completely with a non zero frequency at T_O , but the corresponding frequency hardening on cooling signatures still the phase change. Finally, for $x=0.62$, the soft mode dispersion at room temperature indicates that in this sample the tetragonal $I4_1/acd$ structure is marginally stable, and no evidence for the corresponding phase transition in the temperature dependence of the soft-mode frequency was found. We have interpreted these results in terms of a pronounced order-disorder character of the continuous tilt transition close to the critical concentration $x_c = 0.5$.

In addition, we have determined the rotational mode dispersion in the $[110]$ direction for $\text{Ca}_{1.38}\text{Sr}_{0.62}\text{RuO}_4$. While in Sr_2RuO_4 the corresponding branch exhibits steep softening from the Γ point to the zone boundary, our study in the Ca-substituted sample revealed an almost flat dispersion of the lowest lying phonon modes near X . This observation is consistent with the rotational distorted structure of $\text{Ca}_{1.38}\text{Sr}_{0.62}\text{RuO}_4$ and the expected hardening of the corresponding vibrational mode in the distorted phase.

Chapter 6

Quasi-Ferromagnetic Fluctuations in $\text{Ca}_{2-x}\text{Sr}_x\text{RuO}_4$

This chapter deals with our neutron scattering experiments performed on two single crystals of $\text{Ca}_{2-x}\text{Sr}_x\text{RuO}_4$ in order to investigate the inelastic response of this system near the magnetic instability observed for $x_c=0.5$. The excitation spectrum in both samples strongly differs from that found in the spin-triplet superconductor Sr_2RuO_4 which is dominated by incommensurate peaks near $(0.3, 0.3, q_l)$. In $\text{Ca}_{2-x}\text{Sr}_x\text{RuO}_4$, with $x=0.62$ and 0.52 , we find still incommensurate scattering but situated much closer to the zone-center. The low energy scale of the fluctuations and their extent to the zone center suggest that they are intimately related to the strong increase of the low temperature susceptibility. Furthermore, we argue that these fluctuations originate from Fermi surface nesting effects of the d_{xy} sheet, whose influence becomes compared to Sr_2RuO_4 strongly enhanced due to the changed Fermiology and the dominant role of the van Hove singularity.

6.1 Introduction

Shortly after the discovery of superconductivity in Sr_2RuO_4 it was proposed that its superconducting state is formed by spin-triplet p-wave pairing in analogy to suprafluid ^3He [8]. It was suggested that the pairing mechanism arises from strong ferromagnetic spin fluctuations, which was conjectured from the presence of ferromagnetism in the three-dimensional analogue compound SrRuO_3 [152]. While in the meanwhile various experiments provide strong evidence for unconventional superconductivity in Sr_2RuO_4 , as already discussed in chapter 2, no prominent ferromagnetic spin fluctuations has been observed by inelastic neutron scattering measurements [28–30]. Instead these measurements revealed that the magnetic excitation spectrum is dominated by incommensurate spin fluctuations located at $\mathbf{q}_{\text{ic}} = (\pm 0.3, \pm 0.3, 0)$, i.e., far away from the zone center.

These incommensurate spin fluctuations were first predicted by Mazin and Singh within a RPA approach on the basis of the calculated electronic band structure [45, 126]. The Fermi surface of Sr_2RuO_4 , obtained in LDA calculations and observed experimentally by de Haas-van Alphen experiments [16], consists of three sheets

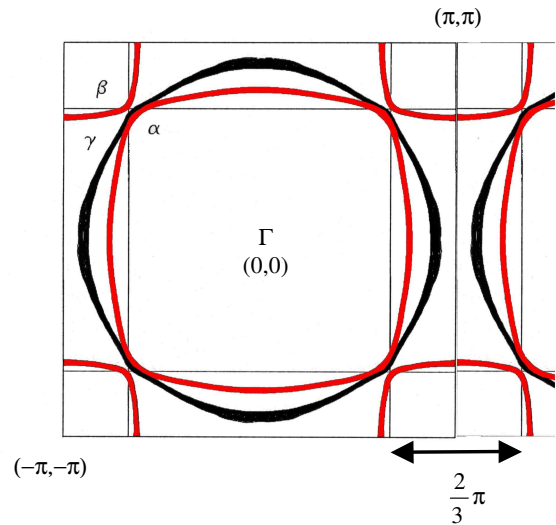


Figure 6.1: The LDA calculated Fermi Surface, taken from Ref. [45]. The two Fermi sheets centered at the Γ point, i.e., γ and β are electron-like, while the α sheet, centered at (π, π) , is hole-like.

which may be regarded as arising from the three Ru t_{2g} orbitals: (i) The $4d_{xy}$ orbital gives rise to a round cylindrical sheet, which is commonly called γ sheet. (ii) In the case of the $4d_{xz}$ and the $4d_{yz}$ orbitals the weak hybridization along the x and y directions, respectively, lead to quasi one dimensional bands which form the almost flat α and β sheets, as shown in Fig. 6.1. The one-dimensionality of the latter two sheets provides an ideal topology for strong Fermi surface nesting effects. Based on the pronounced nesting feature of the α and β sheets, Mazin and Singh predicted the existence of peaks in the real part of the bare susceptibility $\chi_0(\mathbf{q})$. These peaks were calculated at $\mathbf{q}_{\text{ic}} = (\frac{1}{3}, \frac{1}{3}, 0)$ and experimentally confirmed very close to this position, as already mentioned above. Further, the total susceptibility $\chi(\mathbf{q})$ gets enhanced through the Stoner-like interaction which is treated in RPA by:

$$\chi(\mathbf{q}) = \frac{\chi_0(\mathbf{q})}{1 - I(\mathbf{q})\chi_0(\mathbf{q})}, \quad (6.1)$$

with the \mathbf{q} -dependent interaction $I(\mathbf{q})$. Mazin and Singh have shown that the enhancement factor $I(\mathbf{q}_{\text{ic}})\chi_0(\mathbf{q}_{\text{ic}}) = 1.02$ for the nesting positions is only slightly above the critical value, which implies a diverging susceptibility and a magnetic instability at \mathbf{q}_{ic} . And indeed, the temperature and energy dependence of the incommensurate signal indicate that Sr_2RuO_4 appears very close to an incommensurate magnetic ordering [30]. The recent observation of *static* magnetic ordering in only weakly substituted $\text{Sr}_2\text{Ru}_{1-x}\text{Ti}_x\text{O}_4$ with almost identical wave vectors \mathbf{q}_{ic} perfectly confirmed this [153]. The corresponding magnetic ground state, induced by the intrinsic Fermi-surface nesting instability, was identified as a spin-density wave with the ordered moment pointing along c .

The experimental observation of the incommensurate spin fluctuations in Sr_2RuO_4 has raised the question of the relevance of these spin fluctuations to the pairing mechanism in this material. Several theoretical models have been proposed so far which

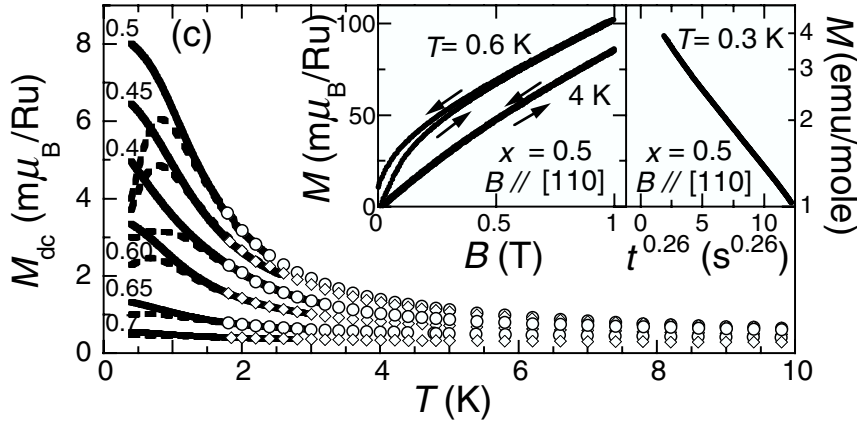


Figure 6.2: Low temperature in-plane magnetic susceptibility of $\text{Ca}_{2-x}\text{Sr}_x\text{RuO}_4$ for $x \geq 0.5$ down to 0.3 K. Solid and broken lines give the results performed in field-cooling (FC) and zero-field-cooling (ZFC) process, respectively. In the inset the field dependence (left) and the relaxation curve (right) of the magnetization M is shown. The data have been taken from Nakatsuji *et al.* [83]

discuss the role of the incommensurate magnetic fluctuations for superconductivity [41–43, 126, 154–156]. Some of these suggests that superconductivity in Sr_2RuO_4 is associated mainly with the ferromagnetic spin fluctuations originating from the γ band, while the incommensurate fluctuations at \mathbf{q}_{ic} do not play a constructive role in the occurrence of spin-triplet superconductivity (cf. chapter 2). From an experimental point of view the question of the magnetic interaction is still of strong interest, since so far the role of the magnetic fluctuations of the γ band has not been experimentally reported. As may be seen in the case of $\text{Sr}_2\text{Ru}_{1-x}\text{Ti}_x\text{O}_4$ it is quite helpful to compare the magnetic excitations in Sr_2RuO_4 to the distinct types of magnetic order which can be induced by substitution. Perhaps, the most suitable system is $\text{Ca}_{2-x}\text{Sr}_x\text{RuO}_4$, which is characterized by a very complex magnetic phase diagram controlled mainly by structural distortions (cf. chapter 4). The end member of this series, Ca_2RuO_4 , is a Mott insulator with an antiferromagnetic ground state, which shows rather different structural properties than his Sr counterpart; in particular the in-plane RuO distances are significantly longer and the RuO_6 octahedra are strongly tilted. Therefore, we think that the antiferromagnetic order in Ca_2RuO_4 is not necessarily relevant for the Sr compound. On the other hand, upon Ca substitution for Sr the macroscopic susceptibility continuously increases pointing to a ferromagnetic instability. Near $x=0.5$ $\chi(T = 2 \text{ K})$ becomes maximal being almost 150 times larger than that of pure Sr_2RuO_4 , with a high Wilson ratio and a critical enhanced electronic specific heat coefficient. More recently Nakatsuji *et al.* have reported the appearance of a ferromagnetic cluster glass below $\sim 1.0 \text{ K}$ for concentrations close to $x = 0.5$ [83]. Figure 6.2 gives the results of their magnetization

measurements for samples with $x \geq 0.5$. While the clear deviation between zero-field cooled and field cooled results for $0.65 < x < 0.50$ below 1.3 K and the field dependence of the magnetization M indicate a ferromagnetic ordering, the time dependence of M demonstrates the glassy nature of the low temperature phase. Hence, for concentrations close to $x=0.5$ $\text{Ca}_{2-x}\text{Sr}_x\text{RuO}_4$ may serve as a promising candidate for the search and the study of the ferromagnetic excitations in layered ruthenates.

6.2 Magnetic Excitations related to the magnetic instability at $x_c=0.5$

6.2.1 Experimentally details

For the experimental study inelastic neutron scattering technique was used. The cross section measured in a magnetic neutron-scattering experiment is related to the pair correlation function between spins, $S(\mathbf{Q}, \hbar\omega)$. According to the fluctuation-dissipation theorem [157], $S(\mathbf{Q}, \hbar\omega)$ is proportional to the imaginary part, $\chi''(\mathbf{Q}, \hbar\omega)$, of the wave vector and energy dependent dynamical spin susceptibility $\chi(\mathbf{Q}, \hbar\omega)$. Thus, the neutron cross section for a paramagnet, such as the samples under investigation at the studied temperatures, can be written as

$$\frac{d^2\sigma}{d\Omega d\omega} = \frac{k_f}{k_i} r_0^2 \frac{2F^2(\mathbf{Q})}{\pi g^2 \mu_B^2} \frac{\chi''(\mathbf{Q}, \hbar\omega)}{1 - \exp(-\hbar\omega/k_B T)} \quad (6.2)$$

where $r_0^2 = 0.292$ barn, $g \simeq 2$ is the Landé factor, \mathbf{k}_i and \mathbf{k}_f are the incident and final neutron wave vectors, and $F(\mathbf{Q})$ is the magnetic form factor. Compared to other experimental techniques which probe the magnetic properties of solids, inelastic magnetic neutron scattering is rather unique since it permits the study over a broad range of momentum and energy transfers. For example the bulk susceptibility measured with a magnetometer is restricted to the small-wavenumber limit, $\mathbf{Q} = 0$, of $\chi'(\mathbf{Q}, \hbar\omega = 0)$, and the nuclear resonance techniques probe only the low energy spin fluctuations of $\chi''(\mathbf{Q}, \hbar\omega \rightarrow 0)$ averaged over momenta \mathbf{Q} .

Most of the inelastic neutron scattering experiments have been carried out on a single crystal of $\text{Ca}_{2-x}\text{Sr}_x\text{RuO}_4$ with $x=0.62$, since only this sample had a large crystal volume (cf. Table 3.1). Additional measurements have been performed on two quite small single crystals with $x=0.52$ which were mounted together and coaligned using individual goniometers, permitting an alignment with a total mosaic spread smaller than 0.6° . For consistency with previous work on Sr_2RuO_4 , we use in this chapter the crystallographic nomenclature pertaining to space group $I4/mmm$ and wave vectors are given in reduced lattice units in units of $2\pi/a = 1.68 \text{ \AA}^{-1}$ and $2\pi/c = 0.50 \text{ \AA}^{-1}$. Furthermore, we use the notation $\mathbf{Q} = \mathbf{q} + \tau$, with \mathbf{Q} the scattering vector, \mathbf{q} the propagation vector, and τ a reciprocal lattice vector. The inelastic data

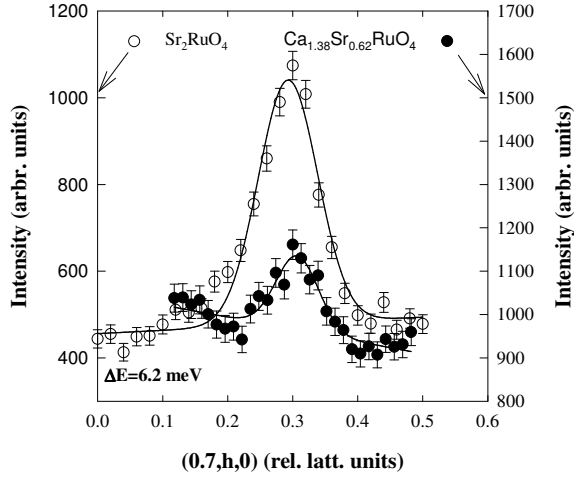


Figure 6.3: Constant-energy scans across the nesting position $\mathbf{Q}_{ic} = (0.7, 0.3, 0)$ along the $[010]$ direction at low temperature for Sr_2RuO_4 (taken from Ref. [30]) and $\text{Ca}_{1.38}\text{Sr}_{0.62}\text{RuO}_4$. The data have been normalized to the intensity of a transverse acoustic phonon, for comparison. The lines represent fits with Gaussians.

were collected on the thermal triple axis spectrometer 1T.1, with fixed final neutron energy of $E_f = 14.7$ meV. As already discussed in section 3.2.3 the broad ΔQ width of the observed signals allowed us to open the diaphragms determining the beam more widely than usually ($\simeq 98$ mm for the diaphragm in front of the analyzer and $\simeq 26$ mm for that in front of the detector), in order to gain counting statistics. The samples were mounted in most experiments with $[001]$ vertical, so that the entire two dimensional in-plane reciprocal lattice could be studied.

6.2.2 Evidence for strong magnetic fluctuations close to the zone center

When we began our experiments on $\text{Ca}_{1.38}\text{Sr}_{0.62}\text{RuO}_4$, we knew that the most intense magnetic fluctuations in parent Sr_2RuO_4 were located at $\mathbf{Q}_{ic} = \mathbf{q}_{ic} + \mathbf{G}$, where \mathbf{G} is a reciprocal lattice vector and $\mathbf{q}_{ic} = (0.3, 0.3, q_l)$. On the other hand the critical enhanced magnetic susceptibility at $x=0.5$ pointed toward a ferromagnetic instability, which should in general give rise to a sizable magnetic response at the two-dimensional zone center (100) (note that in the basic space-group $I4/mmm$ (100) is not a zone-center, but a reciprocal lattice point of a single RuO_2 layer). In order to discover the dominant features in the magnetic excitation spectrum of $\text{Ca}_{1.38}\text{Sr}_{0.62}\text{RuO}_4$ we performed extensive measurements close to the corresponding reciprocal lattice points in the $(h, k, 0)$ plane.

First, we compare in Fig. 6.3 scans across the incommensurate spot $\mathbf{Q}_{ic} = (0.7, 0.3, 0)$ at a constant energy transfer of 6.2 meV for Sr_2RuO_4 and for the Ca substituted compound. These scans demonstrate that the incommensurate signal related to the Fermi surface nesting of the α and β sheets survives in $\text{Ca}_{1.38}\text{Sr}_{0.62}\text{RuO}_4$, but is reduced by a factor of $\simeq 3$ relative to that in Sr_2RuO_4 . In contrast to this pronounced intensity reduction, the fitted peak position and width of the signal in $\text{Ca}_{1.38}\text{Sr}_{0.62}\text{RuO}_4$ show almost no differences to the values for Sr_2RuO_4 reported in Ref. [28, 30].

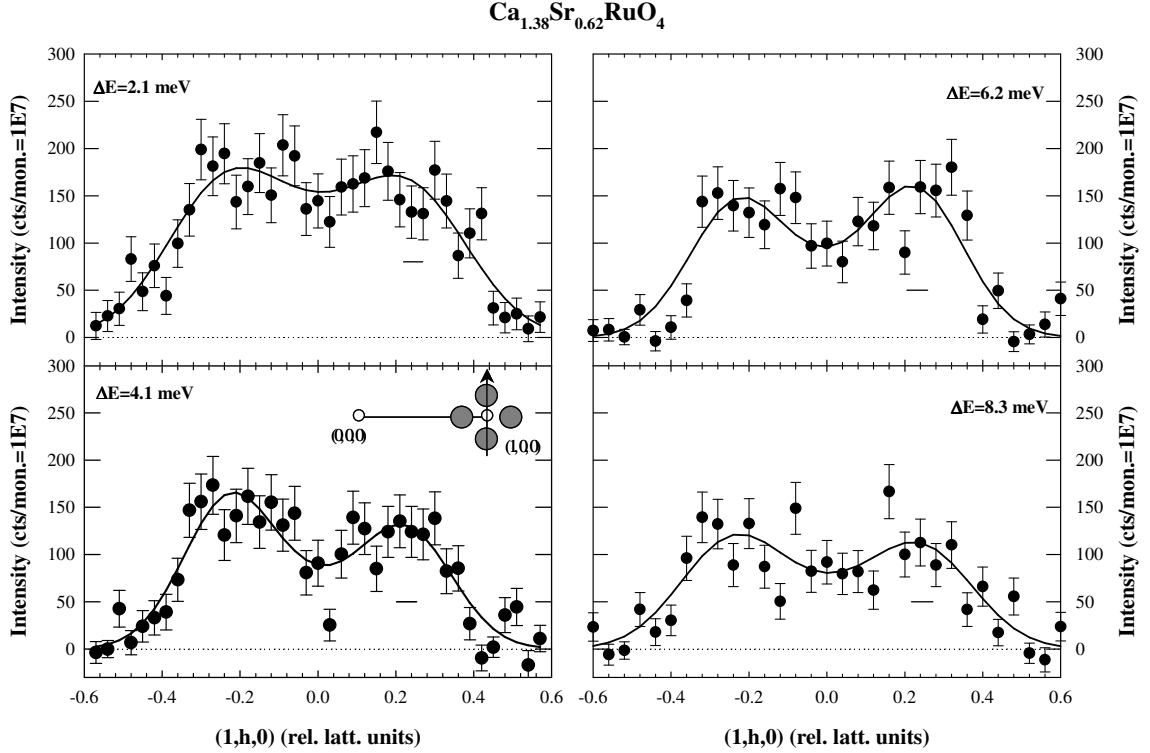


Figure 6.4: Constant-energy scans performed at different energy transfers around $\mathbf{Q} = (1, 0, 0)$ along the $[0, 1, 0]$ direction at $T=1.5$ K. The scattering angle dependent background was subtracted for clarity. The horizontal bars indicate the spectrometer resolution. The solid lines are fits to Gaussian functions (for details see Fig. 6.7 and text). The data were acquired with monitor 1E7, which corresponds to a counting time of approximately 7 min at 4.1 meV.

In contrast strong scattering has been observed in $\text{Ca}_{1.38}\text{Sr}_{0.62}\text{RuO}_4$ near (100) . Figure 6.4 shows corresponding \mathbf{Q} scans collected along the $[010]$ direction with energy transfers of 2.1, 4.2, 6.2, and 8.3 meV at 1.5 K. In all scans a clear double peak structure was observed, with peaks at the *incommensurate* positions $\mathbf{Q}_\eta = (1, \pm 0.22(2), 0)$. Interestingly, the peak position in these scans does not depend on energy. The observed peaks are strongly broadened in respect to the experimental resolution. Fits to the data by Gaussian profiles¹ give intrinsic ΔQ -widths (full width at half maximum) of 0.45 \AA^{-1} , which does not change significantly with energy transfer. These peak widths are much larger than that reported for the magnetic excitations in Sr_2RuO_4 at \mathbf{q}_{ic} , with $\Delta Q = 0.13 \text{ \AA}^{-1}$ [28], indicating that the corresponding correlations are extremely short-ranged. Concerning the peak amplitudes,

¹Note that we have taken always account of the four spots, by superposition of several Gauss peaks (see below).

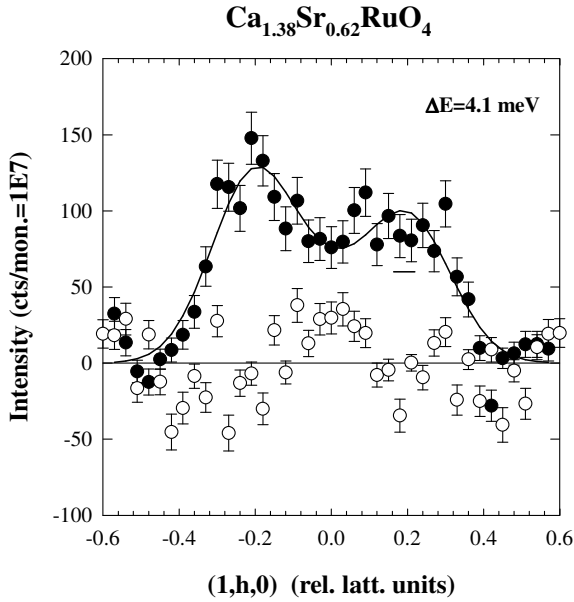


Figure 6.5: Constant-energy scans performed at $\Delta E = 4.1 \text{ meV}$ around $\mathbf{Q}=(1,0,0)$ along the $[0, 1, 0]$ direction at $T=1.5 \text{ K}$ (\bullet) and $T=295 \text{ K}$ (\circ). The scattering angle dependent background was subtracted for clarity. The horizontal bar indicates the spectrometer resolution.

the signal at \mathbf{Q}_η in $\text{Ca}_{1.38}\text{Sr}_{0.62}\text{RuO}_4$ is by a factor of $\simeq 4$ stronger than the corresponding incommensurate spot at $(0.7, 0.3, 0)$ shown in Fig. 6.3. In addition to the rather large ΔQ widths of the signal at \mathbf{Q}_η , this indicates that a huge part of spectral weight is concentrated close to $(1, 0, 0)$, which may be considered as a zone-center of the two-dimensional lattice.

The intrinsic nature of these peaks was demonstrated by the observation of similar intensity around the symmetry related $(0, 1, 0)$ point. Furthermore, the intensity at $\mathbf{Q} = (1, \pm 0.22(2), 0)$ has already disappeared at room-temperature, see Fig. 6.5, demonstrating that the scattering is not related to simple lattice vibrations, for which an increase of the intensity with temperature would be expected. We will come back to this point when discussing the temperature dependence of the incommensurate signal in more detail in one of the following sections.

Unfortunately, the study of the extent of the signal in the $(h, k, 0)$ plane of the reciprocal space proved to be very difficult, due to a strong and Q dependent background contribution, which gets significantly enhanced for small scattering angles. This background arises from the instrumental setup of the utilized triple-axis spectrometer and does not stem from the sample, as we have identified by performing scans without the sample. From these scans one determines an increase of the instrument background towards lower scattering angles from $\simeq 2 \text{ cts/min}$ at $Q = 1.66 \text{ \AA}^{-1}$ (corresponds to $\mathbf{Q} = (1, 0, 0)$), to $\simeq 20 \text{ cts/min}$ at $Q = 1.00 \text{ \AA}^{-1}$ (corresponds to $\mathbf{Q} = (0.6, 0, 0)$) for an energy-transfer of $\Delta E = 4.1 \text{ meV}$. Usually the measured background with a triple-axis spectrometer is considerably less than 1 ct/min including sample-induced effects [71]. In our particular case the origin of the additional background is most likely due to fast neutrons ($E_0 \geq 200 \text{ meV}$) and the appropriate scattering geometry with relative low scattering angles. The high-energy neutrons,

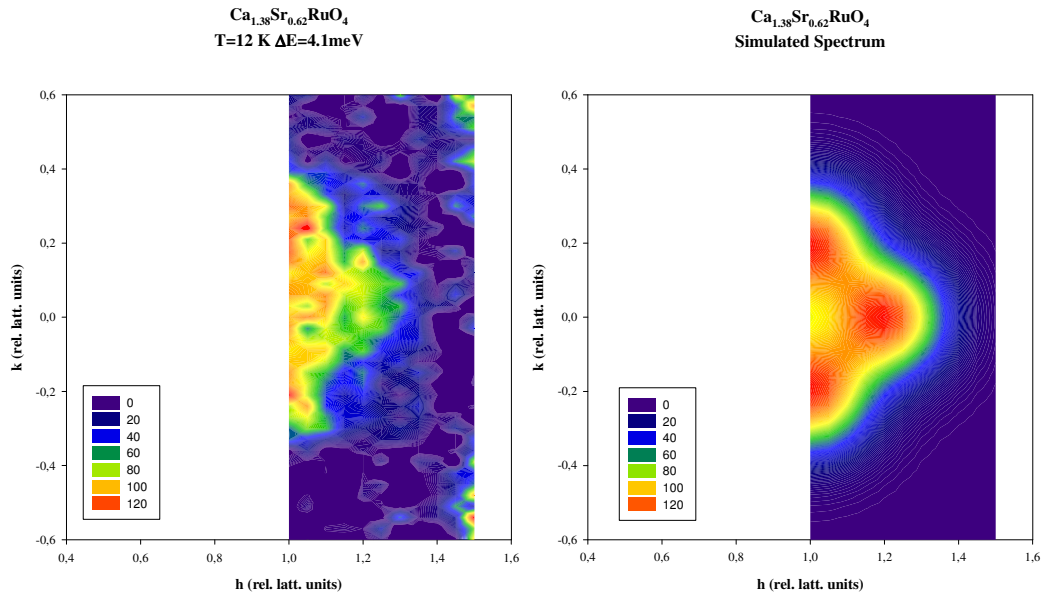


Figure 6.6: *Left:* Contour plot of the measured excitation near $\mathbf{Q} = (1, 0, 0)$ in $\text{Ca}_{1.38}\text{Sr}_{0.62}\text{RuO}_4$ at $T=12\text{ K}$ and at an energy transfer of 4.1 meV . Due to the enhanced background contribution at lower scattering angles the scans were restricted to Q -values larger than 1.66 \AA^{-1} . For clarity the background has been subtracted and the data has been corrected for the magnetic form factor of Ru^+ [120]. *Right:* Schematic representation of the excitation, assuming four peaks at $(1 \pm \eta, 0, 0)$ and at $(1, \pm\eta, 0)$ with Gaussian profiles and the experimentally determined results.

which are always present in the incident beam, can proceed almost unhindered the sample environment and may pass also the beam stop. While for common Q - and ΔE -values the contribution of fast neutrons to the background is at an insignificant level, since their path never crosses the detector, it becomes more and more important at lower scattering angles. For small Q -values one of the detector flanks approaches the undeviated beam and a significant proportion of high-energy neutrons can enter the counter in spite of the detector shielding, forming the observed background. This consideration was, furthermore, confirmed by measuring the background with the analyzer crystal rotated 5° away from the Bragg condition, leading to no significant reduction of the background signal. Due to the rather weak intensity of the studied signal and the limited crystal volume this troublesome background contribution prevented a more detailed analysis of the incommensurate fluctuations in $\text{Ca}_{1.38}\text{Sr}_{0.62}\text{RuO}_4$ towards lower scattering angles.

In order to avoid this problem we tried to extend our analysis to symmetry-equivalent points in reciprocal space, like for example $\mathbf{Q} = (3, 0, 0)$ or $(2, 1, 0)$ (note that $(2, 0, 0)$ and $(1, 1, 0)$ are strong Bragg reflections, in whose proximity a strongly enhanced background for the performed inelastic scans at low energy is expected).

But no residual intensity could be observed around these reciprocal lattice points for different energy transfers. This observation is consistent with the decrease of the Ru magnetic form factor as function of Q [121], providing strong evidence for the magnetic nature of the observed excitations. Finally, the extent of the incommensurate signal in the $(h, k, 0)$ plane of the reciprocal space could be established by mapping out the intensity for $(Q_x, Q_y, 0)$ with $1.0 \leq Q_x \leq 1.5$ and $-0.6 \leq Q_y \leq 0.6$ at $T=12$ K and at a constant energy transfer of 4.1 meV. The data collected under these conditions is shown in Fig. 6.6 after subtraction of the scattering angle dependent background and after correction for the magnetic form factor of Ru^+ [120]. From these scans it now becomes clear that the intensity distribution in $\text{Ca}_{1.38}\text{Sr}_{0.62}\text{RuO}_4$ consists of four single peaks, which are symmetrically distributed around $\mathbf{Q} = (1, 0, 0)$ at the incommensurate wave vector $\mathbf{q}_\eta = (0.22(2), 0, 0)$ (note that the existence of the peak at $(1 - 0.22(2), 0, 0)$ can be deduced from simple symmetry arguments). Since the four peaks at $\mathbf{q}_\eta = (0, \pm 0.22(2), 0)$ and $\mathbf{q}_\eta = (\pm 0.22(2), 0, 0)$ are rather broad, they overlap and have significant extension to $\mathbf{q} = (0, 0, 0)$. Compared to this strong scattering around the zone-center, the intensity at the incommensurate position $\mathbf{q}_{ic} = (0.3, 0.3, 0)$ related to the Fermi surface nesting effect of the α and β bands is extremely weak, as may be seen from the mapping depicted in Fig. 6.6. Also, one can recognize some additional weak intensity around $(1.5, \pm 0.5, 0)$ which, however, is mainly related to phonon scattering, as we infer from the strong intensity increase upon heating. Most probably this phononic contribution can be attributed to the rotational mode (cf. chapter 5). This contribution makes its very difficult to estimate the existence of hypothetical low-energy excitations with wave vector close to $(\frac{1}{2}, \frac{1}{2}, 0)$, i.e. the ordering wave vector of the two dimensional antiferromagnetic state. Nevertheless, from Fig. 6.6 it can be excluded that these excitations (if present) have a similar intensity distribution as those at the zone center.

Before we proceed, some general remarks about the data treatment have to be made. Most of the measurements were performed by purely transverse scans through $\mathbf{Q} = (1, 0, 0)$ in $[010]$ direction, as schematically indicated in Fig. 6.7. Due to the rather large ΔQ -width of the peaks, the collected data of these scans should be interpreted as a superposition of the two peaks which lie on the $(0, h, 0)$ axis in scan direction and the two surrounding peaks at $\mathbf{Q}_\eta = (1 \pm \eta, 0, 0)$ in perpendicular direction. In order to take account of these different contributions, we have fitted the data by the following simple model:

$$I(\mathbf{Q} = (1, h, 0), \hbar\omega) = y_0 + m \cdot h + y(|\mathbf{Q}|) + I_\eta e^{-\frac{1}{2}(\frac{h-\eta}{\sigma})^2} + I_{-\eta} e^{-\frac{1}{2}(\frac{h+\eta}{\sigma})^2} + (I_\eta + I_{-\eta}) e^{-\frac{1}{2}\frac{(h^2+\eta^2)}{\sigma^2}} \quad (6.3)$$

where $y_0 + m \cdot h$ represents the constant or slopping sample background intensity and $y(|\mathbf{Q}|)$ is the scattering angle dependent instrument background contribution. While y_0 and m were refined independently during each fitting procedure, $y(|\mathbf{Q}|)$ was determined from a fit to all scans performed at the lowest temperatures. The next two terms in Eq. (6.3) correspond to the Gaussian profiles of the two peaks which

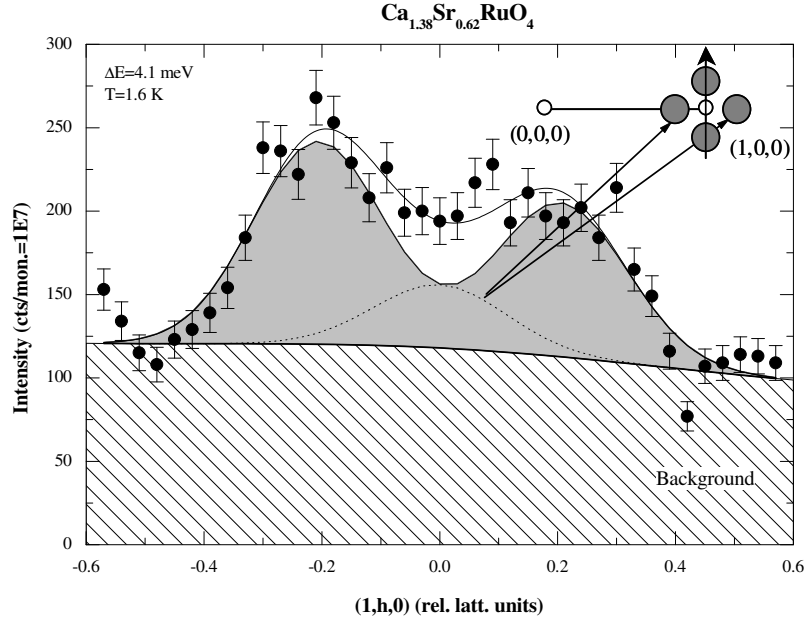


Figure 6.7: Raw constant-energy scan across $\mathbf{Q} = (1, 0, 0)$ at an energy transfer of 4.1 meV and at $T=1.5 \text{ K}$. Exemplarily, we show the separate contributions we have applied to fit the experimental data: (i) the background, consisting of a scattering angle dependent and a constant part (hatched area) (ii) the contribution from the symmetry related positions $\mathbf{Q}_\eta = (1 \pm 0.2, 0, 0)$, due to the broad nature of the signal (dashed line), and (iii) the two peaks at $\mathbf{Q}_\eta = (1, \pm 0.2, 0)$ in scan direction, fitted by a Gaussian peak distribution (grey area). The schematic drawing of the reciprocal space indicates the position of the fluctuations around $\mathbf{Q} = (1, 0, 0)$.

lie in scan direction. Since these peaks are distributed almost symmetrically around $\mathbf{Q} = (1, 0, 0)$, we assumed an unique \mathbf{Q} -position, $\mathbf{Q} = (1, \pm\eta, 0)$ with an identical η parameter and identical ΔQ -widths σ . The last term in Eq. (6.3) describes the contribution to the scattered intensity at $\mathbf{Q} = (1, h, 0)$ which originates from the two peaks perpendicular to the scan direction due to their significant extension to the scan path. Here again we assumed that the excitation intensity is peaked at the four equivalent positions $\mathbf{Q} = (1 \pm \eta, 0, 0)$ and $\mathbf{Q} = (1, \pm\eta, 0)$ with comparable amplitudes. The contribution of each of these terms to the fit of the data is illustrated in Fig. 6.7. In addition to this fitting model the measured intensities were corrected for the improper monitor normalization in the constant- \mathbf{Q} , final Energy fixed mode. In this mode the presence of harmonics in the incident beam and the fact that the harmonic content changes significantly with the incident energy yield to an improper normalization of the monitor for various incident energies. We corrected for this effect by the following empirical formula: $f(k_i) = 1 - z_1 \exp(-z_2 k_i^2 + z_3 k_i^4)$, with k_i the incident energy in \AA^{-1} and $z_1 = 1.0944$, $z_2 = 0.1390 \text{ \AA}^2$, and $z_3 = -0.0037 \text{ \AA}^4$.

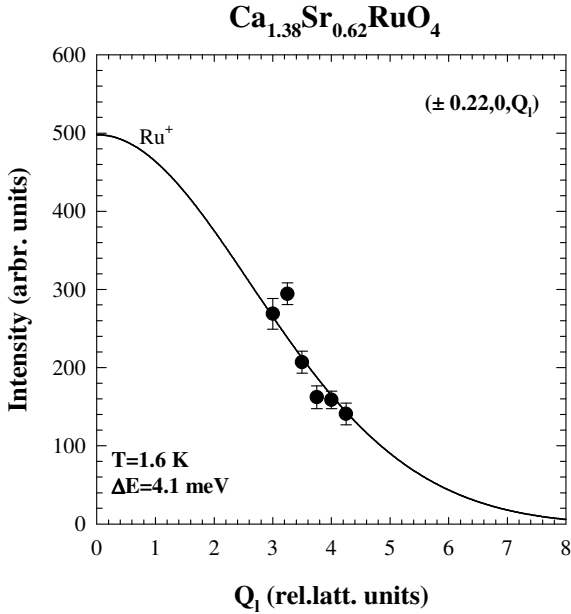


Figure 6.8: Amplitude of the incommensurate signal as function of Q_l at $\Delta E = 4.1$ meV and $T=1.6$ K, as obtained from scans along the [100] direction around $\mathbf{Q} = (0, 0, Q_l)$. The given amplitudes are derived from the corresponding peaks at $(\pm 0.22, 0, Q_l)$ by averaging of the two extracted peak heights. The solid line corresponds to the square of the Ru^+ magnetic form factor.

Making use of the described fitting model a quantitative analysis of the measured data is now possible. Let us first discuss the intensity variation of the incommensurate signal along \mathbf{c}^* , which was obtained from scans along the [100] direction around $\mathbf{Q} = (0, 0, Q_l)$ for different fixed values of Q_l at an energy transfer of 4.1 meV. For these measurements the crystal was aligned with the (100) and (001) axes in the scattering plane of the spectrometer. As may be seen in Fig. 6.8 the peak amplitude decreases continuously by varying Q_l in a range between 3 and 4.25 r.l.u. The decrease of the signal agrees rather well with the dependence expected from the Ru^+ magnetic form factor, indicating the magnetic origin of the scattering observed around the zone center.

Let us now consider the energy dependence of the peak amplitudes, which are according to Eq. (6.2) proportional to the imaginary part of the dynamical spin susceptibility $\chi''(\mathbf{Q}, \hbar\omega)$ at $\mathbf{Q}_\eta = (1, \pm 0.22(2), 0)$. Figure 6.9 gives the results of the corresponding fits to the data, which were measured for different transferred energies between 2.1 and 8.3 meV at $T=1.6$ K (see Fig. 6.4). In the studied energy range the intensity decreases slightly with increasing ω , implying a strong spectral response even at low energies. We have fitted this energy dependence by a single relaxor behavior

$$I(\mathbf{Q}_\eta, \hbar\omega) \sim \chi''(\mathbf{Q}_\eta, \hbar\omega) = \chi'(\mathbf{Q}_\eta, 0) \frac{\Gamma\omega}{\Gamma^2 + \omega^2} \quad (6.4)$$

which relates according to the Kramers-Kronig relation the imaginary part $\chi''(\mathbf{Q}_\eta, \hbar\omega)$ of the generalized dynamical susceptibility with the corresponding real part $\chi'(\mathbf{Q}_\eta, 0)$ at $\hbar\omega = 0$ [158]. For the characteristic damping energy we find $\Gamma = 2.8 \pm 0.2$ meV, which is much less than 9 meV reported for the incommensurate spin fluctuations in

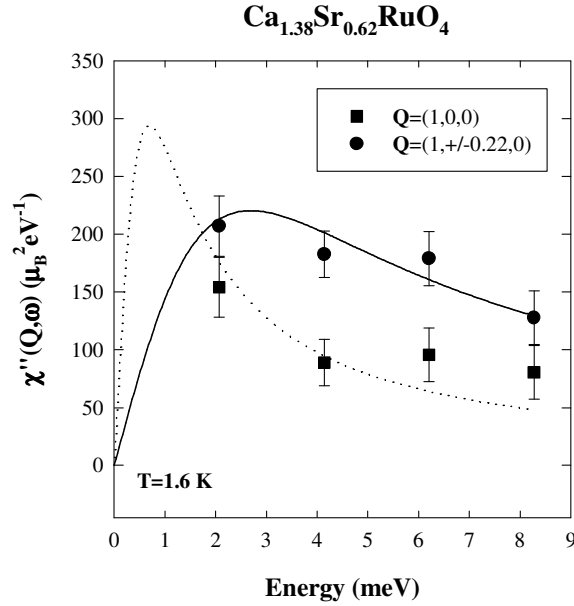


Figure 6.9: Energy dependence of the averaged peak amplitude of the incommensurate signal and the corresponding extension to $\mathbf{Q} = (1, 0, 0)$. The solid line represents a fit with a single relaxor as described in the text, while the broken line is calculated by Eq. (6.4) with a $\chi'(\mathbf{Q} = 0, 0)$ which correspond to the reported enhancement of the uniform low temperature susceptibility of about a factor 60 compared to that of Sr_2RuO_4 with $\chi'(\mathbf{Q} = 0, 0) = 30 \mu_B^2 \text{eV}^{-1}$ [2, 67].

Sr_2RuO_4 , indicating that $\text{Ca}_{1.38}\text{Sr}_{0.62}\text{RuO}_4$ is extremely close to a magnetic instability at $\mathbf{q}_\eta = (\pm 0.22, 0, 0)$, in spite of the rather broad Δq width of the peaks.

Furthermore, it appears most likely that the observed fluctuations are responsible for the dramatic enhancement of the *static* susceptibility in $\text{Ca}_{2-x}\text{Sr}_x\text{RuO}_4$ close to $x_c = 0.5$. Qualitatively this is quite easy to understand, because the intensity distribution of the signal at $\mathbf{q}_\eta = (\pm 0.22, 0, 0)$ and $\mathbf{q}_\eta = (0, \pm 0.22, 0)$ is extremely broad in \mathbf{q} space, with a significant contribution to zone-center $\mathbf{q} = (0, 0, 0)$, as illustrated in Fig. 6.9. However, to make an accurate evaluation of the contribution of the excitations to the static susceptibility the scattered intensity $I(\mathbf{Q}, \hbar\omega)$ has to be put on an absolute scale. A first rough estimation of the absolute value of $I(\mathbf{Q}, \hbar\omega)$ can be given by comparing the intensity of the incommensurate signal at \mathbf{q}_{ic} of $\text{Ca}_{1.38}\text{Sr}_{0.62}\text{RuO}_4$ to that of Sr_2RuO_4 (see Fig. 6.3), for which $I(\mathbf{q}_{\text{ic}}, \hbar\omega)$ have been determined on an absolute scale in Ref. [67]. Normalizing the data by this procedure, it is possible to compare the observed spectral response with that expected from the static susceptibility reported by Nakatsuji *et. al* [2]. This is illustrated in Fig. 6.9 by the broken line under the additional assumption that the spectral response at $\mathbf{Q} = (1, 0, 0)$ can be described following Eq. (6.4). The agreement between the observed neutron scattering spectrum and the calculated curve

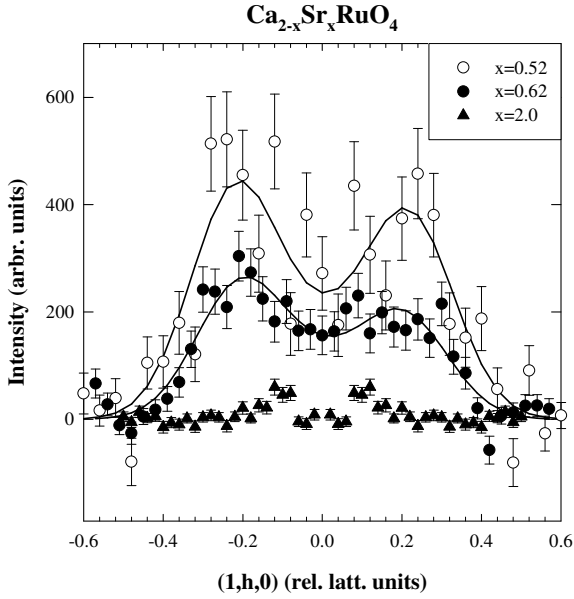


Figure 6.10: Comparison of the inelastic signal around $\mathbf{Q} = (1, 0, 0)$ in $\text{Ca}_{2-x}\text{Sr}_x\text{RuO}_4$ for $x=2.0$, 0.62 , and 0.52 at an energy transfer of 4.1 meV ($x=2.0$ and 0.62) and 2.1 meV ($x=0.52$). For comparison, the data were normalized to the intensity of a transverse acoustic phonon and the background have been subtracted. The data for the pure compound ($x=2.0$) was taken from Ref. [159].

in the covered energy range is quite satisfactory. This indicates that the low-energy excitations may account also quantitatively for the macroscopic static susceptibility. However, agreement is achieved only with a rather low damping energy, yielding to a strong increase of the scattered intensity below 2 meV. It is noted, that such a large intensity increase at $\mathbf{Q} = (1, 0, 0)$ is still consistent with the simultaneous signal reduction at $\mathbf{Q}_\eta = (1, \pm 0.22(2), 0)$ and $\mathbf{Q}_\eta = (1, \pm 0.22(2), 0)$, due to the observed broadening of the incommensurate signal for energy transfers smaller or in the order of the studied thermal energy $k_B T$, as will be discussed in the next section. Unfortunately, the measurements could not be extended to the lower-energy side because of contaminations by incoherent scattering. In view of this problem, a detailed analysis of the excitation spectrum for small energy transfers ($\Delta E \leq 2$ meV) using a cold-triple axis spectrometer would be highly desirable. The presence of an optical phonon mode at about 14 meV prevented on the other hand a more detailed analysis up to higher energies.

Another important point, supporting our idea that the origin of the enhanced low temperature macroscopic susceptibility is attributable to the observed low-energy fluctuations, is the fact that the incommensurate signal increases significantly with Ca substitution when approaching the critical concentration $x_c=0.5$ (cf. Fig. 4.1). This is illustrated in Fig. 6.10, which shows constant energy scans across $\mathbf{Q} = (1, 0, 0)$ for $\text{Ca}_{2-x}\text{Sr}_x\text{RuO}_4$ with $x=2.0$, 0.62 , and 0.52 , respectively. While for the pure Sr compound one does not find any signal distinguishable from background, the two Ca substituted samples show both the strong and broad incommensurate signal near $\mathbf{Q}_\eta = (1, \pm 0.2, 0)$. Comparing the signals for $x=0.52$ and $x=0.62$ a clear intensity increase with Ca substitution can be deduced in agreement with the reported enhancement of the low temperature susceptibility. Within the statistical errors, the

peak widths and positions are the same for the two samples.

6.2.3 The temperature dependence of the incommensurate signal

In the previous section we have reported the existence of strong incommensurate fluctuations at low temperatures located symmetrically around the two-dimensional ferromagnetic zone-center $(1, 0, 0)$. These fluctuations were followed also as a function of temperature at several energy transfers. Figure 6.11 shows representative constant energy scans through the incommensurate peaks for two values of energy transfer at five different temperatures. At lowest temperatures, the two peaks associated with the incommensurate fluctuations are clearly separable, despite their rather large ΔQ -width. With increasing temperature the peaks broaden significantly and merge together, while the intensity of the signal disappears gradually. At room temperature the signal is already indistinguishable from the background in the studied energy range up to 8.3 meV. However, the most important and unusual effect of the data is that the peak broadening at a fixed temperature is much more pronounced at low than at high energy transfers. This effect can be seen for example at intermediate T values by comparing the scans in Fig. 6.11: While at $T = 60$ K (which converts to an energy of $k_B T = 5.2$ meV) and a fixed energy transfer of 8.3 meV still a double peak structure is visible, the equivalent data at $\Delta E = 4.1$ meV show only one broad intensity profile. Besides this interpretation of the temperature evolution of the peak shape as a *melting* of the incommensurate fluctuations, an alternative description of our data could be obtained by assuming that upon heating the incommensurate peaks exhibit no broadening, while an additional broad peak at the zone center $(1, 0, 0)$ compensate for the intensity loss. This would indicate a crossover in the nature of the low energy magnetic correlations from incommensurate fluctuations at low temperatures to purely ferromagnetic fluctuations at high temperatures. However such a change in the nature of magnetic fluctuations is very unlikely, since one should expect it to be reflected in the temperature dependence of macroscopic properties, for which no indication has been found [2, 3].

So far, we have given a qualitative survey of the temperature dependence of the incommensurate fluctuations. In order to analyse the critical behaviors of the amplitudes and widths of the peaks more precisely, we have fitted our data by the model described by Eq. 6.3. Since our findings point to a broadening of the peaks with almost no changes of the incommensurate positions, all fitting procedures were conducted with η fixed to its low temperature value of 0.22(2). With this minimal set of parameters (note that only I_η and σ were adjusted to describe the observed peak profiles) a satisfactory description for all studied ω and T values is achieved. The solid lines in Fig. 6.11 denote the corresponding fit results.

In Fig. 6.12 we summarize the temperature evolution of the inelastic response at

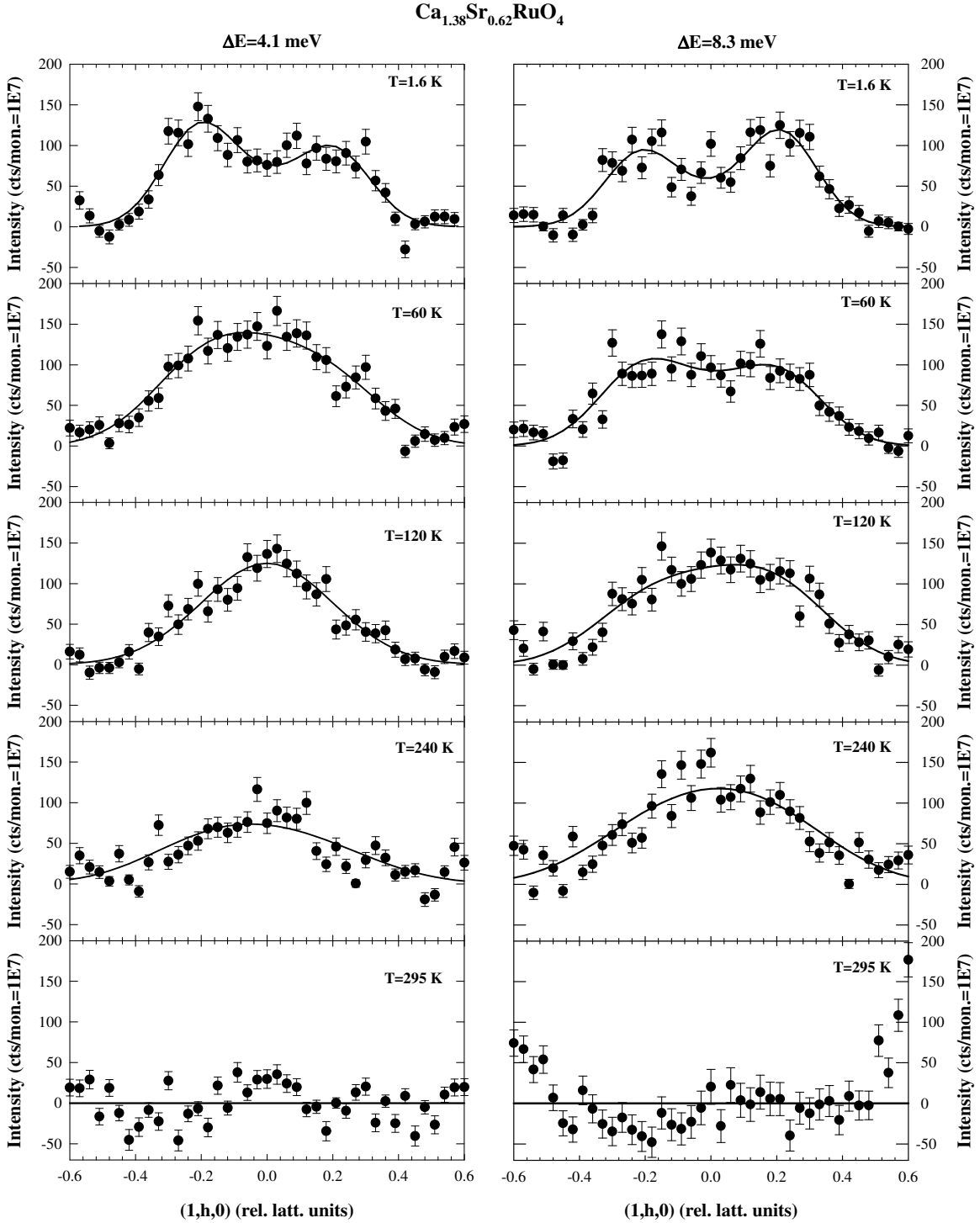


Figure 6.11: Scans along the $[010]$ direction around $\mathbf{Q} = (1, 0, 0)$ at an fixed energy transfer of 4.1 meV (left) and 8.3 meV (right), for five different temperatures: 1.5, 60, 120, 240, and 295 K. Solid lines denote fits with Gaussian as described in the text. For clarity, the background has been subtracted for each scan.

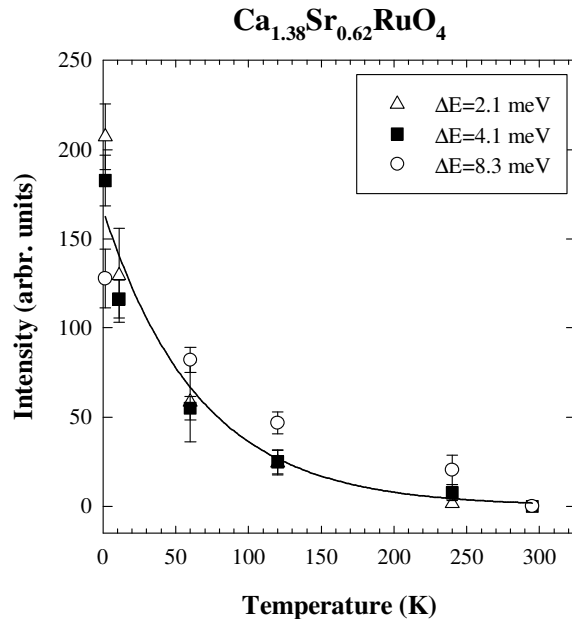


Figure 6.12: Temperature dependence of the averaged peak amplitudes at various fixed energy transfers, after correction by the Bose factor, $n(\omega) + 1 = (1 - \exp(-\hbar\omega/k_B T))^{-1}$ and subtraction of the background. The lines serve as guide to the eye.

the incommensurate peak position for various fixed energy transfers. The peak amplitudes decrease strongly with increasing temperature (note that the data has been corrected for the Bose factor, so that the given values are directly proportional to $\chi''(Q_\eta, \hbar\omega)$). However, still more pronounced is the effect of temperature on the ΔQ width of the incommensurate peaks, which is illustrated in Fig. 6.13. While at lowest temperature ($T=1.6$ K) we observe an energy-independent peak width, the raise of temperature causes a drastic broadening, which varies systematically with energy. For an energy transfer of $\Delta E = 2.1$ meV the spectra at $\mathbf{Q} = (1, \pm 0.22(2), 0)$ broadens dramatically upon heating, whereas the effect of broadening decreases gradually with increasing energy transfer. This behavior suggests that the data can be described in terms of a $\Delta E/k_B T$ dependency. Indeed, when plotted against $\Delta E/k_B T$ (see right part of Fig. 6.13) all of the data fall on a single curve with a simple exponential form, as indicated by the semi-logarithmic scale in the inset of Fig. 6.13. Moreover, it turns out that the peak width starts to diverge for thermal energies $k_B T \geq \Delta E$; as a consequence the magnetic correlation length strongly decreases if the thermal energy $k_B T$ overpasses the energy transfer. This behavior is in striking contrast to the reported $\Delta E/k_B T$ scaling concepts of the magnetic fluctuations in the high-temperature superconductor $(\text{La}, \text{Sr})_2\text{CuO}_4$ or in the heavy fermion system $\text{CeCu}_{5.9}\text{Au}_{0.1}$ for which temperature T and energy E are interchangeable [160, 161]. Our results suggest the sensitivity of space and time correlations of the fluctuations on thermally activated processes. Possibly, there is a finite coupling between the magnetic fluctuations, which have in analogy to mode coupling in ferromagnets important consequences on the critical dynamics. At the moment we may not exclude other explanations, most likely related to the cluster glass like behavior of $\text{Ca}_{2-x}\text{Sr}_x\text{RuO}_4$ for concen-

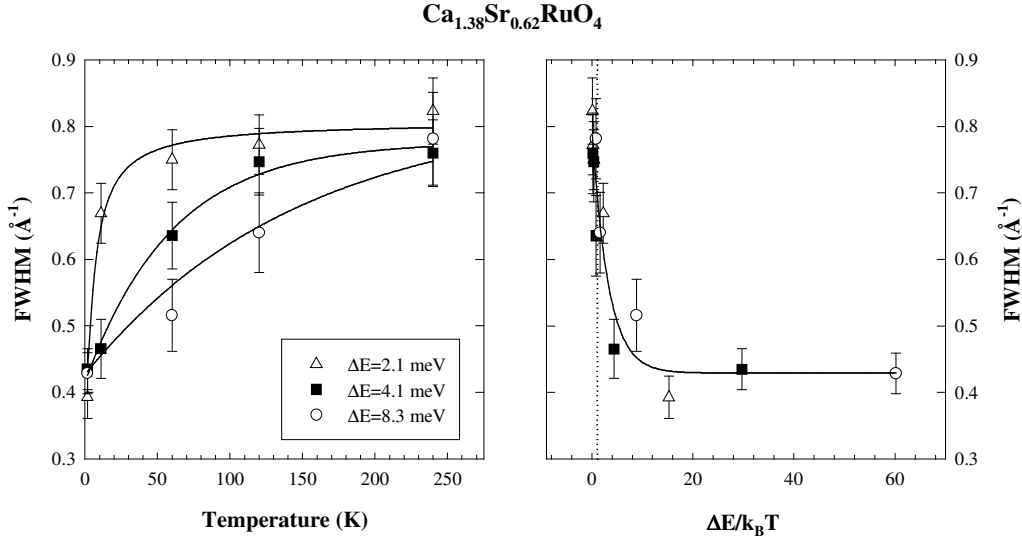


Figure 6.13: *Left:* Temperature dependence of the full width at half maximum (FWHM) at various fixed energy transfers. The line is intended as guide to the eye. *Right:* FWHM as a function of $\Delta E/k_B T$, indicating the nearly divergence for thermal energies $k_B T \geq \Delta E$ (the dashed vertical line corresponds to $\Delta E/k_B T = 1$). The solid line represents the fitting by an exponential decay.

trations around $x \simeq 0.5$ and temperatures below $T_f \simeq 1.0$ K [83]. There are two scenarios which may occur: First, the formation of cluster with short-range magnetic order could be attributed to the ordering of the incommensurate fluctuations at \mathbf{q}_η , similar to the development of short range magnetic order in Sr_2RuO_4 upon Ti substitution [153]. The anomalous line broadening at temperatures above T_f might then be ascribed to the dynamics of the corresponding fluctuating spin clusters and the temperature dependent interaction among these clusters, just as observed in the spin glass alloys CuMn and PdMn [162, 163]. Another possible scenario might be a crossover from incommensurate inelastic scattering to short range ferromagnetic ordering at low temperatures. The associated scattering would be enhanced at low T and low ΔE and superposes and exceed the incommensurate inelastic magnetic response. In order to elucidate this problem further studies towards low T and low ΔE are needed.

In conclusion, both the peak amplitudes and the width of the magnetic excitations are strongly temperature dependent, corresponding to growing magnetic correlations towards low temperatures. Such a temperature dependence is consistent with a classical spin system approaching a magnetic phase transition, for which typically a diverging magnetic susceptibility and correlation length are expected. Apart from this ordinary behavior, the energy dependency of the peak width for fixed temperatures appears quite complicated, indicating that the observed magnetic fluctuations

have an underlying energy scale comparable to the thermal energy.

6.3 Variation of the Fermi surface topography: Possible origin of the incommensurate Quasi-Ferromagnetic Fluctuations

In view of the presented experimental results in this chapter, one may ask "From what does the observed strong incommensurate fluctuations close to the zone center originate?" . According to band structure calculations there are two competing magnetic instabilities in the normal state of Sr_2RuO_4 : the incommensurate antiferromagnetic order due to the nesting of the α and β bands and a ferromagnetic instability due to a van Hove singularity (vHs) in the γ band just above the Fermi level E_F . While the incommensurate spin fluctuations in Sr_2RuO_4 have been confirmed by neutron scattering techniques, the experimental evidence for the ferromagnetic spin fluctuations is less clear: At present no ferromagnetic fluctuations have been detected in neutron studies, whereas ^{17}O and Ru NMR measurements do show a weak exchange enhancement.

However, in the Ca substituted samples the dominant role of ferromagnetic coupling in the γ band has been recently suggested. Polarized neutron diffraction measurements in $\text{Ca}_{1.5}\text{Sr}_{0.5}\text{RuO}_4$ under a magnetic field revealed a strongly anisotropic spin density distribution at the Ru site [121], which is reminiscent of the spatial distribution of the $4d_{xy}$ orbital. This observation suggests that the main part of the spin density arise from the two dimensional γ band, which may be hence considered as the driving element for the magnetic instability at $x_c = 0.5$. As already discussed in detail in section 4.5.2 this can be simply understood by the effect of the rotation of the RuO_6 octahedra on the d_{xy} band [111]. The rotation of the octahedra causes a flattening and lowering of this band, which brings the corresponding van Hove singularity (vHs), closer to the Fermi energy E_F . Since the d_{xy} vHs in Sr_2RuO_4 appears slightly above the Fermi level (LDA band structure calculations place it 60 meV above E_F [17, 18]), the downward shift of the d_{xy} band induces a high density of states around the Fermi level for which one would expect at first sight an enhancement of ferromagnetic spin fluctuations. Along with this downward shift of the d_{xy} band the population of the d_{xz} and d_{yz} states becomes reduced as discussed in Ref. [111], so that compared with Sr_2RuO_4 much of the nesting between the α and β sheets is removed. This population reduction might perfectly explain the observed intensity reduction of the incommensurate signal at \mathbf{q}_{ic} in $\text{Ca}_{1.38}\text{Sr}_{0.62}\text{RuO}_4$.

On the other hand, our results do not completely agree with simple ferromagnetic spin fluctuations, which would lead to a paramagnon-like signal centered around the zone center, but point to some further effect in order to explain the clearly incommensurate scattering at \mathbf{q}_η in $\text{Ca}_{2-x}\text{Sr}_x\text{RuO}_4$ close to $x_c = 0.5$. A plausible explanation

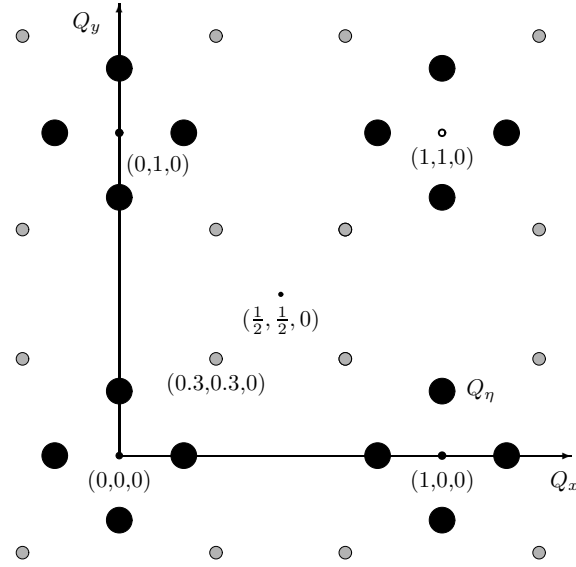


Figure 6.14: Map of the $(hk0)$ plane in reciprocal space, representing the location of the inelastic scattering observed for $\text{Ca}_{2-x}\text{Sr}_x\text{RuO}_4$ close to $x_c = 0.5$. Large filled circles indicate the position of the most intense fluctuations close to the zone center, while the smaller circles show the position of incommensurate peaks close to $\mathbf{q}_{\text{ic}} = (0.3, 0.3, 0)$, which dominate the excitation spectrum in Sr_2RuO_4 .

for the incommensurability of the observed magnetic fluctuations can be given if one assumes that the rotation of the octahedra does not only shift the vHs closer to E_F , but pulls it even slightly below the Fermi level. In general, the crossing of the vHs by E_F is expected to change the topology of the Fermi surface. In Fig. 6.15 we illustrate these changes, comparing the γ Fermi surface topologies derived from LDA band structure analysis using nonhybridizing two-dimensional tight-binding bands (i.e., $\epsilon_{xy}(\mathbf{k}) = -0.50 \text{ eV} - 0.88 \text{ eV}[\cos(ak_x) + \cos(ak_y)] - 0.56 \text{ eV}\cos(ak_x)\cos(ak_y)$) [164], for pure Sr_2RuO_4 and for a 0.1 eV downward shift of the γ band. According to calculations of Fang and Terakura [111] this shift corresponds approximately to the effect one would expect for the rotational distortion present in $\text{Ca}_{2-x}\text{Sr}_x\text{RuO}_4$ close to $x_c = 0.5$. As a result of the lowering of the γ band, the electron surface in the two dimensional plane of the extended Brillouin zone becomes a hole surface centered around the X point. Moreover, the hole-like portions becomes very straight at the corners (probably more than expected from the above given calculation) representing a good condition for Fermi surface nesting effects. Within this picture the observed magnetic fluctuations can be directly correlated with the nesting characteristics of the changed γ sheet. But this "vHS nesting" should be carefully distinguished from the conventional nesting, as seen for example in Sr_2RuO_4 . In conventional nesting the density of states is featureless, so that peaks in the spin susceptibility $\chi(\mathbf{q}, \hbar\omega)$

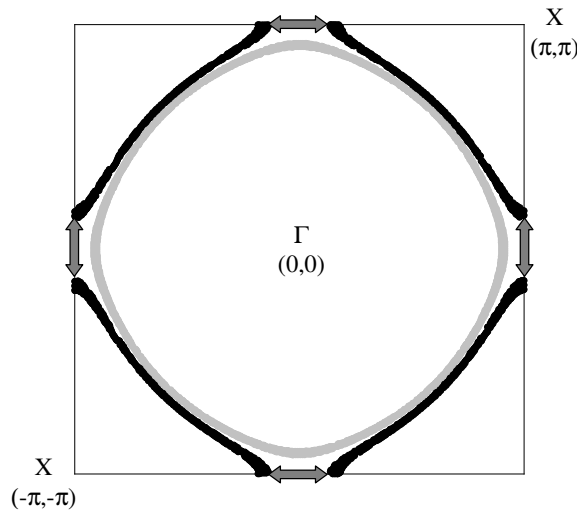


Figure 6.15: Sketch of the calculated Fermi surfaces of the γ sheet, indicating the influence of the downward shift of the d_{xy} band due to the rotation of the octahedra (after Liebsch and Lichtenberg, Ref. [164], and Fang and Terakura, Ref. [111]). The grey line shows the electronlike sheet of Sr_2RuO_4 and the black line the hole-like surface which one obtains for a 0.1 eV downward shift of the d_{xy} band. The change of the Fermi surface topology leads to straight hole-like portions which might produce nesting effects, as indicated by the arrows.

can occur only if two parts of the Fermi surface separated by a common wave vector \mathbf{q} run parallel over a considerable distance. Near a vHs the density of states is already strongly enhanced, so if a vector \mathbf{q} joins two vHs's a peak in the spin susceptibility can be observed. As indicated by arrows in Fig. 6.15, the \mathbf{q} vector that connects the corners of the hole pockets is $(\pm 0.12, 0)$ or $(0, \pm 0.12)$ in units of $2\pi/a$ and thus smaller than the experimentally found wave vector. But already slight changes of the downward shift of the γ band can successfully account for this discrepancy (note that recent quantum oscillation measurement in Sr_2RuO_4 locates the γ vHs closer to E_F than predicted by LDA calculations [165]).

There is support in experiments that for $\text{Ca}_{2-x}\text{Sr}_x\text{RuO}_4$ the topology of the Fermi surface changes with varying Sr content - or more generally stated with increasing rotation of the RuO_6 octahedra - towards $x_c = 0.5$. First, the Hall coefficient changes sign upon substitution [166], being suggestive of the change of the γ sheet from electronlike to holelike, while the α and β sheets remain holelike and electronlike, respectively. Second, early photoemission measurements in Sr_2RuO_4 [167, 168] revealed a Fermi surface topography, similar to that depicted in Fig. 6.15 with a holelike γ sheet. Obviously, these first measurements were inconsistent with the Fermi surface reported by de Haas-van Alphen experiments [16]. However, more recent ARPES results have shown that a possible reason for this discrepancy can be found in a sur-

face effect [169, 170], which seems to arise from a reconstruction of the surface due to the rotation of the RuO_6 octahedra, as determined by low-energy electron diffraction [171]. Moreover, a more indirect evidence for a topological change of the Fermi surface comes from recent inelastic neutron scattering studies on Sr_2RuO_4 [30]. The authors observed in addition to the pronounced nesting peaks at $\mathbf{q}_{ic} = (0.3, 0.3, 0)$ a weak, not well defined signal at $\mathbf{q} = (0.15, 0.15, 0)$, which they interpret based on a RPA analysis as arising from the γ band. We emphasize that this rather weak scattering in pure Sr_2RuO_4 and the observed incommensurate signal in $\text{Ca}_{2-x}\text{Sr}_x\text{RuO}_4$ for $x=0.62$ and 0.52 appear to be both related to the γ sheet, whereas the obvious differences, i.e. the distinct location of these fluctuations in reciprocal space and the strongly enhanced spectral weight in the Ca substituted samples, may be explained by the change of the topology of the Fermi surface in conjunction with the dominant role of the vHs.

As a result of the crossing of the vHs by E_F with changing x a large number of properties such as the lattice parameters, magnetic susceptibility, specific heat, etc. should be affected. Especially, at the critical concentration at which E_F touches vHs these properties are expected to show strong anomalies, in contrast to the so far reported thermodynamic properties which vary continuously with increasing x up to $x_c = 0.5$ [2, 3]. The absence of any singular behavior with varying composition might be explained in terms of a phase separation process: In order to avoid the coincidence of the vHs and E_F , the system forms a mixture of a phase with an undistorted structure and $E_{\text{vHs}} > E_F$ and a second phase with a rotational distorted structure and $E_{\text{vHs}} < E_F$. Thus, with increasing x one never reaches a critical concentration at which E_F and the vHs coincides because alloying with Ca increases only the fraction of the rotational distorted phase with the vHs below E_F . An intriguing way to test this idea is by applying pressure for a given x . Hydrostatic pressure may serve as a second variable to change the topology of the Fermi surface by passing the vHs through E_F , as already discussed in the classical work of Lifshitz [172].

Another ambiguity is the fact that the vicinity of the vHs and the shape of the γ sheet should lead also to strong antiferromagnetic fluctuations with wave vectors close to $(1/2, 1/2, 0)$. But according to our measurements, these fluctuations seem to be less prominent than the low-energy excitations close to the zone center Γ (note, that we cannot unambiguously exclude some magnetic intensity at $(1/2, 1/2, 1/2)$, see discussion above). One possible reason for this might be the q dependence of the Stoner factor, which reflects the general ferromagnetic tendency in ruthenates due to substantial oxygen density of states at the Fermi level [45, 121]. For example in Sr_2RuO_4 LSDA calculations revealed a Stoner factor $I(q)$ which decreases by a factor of 14% for q values at $(1/2, 1/2, 0)$ compared to that at Γ . Since the wave vector dependent susceptibility $\chi(q)$ gets enhanced through the Stoner-like interaction by a factor $1/(1 - I(q)\chi(q))$ it is obvious that the susceptibility is very sensitive to the precise value of the Stoner factor $I(q)$ for a given value of \mathbf{q} . Of course, detailed calculations must be performed to establish this interpretation definitely.

In summary, one may explain the observed incommensurate magnetic fluctuations in $\text{Ca}_{2-x}\text{Sr}_x\text{RuO}_4$ close to the critical point at $x=0.5$, as arising from a change of the γ Fermi surface topography. We argue that a crossover from an electron-like to a hole-like γ Fermi surface is induced by the rotations of the RuO_6 octahedra. On the one hand this enhances ferromagnetic fluctuations due an enhancement of the density of states close to the Fermi-level, but gives also rise to some nesting features at wave vectors which connects two vHst's. Therefore, we conclude that the enhanced influence of the γ band for compositions close to $\text{Ca}_{1.5}\text{Sr}_{0.5}\text{RuO}_4$ causes contributions to the magnetic susceptibility near the zone-center, which is sensitive to the shape of the Fermi sheet.

Chapter 7

Summary

In this thesis we aimed at exploring the structural and magnetic phase diagram of $\text{Ca}_{2-x}\text{Sr}_x\text{RuO}_4$ using neutron scattering techniques. Our detailed experimental studies show that the magnetic and electronic properties are closely correlated to the observed structural distortions induced by the isovalent Ca substitution. First, with the substitution of Sr by Ca in $\text{Ca}_{2-x}\text{Sr}_x\text{RuO}_4$ the system undergoes a structural phase transition characterised by the rotation of the RuO_6 octahedron around the c axis. Upon further Ca substitution a second structural phase transition sets in around $x \simeq 0.5$, which is characterised by an additional tilt of the octahedron around an in-plane axis. Further reduction of the Sr concentration drives the system via a first order transition from a metallic phase to an antiferromagnetic insulating ground state, accompanied by a characteristic flattening of the RuO_6 octahedron along the c axis.

The purely rotational distortion should be related to the continuous increase of the low temperature susceptibility, which for $\text{Ca}_{1.5}\text{Sr}_{0.5}\text{RuO}_4$ is about 150 times larger than that in Sr_2RuO_4 . This enhancement can be understood by the effect of the rotation angle on the electronic band structure [111], which results in a narrowing and a downward shift of the d_{xy} band. The onset of the tilt distortion at $x=0.5$ coincides with a drop in the susceptibility and the appearance of low temperature magnetic order as evidenced by irreversibilities in the magnetic susceptibility [2]. However, no indication of a long range magnetic structure corresponding to this has been found. The metal-insulator transition in $\text{Ca}_{2-x}\text{Sr}_x\text{RuO}_4$ occurs upon varying either the substitution level x , the temperature or the external pressure. The accompanying first order structural transition is characterized by a significant increase of the in-plane bond lengths, by a reduction of the Ru-O(2) distances, and by an increase of the tilt angle. Within a Mott scenario one may phenomenologically understand the insulating behavior, since both tilting and increase of the in-plane distances should strongly reduce the bandwidth. In particular the band corresponding to the d_{xy} orbital should become more localized and lower in energy.

In order to further characterize the continuous phase transition from the tetragonal to the orthorhombic structure in $\text{Ca}_{2-x}\text{Sr}_x\text{RuO}_4$ with $0.2 \leq x \leq 0.5$, the dispersion of the low lying phonon branches has been investigated by inelastic-neutron-scattering. Single crystals with Sr concentrations $x=0.62$, 0.5 , and 0.2 were studied. The cor-

responding rotational mode exhibits conventional behavior with no indication of a steep dispersion close to the original zone boundary point, as might be expected due to the rotational distorted structure. In contrast, the tilt mode shows characteristic soft-mode behavior at the tetragonal to orthorhombic transition for $x=0.2$. For $x=0.62$ and 0.5 , which are close to the composition where the tilt distortion vanishes, the corresponding soft mode behavior is much less prominent which we contribute to a pronounced order-disorder character of the continuous tilt transition.

The magnetic excitations in $\text{Ca}_{2-x}\text{Sr}_x\text{RuO}_4$ close to the concentration where the static low temperature susceptibility is maximal have been analyzed by inelastic neutron scattering. The excitation spectrum in such a sample is no longer dominated by the nesting excitations which are present in Sr_2RuO_4 ; instead we find incommensurate scattering at wave vectors close to the zone center. The peaks that dominate the magnetic fluctuations are rather broad in \mathbf{Q} space and have significant extension to the two-dimensional zone-center. We argue, that together with the small characteristic energy these features may account for the strong enhancement of the low temperature macroscopic susceptibility towards the critical concentration $x_c = 0.5$. We propose a phenomenological model to explain the incommensurate fluctuations in $\text{Ca}_{2-x}\text{Sr}_x\text{RuO}_4$ for x close to 0.5 . Within this model the incommensurate peaks can be directly correlated with nesting features of the γ sheet, which is strongly affected by the corresponding van Hove singularity. It turns out that the van Hove singularity dominates not only the density of states at and near E_F , but may lead, when passing through E_F , to a topological change of the Fermi surface which give rise to new nesting features. This nesting effect would occur at incommensurate wave vector which are in qualitative agreement with our data.

In addition, we have presented the effect of temperature on the incommensurate spin fluctuations in $\text{Ca}_{1.38}\text{Sr}_{0.62}\text{RuO}_4$. Both the peak amplitudes and the width of the magnetic excitations are strongly temperature dependent, corresponding to growing magnetic correlations towards low temperatures. Such a temperature dependence is consistent with a system approaching a magnetic phase transition, for which typically a diverging magnetic susceptibility and correlation length are expected. Apart from this ordinary behavior, the energy dependence of the peak width for fixed temperatures appears quite complicated, indicating that the observed magnetic fluctuations have an underlying energy scale comparable to the thermal energy.

References

- [1] M. Imada, A. Fujimori, and Y. Tokura, *Review of Modern Physics* **70**, 1039 (1998).
- [2] S. Nakatsuji and Y. Maeno, *Physical Review Letters* **84**, 2666 (2000).
- [3] S. Nakatsuji and Y. Maeno, *Physical Review B* **62**, 6458 (2000).
- [4] Y. Maeno, H. Hashimoto, K. Yoshida, S. NishiZaki, T. Fujita, J. G. Bednorz, and F. Lichtenberg, *Nature* **372**, 532 (1994).
- [5] Y. Maeno, T. M. Rice, and M. Sigrist, *Physics Today* **54**, 42 (2001).
- [6] M. Braden, G. André, S. Nakatsuji, and Y. Maeno, *Physical Review B* **58**, 847 (1998).
- [7] A. P. Mackenzie, R. K. W. Haselwimmer, A. W. Tyler, G. G. Lonzarich, Y. Mori, S. NishiZaki, and Y. Maeno, *Physical Review Letters* **80**, 111 (1998).
- [8] T. M. Rice and M. Sigrist, *Journal of Physics: Condensed Matter* **7**, L643 (1995).
- [9] G. Baskaran, *Physica B* **223 & 224**, 490 (1996).
- [10] J. J. Neumeier, M. F. Hundley, M. G. Smith, J. D. Thompson, C. Allgeier, H. Xie, W. Yelon, and J. S. Kim, *Physical Review B* **50**, 17910 (1994).
- [11] T. Vogt and D. J. Buttrey, *Physical Review B* **52**, R9843 (1995).
- [12] O. Chmaissem, J. D. Jorgensen, H. Shaked, S. Ikeda, and Y. Maeno, *Physical Review B* **57**, 5067 (1998).
- [13] M. Braden, A. H. Moudden, S. NishiZaki, Y. Maeno, and T. Fujita, *Physica C* **279**, 248 (1997).
- [14] Y. Maeno, K. Yoshida, H. Hashimoto, S. NishiZaki, S. I. Ikeda, M. Nohara, T. Fujita, A. P. Mackenzie, N. E. Hussey, J. G. Bednorz, et al., *Journal of the Physical Society of Japan* **66**, 1405 (1997).
- [15] Y. Maeno, *Physica C* **282-287**, 206 (1997).

- [16] A. P. Mackenzie, S. R. Julian, A. J. Diver, G. J. McMullan, M. P. Ray, G. G. Lonzarich, Y. Maeno, S. NishiZaki, and T. Fujita, *Physical Review Letters* **76**, 3786 (1996).
- [17] T. Oguchi, *Physical Review B* **51**, 1385 (1995).
- [18] D. J. Singh, *Physical Review B* **52**, 1358 (1995).
- [19] T. M. Rice, *Nature (London)* **396**, 627 (1998).
- [20] Y. Maeno, S. NishiZaki, and Z. Q. Mao, *Journal of Superconductivity* **12**, 535 (1999).
- [21] Y. Maeno, H. Yaguchi, and K. Deguchi, in *Ruthenate and Rutheno-Cuprates Materials* (Springer Verlag Berlin Heidelberg, 2002), pp. 1–15.
- [22] A. Mackenzie, Y. Maeno, and S. Julian, *Physics World* **04**, 535 (2002).
- [23] A. P. Mackenzie and Y. Maeno, *Reviews of Modern Physics* **75**, 657 (2003).
- [24] K. Ishida, Y. Kitaoka, K. Asayama, S. Ikeda, S. Nishizaki, and Y. Maeno, *Physical Review B* **56**, R505 (1997).
- [25] K. Ishida, H. Mukuda, Y. Kitaoka, K. Asayama, Z. Q. Mao, Y. Mori, and Y. Maeno, *Nature (London)* **396**, 658 (1998).
- [26] J. A. Duffy, S. M. Hayden, Y. Maeno, Z. Mao, J. Kulda, and G. J. McIntyre, *Physical Review Letters* **85**, 5412 (2000).
- [27] G. M. Luke, Y. Fudamoto, K. M. Kojima, M. I. Larkin, J. Merrin, B. Nachumi, Y. J. Uemura, Y. Maeno, Z. Q. Mao, Y. Mori, et al., *Nature (London)* **394**, 558 (1998).
- [28] Y. Sidis, M. Braden, P. Bourges, B. Hennion, S. NishiZaki, Y. Maeno, and Y. Mori, *Physical Review Letters* **83**, 3320 (1999).
- [29] F. Servant, B. Fåk, S. Raymond, J. P. Brison, P. Lejay, and J. Flouquet, *Physical Review B* **65**, 184511 (2002).
- [30] M. Braden, Y. Sidis, P. Bourges, P. Pfeuty, J. Kulda, Z. Mao, and Y. Maeno, *Physical Review B* **66**, 064522 (2002).
- [31] S. NishiZaki, Y. Maeno, and Z. Mao, *Journal of Low Temperature Physics* **117**, 1581 (1999).
- [32] S. NishiZaki, Y. Maeno, and Z. Mao, *Journal of the Physical Society of Japan* **69**, 572 (2000).

-
- [33] I. Bonalde, B. Yanoff, M. B. Salamon, D. J. Van Harlingen, E. M. E. Chia, Z. Q. Mao, and Y. Maeno, *Physical Review Letters* **85**, 4775 (2000).
- [34] C. Lupien, W. A. MacFarlane, C. Proust, L. Taillefer, Z. Q. Mao, and Y. Maeno, *Physical Review Letters* **86**, 5986 (2001).
- [35] K. Ishida, H. Mukuda, Y. Kitaoka, Z. Q. Mao, Y. Mori, and Y. Maeno, *Physical Review Letters* **84**, 5387 (2000).
- [36] M. A. Tanatar, M. Suzuki, S. Nagai, Z. Q. Mao, Y. Maeno, and T. Ishiguro, *Physical Review Letters* **86**, 2649 (2001).
- [37] M. A. Tanatar, S. Nagai, Z. Q. Mao, Y. Maeno, and T. Ishiguro, *Physical Review B* **63**, 064505 (2001).
- [38] D. F. Agterberg, *International Journal of Modern Physics B* **16**, 3233 (2002).
- [39] Y. Hasegawa, K. Machida, and M. Ozaki, *Journal of the Physical Society of Japan* **69**, 336 (2000).
- [40] H. Won and K. Maki, *Europhysics Letters* **52**, 427 (2000).
- [41] K. Miyake and O. Narikiyo, *Physical Review Letters* **83**, 1423 (1999).
- [42] M. Graf and A. V. Balatsky, *Physical Review B* **62**, 9697 (2000).
- [43] M. E. Zhitomirsky and T. M. Rice, *Physical Review Letters* **87**, 057001/1 (2001).
- [44] K. Deguchi, M. Tanatar, Z. Mao, T. Ishiguro, and Y. Maeno, Los Alamos National Laboratory, Preprint Archive, Condensed Matter pp. cond-mat/0210537 (2002).
- [45] I. I. Mazin and D. J. Singh, *Physical Review Letters* **79**, 733 (1997).
- [46] O. Friedt, M. Braden, G. André, P. Adelman, S. Nakatsuji, and Y. Maeno, *Physical Review B* **63**, 174432 (2001).
- [47] M. Braden, W. Reichardt, S. NishiZaki, Y. Mori, and Y. Maeno, *Physical Review B* **57**, 1236 (1998).
- [48] P. G. Radaelli, D. G. Hinks, A. W. Mitchell, B. A. Hunter, J. L. Wagner, B. Dabrowski, K. G. Vandervoort, H. K. Viswanathan, and J. D. Jorgensen, *Physical Review B* **49**, 4163 (1994).
- [49] J. D. Axe, A. H. Moudden, D. Hohlwein, D. E. Cox, K. M. Mohatny, A. R. Moodenbaugh, and Y. Xu, *Physical Review Letters* **62**, 2751 (1989).

- [50] M. Braden, G. Heger, P. Schweiss, Z. Fisk, K. Gamayunov, I. Tanaka, and H. Kojima, *Physica C* **191**, 455 (1992).
- [51] M. Braden, P. Schweiss, G. Heger, W. Reichardt, Z. Fisk, K. Gamayunov, I. Tanaka, and H. Kojima, *Physica C* **223**, 396 (1994).
- [52] S. Nakatsuji and Y. Maeno, *Journal of Solid State Chemistry* **156**, 26 (2001).
- [53] S. Nakatsuji, Ph.D. thesis, Graduate School of Science, Kyoto University (2000).
- [54] V. K. Tagirov, D. M. Chizhikov, E. K. Kazenas, and L. K. Shubochkin, *Russian Journal of Inorganic Chemistry* **20**, 1133 (1975).
- [55] S. Nakatsuji, private communication (2001).
- [56] U. Ammerahl, Ph.D. thesis, University of Cologne (2000).
- [57] P. Reutler, Ph.D. thesis (in preparation), University of Aachen (2003).
- [58] F. Lichtenberg, A. Catana, J. Mannhart, and D. G. Schlom, *Applied Physical Letters* **60**, 1138 (1992).
- [59] Y. Maeno, T. Ando, Y. Mori, E. Ohmichi, S. Ikeda, S. NishiZaki, and S. Nakatsuji, *Physical Review Letters* **81**, 3765 (1998).
- [60] Z. Q. Mao and Y. Maeno, *Physica C* **341-348**, 787 (2000).
- [61] Z. Q. Mao, Y. Maeno, and H. Fukazawa, *Material Research Bulletin* **35**, 1813 (2000).
- [62] C. Pfleiderer, *Private communication* (2001).
- [63] Z. Q. Mao, Y. Mori, and Y. M. and, *Physical Review B* **60**, 610 (1999).
- [64] V. F. Sears, *Neutron News* **3**, 26 (1992).
- [65] *Equipements expérimentaux*, Laboratoire Léon Brillouin (1995).
- [66] J. Rossat-Mignot, in *Methods of Experimental Physics* (Academic Press Inc., 1987), vol. 23, p. 69.
- [67] Y. Sidis, M. Braden, P. Bourges, B. Hennion, S. NishiZaki, Y. Maeno, and Y. Mori, *Physica B* **281&282**, 967 (2000).
- [68] G. E. Bacon, *Neutron Diffraction* (Clarendon Press Oxford, 1975).

-
- [69] G. L. Squires, *Introduction to the theory of thermal neutron scattering* (Cambridge University Press, 1978).
- [70] W. Marshall and S. W. Lovesey, *Theory of thermal neutron scattering* (Oxford University Press, 1971).
- [71] G. Shirane, S. M. Shapiro, and J. M. Tranquada, *Neutron Scattering with a Triple-Axis Spectrometer Basic Techniques* (Cambridge University Press, 2002).
- [72] H. M. Rietveld, *Acta Crystallographica* **22**, 151 (1967).
- [73] H. M. Rietveld, *Journal of Applied Crystallography* **2**, 65 (1969).
- [74] R. A. Young, ed., *The Rietveld Method* (Oxford University Press, 1996).
- [75] C. Giacovazzo, H. L. Monaco, D. Viterbo, F. Scordari, G. Gilli, G. Zanotti, and M. Catti, *Fundamentals of Crystallography* (Oxford University Press, 1992).
- [76] J. Rodríguez-Carvajal, *PSI-Proceedings* **93-01**, 73 (1993).
- [77] U. Zucker, E. . Perenthaler, W. Kuhs, R. Bachmann, and H. Schulz, *Journal of Applied Crystallography* **16**, 358 (1983).
- [78] W. Reichardt, *Hand Control Program TAS 1T.1* (2002).
- [79] G. Cao, S. McCall, M. Shepard, and J. E. Crow, *Physical Review B* **56**, R2916 (1997).
- [80] G. Cao, S. McCall, V. Dobrosavljevic, C. S. Alexander, J. E. Crow, and R. P. Guertin, *Physical Review B* **61**, R5053 (2000).
- [81] C. S. Alexander, G. Cao, V. Dobrosavljevic, S. McCall, J. E. Crow, E. Lochner, and R. P. Guertin, *Physical Review B* **60**, R8422 (1999).
- [82] R. D. Shannon, *Acta Crystallographica A* **32**, 751 (1976).
- [83] S. Nakatsuji, D. Hall, L. Balicas, Z. Fisk, K. Sugahara, M. Yoshioka, and Y. Maeno, *Physical Review Letters* **90**, 137202 (2003).
- [84] S. Nakatsuji and Y. Maeno, *Journal of Low Temperature Physics* **117**, 1593 (1999).
- [85] H. T. Stokes and D. M. Hatch, *Isotropy Subgroups of the 230 Crystallographic Space Groups* (World Scientific, Signapore, 1988).
- [86] J. Rodríguez-Carvajal, J. L. Martínez, J. Pannetier, and R. Saez-Puche, *Physical Review B* **38**, 7148 (1988).

- [87] J. Rodríguez-Carvajal, M. T. Fernandez-Diaz, and J. L. Martinez, *Journal of Physics: Condensed Matter* **3**, 3215 (1991).
- [88] O. Friedt, Master's thesis, University of Cologne (1998).
- [89] M. K. Crawford, M. A. Subramanian, R. L. Harlow, J. A. Fernandez-Baca, Z. R. Wang, and D. C. Johnston, *Physical Review B* **49**, 9198 (1994).
- [90] M. A. Subramanian, M. K. Crawford, R. L. Harlow, T. Ami, J. A. Fernandez-Baca, Z. R. Wang, and D. C. Johnston, *Physica C* **235-240**, 743 (1994).
- [91] Q. Huang, J. L. Soubeyroux, O. Chmaissem, I. Natali Sora, A. Santoro, R. J. Cava, J. J. Krajewski, and W. F. Peck jr., *Journal of Solid State Chemistry* **112**, 355 (1994).
- [92] M. E. Leonowicz, K. R. Poeppelmeier, and J. M. Longo, *Journal of Solid State Chemistry* **59**, 71 (1985).
- [93] J. Takahashi and N. Kamegashira, *Material Research Bulletin* **28**, 565 (1993).
- [94] M. Braden, W. Paulus, A. Cousson, P. Vigoureux, G. Heger, A. Goukassov, P. Bourges, and D. Petitgrand, *Europhysics Letters* **25**, 625 (1994).
- [95] P. Vigoureux, M. Braden, A. Gukasov, W. Paulus, P. Bourges, A. Cousson, D. Petitgrand, J. P. Lauriat, M. Meven, S. N. Barilo, et al., *Physica C* **273**, 239 (1997).
- [96] R. J. Bouchard and J. L. Gillson, *Material Research Bulletin* **7**, 873 (1972).
- [97] T. Kiyama, K. Yoshimura, K. Kosuge, Y. Ikeda, and Y. Bando, *Physical Review B* **54**, R756 (1996).
- [98] J. Rodríguez-Carvajal, M. Hennion, F. Moussa, A. H. Moudden, L. Pinsard, and A. Revcolevschi, *Physical Review B* **57**, R3189 (1998).
- [99] M. Cwik, T. Lorenz, J. Baier, R. Müller, G. André, F. Bourée, F. Lichtenberg, and M. Braden (2003), preprint.
- [100] O. Friedt, M. Braden, G. André, P. Adelman, S. Nakatsuji, and Y. Maeno, *Applied Physics A* **74**, 1627 (2002).
- [101] S. Nakatsuji, S. I. Ikeda, and Y. Maeno, *Journal of the Physical Society of Japan* **66**, 1868 (1997).
- [102] N. F. Mott, *Metal-Insulator Transitions* (Taylor & Francis, London, 1990), 2nd ed.

-
- [103] D. B. McWhan, T. M. Rice, and J. P. Remeika, *Physical Review Letters* **23**, 1384 (1969).
- [104] V. I. Anisimov, I. A. Nekrasov, D. E. Kondakov, T. M. Rice, and M. Sigrist, *The European Physical Journal B* **25**, 191 (2002).
- [105] T. Mizokawa, L. H. Tjeng, G. A. Sawatzky, G. Ghiringhelli, O. Tjernberg, N. B. Brookes, H. Fukazawa, S. Nakatsuji, and Y. Maeno, *Physical Review Letters* **87**, 077202 (2001).
- [106] M. Kurokawa and T. Mizokawa, *Physical Review B* **66**, 024434 (2002).
- [107] G. H. Lander, P. J. Brown, J. Spalek, and J. M. Honig, *Physical Review B* **40**, 4463 (1989).
- [108] J. Plessel, Ph.D. thesis, University of Cologne (2002).
- [109] *The ILL Yellow Book*, Institut Laue Langevin (2001).
- [110] F. Nakamura, T. Goko, M. Ito, T. Fujita, S. Nakatsuji, H. Fukazawa, Y. Maeno, P. Alireza, D. Forsythe, and S. R. Julian, *Physical Review B* **65**, 220402(R)/1 (2002).
- [111] Z. Fang and K. Terakura, *Physical Review B* **64**, 020509/1 (2001).
- [112] H. Takahashi, H. Shaked, B. A. Hunter, P. G. Radaelli, R. L. Hittermann, D. G. Hinks, and J. D. Jorgensen, *Physical Review B* **50**, 3221 (1994).
- [113] P. Steffens, Master's thesis (in preparation), University of Cologne (2003).
- [114] S. Nakatsuji, T. Ando, Z. Mao, and Y. Maeno, *Physica B* **259-261**, 259 (1999).
- [115] H. Fukazawa and Y. Maeno, *Journal of the Physical Society of Japan* **70**, 460 (2001).
- [116] A. D. Bruce and R. A. Cowley, *Structural Phase Transitions* (Taylor & Francis LTD, 1981).
- [117] K. Yamada, M. Matsuda, Y. Endoh, B. Keimer, R. J. Birgeneau, S. Onodera, J. Mizusaki, T. Matsuura, and G. Shirane, *Physical Review B* **39**, 2336 (1989).
- [118] M. K. Crawford, R. L. Harlow, E. M. McCarron, W. E. Farneth, N. Herron, H. Chou, and D. E. Cox, *Physical Review B* **47**, 11623 (1993).
- [119] K. Nakajima, Y. Endoh, K. Yamada, S. Hosoya, N. Kaneko, and J. Wada, *Journal of the Physical Society of Japan* **64**, 716 (1995).

- [120] P. J. Brown, *International Tables for Crystallography* (Kluwer Academic, Dordrecht, 1992).
- [121] A. Gukasov, M. Braden, R. J. Papoular, S. Nakatsuji, and Y. Maeno, *Physical Review Letters* **89**, 087202 (2002).
- [122] J. B. Goodenough, *Magnetism and the Chemical Bond* (John Wiley & Sons, New York-London, 1963).
- [123] T. Hotta and E. Dagotto, *Physical Review Letters* **88**, 017201 (2002).
- [124] L. M. Woods, *Physical Review B* **62**, 7833 (2000).
- [125] K. Park, *Journal of Physics: Condensed Matter* **13**, 9231 (2001).
- [126] I. I. Mazin and D. J. Singh, *Physical Review Letters* **82**, 4324 (1999).
- [127] R. Jin, J. R. Thompson, J. He, J. M. Farmer, N. Lowhorn, G. A. Lamberton, T. M. Tritt, and D. Mandrus, Los Alamos National Laboratory, Preprint Archive, Condensed Matter pp. 1–5, arXiv:cond-mat/0112405 (2001).
- [128] V. M. Goldschmidt, *Naturwissenschaften* **14**, 477 (1926).
- [129] I. D. Brown and D. Altermatt, *Acta Crystallographica B* **41**, 244 (1985).
- [130] I. D. Brown, *Journal of Solid State Chemistry* **82**, 122 (1989).
- [131] M. Braden, Ph.D. thesis, University of Cologne (1992).
- [132] N. E. Brese and M. O’Keeffe, *Acta Crystallographica B* **47**, 192 (1991).
- [133] B. Büchner, Ph.D. thesis, University of Cologne (1994).
- [134] M. Cramm, Ph.D. thesis, University of Cologne (1999).
- [135] M. Cramm, Master’s thesis, University of Cologne (1991).
- [136] M. Braden, W. Reichardt, E. Elkaim, J. P. Lauriat, S. Shiryayev, and S. N. Barilo, *Physical Review B* **62**, 6708 (2000).
- [137] M. Braden, M. Meven, W. Reichardt, L. Pintschovius, M. T. Fernandez-Diaz, G. Heger, F. Nakamura, and T. Fujita, *Physical Review B* **63**, 140510 (2001).
- [138] Q. Huang, J. W. Lynn, R. W. Erwin, J. Jarupatrakorn, and R. J. Cava, *Physical Review B* **58**, 8515 (1998).
- [139] M. T. Dove, *Introduction to Lattice Dynamics* (Cambridge University Press, 1993).

-
- [140] M. T. Dove, *American Mineralogist* **82**, 213 (1997).
- [141] J. F. Scott, *Reviews of Modern Physics* **46**, 83 (1974).
- [142] G. Shirane, *Review of Modern Physics* **46**, 437 (1974).
- [143] M. Braden, in *Neutron Scattering* (Forschungszentrum Jülich GmbH, 2000), chap. 13.
- [144] R. J. Birgeneau, C. Y. Chen, D. R. Gabbe, H. P. Jenssen, M. A. Kastner, C. J. Peters, P. J. Picone, T. Thio, T. R. Thurston, H. L. Tuller, et al., *Physical Review Letters* **59**, 1329 (1987).
- [145] P. Böni, J. D. Axe, G. Shirane, R. J. Birgeneau, D. R. Gabbe, H. P. Jenssen, M. A. Kastner, C. J. Peters, P. J. Picone, and T. R. Thurston, *Physical Review B* **38**, 185 (1988).
- [146] T. R. Thurston, R. J. Birgeneau, D. R. Gabbe, H. P. Jenssen, M. A. Kastner, P. J. Picone, N. W. Preyer, J. D. Axe, P. Böni, and G. Shirane, *Physical Review B* **39**, 4327 (1989).
- [147] L. Pintschovius, *Festkörperprobleme* **30**, 183 (1990).
- [148] M. Braden, W. Schnelle, W. Schwarz, N. Pyka, G. Heger, Z. Fisk, K. Gamayunov, I. Tanaka, and H. Kojima, *Zeitschrift für Physik B* **94**, 29 (1994).
- [149] S. Sugai, *Physical Review B* **39**, 4306 (1989).
- [150] J. L. Martínez, M. T. Fernández-Díaz, J. Rodríguez-Carvajal, and P. Odier, *Physical Review B* **43**, 13766 (1991).
- [151] L. Pintschovius, J. M. Bassat, P. Odier, F. Gervais, G. Chevrier, W. Reichardt, and F. Gompf, *Physical Review B* **40**, 2229 (1989).
- [152] J. M. Longo, P. M. Raccah, and J. B. Goodenough, *Journal of Applied Physics* **39**, 1327 (1968).
- [153] M. Braden, O. Friedt, Y. Sidis, P. Bourges, M. Minakata, and Y. Maeno, *Physical Review Letters* **88**, 197002 (2002).
- [154] T. Kuwabara and M. Ogata, *Physical Review Letters* **85**, 4586 (2000).
- [155] M. Sato and M. Kohmoto, *Journal of the Physical Society of Japan* **69**, 3505 (2000).

- [156] T. Nomura and K. Yamada, *Journal of the Physical Society of Japan* **69**, 1856 (2000).
- [157] S. W. Lovesey, *Theory of Neutron Scattering from Condensed Matter*, vol. 2 (Clarendon, Oxford, 1984).
- [158] R. W. White, *Quantum Theory of Magnetism* (McGraw-Hill, Inc., 1970).
- [159] M. Braden, Y. Sidis, P. Bourges, and B. Hennion (2001), (unpublished results).
- [160] G. Aeppli, T. E. Mason, S. M. Hayden, H. A. Mook, and J. Kulda, *Science* **278**, 1432 (1997).
- [161] A. Schröder, G. Aeppli, E. Bucher, R. Ramazashvili, and P. Coleman, *Physical Review Letters* **80**, 5623 (1998).
- [162] Y. Tsunoda, N. Kunitomi, and J. W. Cable, *Journal of Applied Physics* **57**, 3753 (1985).
- [163] Y. Tsunoda, N. Hiruma, J. L. Robertson, and J. W. Cable, *Physical Review B* **56**, 11051 (1997).
- [164] A. Liebsch and A. Lichtenstein, *Physical Review Letters* **84**, 1591 (2000).
- [165] C. Bergemann (2003), (unpublished results).
- [166] L. M. Galvin, R. S. Perry, A. W. Tyler, A. P. Mackenzie, S. Nakatsuji, and Y. Maeno, *Physical Review B* **63**, 161102 (2001).
- [167] T. Yokoya, A. Chainani, T. Takahashi, H. Ding, J. C. Campuzano, H. Katayama-Yoshida, M. Kasai, and Y. Tokura, *Physical Review B* **54**, 13311 (1996).
- [168] D. H. Lu, M. Schmidt, T. R. Cummins, S. Schuppler, F. Lichtenberg, and J. G. Bednorz, *Physical Review Letters* **76**, 4845 (1996).
- [169] A. Damascelli, D. H. Lu, K. M. Shen, N. P. Armitage, F. Ronning, D. L. Feng, C. Kim, Z.-X. Shen, T. Kimura, Y. Tokura, et al., *Physical Review Letters* **85**, 5194 (2000).
- [170] K. M. Shen, A. Damascelli, D. H. Lu, N. P. Armitage, F. Ronning, D. L. Feng, C. Kim, Z.-X. Shen, D. J. Singh, I. I. Mazin, et al., *Physical Review B* **64**, 180502 (2000).
- [171] R. Matzdorf, Z. Fang, Ismail, J. Zhang, T. Kimura, Y. Tokura, K. Terakura, and E. W. Plummer, *Science* **289**, 746 (2000).
- [172] I. M. Lifshitz, *Soviet Physics JETP* **11**, 1130 (1960).

Appendix

List of publications

- i. Structural and magnetic aspects of the metal-insulator transition in $\text{Ca}_{2-x}\text{Sr}_x\text{RuO}_4$, O. Friedt, M. Braden, G. André, P. Adelman, S. Nakatsuji, and Y. Maeno, *Physical Review B*, Vol. **63**, 174432 (2001).
- ii. Neutron diffraction study of the crystal structure of $\text{Ca}_{1.5}\text{Sr}_{0.5}\text{RuO}_4$, O. Friedt, M. Braden, G. André, S. Nakatsuji, and Y. Maeno, *Applied Physics A* **74**, 1627 (2002).
- iii. Incommensurate Magnetic Ordering in $\text{Sr}_2\text{Ru}_{1-x}\text{Ti}_x\text{O}_4$, M. Braden, O. Friedt, Y. Sidis, P. Bourges, M. Minakata, and Y. Maeno, *Physical Review Letters*, Vol. **88**, 197002 (2002).
- iv. Growth of $\text{La}_{1-x}\text{Sr}_{1+x}\text{MnO}_4$ single crystals and characterization by scattering techniques, P. Reutler, O. Friedt, B. Büchner, M. Braden, A. Revcolevschi, *Journal of Crystal Growth*, Vol. **249**, 222 (2003).
- v. Magnetic excitations in 214-ruthenates, M. Braden, O. Friedt, Y. Sidis, P. Bourges, P. Pfeuty, and Y. Maeno, in *Ruthenate and Rutheno-Cuprate Materials*, Lecture Notes in Physics, Vol. 603, (Springer-Verlag, Berlin, 2002), p. 15 ff.
- vi. Magnetic excitations in 214-ruthenates, M. Braden, O. Friedt, Y. Sidis, P. Bourges, P. Pfeuty, S. Nakatsuji, Z. Mao, N. Kikugawa, M. Minakata, and Y. Maeno, *Physica C* (2003), accepted.

Structural and magnetic aspects of the metal-insulator transition in $\text{Ca}_{2-x}\text{Sr}_x\text{RuO}_4$

O. Friedt

Laboratoire Léon Brillouin, CEA/CNRS, F-91191 Gif-sur-Yvette Cedex, France

M. Braden

*Laboratoire Léon Brillouin, CEA/CNRS, F-91191 Gif-sur-Yvette Cedex, France
and Forschungszentrum Karlsruhe, IFP, Postfach 3640, D-76021 Karlsruhe, Germany*

G. André

Laboratoire Léon Brillouin, CEA/CNRS, F-91191 Gif-sur-Yvette Cedex, France

P. Adelmann

Forschungszentrum Karlsruhe, IFP, Postfach 3640, D-76021 Karlsruhe, Germany

S. Nakatsuji

Department of Physics, Kyoto University, Kyoto 606-8502, Japan

Y. Maeno

*Department of Physics, Kyoto University, Kyoto 606-8502, Japan
and CREST, Japan Science and Technology Corporation, Kawaguchi, Saitama 332-0012, Japan
(Received 15 July 2000; revised manuscript received 21 December 2000; published 12 April 2001)*

The phase diagram of $\text{Ca}_{2-x}\text{Sr}_x\text{RuO}_4$ has been studied by neutron diffraction on powder and single-crystalline samples. The experiments reveal antiferromagnetic order and structural distortions characterized by tilts and rotations of the RuO_6 octahedra. There is strong evidence that the structural details of the iso-valent samples tune the magnetic as well as the electronic behavior. In particular we observe for low Sr concentration a metal-insulator transition associated with a structural change and magnetic ordering.

DOI: 10.1103/PhysRevB.63.174432

PACS number(s): 75.50.Ee, 61.12.-q, 64.70.-p, 74.70.-b

I. INTRODUCTION

Layered perovskite ruthenates have attracted considerable interest since the discovery of superconductivity in Sr_2RuO_4 , which remains to date the only known superconductor isostructural to the cuprates.¹ It is, therefore, expected that this material can give further insight into the mechanism of high-temperature superconductivity. However, the origin of the spin-triplet pairing in Sr_2RuO_4 (Ref. 2) is far from understood. There is reasonable evidence that in this material a coupling between electrons and magnetism is essential: for example, magnetic susceptibility³ and low-temperature specific heat⁴ exhibit similar enhancements. It has been suggested that ferromagnetic fluctuations dominate the interaction leading to an unconventional pairing of p -wave symmetry.⁵ This suggestion was mainly inspired by the fact that the perovskite SrRuO_3 is indeed an itinerant ferromagnet.⁶ The substitution of Sr by Ca in the layered compound yields rather different physical properties. First Ca_2RuO_4 is an insulator at low temperatures⁷ and second it orders antiferromagnetically,^{8,9} which clearly indicates that considering Sr_2RuO_4 as being close to ferromagnetic order is an oversimplification. More recently band structure analyses on Sr_2RuO_4 have predicted that the magnetic susceptibility presents dominating peaks at incommensurate wave vector positions $q_0 = (2\pi/3a, 2\pi/3a, 0)$, which arise from Fermi-surface nesting.¹⁰ Inelastic neutron scattering studies have perfectly confirmed these features.¹¹ In order to get insight

into the relation between these incommensurate peaks in the Sr_2RuO_4 susceptibility and the antiferromagnetic order in Ca_2RuO_4 it seems essential to study the entire phase diagram of $\text{Ca}_{2-x}\text{Sr}_x\text{RuO}_4$.

The physics of $\text{Ca}_{2-x}\text{Sr}_x\text{RuO}_4$ attracts interest not only in the context of the superconductivity in Sr_2RuO_4 . In our first paper we have demonstrated that in a sample containing excess oxygen $\text{Ca}_2\text{RuO}_{4.07}$, one finds a structural transition from a metallic high-temperature phase into a nonmetallic distorted low-temperature phase hence a metal-insulator transition.⁸ The observation of the antiferromagnetic order in the nonmetallic phase suggests the interpretation that this transition is of the Mott type. The high-temperature metallic phase of $\text{Ca}_2\text{RuO}_{4.07}$ is characterized by an octahedron shape almost identical to that observed in Sr_2RuO_4 , whereas the in-plane Ru-O bond lengths are significantly enhanced in the low-temperature insulating phase. In addition there is a stronger tilt of the RuO_6 octahedra in the low-temperature phase. The structural transition is of the first order type, as seen in the large hysteresis with coexistence of the two phases, and presents a lattice expansion of $\Delta V/V \sim 1\%$ upon cooling. Recently Alexander *et al.* have found a sudden increase in the resistivity of stoichiometric Ca_2RuO_4 at 357 K,¹² suggesting that the metal insulator transition seen in $\text{Ca}_2\text{RuO}_{4.07}$ occurs just at higher temperature in the stoichiometric compound. Nakatsuji *et al.* have revealed the entire magnetic phase diagram of $\text{Ca}_{2-x}\text{Sr}_x\text{RuO}_4$, and found the metal-insulator transition by resistivity and magnetic suscep-

tibility measurements.^{13,14} They observe that the anomalies in the resistivity are rapidly shifted to lower temperature for increasing Sr content, for $x > 0.2$ the samples stay metallic down to low temperature. Also Cao *et al.* report a decrease of the metal-insulator transition temperature upon Sr doping; in addition they observe the similar suppression for La doping.¹⁵ However, no diffraction study on structural aspects of the metal-insulator transition as function of doping has been reported so far.

In many aspects the metal-insulator transition in $\text{Ca}_{2-x}\text{Sr}_x\text{RuO}_4$ resembles that in V_2O_3 ;^{16,17} the simpler crystal structure in the case of the ruthenate should be favorable for the analyses and their understanding. We have extended our previous diffraction studies to the entire Sr-content range in $\text{Ca}_{2-x}\text{Sr}_x\text{RuO}_4$ proving that the structural distortion accompanying the metal insulator transition persists to $x \sim 0.15$. For higher Sr content we find a distinct crystal structure, space group $I4_1/acd$, which again presents a structural phase transition upon cooling, however, between two metallic phases.

II. EXPERIMENTAL

The stoichiometric sample of Ca_2RuO_4 , used already in our previous work has been further analyzed at higher temperatures. In addition we have prepared samples of $\text{Ca}_{2-x}\text{Sr}_x\text{RuO}_4$ with $x=0.1, 0.2, 0.5, 1.0,$ and 1.5 by the technique described in Ref. 7, details will be given elsewhere.¹⁸ Thermogravimetric studies indicate a stoichiometric oxygen content in these mixed compounds. All samples were characterized by x-ray diffraction and by magnetic measurements.

Neutron diffraction studies were performed at the Orphée reactor using the two diffractometers 3T.2 ($\lambda=1.226 \text{ \AA}$) and G4.1 ($\lambda=2.43 \text{ \AA}$). With the shorter wavelength instrument it is possible to perform complete Rietveld structure analyses whereas the longer wavelength multi-counter machine offers a higher flux permitting the measurement of temperature dependencies. For more details of the diffraction analyses see our first paper.⁸

Two single-crystals with $x=0.2$ and $x=0.5$ were obtained by a floating zone technique; these were examined on the two-axis diffractometer 3T.1 using pyrolytic graphite monochromator and filters.

III. RESULTS AND DISCUSSION

A. Metal insulator transition in $\text{Ca}_2\text{RuO}_{4.0}$ and in $\text{Ca}_{1.9}\text{Sr}_{0.1}\text{RuO}_4$

The strong temperature dependence of the structural parameters of $\text{Ca}_2\text{RuO}_{4.0}$ observed near room temperature indicates a structural phase transition in the temperature range 350–400 K. Indeed such a transition has been recently reported by Alexander *et al.* based on x-ray diffraction and resistivity studies.¹² In a first view, one might argue that the transition in $\text{Ca}_2\text{RuO}_{4.07}$ is just shifted to higher temperature in the stoichiometric sample, but the detailed structure analysis presents significant differences.

Using a cryofurnace the structure was studied on G4.1 by recording a complete hysteresis cycle. At temperatures near 340 K, we already observe two phases, the low-temperature

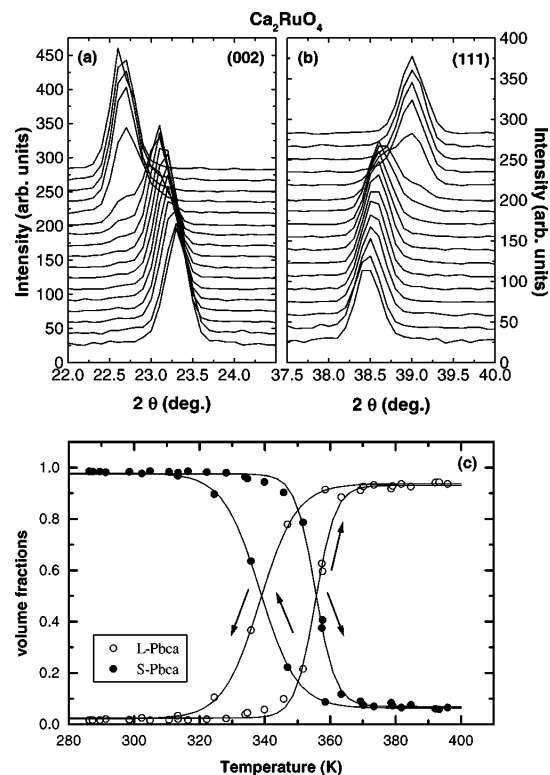


FIG. 1. Comparison of the high flux powder diffraction patterns, showing the (002) (a) and (111) (b) reflections, obtained in $\text{Ca}_2\text{RuO}_{4.0}$ between 286 and 400 K. The bottom curves correspond to $T=286 \text{ K}$. The upper ones were taken approximately every 5 K up to 398 K. (c) Temperature dependence of the partial volume fractions of the *L-Pbca* and *S-Pbca* phases for $\text{Ca}_2\text{RuO}_{4.0}$. The temperature variation is indicated by arrows.

phase is characterized by a small *c*-lattice parameter (*S-Pbca*) compared to the high-temperature phase with long *c* (*L-Pbca*); the averaged in-plane parameter exhibits the opposite behavior as can be seen in Fig. 1(b). The transition in stoichiometric $\text{Ca}_2\text{RuO}_{4.0}$ is sharper than in $\text{Ca}_2\text{RuO}_{4.07}$; at 365 K it is almost complete, and at 395 K there is no sign of the low-temperature *S-Pbca* phase in the high flux patterns, parts of the high flux patterns are shown in Figs. 1(a), 1(b). To avoid possible variation in oxygen stoichiometry during the hysteresis cycle, the temperature was limited to 400 K. Also the high resolution pattern obtained at 400 K can be refined by a single *S-Pbca* phase, the results are given in Table I. [Throughout the paper we use the same notations as in Ref. 8; O(1) denotes the oxygen in the RuO_2 planes and O(2) the apical one. The rotation angle is unique and designed by Φ , whereas the tilt angle may be determined at the two oxygen sites $\Theta\text{-O}(1)$ and $\Theta\text{-O}(2)$; in the notation used here the tilt is always around an axis close to the *b* axis in *Pbca*.] In Fig. 1(c) we show the temperature dependence of the *L*- and *S-Pbca*-phase volumes. The transition temperature obtained in up-strike, $T_S=356 \text{ K}$, is in

TABLE I. Results of the high resolution powder diffraction analyses on $\text{Ca}_{2-x}\text{Sr}_x\text{RuO}_4$ at 300 and at 10 K. O(1) denotes the oxygen in the RuO_2 planes and O(2) the apical one. The rotation angle is unique and designed by Φ whereas the tilt angle may be determined at the two oxygen sites, Θ -O(1) and Θ -O(2). Note that in $Pbca$ the tilt is always around the b axis, whereas the orthorhombic splitting may change sign. U_{\parallel} and U_{\perp} denote the mean-square atomic displacements parallel and perpendicular to the Ru-O bonds. $\text{O}(1)\text{-O}(1)_{\parallel a,b}$ denote the length of the edge of the octahedron basal plane along a, b , respectively. Errors are given in parentheses and result from the least square fitting; therefore they do not take account of systematic errors and underestimate effects of correlations.

| Composition | $x=0.0$ | $x=0.0$ | $x=0.1$ | $x=0.1$ | $x=0.2$ | $x=0.2$ | $x=0.5$ | $x=0.5$ |
|--|------------|------------|------------|------------|------------|-------------|-----------------------|-----------------------|
| temperature | 180 K | 400 K | 10 K | 300 K | 10 K | 300 K | 10 K | 300 K |
| space group | $S-Pbca$ | $L-Pbca$ | $S-Pbca$ | $L-Pbca$ | $L-Pbca$ | $L-Pbca$ | $I4_1/acd$ | $I4_1/acd$ |
| a (\AA) | 5.3945(2) | 5.3606(3) | 5.4207(4) | 5.3494(3) | 5.3304(4) | 5.3295(5) | 5.3195(1) | 5.3395(1) |
| b (\AA) | 5.5999(3) | 5.3507(3) | 5.4802(6) | 5.3420(3) | 5.3190(5) | 5.3232(4) | .. | .. |
| c (\AA) | 11.7653(5) | 12.2637(4) | 11.9395(6) | 12.3219(4) | 12.4094(7) | 12.4506(7) | $2 \times 12.5867(3)$ | $2 \times 12.5749(3)$ |
| Vol (\AA^3) | 355.41(3) | 351.76(2) | 354.67(5) | 352.12(3) | 351.84(5) | 353.22(5) | $2 \times 356.17(1)$ | $2 \times 358.51(1)$ |
| $ e $ | 0.0187 | 0.0009 | 0.0055 | 0.007 | 0.0011 | 0.0006 | / | / |
| R_{wp} (%) | 5.81 | 5.39 | 5.16 | 5.84 | 5.95 | 5.48 | 5.15 | 4.26 |
| Ca x | 0.0042(4) | 0.0110(5) | 0.0083(4) | 0.0099(6) | 0.0133(7) | 0.0103(15) | 0 | 0 |
| y | 0.0559(4) | 0.0269(5) | 0.0425(4) | 0.0214(6) | 0.0169(9) | 0.0157(12) | 1/4 | 1/4 |
| z | 0.3524(2) | 0.3479(1) | 0.3505(2) | 0.3481(1) | 0.3475(2) | 0.3482(2) | 0.5492(1) | 0.5494(1) |
| U_{iso} (\AA^2) | 0.0052(5) | 0.0112(4) | 0.0039(5) | 0.0053(6) | 0.0073(4) | 0.0138(9) | 0.0022(3) | 0.0090(3) |
| Ru U_{iso} (\AA^2) | 0.0025(4) | 0.0050(4) | 0.0011(3) | 0.0045(4) | 0.0007(4) | 0.0029(5) | 0.0014(3) | 0.0042(3) |
| O(1) x | 0.1961(3) | 0.1939(4) | 0.1974(3) | 0.1934(4) | 0.1958(6) | 0.1944(6) | 0.1933(2) | 0.1949(2) |
| y | 0.3018(4) | 0.3064(4) | 0.3016(3) | 0.3056(4) | 0.3064(6) | 0.3070(6) | $x + 1/4$ | $x + 1/4$ |
| z | 0.0264(2) | 0.0147(2) | 0.0229(1) | 0.0127(2) | 0.0126(3) | 0.0075(6) | 1/8 | 1/8 |
| $U_{\perp \text{ plane}}$ (\AA^2) | 0.0047(5) | 0.0116(6) | 0.0024(6) | 0.0100(5) | 0.0023(9) | 0.0088(8) | 0.0052(16) | 0.0092(16) |
| $U_{\parallel \text{ plane}}$ (\AA^2) | 0.0055(5) | 0.0033(5) | 0.0031(6) | 0.0020(6) | 0.0005(2) | 0.0054(5) | 0.0024(8) | 0.0040(7) |
| $U_{\text{long axis}}$ (\AA^2) | 0.0112(10) | 0.0205(8) | 0.0171(9) | 0.0245(12) | 0.0166(16) | 0.0228(18) | 0.0152(6) | 0.0211(6) |
| O(2) x | -0.0673(3) | -0.0386(3) | -0.0583(2) | -0.0340(4) | -0.0368(5) | -0.0187(14) | 0 | 0 |
| y | -0.0218(4) | -0.0067(4) | -0.0141(4) | -0.0079(6) | -0.0078(5) | -0.0051(10) | 1/4 | 1/4 |
| z | 0.1645(2) | 0.1656(1) | 0.1645(1) | 0.1649(1) | 0.1652(2) | 0.1644(2) | 0.4568(1) | 0.4568(1) |
| U_{\perp} (\AA^2) | 0.0093(5) | 0.0169(6) | 0.0070(5) | 0.0151(5) | 0.0044(7) | 0.0162(10) | 0.0084(3) | 0.0142(3) |
| U_{\parallel} (\AA^2) | 0.0042(8) | 0.0117(8) | 0.0053(9) | 0.0079(7) | 0.0035 | 0.0051(10) | 0.0050(7) | 0.0080(7) |
| Ru-O(1) (\AA) | 2.004(2) | 1.949(2) | 1.987(2) | 1.939(2) | 1.927(3) | 1.928(4) | 1.929(1) | 1.933(1) |
| | 2.018(2) | 1.950(2) | 1.988(2) | 1.948(2) | 1.942(3) | 1.937(3) | / | / |
| Ru-O(2) (\AA) | 1.973(1) | 2.042(1) | 1.991(2) | 2.040(2) | 2.060(3) | 2.050(3) | 2.059(3) | 2.057(3) |
| Ru-O _{aver} (\AA) | 1.998 | 1.980 | 1.989 | 1.973 | 1.976 | 1.972 | 1.972 | 1.974 |
| O(1)-O(1) $_{\parallel a}$ (\AA) | 2.828(1) | 2.771(1) | 2.822(1) | 2.758(1) | 2.750(2) | 2.739(2) | 2.727(2) | 2.734(2) |
| O(1)-O(1) $_{\parallel b}$ (\AA) | 2.860(1) | 2.742(1) | 2.799(1) | 2.739(1) | 2.722(1) | 2.727(2) | .. | .. |
| Vol RuO_6 (\AA^3) | 10.64 | 10.34 | 10.48 | 10.27 | 10.28 | 10.21 | 10.21 | 10.25 |
| Θ -O(1) (deg.) | 12.69(10) | 7.49(10) | 11.16(5) | 6.52(10) | 6.6(2) | 3.9(3) | / | / |
| Θ -O(2) (deg.) | 11.19(8) | 5.91(7) | 9.40(7) | 5.25(11) | 5.59(11) | 2.9(3) | / | / |
| Φ (deg.) | 11.93(5) | 12.77(6) | 11.77(5) | 12.65(6) | 12.47(9) | 12.69(10) | 12.78(3) | 12.43(3) |

excellent agreement with that observed by Alexander *et al.*¹² $T_S = 357$ K. The observed hysteresis of about 20 K clearly confirms the first order nature of the transition. We conclude that the combined electronic and structural transition first observed in $\text{Ca}_2\text{RuO}_{4.07}$ also occurs in the stoichiometric compound.

In order to complete the study of the phase transition in $\text{Ca}_2\text{RuO}_{4.0}$ high resolution patterns have been recorded at 400 and at 180 K. The structure of the high-temperature $L-Pbca$ phase could not be established unambiguously in $\text{Ca}_2\text{RuO}_{4.07}$.⁸ Space group $Pbca$ combines a rotation of the octahedra around the c axis with a tilt around an axis parallel

to an edge of the octahedron basal plane. In contrast in space group $P2_1/c$ the tilt can be about an arbitrary direction, in particular around a Ru-O bond. The difference in the two symmetries may be easily tested in the O(1) positions, the tilt around the Ru-O bond displaces only one O(1)-site parallel to c , whereas the tilt around an axis parallel to the edge displaces all O(1) positions about the same distance. In other words, in $Pbca$ all O(1) sites are equivalent whereas there are two of them in $P2_1/c$. In the cuprates the two tilt schemes correspond to the LTO and LTT phases, see, for example, Ref. 19. In the excess oxygen compound a better description of the data was obtained in space group $P2_1/c$

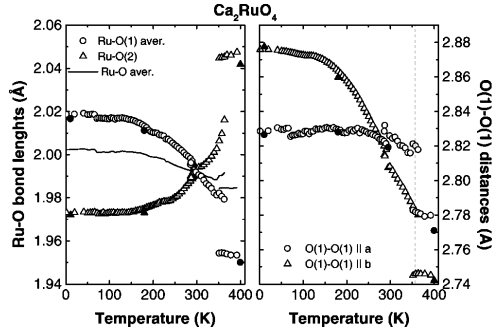


FIG. 2. Temperature dependence of the Ru-O(1)-bond distances in $\text{Ca}_2\text{RuO}_{4.0}$ and that of the edge lengths of the octahedron basal plane.

and in particular free refinement of the two distinct O(1) displacements along c led to significant difference with one displacement almost vanishing, leading to a LTT equivalent tilt scheme. The structure was finally refined with one O(1) site being fixed at $z=0$. In case of the stoichiometric compound at 400 K this is definitely not an appropriate model. In space group $Pbca$ one obtains a R value of 5.39% which increases to 5.62% for the $P2_1/c$ model with one z -O(1) fixed to zero. Refining the $P2_1/c$ phase independently still gives a lower R value than $Pbca$, but this difference is not significant any more. Therefore we conclude that the high-temperature structure in $\text{Ca}_2\text{RuO}_{4.0}$ has the same space group $Pbca$ as the low-temperature structure. We differentiate these phases as L - $Pbca$ and S - $Pbca$, respectively, due to their different c parameters. The large amount of excess oxygen seems to be responsible for the distinct diffraction pattern in $\text{Ca}_2\text{RuO}_{4.07}$.

Combining the new and the previous results⁸ we get the entire picture of the phase transition in $\text{Ca}_2\text{RuO}_{4.0}$. Figure 2 presents the Ru-O bond lengths, which show a discontinuous change at the L - $Pbca$ - S - $Pbca$ transition: the in-plane bonds become elongated and the out-of-plane one is shrinking upon cooling. Close to the transition—but in the S - $Pbca$ phase—the octahedron is still elongated along c in the temperature range 300–330 K. Upon further cooling one observes a continuous and even larger change in the same sense: the octahedron at low temperature is finally flattened along c . The edge lengths of the octahedron basal plane also show a discontinuous effect at the transition followed by a pronounced change in the S - $Pbca$ phase. In accordance to the elongation of the Ru-O(1) bonds these lengths increase upon cooling into the S - $Pbca$ phase where they are still split, the octahedron basal plane is shorter along the tilt axis immediately below the transition. Upon further cooling, the ratio, however, becomes inverted, and the basal plane is strongly stretched along the tilt axis.

In La_2CuO_4 (Ref. 19) and also in all L - $Pbca$ phase ruthenates studied here, the orthorhombic splitting is opposite to the expectation of a rigid tilt, i.e., the lattice is longer perpendicular to the tilt axis. This effect originates from the

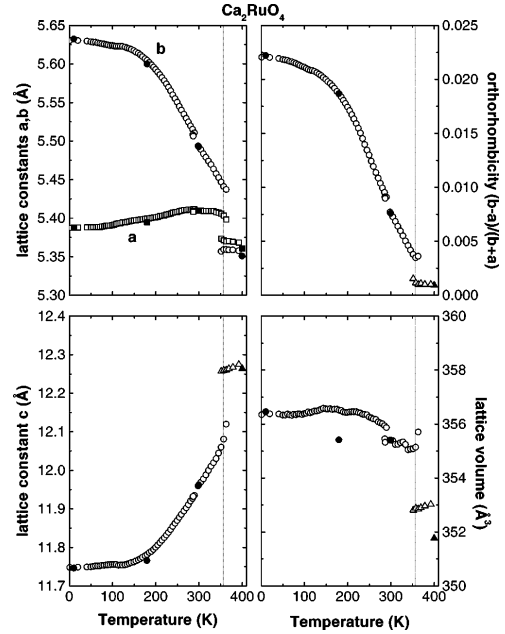


FIG. 3. Temperature dependence of the lattice parameters in $\text{Ca}_2\text{RuO}_{4.0}$. Open symbol designate the results obtained from the high-flux patterns and closed symbols those from the high-resolution studies.

forces in the La-O or Sr-O layer where one distance strongly decreases due to the opposite displacements of an apical oxygen and a neighboring La/Sr site. The stretching of the lattice perpendicular to the tilt axis reduces the pronounced shrinking of this bond and may be seen in the orthorhombic splitting. One should hence consider this behavior as the normal one arising from the structural arrangement. Nevertheless the elongation of the octahedron basal plane might influence the electronic and magnetic properties, see the discussion below. The orthorhombic lattice in $\text{Ca}_2\text{RuO}_{4.0}$, however, is elongated along the tilt axis at low temperature much more than what might be expected for a rigid octahedron tilt; the lattice constants are given in Fig. 3. It is the stretching of the octahedra that causes this orthorhombic splitting, and this behavior should be considered as highly anomalous.

The transition from L - $Pbca$ to S - $Pbca$ is further characterized by an increase in the tilt angles Θ -O(1) [Θ -O(2)] increase from 7.5° [5.9°] at 400 K to 11.2° [9.2°] at 295 K. Upon cooling in the S - $Pbca$ phase these angles first continue to increase till about 180 K and are almost constant below, see Fig. 6 in Ref. 8. The rotation angle decreases by about one degree during the transition into the S - $Pbca$ phase and is constant over the whole S - $Pbca$ temperature range.

In $\text{Ca}_{1.9}\text{Sr}_{0.1}\text{RuO}_4$ we find a structural transition similar to that observed in $\text{Ca}_2\text{RuO}_{4.0}$. Figure 4 presents the volume fractions of the L - $Pbca$ and S - $Pbca$ phases as a function of

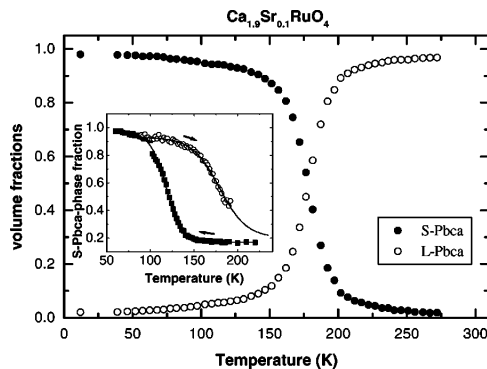


FIG. 4. Temperature dependence of the volume fractions of the *L-Pbca* and *S-Pbca* phases in $\text{Ca}_{1.9}\text{Sr}_{0.1}\text{RuO}_4$ measured on the high flux neutron diffractometer. The inset shows the hysteresis of the transition as obtained by x-ray diffraction.

temperature. The inset presents the hysteresis of the transition which amounts to about 50 K. For the discussion of any temperature dependent property one has to take account of this hysteresis.

The high resolution room-temperature data in the metallic *L-Pbca* phase is again difficult to analyze. Refinements in space group *Pbca* and in space group $P2_1/c$ with or without fixed O(1) site are very close concerning their *R* values. However, as in $\text{Ca}_2\text{RuO}_{4.0}$ —and in contrast to $\text{Ca}_2\text{RuO}_{4.07}$ —the $P2_1/c$ fit does not suggest different O(1)-*z* displacements. Powder diffraction alone, however, is unable to differentiate between *Pbca* and $P2_1/c$ space groups. A diffraction experiment on a single crystal of almost identical composition $\text{Ca}_{1.85}\text{Sr}_{0.15}\text{RuO}_4$, definitely excludes the tilt around the Ru-O bond.²⁰ Since $P2_1/c$ is a subgroup of *Pbca*, the description of Bragg reflection data must be better. However, an extremely small improvement of the *R* value 5.065% for the $P2_1/c$ model compared to 5.078% for the *Pbca* model, does not support the symmetry reduction.²⁰ Therefore, we feel confident to analyze the powder diffraction patterns on excess oxygen free samples in the *L-Pbca* structure.

The transition in $\text{Ca}_{1.9}\text{Sr}_{0.1}\text{RuO}_4$ is much better defined than that in $\text{Ca}_2\text{RuO}_{4.07}$ and there is no *L-Pbca* phase remaining at low temperature. Therefore, it has been possible to analyze the structural details in this compound with the *G4.1* data. Again high resolution patterns have been recorded at 295 and at 11 K with the results of the refinements given in Table I; high flux patterns were measured in temperature steps of 5 K upon heating. Figure 5 presents the temperature dependence of the lattice parameters showing similar discontinuities at the transition, $T_S \approx 175$ K upon heating, as the stoichiometric sample.

In contrast to $\text{Ca}_2\text{RuO}_{4.0}$, the temperature dependence of the structural parameters within the *S-Pbca* phase is only small. In analogy to Fig. 2, Fig. 6 presents the temperature dependent shape of the octahedra in $\text{Ca}_{1.9}\text{Sr}_{0.1}\text{RuO}_4$ (the slight deviations between the high resolution and high flux results must be attributed to the insufficient extent in *Q* space

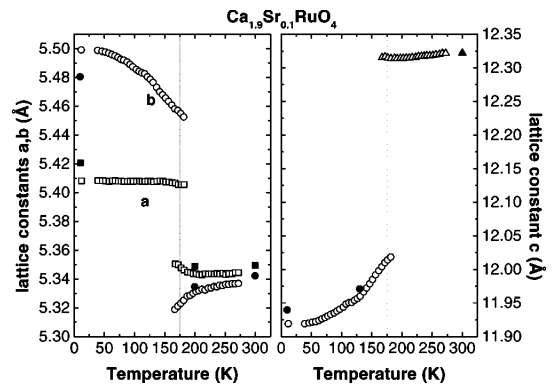


FIG. 5. Temperature dependence of the lattice parameters in $\text{Ca}_{1.9}\text{Sr}_{0.1}\text{RuO}_4$; open symbols designate the results obtained from the high flux studies and closed symbols those from the high resolution experiments.

of the latter data combined with the smaller orthorhombic splitting; nevertheless there is no doubt that these results show the correct tendencies). In $\text{Ca}_{1.9}\text{Sr}_{0.1}\text{RuO}_4$ too we find the discontinuous change at T_S : an increase in the in-plane bond lengths and a shrinking of the Ru-O(2) distance. But in contrast to the stoichiometric compound the octahedron remains slightly elongated along *c* till the lowest temperatures. Also the octahedron edges parallel to the *a, b* plane present the same discontinuous changes as $\text{Ca}_2\text{RuO}_{4.0}$ but not the continuous stretching along *b* in the *Pbca* phase. In particular, the octahedron remains elongated along the *a* axis, i.e., perpendicular to the tilt axis. Due to the larger tilt this elongation may no longer overcompensate the lattice shrinking in the *a* direction, the orthorhombic lattice is therefore longer along *b*.

In $\text{Ca}_{1.9}\text{Sr}_{0.1}\text{RuO}_4$ we also find the jump of the tilt angles at T_S which remain almost constant in the *Pbca* phase. The transition in $\text{Ca}_{1.9}\text{Sr}_{0.1}\text{RuO}_4$ may be characterized as being identical to the one in the pure compound. However, as there

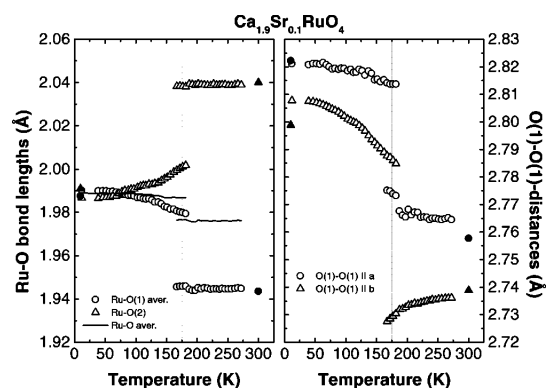


FIG. 6. Temperature dependence of the Ru-O bond distances and that of the octahedron basal-plane-edge lengths in $\text{Ca}_{1.9}\text{Sr}_{0.1}\text{RuO}_4$.

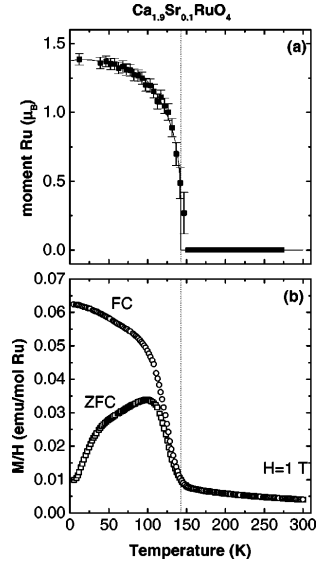


FIG. 7. (a) Temperature dependence of ordered magnetic moment obtained by refinement of the B -centered antiferromagnetic structure of La_2NiO_4 -type in $\text{Ca}_{1.9}\text{Sr}_{0.1}\text{RuO}_4$; (b) temperature dependence of the field-cooled and zero-field-cooled susceptibility. All dependences were recorded upon heating.

are only minor changes of the structural parameters for $\text{Ca}_{1.9}\text{Sr}_{0.1}\text{RuO}_4$ below the phase transition, one may conclude that the structure observed in the pure compound slightly below the transition, is stable to the lowest temperatures for the Sr concentration $x=0.1$; positional and lattice parameters of $\text{Ca}_2\text{RuO}_{4.0}$ at 295 K and $\text{Ca}_{1.9}\text{Sr}_{0.1}\text{RuO}_4$ at 10 K are almost identical, see Table I and Ref. 8.

$\text{Ca}_{1.9}\text{Sr}_{0.1}\text{RuO}_4$ exhibits antiferromagnetic order below $T_N=143$ K, see Fig. 7. There is only one magnetic transition observed in neutron diffraction, and the magnetic arrangement is the B -centered one of La_2NiO_4 type, similar to the observation in Ca_2RuO_4 .⁸ One may note that the direction of the ordered moment in $\text{Ca}_{1.9}\text{Sr}_{0.1}\text{RuO}_4$ remains the b axis, though the shape of the octahedron is different to that of the pure compound. The tilt-direction seems hence to be the element determining the spin-direction and not the stretching of the octahedron, which underlines the importance of anti-symmetric coupling parameters.

The low-temperature susceptibility in $\text{Ca}_{1.9}\text{Sr}_{0.1}\text{RuO}_4$ which has to be attributed to a Dzyaloshinski-Moriya interaction, is even higher than the values reported for La-substituted Ca_2RuO_4 ,¹⁵ therefore, one may assume that magnetic order in these samples too is mainly antiferromagnetic in nature. Nakatsuji *et al.* have observed also the electronic transition associated with an upturn in the resistivity in a series of samples of $\text{Ca}_{2-x}\text{Sr}_x\text{RuO}_4$ in the Sr concentration range up to $x=0.2$.¹³ The details of the coupling between structural magnetic and electronic transition for the highly

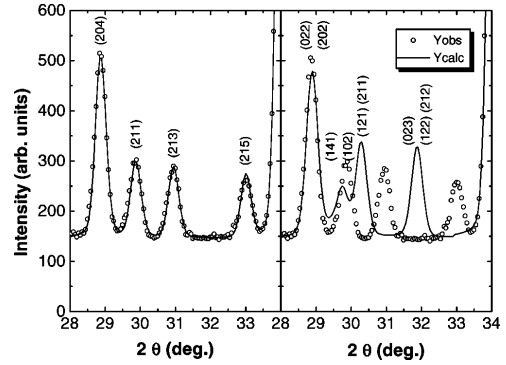


FIG. 8. Comparison of the powder diffraction patterns calculated for the rotational distortion in space group $I4_1/acd$ ($c \sim 24$ Å; left) and in space group Pbc_a ($c \sim 12$ Å; right). The calculated patterns are compared to high resolution data observed for $\text{Ca}_{1.5}\text{Sr}_{0.5}\text{RuO}_4$.

Sr-doped samples need further clarification. The analysis of the existing data obtained in a cooling cycle is hampered by the fact that the down-strike structural transition is below the intrinsic T_N in the $S-Pbc_a$ phase; single crystals, however, crack at the transition and therefore resistivity measurements upon heating become difficult to interpret.

B. Structure of $\text{Ca}_{2-x}\text{Sr}_x\text{RuO}_4$ with $x=0.2, 0.5$, and 1.0

Upon further increase of the Sr concentration the metal-insulator transition is suppressed slightly above $x=0.15$.¹³ The powder sample of $\text{Ca}_{1.8}\text{Sr}_{0.2}\text{RuO}_4$ studied here does not exhibit the anomalous resistivity increase, nor does the one with $x=0.5$.

The high resolution powder patterns on $\text{Ca}_{1.8}\text{Sr}_{0.2}\text{RuO}_4$ indicate a mixture of the $L-Pbc_a$ phase with a second phase whose space group was identified as being $I4_1/acd$. Also the sample with still higher Sr content, $\text{Ca}_{1.5}\text{Sr}_{0.5}\text{RuO}_4$, showed the same symmetry. In space group $I4_1/acd$ the octahedra are rotated around the c axis, but, with a stacking different to that in Pbc_a ; in addition the tilt of the octahedra is not allowed. In $I4_1/acd$ the RuO_2 planes separated by 12.5 Å are distorted with an opposite phase which yields a doubling of the c parameter. This symmetry is well known from related compounds such as Sr_2IrO_4 (Refs. 21 and 22) or Sr_2RhO_4 .²³ The observation of a phase with only a rotational distortion agrees furthermore to the analysis of the phonon dispersion in Sr_2RuO_4 ; it was reported that only the rotational mode is close to instability.²⁴ By neutron diffraction the $I4_1/acd$ and Pbc_a phases may be easily distinguished, since the superstructure reflections related to the rotation occur at different l values due to the distinct stacking, see for example the positions of the $(2\ 1\ 1)$ reflections shown in Fig. 8.

The volume fraction of the $I4_1/acd$ phase in $\text{Ca}_{1.8}\text{Sr}_{0.2}\text{RuO}_4$ is small and upon cooling it decreases from 21% at room temperature to 12% at 11 K; this indicates that

the first order phase boundary between $L\text{-}Pbca$ and $I4_1/acd$ is close to this composition. A single crystal of nominal the same composition $x=0.2$ showed a different structure: a single phase $I4_1/acd$ structure at room temperature followed by a second order transition upon cooling. A minor deviation from the nominal stoichiometry or a subtle influence in the real structure may be responsible for this difference. We emphasize that this is the only case where we do not find perfect agreement between single crystal and powder samples. On the 3T.1 diffractometer the intensities of different reflections were followed as function of temperature for the single crystal of $\text{Ca}_{1.8}\text{Sr}_{0.2}\text{RuO}_4$. At low temperature several reflections—for example, (3 0 4) in $I4_1/acd$ notation—appear which are forbidden in the $I4_1/acd$ symmetry. The transition is continuous with only a minor first order contribution close to the transition. The type of the observed superstructure reflections clearly indicates that the low temperature phase possesses a nonvanishing tilt. The intensity profiles show strong orthorhombic splitting and the characteristics of twinning similar to observations in the orthorhombic phase in $(\text{La}/\text{Sr})_2\text{CuO}_4$.¹⁹ The most likely space group therefore arises from the combination of the $I4_1/acd$ rotation with the octahedron tilt of the LTO type: $Pbca$ where, however, the c axis is doubled in respect to the $L\text{-}Pbca$ and $S\text{-}Pbca$ phases discussed above. A preliminary Bragg intensity data set can be satisfactorily described within this space group.²⁰ Interestingly the tilt distortion exhibits a different period along the c axis, i.e., just one c -parameter ($c \sim 12 \text{ \AA}$) whereas the period of the rotation is $2c$. In general the tilt-phonon-modes show a finite dispersion fixing the stacking sequence, which arises from displacements of the apical oxygens.²⁴ The interaction of the two order parameters corresponding to different propagation vectors $\mathbf{q}_{\text{tilt}} = (0.5, 0.5, 0)$ and $\mathbf{q}_{\text{rotation}} = (0.5, 0.5, 0.5)$, might be an interesting problem; it certainly explains the first order phase transition occurring near $x=0.2$ as a function of Sr content. The stronger tilt near $x=0.2$ forces the rotational distortion, whose stacking sequence is much less defined,²⁴ into the same one- c period. We conclude that for a Sr concentration close to $x=0.2$, the structure needs a tilt distortion either in the subgroup of $I4_1/acd$ (single crystal) or in $Pbca$ (powder).

The high resolution powder patterns obtained on $\text{Ca}_{1.5}\text{Sr}_{0.5}\text{RuO}_4$ clearly indicate an unique $I4_1/acd$ phase. There is only little temperature dependence in the structure of $\text{Ca}_{1.5}\text{Sr}_{0.5}\text{RuO}_4$ as it is shown in Table I. In the $I4_1/acd$ structure, there are only three positional parameters $z\text{-Ca}$, $z\text{-O}(2)$, and $x\text{-O}(1)$ and only the latter changes significantly related to the increase of the octahedron rotation angle by about 3% between 295 and 11 K, from $12.43(3)^\circ$ to $12.78(3)^\circ$. In the high flux patterns, no indication for long range magnetic order has been observed yielding an upper limit for a long range ordered magnetic moment of $0.15\mu_B$.

A small single crystal of $\text{Ca}_{1.5}\text{Sr}_{0.5}\text{RuO}_4$ has been studied on the 3T.1 thermal neutron diffractometer as a function of temperature. The temperature dependence of the superstructure intensity shown in Fig. 9, indicates a second order phase transition similar to the one observed for $x=0.2$. The smaller Ca content causes a reduced transition temperature

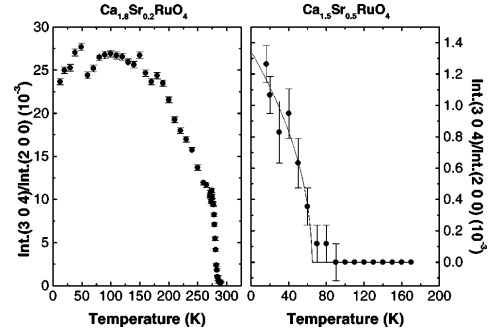


FIG. 9. Temperature dependence of (3 0 4) ($I4_1/acd$ notation) superstructure reflection intensity scaled to that of the (200) fundamental reflection in two single crystals of compositions $\text{Ca}_{1.8}\text{Sr}_{0.2}\text{RuO}_4$ (left) and $\text{Ca}_{1.5}\text{Sr}_{0.5}\text{RuO}_4$ (right).

and a weaker tilt at low temperature, as can be deduced from the smaller relative intensity observed in this crystal, see Fig. 9. In the powder sample of the same composition $x=0.5$, we find only a weak anomaly in the c -axis parameter, observed at 65 K. The c parameter should be quite sensitive to an octahedron tilt, since the projection of the octahedra along c varies with the cosine of the tilt angle. As may be seen in Fig. 9, the superstructure reflections observed on the single crystal are not strong enough to be detected by powder neutron diffraction.

The compound with $x=1.0$ was studied at room temperature and at 11 K by high resolution diffraction. We find at both temperatures a pure $I4_1/acd$ phase, however, there is evidence for disorder in the rotation scheme. The refinement was significantly improved by splitting the O(1) position into two sets of positions $(x, |x| + \frac{1}{4}, \frac{1}{8})$, with $x = \pm \delta$ similar to the observation in Ref. 22 for Sr_2IrO_4 . The average rotation angle is temperature independent, $10.80(3)^\circ$ at room temperature and $10.75(3)^\circ$ at low temperature. Assuming that the square of the rotation angle varies linearly with the concentration, one would estimate the critical concentration for the appearance of the pure rotation distortion near $x=2.5$. From this consideration one would expect pure Sr_2RuO_4 to exhibit the same rotation in obvious contradiction to the observation that it remains undistorted till low temperature.²⁵ For a Sr concentration of $x=1.5$ we already do not find any long range rotation distortion order in the powder sample. However, there is sizable diffuse scattering—strong enough to be detected by powder diffraction—indicating that the rotation distortion still exists on a short range scale. The single crystal diffraction studies on the pure Sr_2RuO_4 ,²⁵ which are more sensitive to diffuse scattering than powder diffraction, did not reveal any indication for a local rotational distortion.

C. Phase diagram of $\text{Ca}_{2-x}\text{Sr}_x\text{RuO}_4$

According to the studies presented above the structural and magnetic phase diagram of $\text{Ca}_{2-x}\text{Sr}_x\text{RuO}_4$ is rather complicated, a schematic picture is given in Fig. 10, which also presents the results of the magnetic studies by Nakatsuji

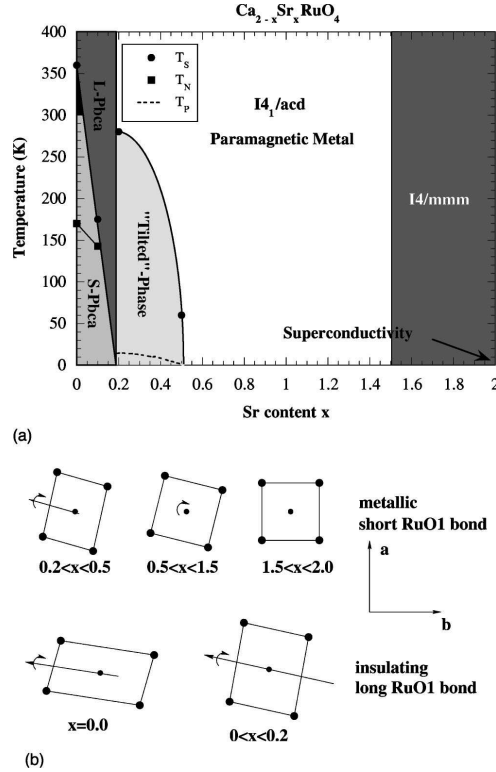


FIG. 10. Phase diagram of $\text{Ca}_{2-x}\text{Sr}_x\text{RuO}_4$ including the different structural and magnetic phases and the occurrence of the maxima in the magnetic susceptibility (Ref. 13). In the lower part, we schematically show the tilt and rotation distortion of the octahedra [only the basal square consisting of the Ru (small points) and the O(1) (larger points) is drawn] together with the elongation of the basal planes. Note that all phases are metallic except for $S\text{-Pbca}$.

*et al.*¹³ In addition the tilt and rotation angles together with the deformation of the octahedron basal plane are depicted. At low temperature and for decreasing Sr concentration, one passes from the undistorted K_2NiF_4 structure in pure Sr_2RuO_4 , space group $I4/mmm$, to a simple rotation $I4_1/acd$ in agreement to the low lying rotation mode in the pure compound.²⁴ An estimated boundary is included in the diagram in Fig. 10, though the transition is found to exhibit order-disorder character. For a Sr concentration of $x=1.5$ only diffuse scattering representative of a short range rotational distortion is present. For $x=1.0$ the rotational angle already amounts to 10.8° ; the rapid suppression of the structural distortion in Sr-rich samples appears to be extraordinary it might hide some further effect. For much smaller Sr content, near $x=0.5$, a combination of rotation and small tilt is found. This is realized either in a subgroup of $I4_1/acd$ or in $Pbca$. Further decrease of the Sr-content leads finally to

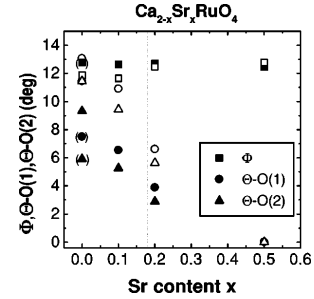


FIG. 11. The Sr concentration dependence of the tilt $\Theta\text{-O}(1)$ and $\Theta\text{-O}(2)$ and rotation angle Φ in $\text{Ca}_{2-x}\text{Sr}_x\text{RuO}_4$. The filled symbols denote the results obtained at $T=300\text{ K}$ (those with brackets are obtained at $T=400\text{ K}$) and the open symbols are those at $T=10\text{ K}$, the dashed line indicates the critical concentration below which one observes the insulating $S\text{-Pbca}$ phase at low temperature.

the combination of the rotation and the large tilt in the $S\text{-Pbca}$ phase. The Sr dependence of the tilt and rotation angles is resumed in Fig. 11. Most interestingly all these structural transitions are closely coupled to the physical properties.

The purely rotational distortion should be related to the c -axis resistivity since it modifies the overlap of the O orbitals in the c direction. This rotation phase becomes unstable against the tilt for Sr concentrations lower than 0.5, since in the single crystal with $x=0.5$ only a minor distortion has been observed, which remained undetectable in the powder sample. For the Sr concentration of $x=0.2$ we already find tilt angles of about 7° at low temperature by powder neutron diffraction. Near $x=0.5$ there is hence the quantum critical point of the continuous tilt transition which coincides with a maximum in the low temperature magnetic susceptibility. For $x=0.5$, Nakatsuji *et al.* report a low-temperature magnetic susceptibility about 100 times larger than that of pure Sr_2RuO_4 .¹³ This suggests that the low-lying tilt modes are strongly coupled to the magnetism. This interpretation is further supported by the fact that in all magnetically ordered structures $x=0.0$, $x=0.1$, and in $\text{Ca}_2\text{RuO}_{4.07}$, the spin direction is parallel to the tilt axis in spite of a different octahedron shape as it is schematically drawn in Fig. 10. Decrease of the Sr content below $x=0.5$ stabilizes the tilt and causes a maximum in the temperature dependence of the susceptibility at $T=T_p$, indicated in Fig. 10.¹³ T_p , however, does not coincide with the structural transition from $I4_1/acd$ to the tilted phase but is much lower. We speculate that the susceptibility maximum arises from an increase of antiferromagnetic fluctuations induced by the tilt.

There is another anomalous feature in the temperature dependent susceptibility of samples with $0.2 < x < 0.5$: Nakatsuji *et al.* find a strong magnetic anisotropy between the a and b directions of the orthorhombic lattice.¹³ In relation to the magnetic order in the insulating compounds it appears again most likely that the tilt axis, which is parallel b , is the cause of the huge anisotropy. However, there might be an

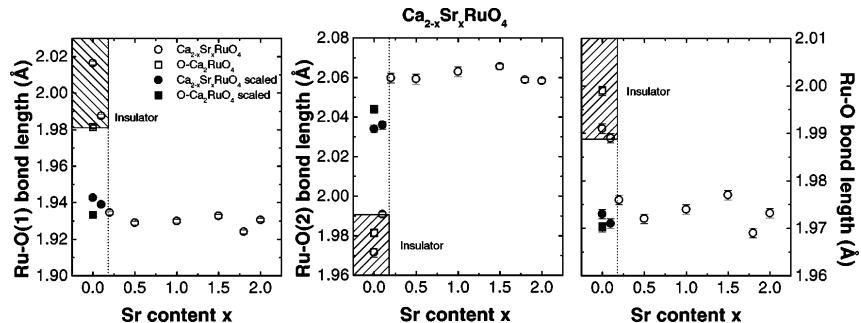


FIG. 12. Composition dependence of the Ru-O(1)-, Ru-O(2)-, and averaged Ru-O-bond distances in $\text{Ca}_{2-x}\text{Sr}_x\text{RuO}_4$ at 10 K open symbol. Filled symbols were obtained by extrapolating the distances obtained in the high temperature metallic phase to 10 K using the thermal expansion of Sr_2RuO_4 ; the dashed line designates the critical concentration for the metal insulator transition.

additional more complex effect related to the band structure, which is described for Sr_2RuO_4 , for example, in Ref. 10. Three bands are crossing the Fermi level a quasi-two-dimensional band related to the d_{xy} orbitals and quasi-one-dimensional bands related to d_{xz} and d_{yz} orbitals. The elongation of the octahedron basal plane will lift the degeneracy between d_{xz} and d_{yz} orbitals (in order to demonstrate this, one may choose an orbital set rotated around the c axis by 45°) and might via this mechanism enhance the anisotropy.

For Sr concentrations lower than 0.2 we find the $Pbca$ symmetry and the first order phase transition leading to the insulating $S-Pbca$ phase. The metal-insulator transition is hence observed as a function of concentration as well as a function of temperature.

In the Sr range $0.2 \leq x \leq 2$ all samples are found to be metallic at low temperature and there is little variation of the octahedron shape and in particular of the in-plane Ru-O bond lengths when compared to that observed in Sr_2RuO_4 .^{25,26} The concentration dependent octahedron shape is shown in Fig. 12. Metallic 214 ruthenates appear to be identical at least concerning their Ru-O bond distances. The minor deviation near $x=0.2$ may be explained by the relaxed constraint in the tilted structure. For smaller Sr content the metal-insulator transition occurs, but one may still compare to the Ru-O(1) bonds in the metallic high temperature phase. For this purpose we have scaled the high resolution results in the metallic phase of the three samples presenting the metal insulator transition $\text{Ca}_2\text{RuO}_{4.0}$, $\text{Ca}_2\text{RuO}_{4.07}$ and $\text{Ca}_{1.9}\text{Sr}_{0.1}\text{RuO}_4$, by the thermal expansion of Sr_2RuO_4 .²⁶ The scaling by the thermal expansion of pure Sr_2RuO_4 is not fully justified, since the temperature dependent tilt and rotation should alter the thermal expansion. This and the insertion of additional oxygen should explain the minor deviations. Also the scaled values for samples which are insulating at low temperature are comparable to pure Sr_2RuO_4 . This demonstrates the equivalence of the metal-insulator transition as a function of temperature and as a function of concentration.

Concerning the metal-insulator transition it appears necessary to separate two effects. In all samples exhibiting an insulating low temperature phase there is an increase of the in-plane bond lengths and a reduction of the Ru-O(2) dis-

tance accompanied with the increase of the tilt angle. This effect has to account for the nonmetallic behavior. Within a Mott-scenario¹⁶ one may phenomenologically explain the effect, since both tilting and increase of the in-plane distances should strongly reduce the band-width. In particular the band corresponding to the d_{xy} orbital should become more localized and lower in energy. The second effect is found only in the stoichiometric compound where the transition is not complete immediately below T_S ; instead the octahedron becomes flattened mainly due to the elongation of the basal plane along the b axis which is the direction of the spins in the antiferromagnetic ordered structure. We do not think that this rather peculiar behavior can be explained by simple structural arguments. It appears likely that the spin-orbit coupling in the nonmetallic phase causes the low-temperature structural anomalies. The reason why similar effects do not occur in $\text{Ca}_2\text{RuO}_{4.07}$ and in $\text{Ca}_{1.9}\text{Sr}_{0.1}\text{RuO}_4$ might be found in their remaining itinerant character. Spin-orbit coupling also forces the spin direction parallel to the tilt axis, which will strongly reduce the weak ferromagnetism along the c direction. Due to the flattening the d_{xy} orbital should be well separated in energy and be filled, see also the discussion in Ref. 14. The remaining two electrons occupy the d_{xz} and d_{yz} orbitals whose degeneracy is lifted by the elongation of the octahedron basal plane along b by spin-orbit coupling or by a Jahn-Teller effect.⁸

IV. CONCLUSION

The phase diagram of $\text{Ca}_{2-x}\text{Sr}_x\text{RuO}_4$ shows a variety of different structural, magnetic, and electronic phases. The distinction between metallic and insulating compounds appears to arise from an enhanced in-plane Ru-O bond distance and a larger tilt. This behavior suggests the interpretation as a Mott transition related to the lowering in energy of the d_{xy} band. Samples with strongly flattened octahedra are driven nonmetallic by the structural transition, whereas in a sample with a reduced flattening the metal-insulator transition is close to the magnetic ordering. The local character of the moments in the insulator induces an additional structural distortion via spin-orbit coupling.

In the part of the phase diagram where samples stay metallic to low temperature, first a rotation and second a tilt distortion develops upon increase of the Ca content. This should be considered as the purely structural consequence of the smaller ionic radius of the Ca. The observation of the maxima in the temperature dependence of the magnetic susceptibility only for samples presenting an octahedron tilt, and the fact that the maximum low-temperature susceptibility is found near the composition where the tilt distortion vanishes, clearly indicate strong magnetoelastic coupling.

The tilt seems to play a key role in the magnetoelastic coupling since in all magnetically ordered structures the spin direction is parallel to the tilt even though the shape of the octahedron is rather distinct. Furthermore, in the intermediate metallic region, $0.2 < x < 0.5$, which exhibits a tilt distortion,

a strong anisotropy is found for the susceptibility parallel and perpendicular to the tilt axis. Due to purely structural constraints the tilt leads to an elongation of the octahedron basal plane, which may lift the degeneracy of the d_{xz} and d_{yz} orbitals.

The magnetic and electronic degrees of freedom in the 214 ruthenates are hence closely coupled to each other and also to the lattice. Whether one of these couplings—and which one—is responsible for the occurrence of superconductivity in Sr_2RuO_4 , however, remains an open question.

ACKNOWLEDGMENTS

We wish to acknowledge D. I. Khomskii, I. I. Mazin, and P. Pfeuty for stimulating discussions.

-
- ¹Y. Maeno, H. Hashimoto, K. Yoshida, S. Nishizaki, T. Fujita, J. G. Bednorz, and F. Lichtenberg, *Nature (London)* **372**, 532 (1994).
- ²K. Ishida, H. Mukuda, Y. Kitaoka, K. Asayama, Z. Q. Mao, Y. Mori, and Y. Maeno, *Nature (London)* **396**, 658 (1998).
- ³J. J. Neumeier, M. F. Hundley, M. G. Smith, J. D. Thompson, C. Allgeier, H. Xie, W. Yelon, and J. S. Kim, *Phys. Rev. B* **50**, 17 910 (1994).
- ⁴Y. Maeno, K. Yoshida, H. Hashimoto, S. Nishizaki, S. Ikeada, M. Nohara, T. Fujita, A. P. Mackenzie, N. E. Hussey, J. G. Bednorz, and F. Lichtenberg, *J. Phys. Soc. Jpn.* **66**, 1405 (1997).
- ⁵T. M. Rice and M. Sigrist, *J. Phys.: Condens. Matter* **7**, L643 (1995).
- ⁶A. Callaghan, C. W. Moeller, and R. Ward, *Inorg. Chem.* **5**, 1572 (1966); J. M. Longo, P. M. Raccach, and J. B. Goodenough, *J. Appl. Phys.* **39**, 1372 (1968).
- ⁷S. Nakatsuji, S. Ikeda, and Y. Maeno, *J. Phys. Soc. Jpn.* **66**, 1868 (1997).
- ⁸M. Braden, G. André, S. Nakatsuji, and Y. Maeno, *Phys. Rev. B* **58**, 847 (1998).
- ⁹G. Cao, S. McCall, M. Shephard, J. E. Crow, and R. P. Guertin, *Phys. Rev. B* **56**, R2916 (1997).
- ¹⁰I. I. Mazin and D. J. Singh, *Phys. Rev. Lett.* **79**, 733 (1997).
- ¹¹Y. Sidis, M. Braden, P. Bourges, B. Hennion, S. Nishizaki, Y. Maeno, and Y. Mori, *Phys. Rev. Lett.* **83**, 3320 (1999).
- ¹²C. S. Alexander, G. Cao, V. Dobrosavljevic, S. McCall, J. E. Crow, E. Lochner, and R. P. Guertin, *Phys. Rev. B* **60**, R8422 (1999); note that the temperature dependence of the lattice constants does not agree to our results.
- ¹³S. Nakatsuji, T. Ando, Z. Mao, and Y. Maeno, *Physica C* **259**, 949 (1999); S. Nakatsuji and Y. Maeno, *Phys. Rev. Lett.* **84**, 2666 (2000).
- ¹⁴S. Nakatsuji and Y. Maeno, *Phys. Rev. B* **62**, 6458 (2000).
- ¹⁵G. Cao, S. McCall, C. S. Alexander, J. E. Crow, and R. P. Guertin, *Phys. Rev. B* **61**, R5053 (2000).
- ¹⁶N. F. Mott, *Metal-Insulator Transitions*, 2nd ed. (Taylor & Francis, London, 1990).
- ¹⁷W. Bao, C. Broholm, G. Aeppli, S. A. Carter, P. Dai, T. F. Rosenbaum, J. M. Honig, P. Metcalf, and S. F. Trevino, *Phys. Rev. B* **58**, 12 727 (1998).
- ¹⁸S. Nakatsuji *et al.* (unpublished).
- ¹⁹M. Braden, P. Schweiss, G. Heger, W. Reichardt, Z. Fisk, K. Gamayunov, I. Tanaka, and H. Kojima, *Physica C* **223**, 396 (1994).
- ²⁰M. Braden *et al.* (unpublished).
- ²¹M. K. Crawford, M. A. Subramanian, R. L. Harlow, J. A. Fernandez-Baca, Z. R. Wang, and D. C. Johnston, *Phys. Rev. B* **49**, 9198 (1994).
- ²²Q. Huang, J. L. Soubeyroux, O. Chmaissem, I. Natali Sora, A. Santoro, R. J. Cava, J. J. Krajewski, and W. F. Peck, Jr., *J. Solid State Chem.* **112**, 355 (1994).
- ²³M. A. Subramanian, M. K. Crawford, R. L. Harlow, T. Ami, J. A. Fernandez-Baca, Z. R. Wang, and D. C. Johnston, *Physica C* **235–240**, 743 (1994).
- ²⁴M. Braden, W. Reichardt, S. Nishizaki, Y. Mori, and Y. Maeno, *Phys. Rev. B* **57**, 1236 (1998).
- ²⁵M. Braden, H. Moudou, S. Nishizaki, Y. Maeno, and T. Fujita, *Physica C* **273**, 248 (1997).
- ²⁶O. Chmaissem, J. D. Jorgensen, H. Shaked, S. Ikeda, and Y. Maeno, *Phys. Rev. B* **57**, 5067 (1998).

Neutron diffraction study of the crystal structure of $\text{Ca}_{1.5}\text{Sr}_{0.5}\text{RuO}_4$

O. Friedt¹, M. Braden^{1,2}, G. André¹, S. Nakatsuji³, Y. Maeno^{3,4}

¹ Laboratoire Léon Brillouin, C.E.A./C.N.R.S., F-91191 Gif-sur-Yvette CEDEX, France

² Forschungszentrum Karlsruhe, IFP, Postfach 3640, D-76021 Karlsruhe, Germany

³ Department of Physics, Kyoto University, Kyoto 606-8502, Japan

⁴ CREST, Japan Science and Technology Corporation, Kawaguchi, Saitama 332-0012, Japan

Received: date / Revised version: date

Abstract We have investigated the temperature dependence of the crystal structure of $\text{Ca}_{1.5}\text{Sr}_{0.5}\text{RuO}_4$ by powder and single crystal neutron diffraction in the temperature range from 1.5 to 300 K. Both an anomaly in the temperature dependence of the c lattice parameter and the observation of characteristic superstructure reflections indicate a continuous transition from the $I4_1/acd$ structure, in which the corner sharing RuO_6 octahedra are rotated about the c axis, to a low temperature phase with an additional rotation of the octahedra around an axis lying in the RuO_2 planes. The occurrence of this additional tilt distortion coincides with the previously observed change of the magnetic properties, from the nearly ferromagnetic state to the antiferromagnetic correlated state.

PACS number(s): 64.70.-p, 61.12.Ld, 74.70.-b

1 Introduction

Among the various Mott transition systems, in which the metal-insulator transitions are not driven by carrier doping (e. g. V_2O_3 , RENiO_3 [1]), the isoelectronic alloy series $\text{Ca}_{2-x}\text{Sr}_x\text{RuO}_4$ is rather unique because of its quasi-two-dimensional electronic structure [2] and the presence of the spin-triplet superconductor Sr_2RuO_4 [3, 4], as one of its end members. Shortly after the discovery of superconductivity in Sr_2RuO_4 it has been proposed, mainly inspired by the ferromagnetism in SrRuO_3 [5], that the superconducting coupling mechanism is mediated by ferromagnetic fluctuations. However, the other end member of this series, Ca_2RuO_4 is an antiferromagnetic insulator at low temperatures, with a highly distorted K_2NiF_4 -type crystal structure [6–9]. Since the substitution is isovalent, the structural distortions, characterized by rotation and tilting of the RuO_6 -octahedra, seem to play a

Send offprint requests to: O. Friedt¹, friedt@llb.saclay.cea.fr, Fax:33-(0)169088261

crucial role for the tuning of the distinct electronic and magnetic properties observed in $\text{Ca}_{2-x}\text{Sr}_x\text{RuO}_4$.

Recently S. Nakatsuji *et al.* [2] reported a drastic enhancement of the low-temperature magnetic susceptibility for $x \simeq 0.5$. While Sr_2RuO_4 is a paramagnetic metal, the Ca substitution for Sr leads to a continuous increase of the low-temperature susceptibility, indicating the enhancement of a ferromagnetic instability. Near $x \simeq 0.5$ $\chi(T \simeq 0)$ becomes maximal being almost 100 times larger than that of pure Sr_2RuO_4 . Decrease of the Sr content below $x = 0.5$ drives the system from the nearly ferromagnetic metallic state ($x \simeq 0.5$), via an intermediate antiferromagnetic correlated metallic state ($0.2 < x < 0.5$), to the antiferromagnetic insulating state for $x < 0.2$. As a continuation of previous structural studies [6, 7], we present in this brief report the results of neutron diffraction experiments carried out on a powder and single crystal sample with a Sr content $x = 0.5$, for which $\chi(T \simeq 0)$ is maximal.

2 Experimental

The polycrystalline $\text{Ca}_{1.5}\text{Sr}_{0.5}\text{RuO}_4$ sample used in this work was synthesized by standard ceramic processing methods as described elsewhere [10]. A single crystal of nominally the same composition $x = 0.5$ was prepared using a floating zone method in an infrared furnace [11].

Neutron powder diffraction experiments have been performed as a function of temperature using the high flux diffractometer G4.1 ($\lambda = 2.43 \text{ \AA}$) installed at the Orphée reactor. The temperature dependence of characteristic superstructure reflection intensities was studied by single crystal neutron diffraction on the two-axis-diffractometer 3T.1 using pyrolytic graphite monochromator and filters.

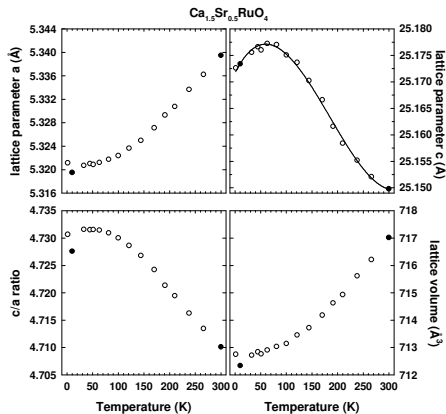


Fig. 1 Temperature dependence of lattice parameters of $\text{Ca}_{1.5}\text{Sr}_{0.5}\text{RuO}_4$. The open symbols denote the results obtained on G4.1 and the filled ones correspond to data taken from [7].

3 Results and discussion

The structure of $\text{Ca}_{1.5}\text{Sr}_{0.5}\text{RuO}_4$ has been recently reported to be tetragonal, space group $I4_1/acd$, with lattice parameters $a = 5.3395(1)$ Å and $c = 25.1498(6)$ Å at room temperature [7]. In space group $I4_1/acd$ the RuO_6 -octahedra are rotated around the c -axis with the octahedra separated by $c/2$ being distorted with an opposite phase. This explains the doubling of the c parameter in respect to the $I4/mmm$ symmetry. A similar structural distortion has been observed in the related compounds Sr_2IrO_4 , Sr_2RhO_4 and Ca_2MnO_4 [12–15] and agrees furthermore with the analysis of the phonon dispersion in Sr_2RuO_4 [16], which revealed that the system is very close to the structural instability with respect to the RuO_6 rotation.

The structure of $\text{Ca}_{1.5}\text{Sr}_{0.5}\text{RuO}_4$ was studied on G4.1 between 1.5 and 270 K. Figure 1 shows the temperature dependence of the lattice parameters. While the a parameter and the volume of the unit cell decrease upon cooling, showing an usual thermal expansion, the c parameter and the c/a -ratio increase at first, before decreasing below $T \simeq 65$ K. The negative thermal expansion of the c -axis between 100 and 300 K is rather peculiar for an layered oxide with K_2NiF_4 structure type, but seems to be a characteristic property of the $I4_1/acd$ symmetry [12,13,15]. At first sight this anomalous feature might be attributed to the increase of the octahedron rotation angle Φ upon cooling (between 295 and 11 K Φ increases from $12.43(3)^\circ$ to $12.78(3)^\circ$ [7]), since of the free positional parameter in $I4_1/acd$ structure only the x position of the oxygen in the RuO_2 planes changes significantly. However, the small temperature dependence

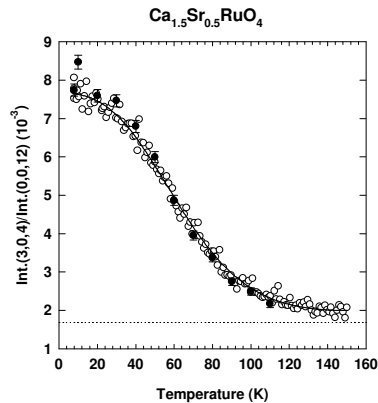


Fig. 2 Dependence of the intensity of the (304) superstructure reflection normalized to that of the (0012) fundamental reflection as function of temperature for a $\text{Ca}_{1.5}\text{Sr}_{0.5}\text{RuO}_4$ single crystal; the measurement was performed on the neutron diffractometer 3T.1. The data has been collected upon heating continuously with a rate of 0.5 K/min. (open circles) and at stabilized temperatures (filled circles).

of the rotation angle Φ excludes this as an explanation of the total effect occurring in c . Already pure Sr_2RuO_4 shows, in comparison with apparent layered K_2NiF_4 -type structures like $(\text{La,Sr})_2\text{CuO}_4$ or $(\text{La,Sr})_2\text{NiO}_4$ [18, 19], an unusual small thermal expansion of the c -axis: on cooling from 295 to 10 K the decrease of the a -axis is twice as large as that of the c -axis [20]. Since Sr_2RuO_4 remains undistorted down to lowest temperatures and is, furthermore, very close to the rotational instability, the observed anomalies of the thermal expansion of the c -axis of $\text{Ca}_{1.5}\text{Sr}_{0.5}\text{RuO}_4$ and the small contraction in pure Sr_2RuO_4 may instead have a dynamical origin rather than a static one. Therefore we conclude that some phonon mode Grüneisen parameters are negative, most likely those of the rotational modes.

The collected high flux patterns show no further indication of a phase transition, however the study of a small single crystal with nominally the same stoichiometry, on the two-axis-diffractometer 3T.1 revealed the appearance of several additional superlattice reflections, the $(h0l)$, with h odd and l even, which are forbidden in $I4_1/acd$ symmetry. In Figure 2 we show the temperature dependence of the (304) reflection intensity, which appears below $T \simeq 100$ K. The transition is continuous and the observed superstructure reflections clearly indicate a structural distortion, characterized by the tilt of the RuO_6 octahedra around an axis lying in the RuO_2 plane. As we deduce from the l dependence of these superstructure reflections the tilt distortion exhibits a different stacking period along the c -axis, with a 12.6 Å

periodicity, whereas the periodicity of the rotational distortion is $c \sim 25.2 \text{ \AA}$. Although the intensity of the superstructure reflections observed from the single crystal are not strong enough to be detected by neutron powder diffraction, the tilt deformations below 100 K explain the observed decrease of the c parameter, since the projection of the octahedra along c varies with the cosine of the tilt angle. We emphasize, that neither the collected high flux powder patterns nor the single crystal diffraction study revealed any indication for long range magnetic order down to $T = 1.5 \text{ K}$.

Recently band structure calculations [21,22] indicated a dominant role for the observed rotational and tilt deformations in the magnetic and electronic properties of $\text{Ca}_{2-x}\text{Sr}_x\text{RuO}_4$. In particular this theory suggests a significant enhancement of the ferromagnetic coupling due to the rotation of the RuO_6 octahedra, while the occurrence of the tilt deformation in the already rotationally distorted structure favors the antiferromagnetic state. This agrees well with our finding that the maximum in low temperature susceptibility coincides with the onset of the tilt distortion.

4 Conclusion

In summary we have presented a detailed study of the crystal structure of $\text{Ca}_{1.5}\text{Sr}_{0.5}\text{RuO}_4$ by neutron powder and single crystal diffraction. The negative thermal expansion of the c -axis suggests a negative Grüneisen parameter for the rotational mode of $\text{Ca}_{2-x}\text{Sr}_x\text{RuO}_4$. The coincidence of the observed tilt deformation in the sample and the maximum in the low-temperature susceptibility demonstrates the presence of a strong magnetoelectric coupling in the 214 ruthenates.

References

1. M. Imada, A. Fujimori, and Y. Tokura, *Rev. Mod. Phys.* **70**, 1039 (1998).
2. S. Nakatsuji, T. Ando, Z. Mao, and Y. Maeno, *Physica C* **259**, 949 (1999); S. Nakatsuji and Y. Maeno, *Phys. Rev. B* **62**, 6458 (2000); S. Nakatsuji and Y. Maeno, *Phys. Rev. Lett.* **84**, 2666 (2000).
3. Y. Maeno, H. Hashimoto, K. Yoshida, S. Nishizaki, T. Fujita, J.G. Bednorz, and F. Lichtenberg, *Nature (London)* **372**, 532 (1994).
4. K. Ishida, H. Mukuda, Y. Kitaoka, K. Asayama, Z. Q. Mao, Y. Mori, and Y. Maeno, *Nature (London)* **396**, 658 (1998).
5. A. Callaghan, C. W. Moeller, and R. Ward, *Inorg. Chem.* **5**, 1572 (1966); J. M. Longo, P. M. Raccach, and J. B. Goodenough, *J. Appl. Phys.* **39**, 1372 (1968).
6. M. Braden, G. André, S. Nakatsuji, and Y. Maeno, *Phys. Rev. B* **58**, 847 (1998).
7. O. Friedt, M. Braden, G. André, P. Adelman, S. Nakatsuji, and Y. Maeno, *Phys. Rev. B* **63**, 174432 (2001).
8. G. Cao, S. McCall, M. Shephard, J.E. Crow, and R.P. Guertin, *Phys. Rev. B* **56**, R2916 (1997).
9. C. S. Alexander G. Cao, V. Dobrosavljevic, S. McCall, J. E. Crow, E. Lochner, and R. P. Guertin, *Phys. Rev. B* **60**, R8422 (1999).
10. S. Nakatsuji, S. Ikeda, and Y. Maeno, *J. Phys. Soc. Jpn.* **66**, 1868 (1997).
11. S. Nakatsuji and Y. Maeno, *J. Solid State Chem.* **156**, 1 (2001).
12. M. K. Crawford, M. A. Subramanian, R. L. Harlow, J. A. Fernandez-Baca, Z. R. Wang, and D. C. Johnston, *Phys. Rev. B* **49**, 9198 (1994).
13. Q. Huang, J. L. Soubeyroux, O. Chmaissem, I. Natali Sora, A. Santoro, R. J. Cava, J. J. Krajewski, and W. F. Peck, Jr., *J. Solid State Chem.* **112**, 355 (1994).
14. M. A. Subramanian, M. K. Crawford, R. L. Harlow, T. Ami, J. A. Fernandez-Baca, Z. R. Wang, and D. C. Johnston, *Physica C* **235-240**, 743 (1994).
15. J. Takahashi and N. Kamegashira, *Mat. Res. Bull.* **28**, 565 (1993).
16. M. Braden, W. Reichardt, S. Nishizaki, Y. Mori, and Y. Maeno, *Phys. Rev. B* **57**, 1236 (1998).
17. L. M. Galvin, R. S. Perry, A. W. Tyler, A. P. Mackenzie, S. Nakatsuji, and Y. Maeno, *Phys. Rev. B* **63**, 161102 (2001).
18. P. G. Radaelli, D. G. Hinks, A. W. Mitchell, B. A. Hunter, J. L. Wagner, B. Dabrowski, K. G. Vandervoort, H. K. Viswanathan, and J. D. Jorgensen, *Phys. Rev. B* **49**, 4163 (1994).
19. J. Rodríguez-Carvajal, M. T. Fernández-Díaz, and J. L. Martínez, *J. Phys.:Condens. Matter* **3**, 3215 (1991).
20. T. Vogt and D. J. Buttrey, *Phys. Rev. B* **52**, R9843 (1995).
21. V. I. Anisimov, I. A. Nekrasov, D. E. Kondakov, T. M. Rice, and M. Sigrist, *cond-mat/0011460*.
22. Z. Fang and K. Terakura, *cond-mat/103223*.

Declaration

The work described in this thesis was carried out at the Laboratoire Léon Brillouin (CEA-CNRS), CEA-Saclay, and the Université Paris XI Orsay, during the period of April 1999 to January 2003. This thesis represents the author's original work, except where otherwise stated, and no part of it has been submitted for a degree at any other university.

A handwritten signature in black ink, appearing to read 'Oliver Friedt', with a stylized flourish at the end.

Oliver Friedt

Curriculum Vitae

OLIVER FRIEDT

- 28.11.1972 : Born in Cologne, Germany
- 08/1979 - 06/1983 : Elementary school in Cologne
- 08/1983 - 06/1992 : Grammar school in Cologne
- 06/1992 : Recieved the Abitur (A-level equivalent) from the
Georg-Büchner-Gymnasium, Cologne
- 10/1992 - 11/1998 : Study of Physics at the University of Cologne
- 11/1998 : Received the Diploma of Physics from the
University of Cologne
- 04/1999 : Ph.D. student at the Laboratoire Léon Brillouin,
CEA-Saclay, France
- 06/2003 : Ph.D. final examination

Paris, June 20, 2003

Remerciements

Ce travail a été effectué au Laboratoire Léon Brillouin (LLB) du CEA de Saclay. Je tiens à remercier Charles-Henri De Novion et Pierre Monceau, successivement directeurs du LLB pendant les années de ma thèse pour m'y avoir accueilli et pour m'avoir donné la possibilité de travailler dans d'excellentes conditions.

Je tiens également à remercier Prof. Dr. Alexandre Revcolevschi, directeur du Laboratoire de Physico-Chimie de l'Etat Solide à l'Université de Paris Sud pour m'avoir accueillie au sein de son laboratoire, pour l'intérêt qu'il a porté à ce travail et pour l'honneur qu'il me fait de bien vouloir présider le jury de cette thèse. Mes remerciements à Prof. Dr. Manfred Sigrist et Dr. Louis-Pierre Regnault pour avoir accepté d'être les rapporteurs de ce manuscrit, et pour tous leurs commentaires détaillés et suggestions pertinentes. Merci à Dr. Bernard Hennion d'avoir accepté de faire partie de mon jury de thèse, et pour tout l'intérêt qu'il a bien voulu porter à ce travail.

Ce travail a été réalisé sous la responsabilité du Prof. Dr. Markus Braden, qui a orienté cette étude tout au long de son développement pendant les dernières quatre ans. Grâce à ses grandes compétences scientifiques, son enthousiasme et son dynamisme, j'ai pu m'initier à la technique de diffusion élastique et inélastique de neutrons. Également, il a su guider mon esprit, tout en me permettant d'acquérir autonomie et détermination dans mon travail. Nos fréquents discussions et son attention qui a porté à l'évolution de ma thèse auront été très motivants et très instructifs. C'est avec un grand plaisir que je lui adresse mes remerciements.

Cette étude n'aurait pas été possible sans des échantillons de grande qualité élaborés à l'University of Kyoto par Dr. Satoru Nakatsuji et au Forschungszentrum Karlsruhe par Dr. Peter Adelman.

Je suis fort reconnaissant au Dr. Yvan Sidis pour les nombreuses discussions fructueuses que nous avons eu. Son enthousiasme et sa compétence scientifique ont été pour moi un exemple précieux. Également, je tiens à adresser mes remerciements à Dr. Pierre Pfeuty pour l'intérêt qu'il a porté à ce travail, ainsi que pour son investissement au niveau de la discussion des résultats expérimentaux.

Un grand merci à l'équipe de techniciens, P. Boutrouille, P. Baroni, F. Maignan et G. Engel qui ont grandement contribué à la bonne réussite des nombreuses expériences qui constituent l'essentiel de ce travail. Mes remerciements vont également au personnel administratif du LLB, tout particulièrement à Chantal Marais et Christelle Abraham pour leur efficacité et gentillesse.

Je remercie tous les autres thésards et post-docs du laboratoire pour leur assistance, leur encouragement et leur sourire de tous les jours: Sophie, Paula, Aziz, Laurence, Eric, Béatrice, Gaël, Stéphane, Pascale, Saâd, Cécile, Trong-Duc, Naïma, Giulia, Francesco, Ingo et beaucoup d'autres. Merci aussi à l'équipe "Schtroumpf" de l'Universität zu Köln: Daniel, Paul, Timo, Olaf, Matthias et Wolf-Dieter. J'adresse un remerciement particulier à Pascal pour son aide et son amitié dans les différentes

situations que nous avons rencontrés pendant nos séjours en France.

Enfin je remercie mes amis, Jochen, Ramin, Marc, Yvonne, Heike et mes parents, qui malgré la distance géographique, ont toujours été présents au bon moment: merci

!